Hemispheric Asymmetries of Magnetosphere-Ionosphere-Thermosphere Dynamics

by

Nicholas James Perlongo

A dissertation submitted in partial fulfillment
of the requirements for the degree of
Doctor of Philosophy
(Atmospheric, Oceanic, and Space Sciences)
in The University of Michigan
2017

Doctoral Committee:

Professor Aaron Ridley, Chair
Professor John Foster
Professor Mike Liemohn
Assistant Research Scientist Daniel Welling
Associate Professor Shasha Zou

Nicholas James Perlongo

nperlong@umich.edu

ORCID iD: 0000-0003-4780-0737

TABLE OF CONTENTS

LIST OF FIGURES

Figure

LIST OF TABLES

Table

LIST OF ABBREVIATIONS

MHD Magnetohydrodynamics

FACs field aligned currents

TEC Total Electron Content

TECU TEC-Unit, where 1 TECU = $10^{16}[e/m^2]$

M-I-T Magnetosphere-Ionosphere-Thermosphere

M-I Magnetosphere-Ionosphere

I-T Ionosphere-Thermosphere

SAPS Sub-auroral Polarization Streams

SEDs Storm Enhanced Densities

IMF Interplanetary Magnetic Field

EUV Solar Extreme Ultraviolet

$\mathbf{R}_e$ Earth radii

IGRF International Geomagnetic Reference Field

CIRs Co-rotating Interaction Regions

ICME Interplanetary Coronal Mass Ejections

TOI Tongue of Ionization

TADs Traveling Atmospheric Disturbances

CPCP Cross Polar Cap Potential

HP Hemispheric Power

PEFs Penetration Electric Fields

SWMF Space Weather Modeling Framework

GITM Global Ionosphere Thermosphere Model

MSIS Mass Spectrometer and Incoherent Scatter

IRI International Reference Ionosphere

TGCM Thermosphere General Circulation Model

TIGCM Thermosphere Ionosphere General Circulation Model

TIEGCM Thermosphere Ionosphere Electrodynamics General Circulation Model

TIMEGCM Thermosphere Ionosphere Mesosphere Electrodynamics General Circulation Model

RIM Ridley Ionosphere Model

TING Thermosphere Ionosphere Nested Grid

EUVAC EUV Flux Model for Aeronomic Calculations

FISM Flare Irradiance Spectral Model

CTIPe Coupled Thermosphere-Ionosphere-Plasmasphere Electrodynamics

CMIT Coupled Magnetosphere-Ionosphere-Thermosphere

MIX Magnetosphere-Ionosphere Coupler/Solver

LFM Lyon-Fedder-Mobarry

AMIE Assimilative Mapping of Ionospheric Electrodynamics

CCMC Community Coordinated Modeling Center

BATS-R-US Block Adaptive Tree Solar wind Roe-type Upwind Scheme

RBE Radiation Belt Electron

CRCM Comprehensive Ring Current Model

HEIDI Hot Electron Ion Drift Integrator

CIMI Comprehensive Inner Magnetosphere-Ionosphere Model

RCM Rice Convection Model

RCM-E RCM-Equilibrium

RAM Ring Current Atmosphere Interaction Model

RAM-SCB RAM with self-consistent magnetic field

DGCPM Dynamic Global Core Plasma Model

MBI Magnetic Boundary Index

SAMI3 ionosphere-plasmasphere model

GSWM Global Scale Wave Model

ICME Interplanetary Coronal Mass Ejection

UT Universal Time

LT Local Time

MLT Magnetic Local Time

K Kelvin

GPS Global Positioning System

Dst Disturbance Storm Time

GSE Geocentric Solar Ecliptic

GSM Geocentric Solar Magnetospheric

PE Prediction Efficiency

RMSE Root-Mean Square Error

DMSP Defense Meteorlogical Satellite Program

GUVI Global Ultra-Violet Imager

MPA Multiple-Particle Analyzer

SOPA Synchronous Orbiting Particle Analyzer

CHAMP CHAllenging Minisatellite Payload

LANL Los Alamos National Laboratory

NRL National Research Laboratory

ABSTRACT

Hemispheric Asymmetries of Magnetosphere-Ionosphere-Thermosphere Dynamics

by

Nick Perlongo

Chair: Aaron Ridley

The geospace environment, comprised of the magnetosphere-ionosphere-thermosphere system, is a highly variable and non-linearly coupled region. The dynamics of the system are driven primarily by electromagnetic and particle radiation emanating from the Sun that occasionally intensify into what are known as solar storms. Understanding the interaction of these storms with the near Earth space environment is essential for predicting and mitigating the risks associated with space weather that can irreparably damage spacecraft, harm astronauts, disrupt radio and GPS communications, and even cause widespread power outages. The geo-effectiveness of solar storms has hemispheric, seasonal, local time, universal time, and latitudinal dependencies. This dissertation investigates those dependencies through a series of four concentrated modeling efforts.

The first study focuses on how variations in the solar wind electric field impact the thermosphere at different times of the day. Idealized simulations using the Global Ionosphere Thermosphere Model (GITM) revealed that perturbations in thermospheric temperature and density were greater when the universal time of storm onset was such that the geomagnetic pole was pointed more towards the sun. This

universal time effect was greater in the southern hemisphere where the offset of the geomagnetic pole is larger. The second study presents a model validation effort using GITM and the Thermosphere Ionosphere Electrodynamics General Circulation Model (TIE-GCM) compared to GPS Total Electron Content (TEC) observations. The results were divided into seasonal, regional, and local time bins finding that the models performed best near the poles and on the dayside.

Diffuse aurora created by electron loss in the inner magnetosphere is an important input to GITM that has primarily been modeled using empirical relationships. In the third study, this was addressed by developing the Hot Election Ion Drift Integrator (HEIDI) ring current model to include a self-consistent description of the aurora and electric field. The model was then coupled to GITM, allowing for a more physical aurora. Using this new configuration in the fourth study, the ill-constrained electron scattering rate was shown to have a large impact on auroral results. This model was applied to simulate a geomagnetic storm during each solstice. The hemispheric asymmetry and seasonal dependence of the storm-time TEC was investigated, finding that northern hemisphere winter storms are most geo-effective when the North American sector is on the dayside.

Overall, the research presented in this thesis strives to accomplish two major goals. First, it describes an advancement of a numerical model of the ring current that can be further developed and used to improve our understanding of the interactions between the ionosphere and magnetosphere. Second, the time and spatial dependencies of the geospace response to solar forcing were discovered through a series of modeling efforts. Despite these advancements, there are still numerous open questions, which are also discussed.

CHAPTER I

Introduction

The northern and southern lights have long been a source of awe and wonder, but only recently have they and other space weather phenomena become so important to understand. While the Earth does have a protective atmosphere and magnetic field, many technological systems are at risk from space weather. Solar storms can irreparably damage spacecraft, harm astronauts, disrupt radio and Global Positioning System (GPS) communications, and even cause widespread power outages (*Pi et al.*, 1997; *Lanzerotti et al.*, 1998; *Vladimer et al.*, 1999; *Pulkkinen et al.*, 2017). The prediction and/or mitigation of these damaging events are predicated on a thorough understanding of the physical processes that constitute space weather. This is an incredibly challenging task. The space environment is tightly coupled to the solar atmosphere, the conditions of which change drastically on both short and long time scales. Discerning the fundamental physics from observations can be difficult because the distance between data points increases further away from Earth's surface. Space weather further challenges scientists as it harms the spacecraft used to observe it, thereby reducing the time period a satellite can collect data. However, as society's dependence on technology affected by space weather has increased, so have scientists' abilities to learn more about it.

The near Earth space environment is a vast and dynamic region characterized by

a multitude of plasma populations that interact in a dynamic and non-linear fashion. As such, sub-regions have been identified, not only for simplifying the larger system, but for developing numerical models built to specialize in a particular region. The three major regions concerning space weather are the magnetosphere, ionosphere, and the thermosphere. The magnetosphere is the region of space around Earth where its intrinsic magnetic field dominates the movement of particles (*Gold*, 1959). The ionosphere is a conducting layer of ionized gas that exists primarily above approximately 100 km (*Gardiner*, 1969). Ionospheric ions have multiple sources, but the most prevalent is a process called photoionization, where extreme ultraviolet radiation from the Sun splits electrons from neutrals in Earth's upper atmosphere, known as the thermosphere. While ancillary to space weather effects of electromagnetic origin, the thermosphere is also important because its density influences the amount of atmospheric drag satellites experience, which can alter their trajectory and reduce their operational lifetime (*Bruinsma et al.*, 2006). Each of these regions is further divided according to what fundamental physical processes are dominant. For example, it often makes sense to study the thermosphere and ionosphere in terms of specific latitudes because the source terms and magnetic field structure near the equator are significantly different than those in the polar regions where particles radiating from the Sun, called the solar wind, can often penetrate directly into the atmosphere. The increased radiation in the polar region is the reason why pilots and flight attendants are advised to limit their number of trans-polar flights every year (*Meier and Hubiak*, 2010).

Reductionism has revealed many ways in which the sub-regions interact under solar and atmospheric influence. Armed with this knowledge and increasingly powerful computational resources, many researchers have focused on the challenge of improving physical models and coupling them together to more accurately represent the system. An example of this is the Space Weather Modeling Framework (SWMF)

(*Tóth et al.*, 2005), which is a collection of models designed for particular regions. These and other efforts have resulted in significant advances which have begun to fit together the puzzle pieces that comprise space weather.

This chapter describes the most important regions in the geospace environment and how they react under solar forcing.

1.1 Earth's Neutral Atmosphere

The atmosphere as a whole is comprised of 78% nitrogen (N_2) and 21% oxygen (O_2), with additional molecules such as CO_2 and NO filling in the remainder. Air density above the surface decreases exponentially according to what is known as the hydrostatic relationship, given by

$$\frac{dP}{dz} = -\rho g, \tag{1.1}$$

where P is the atmospheric pressure, ρ is the density, g is the acceleration due to gravity, and z is the altitude. If this equation is solved to yield a relationship for density as a function of altitude, an exponential relationship is found:

$$\rho = \rho_0 e^{-\frac{z-z_0}{H}}, \tag{1.2}$$

where the subscripts refer to the surface, or reference height, and H is defined as the scale height,

$$H = \frac{\kappa T}{Mg}, \tag{1.3}$$

where κ is the Boltzmann constant, T is the temperature, and M is the mass of a molecule. This is an important parameter in atmospheric science, because it indicates the distance over which the atmospheric density decreases by a factor of e (~ 2.7). It is especially important in the thermosphere, because the density becomes so low that

the atmospheric constituents begin to separate, and their relative densities begin to change with altitude based on mass.

The Earth's atmosphere is comprised of four neutral layers prescribed by different temperatures/structures. Figure 1.2 provides an overview of each layer with its approximate location and temperature, or electron density in case of the ionosphere, which overlaps with the thermosphere, on the right. Note that the altitude is plotted on a log scale and that the temperature is in Kelvin (K).

The most familiar of these regions is the troposphere, which extends from the surface up to between 10 and 15 km and is characterized by a temperature drop from nearly 300 K to 210 K at the upper boundary, or tropopause. Electromagnetic radiation from the Sun is the Earth's primary energy input. Some of the $\sim$1360 W/m^2 energy flux is absorbed by the surface of the planet. The surface is the primary heat source for the troposphere, which explains why the temperature here decreases until the tropopause.

Above this height, the atmosphere begins to warm again as ozone (O_3) is effective at absorbing the ultraviolet portion of the Sun's radiation. This trend continues through the stratosphere until the ozone heating begins to decrease between 40-50 km. Moving further away from the surface is the mesosphere. This region is very hard to study because it is too high to reach for airplanes and high altitude balloons, but too low for satellites to fly because the air is too dense. This would cause excessive amounts of atmospheric drag and prevent a stable orbit. For this reason, many organizations choose this to be the beginning of space. The United States awards astronaut wings to those who travel above an altitude of 80 km. Temperatures reach a minimum at the mesopause around 100 km, due to radiative cooling of CO_2.

The thermosphere is much harder to describe because its properties depend on forcing from the lower atmosphere as well as the magnetosphere and solar wind. Particularly below 200 km, atmospheric tides and gravity waves introduce structure and

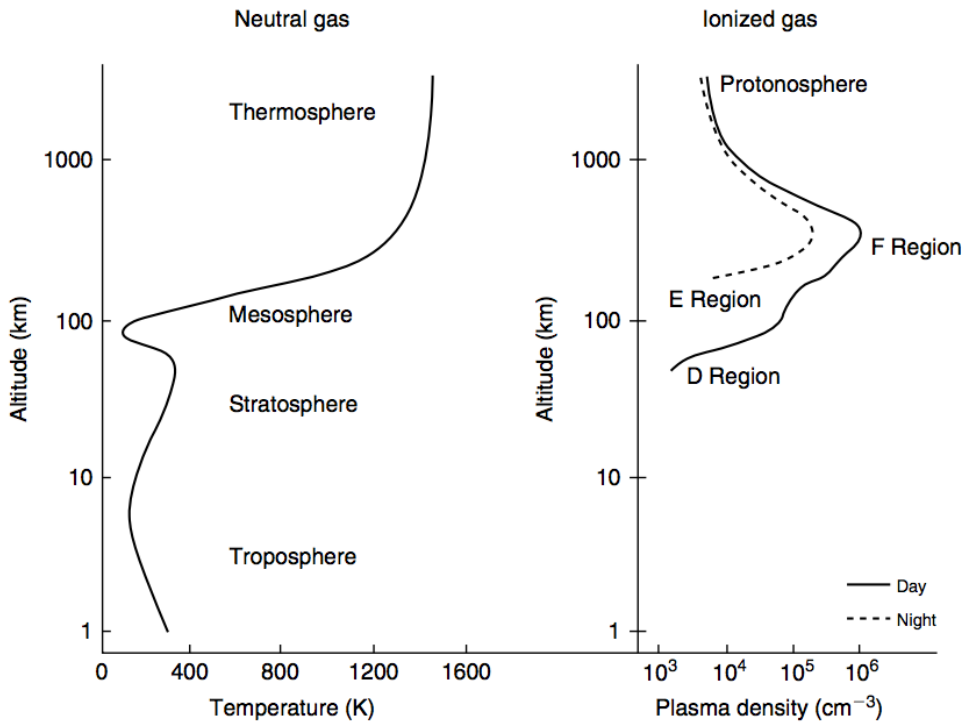

Figure 1.1: Earth's atmospheric layers divided by temperature. The electron density in the ionosphere is also displayed on the right.

density perturbations to the thermosphere (*Groves and Forbes*, 1984). The forcing from above varies significantly with solar activity. The Sun emits more or less electromagnetic and particle radiation depending on an 11 year solar cycle (*Moussas et al.*, 2005). The time of most radiation occurs during solar maximum, the least as solar minimum. The temperature in the thermosphere is both hotter and more variable during solar maximum and can sometimes exceed 2000 K. Based on equation 1.3, an increased temperature can increase the scale height of the molecules, causing the thermosphere as a whole to expand. The temperature can also change due to energy incident on the atmosphere from the magnetosphere and friction with the ions in the co-located ionosphere via a process known as Joule heating (*Richmond and Thayer*, 2000). Solar maximum also increases the prevalence of solar storms that can also increase the thermospheric temperature and density. These are transient events lasting from hours to days where the Sun is particularly active. The origins

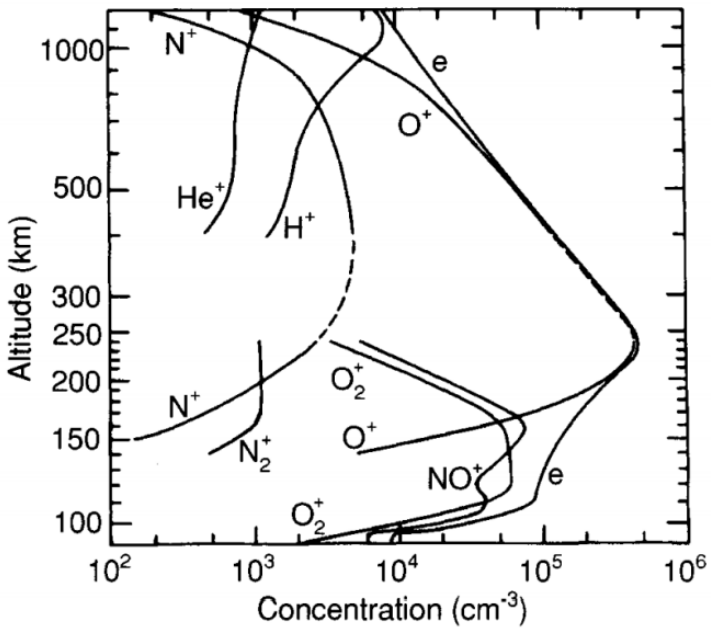

Figure 1.2: Approximate composition of the ionosphere based on solar quiet conditions on the dayside (*Johnson*, 1966).

and repercussions of these storms are introduced in Section 1.5. The thermospheric and ionospheric response to solar storms are presented in numerical modeling studies in Chapters III, V, VI.

1.2 The Ionosphere

Solar radiation in the thermosphere is strong enough to separate electrons from molecules and atoms in a process called photoionization. This creates a conducting layer of the atmosphere commonly known as the ionosphere. As Figure 1.2 suggests, the ionosphere consists of three layers that extend from 60 km to about 1000 km. The D region spatially overlaps with the mesosphere from 60-90 km and is primarily made up of NO^+ and O_2^+. This region of the ionosphere only exists during the daytime when photoionization occurs faster than chemical recombination with the neutral atmosphere.

Between 90 and 150 km lies the E layer of the ionosphere. Most of the bright

aurora is observed at these altitudes, which signals an additional source of ionization in addition to the day-side Solar Extreme Ultraviolet (EUV) driven ionization. The time scale for recombination in this region is on the order of seconds, resulting in significantly depleted electron densities at night if the precipitating particle source is turned off.

Above 150 km is the most permanent feature of the ionosphere, the F layer. The major constituent of the ionosphere switches here from NO^+ and $O_2^+$to O^+. This species remains dominant until 1000 km where H^+ takes over at the inner boundary of the plasmasphere. This transition to O^+ is a reason why the F layer is divided into two sub regions during the day, aptly named F_1 (150- 220 km) and F_2 (220-1000 km). Each of these layers has an electron density peak, but the F_2 layer peak is the largest and most important because it persists through the night. The peak occurs at the point where the confluence of photoionization and loss maximize. The loss comes from advection pushing the ions down, where they charge exchange and dissociatively recombine with neutrals. This means that above the F_2 peak, there is less photoionization because there is less neutral atmosphere to ionize, but below the peak chemical recombination occurs fast enough to reduce the electron density faster. The F_2 peak is very important for space weather because the maximum usable frequency for radio communications is directly dependent on the electron density here, which is known as NmF_2.

The E and F regions are very dynamic because of the interaction with both the thermosphere and magnetosphere. As such, the term Magnetosphere-Ionosphere-Thermosphere (M-I-T) coupling is often used to refer to this area of research. In addition to recombination, the neutrals also influence the ionosphere through ion-neutral coupling. These are complex interactions where the movement of ions can move neutrals, or vice versa (*Testud et al.*, 1975; *Blanc and Richmond*, 1980; *Thayer et al.*, 1995). Neutral winds in the thermosphere generally blow from day to night,

and from the summer to the winter hemisphere. These winds can push ions up or down along the Earth's magnetic field lines. If ions move away regions of higher neutral density (up the field lines), then the recombination rate becomes lower and the electron density increases (*Bramley and Young*, 1968). The ion motion is also controlled by electric fields imposed by the magnetosphere and solar wind. The electromagnetic force on a charged particle, q, is dependent on the surrounding electric, **E**, and magnetic, **B**, fields according to the Lorentz force law given by

$$\mathbf{F} = q(\mathbf{E} + \mathbf{v} \times \mathbf{B}), \tag{1.4}$$

which gives rise to a special case known as the $\mathbf{E} \times \mathbf{B}$ drift where the velocity of the bulk plasma flow of both ions and electrons, $\mathbf{v_E}$ is given by

$$\mathbf{v_E} = \frac{\mathbf{E} \times \mathbf{B}}{B^2}. \tag{1.5}$$

Ionospheric plasma is lost primarily due to processes known as radiative recombination and dissociative recombination. Recombination refers to the chemical process of an electron "re-combining" with a positively charged ion or molecule. A few of the most important chemical reactions are summarized in Table 1.1. The first two equations are dissociative recombination, which occurs when an electron recombines with a molecule and splits it in to atomic species. The third equation is radiative recombination, where the electron combines the atomic ion to create a neutral and releases energy in the form of a photon. The reaction rates in the second column indicated that dissociative recombination occurs much faster than radiative recombination and is therefore more important for the destruction of ionospheric plasma. These reactions are also dependent on the temperature of the plasma. The electron density loss rate has been found to increase when the electron temperature is low and the ion temperature is high (*Zhu et al.*, 2016).

Reaction	Rate Const. [cm^3s^{-1}]	Rx Type
$NO^+ + e^- \longrightarrow N + O$	$4.0 \times 10^{-7} (300/T_e)^{0.5}$	Dis. Recomb.
$O_2{}^+ + e^- \longrightarrow O + O$	$2.4 \times 10^{-7} (300/T_e)^{0.7}$	Dis. Recomb.
$O^+ + e^- \longrightarrow O + \nu$	$3.7 \times 10^{-12} (250/T_e)^{0.7}$	Rad. Recomb.
$O^+ + O_2 \longrightarrow O + O_2{}^+$	2.1×10^{-11}	Charge Ex.
$O^+ + N_2 \longrightarrow NO^+ + N$	1.2×10^{-12}	Intermediate Process
$O^+ + NO \longrightarrow NO^+ + O$	8.0×10^{-13}	Charge Ex.

Table 1.1: Chemical Reaction Rates for Ionospheric Loss.

Ions and neutrals also interact with each other in a process known as charge exchange. A few of these reactions are also summarized in Table 1.1. Charge exchange occurs when the positive charge state of an ion exchanges with a neutral molecule. It is important because the speed of recombination is dependent on the ion as previously discussed. In fact, ionospheric plasma are lost most quickly due to recombination of NO^+ which are produced by charge exchange of O^+ with N_2 (*Volland*, 1995). Since O is the primary constituent of the majority of the thermosphere, a larger O density leads to more O^+. As such, an important thermospheric parameter is the O/N_2 ratio. The higher the ratio, the more ion production there is relative to the amount of recombination occurring as a result of the two step process of charge exchange and dissociative recombination of N_2. The O/N_2 ratio is dependent on geomagnetic activity level, local time, season, and latitude (*Rishbeth et al.*, 1987; *Rishbeth and Müller-Wodarg*, 1999). Especially at mid and lower latitudes, the local O/N_2 ratio is also influenced by the lower atmosphere (e.g *Forbes*, 1996; *Immel*, 2005; *Scherliess et al.*, 2008; *Immel et al.*, 2009; *Goncharenko et al.*, 2010) via eddy diffusion which can cause vertical mixing of neutrals, uplifting N_2 and reducing O.

Bulk flows in the ionosphere are governed by both the $\mathbf{E} \times \mathbf{B}$ drift and the ion and neutral wind dynamos (*Vasylinas*, 2012). This is explicitly given by the simplified

ion momentum equation:

$$\mathbf{0} = c\frac{\mathbf{E}}{B} + \mathbf{v_i} \times \mathbf{B} - \frac{\nu_{in}}{\Omega_i}(\mathbf{v_i} - \mathbf{v_n}), \tag{1.6}$$

where ν_{in} is the ion-neutral collision frequency and Ω_i is the gyro-frequency of the ions. This refers to the basic plasma motion where charged particles spiral around magnetic field lines. The addition of the third term here is especially important below the F region of the ionosphere where ν_{in} is greater. The implication of this is that the ions are more tightly coupled to the magnetic field lines in the F region, and that the neutral wind is more important for plasma flow at lower altitudes. Since electrons are so much smaller than ions their collision frequency with the thermosphere is much smaller than the ions. As a result, the electrons $\mathbf{E} \times \mathbf{B}$ drift at all altitudes in the E and F region ionosphere. Electric currents perpendicular to the magnetic field lines must flow in the ionosphere, such that:

$$\mathbf{j}_\perp = \sigma_P \mathbf{E}' + \sigma_H \hat{\mathbf{B}} \times \mathbf{E}', \tag{1.7}$$

where σ_P is the Pedersen conductivity and σ_H is the Hall conductivity. These are two very important quantities in ionospheric physics because they dictate how easily plasma can flow in the ionosphere. The Pedersen component is most effective at transferring momentum to the thermosphere because its magnitude is larger where the neutral densities are smaller. Conductance is generally much higher on the dayside, but the aurora can increase the nightside conductance by an order of magnitude during large geomagnetic storms. The Joule heating, caused by the dissipation of electromagnetic energy via friction between the plasma and the neutral gas, is also directly proportional to the Pedersen conductivity (*Richmond and Thayer*, 2000).

The neutral wind dynamo can also change the altitude of the ionosphere. At the geomagnetic equator, the Earth's magnetic field lines are nearly horizontal to the

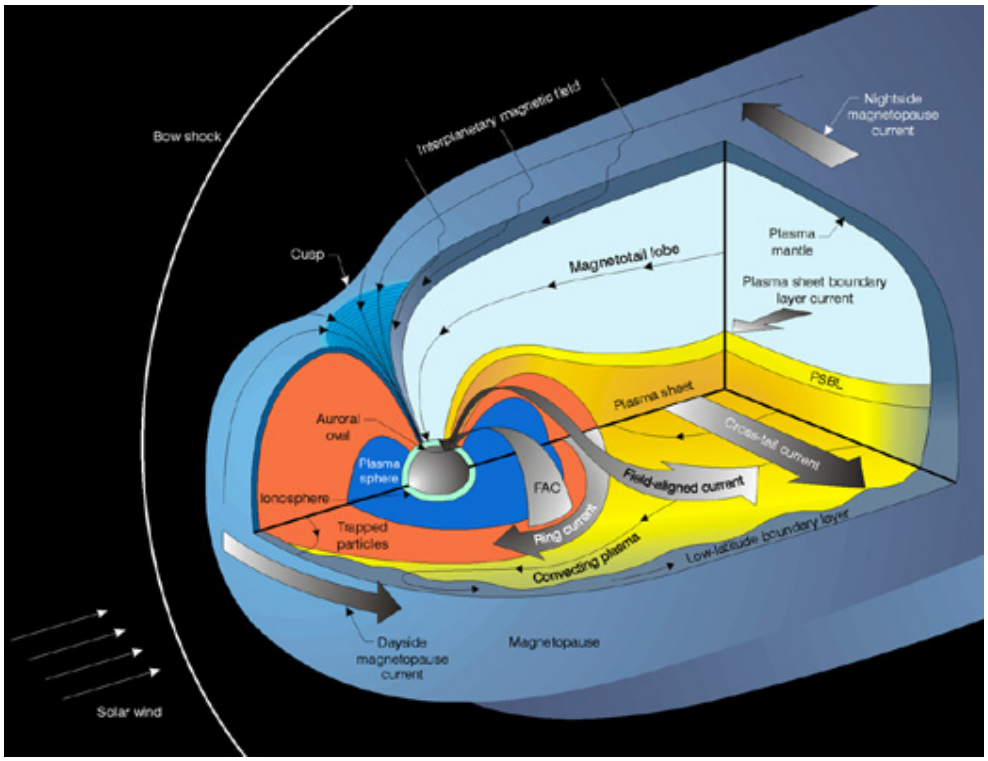

Figure 1.3: Earth's magnetosphere including currents and plasma populations. Courtesy of Southwest Research Institute.

surface, so this drift can push plasma upwards. This mechanism creates two large peaks in electron density +/- 10° from the geomagnetic equator and is known as the equatorial anomaly (*Appleton*, 1946).

1.3 The Magnetosphere

The magnetosphere is shaped by the interaction of Earth's intrinsic magnetic field with the supersonic solar wind. It presents an obstacle to solar wind such that the magnetic field becomes tear drop shaped like a rock in a stream of water. The sunward edge of the magnetosphere is known as the magnetopause and is located about 10 Earth radii (R_e) away where the magnetic pressure of the geomagnetic field balances the dynamic pressure of the solar wind. The magnetotail stretches hundreds of R_e behind the planet. The magnetopause is denoted by the blue boundary in Figure

1.3. Note that the entire upper atmosphere is contained within the thin cyan shell around the Earth in this image. The magnetic north pole on the Earth is located in the geographic south pole. A consequence of this is that the magnetic field direction is towards the northern hemisphere. This is why a compass points north.

The quasi-dipolar magnetic field is both tilted and offset from the center of the planet. This means that there are large asymmetries in the geomagnetic field, both between the poles and in the equatorial region (*Shepherd*, 2014). In addition, there are crustal fields that locally modify the magnetic field (*Mandea and Purucker*, 2005). Stronger and more frequent storms occur during the equinoxes compared to solstices. This has been known for nearly 170 years (*Broun*, 1848; *Sabine*, 1856; *Cliver et al.*, 2000). The Russell-McPherron effect (*Russell and McPherron*, 1973) occurs because Earth's magnetic field equator is inclined compared to the solar equatorial plane. During the equinoxes, more of the Interplanetary Magnetic Field (IMF) B_y in Geocentric Solar Ecliptic (GSE) coordinates contributes to IMF B_z in the Geocentric Solar Magnetospheric (GSM) coordinate system. This increases geomagnetic activity since IMF B_z is the primary controller of magnetic reconnection (*Dungey*, 1961). It has also has been suggested that the seasonal variation of the angle between the solar wind flow direction and Earth's dipole axis changes the efficiency of the coupling between the solar wind and the magnetosphere (*Cliver et al.*, 2000).

Seasonal variations in the Ionosphere-Thermosphere (I-T) system are also driven by the offset between the geomagnetic and geographic poles as well as differences in magnetic flux densities between the two hemispheres (*Förster and Cnossen*, 2013; *Cnossen et al.*, 2012b; *Perlongo and Ridley*, 2016; *Cnossen and Förster*, 2016; *Laundal et al.*, 2016). The distance between the geographic and geomagnetic pole is 8° larger in the southern hemisphere (SH) (*Mandea et al.*, 2000). One might expect the smaller tilt angle in the northern hemisphere (NH) to increase the CPCP and subsequent convection plasma drift speeds (*Cnossen and Richmond*, 2012), but the opposite

occurs (*Papitashvili and Rich*, 2002; *Förster and Haaland*, 2015; *Pettigrew et al.*, 2010). However, there is less spatial variation in neutral winds in the NH (*Förster and Cnossen*, 2013) possibly because the small offset aligns the geographic phenomenon, like pressure gradient and Coriolis forces, with ion drag from the magnetospherically imposed convection electric field (*Cnossen and Förster*, 2016). The magnetic field strength is weaker overall in the SH than in the NH, which has been shown to reduce the high latitude electric field strength, but not the resulting $\mathbf{E} \times \mathbf{B}$ drift (*Cnossen et al.*, 2011, 2012a). This drift is important for TEC because the atmosphere can be expanded via joule heating resulting from friction between ions and neutrals. When this expansion occurs, the electron recombination rate is increased as the neutral density in the F-region is increased. The neutral winds can also push plasma up magnetic field lines to altitudes with lower recombination rates, thereby increasing the TEC. In fact, reduced magnetic flux density has also been found to alter the height of the F_2 peak of the ionosphere (*Cnossen et al.*, 2012a; *Sojka and Schunk*, 1997).

The location of the geomagnetic pole in each hemisphere controls where magnetospheric electric fields and auroral particles deposit energy into the thermosphere. For example, regions of energetic particle precipitation roughly vary in accordance with convection and potential patterns (*Foster et al.*, 1986; *Singh et al.*, 2013; *Mitchell et al.*, 2013), the location of which are heavily influenced by the location of the Earth's geomagnetic pole. The International Geomagnetic Reference Field (IGRF) (*Finlay et al.*, 2010) has determined the geographic location of the northern geomagnetic pole to be 80.37° latitude and -72.63° longitude, and the southern at -80.37° latitude and 107.37° longitude, in 2015.

The movement and composition of the magnetosphere can only be understood in terms of the solar wind and the IMF it carries with it (*Parker*, 1958). The IMF is an extension of the Sun's magnetic field that interacts with the magnetosphere in

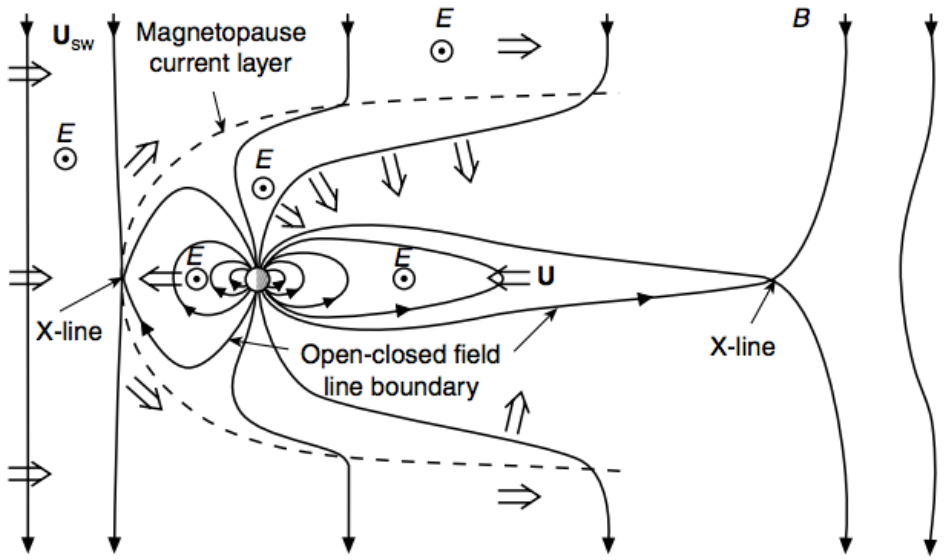

Figure 1.4: Diagram of magnetospheric circulation imposed by the solar wind (*Schunk and Nagy*, 2004).

a process known as magnetic reconnection. A depiction how magnetic reconnection combined with the solar wind drive circulation in and around the magnetosphere is shown in Figure 1.4. Magnetic reconnection occurs when the vertical component of the IMF (B_z), is negative. Since Earth's magnetic field lines cannot cross each other, the northward orientation of the magnetic field at the magnetopause forms an X-line with the southward IMF. It is called an X-line because the magnetic field lines create a similar shape to an "X" before magnetic reconnection occurs. Two important processes occur during magnetic reconnection. The first is that potential energy contained in the magnetic field is converted to kinetic energy and transferred to the plasma along the field lines. The second is that the Earth's magnetic field line breaks like a rubber band and is then swept back towards the magnetotail. During this phase, the magnetic field lines are attached to the Earth on one end, and open to the solar wind on the other, allowing direct entry of plasma to the upper atmosphere. This region of open magnetic field lines is called the polar cap. As the two magnetic field lines move across the polar caps (one in the north, one in the south), magnetic tension brings them back towards each other in the magnetotail, forming another X-line, this

time directed horizontally instead of vertically like at the dayside magnetopause. At this point, plasma is accelerated towards the Earth by an electric field imposed by the solar wind that points from dawn to dusk. This is called the convection electric field in the magnetosphere and is also an $\mathbf{E} \times \mathbf{B}$ drift. This Earthward moving plasma streams along magnetic field lines that are pushed back towards Earth in a process called dipolarization. This entire process of reconnection and the dayside, nightside, and subsequent circulation is known as the Dungey cycle (*Dungey*, 1961).

1.3.1 The Ring Current

The ring current carries the majority of the energy density and plasma pressure in the magnetosphere, making it an important plasma population in the M-I system. An accurate description of the ring current is therefore essential for geophysics systems research as well as space weather applications (*Daglis et al.*, 2009). The ring current is created in the inner magnetosphere between approximately 2.5 and 8 R_e by gradient-curvature drift plasma motions. In a non-uniform magnetic field such as the magnetosphere, particles move into regions of different magnetic field strength, which imposes a drift velocity,

$$\mathbf{v}_{\nabla B} = \frac{K_\perp}{qB} \frac{\mathbf{B} \times \nabla B}{B^2}, \tag{1.8}$$

where $K_\perp$ is the kinetic energy of the particle perpendicular to the magnetic field. Since the drift velocity is inversely proportional to the charge, q, electrons and ions drift in opposite directions. Since particles are following curved magnetic field lines, there is also a curvature drift pointed away from the radius of curvature. When plasma from the magnetotail $\mathbf{E} \times \mathbf{B}$ drifts into a region of larger magnetic field strength, the gradient-curvature drift becomes dominant, driving the ions towards dusk and the electrons towards dawn. This process creates the ring current. The strength of the

ring current can be directly measured at Earth's surface through the measuring of the decrease in the horizontal component of Earth's magnetic field. This is the origin of the Disturbance Storm Time (Dst) index that is used to measure the strength of geomagnetic storms, which energize the ring current and cause large depressions in Earth's magnetic field strength (*Tsyganenko et al.*, 2003; *Le et al.*, 2004). Storms are discussed in Section 1.5.

As particles are depleted from the ring current, they create the diffuse aurora. The diffuse aurora is the more featureless glow that can extend across the horizon. There are also very bright and sometimes rapidly moving arcs that often occur within or poleward of the diffuse auroral oval, known as discrete auroral arcs. Each type of aurora is produced by solar wind interactions with the magnetosphere. Both types are important to understand as they influence the strength and location of electric fields in the Earth's upper atmosphere (*Weimer et al.*, 1985; *Marklund*, 2009).

Electrons in the ring current are predominantly lost to the upper atmosphere via pitch angle scattering by plasma waves in the inner magnetosphere (e.g *Shprits et al.*, 2008a,b; *Thorne et al.*, 2010). The pitch angle of a particle refers to the direction of its velocity relative to the magnetic field line. A pitch angle of 90° means the particle gyrates perpendicular to the field line, 0° means it is moving only along the magnetic field. When particles travel along magnetic field lines into regions of higher magnetic field strength they can reverse directions at what is called a mirror point. Interaction with plasma waves causes the velocity of the electron parallel to the magnetic field to increase. This causes its mirror point to reach a low enough altitude where it can collide with the upper atmosphere before bouncing back to the magnetosphere (*Kennel*, 1969; *Lyons et al.*, 1972). The pitch-angle distributions resulting in precipitation are known as loss cone distributions. The types of waves responsible for such scattering have been found to be dependent on location. Electron cyclotron harmonic waves are dominant beyond 8 R_E (*Ni et al.*, 2012), while whistler

chorus waves on the nightside are the primary cause of auroral precipitation closer to the Earth (*Thorne et al.*, 2010; *Ni et al.*, 2011a,b). Plasmaspheric hiss also contributes to loss (*Lyons et al.*, 1972; *Albert*, 1994).

The inclusion of these wave-particle interactions in ring current models is difficult since measurements of wave distributions, amplitudes, and frequencies are typically not available in tandem with plasma density observations (*Chen et al.*, 2015). Consequently, a number of empirical models have been developed to approximate the pitch angle scattering rates. The first of these assumed strong scattering in all regions (*Schulz*, 1974). Strong scattering is defined as when the pitch angle diffusion coefficient is much greater than $\alpha_c^2\Omega$, where α_c is the particle's pitch angle and Ω is its bounce frequency (*Kennel*, 1969). The mean lifetime of a particle then approaches a minimum value, τ, which is dependent on the pitch angle, but not the diffusion coefficient (*Schulz*, 1974). More recent plasma sheet particle and wave observations have shown that pitch angle diffusion is not strong everywhere (*Schumaker et al.*, 1989; *Gough et al.*, 1979; *Belmont et al.*, 1983; *Roeder and Koons*, 1989; *Meredith et al.*, 1999, 2000). Simulations with only strong pitch angle diffusion have also demonstrated too high of a scattering rate in this limit (*Chen and Schulz*, 2001; *Chen et al.*, 2005, 2015). In light of this, models were developed where the pitch angle diffusion transitions from strong to weak closer to the Earth (*Chen and Schulz*, 2001; *Chen et al.*, 2005), but without dependence on geomagnetic activity. Chorus wave scattering electron lifetimes were then parametrized on the dayside and nightside which varied by energy, geocentric distance, as well as the Kp index (*Gu et al.*, 2012; *Orlova and Shprits*, 2014). Plasmaspheric hiss electron losses were similarly parametrized by *Orlova and Shprits* (2014) and *Orlova et al.* (2016).

Also associated with the ring current are the region 2 field aligned currents (FACs), located near the auroral zone in the ionosphere (*Wolf et al.*, 1982). These currents flow into the ionosphere on the duskside, and away on the dawnside (*Schield et al.*,

1969; *Weimer et al.*, 1987). They are produced by azimuthal pressure gradients and gradients in flux tube volume that arise in the inner magnetosphere (*Vasyliunas*, 1970; *Wolf*, 1970; *Fok et al.*, 2001).

1.4 High-latitude electrodynamics

The magnetic field lines involved with the Dungey cycle depicted in Figure 1.4 are always connected to the ionosphere in at least one hemisphere. This circulation can therefore be mapped to the ionosphere where the plasma flow is largely controlled by the movement of the magnetic field lines. Figure 1.5 is a synoptic view of these footprints combined with the FACs and ionospheric electric fields. This is often called a "two-cell" convection pattern, and is extremely important for M-I-T coupling. The continuous solid black lines represent the footprints of the magnetic field lines with arrows indicating their flow direction. Note that the flow is anti-sunward over the polar cap as field lines reconnect and are swept tailward by the solar wind. Once they reach the nightside X-line they begin to move back towards the dayside on both the dawn and dusk sides in the auroral zone (*Heelis et al.*, 1982). The Pedersen currents flow along the direction of the electric field and close the current loop between the FACs. Hall and Pedersen conductivities regulate the potential pattern in the ionosphere, which then map back along field lines to the magnetosphere (*Nopper and Carovillano*, 1978), driving electric fields and establishing a feedback loop (*Vasyliunas*, 1970). The resulting magnetospheric convection electric field transports plasma into the inner magnetosphere (*Ebihara et al.*, 2004; *Liemohn et al.*, 2005). Often during geomagnetic storms, the plasma pressure in the inner magnetosphere can not react quicjly enough to the rapidly changing reconnection electric field, such that the region 2 FACs are much weaker than the region 1 FACs, resulting in ionospheric electric fields equator-ward of the auroral oval known as Penetration Electric Fields (PEFs) (e.g. *Burke*, 2007). Heavy ion injection to the ring current from plasma

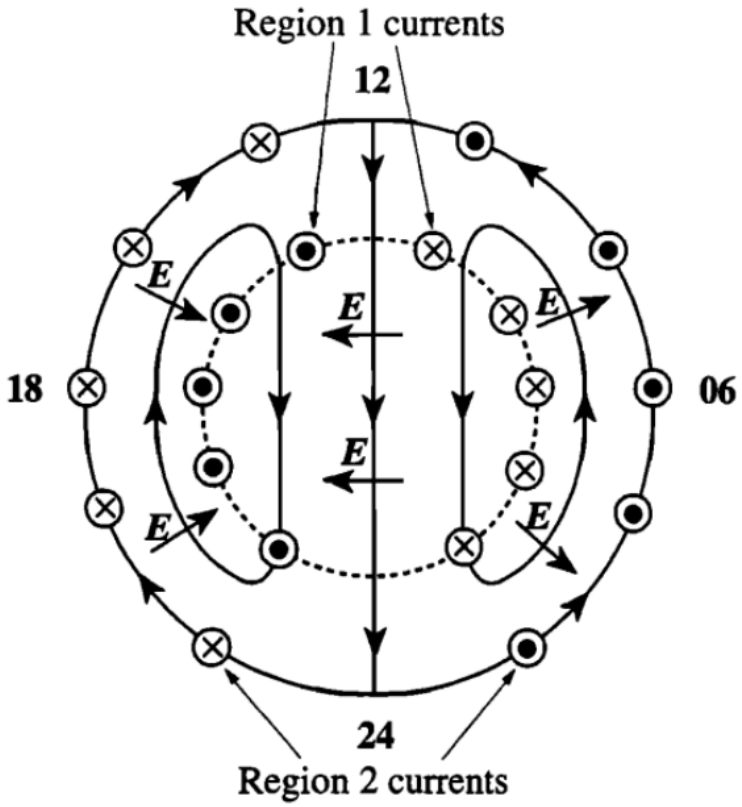

Figure 1.5: Schematic of Dungey-cycle flow mapped into the ionosphere, where the arrowed solid lines are the plasma streamlines, the short arrows give the direction of the electric field, and the dashed line is the open-closed field line boundary. The Hall current flows around the plasma streamlines opposite to the flow, while the Pedersen current flows in the direction of the electric field. The direction of the FAC flow associated with the horizontal divergence of the ionospheric currents is indicated by the circular symbols, where circled dots indicate upward currents out of the ionosphere, while circled crosses indicate downward currents into the ionosphere (*Cowley*, 2000).

accelerated out of the ionosphere has also been shown to influence electrodynamics in the M-I system (*Welling et al.*, 2015b). Simulation studies have revealed that heavy ion outflow can lead to FAC intensification that can influence the electric fields (*Kronberg et al.*, 2014; *Welling et al.*, 2015a).

It should now be evident that the magnetosphere and ionosphere are intricately coupled by the motion of magnetic field lines, current systems, and exchange of plasma through precipitation and outflow. All of these are driven by solar wind-magnetosphere interactions that depend on solar activity.

1.5 Geomagnetic Storms

Much of space weather research is focused around the study of geomagnetic storms, which is simply the term used to describe when a solar storm interacts with the magnetosphere (*Webb et al.*, 2001). There are two major types of solar storms: Co-rotating Interaction Regions (CIRs), and Interplanetary Coronal Mass Ejection (ICME)'s. CIRs occur when ambient solar wind is overtaken by fast solar wind emanating from regions of open magnetic field lines in the solar atmosphere called coronal holes. ICME's refer to ejecta or magnetic clouds (*Zhang et al.*, 2007) that split off from magnetic reconnection at the Sun. In magnetic cloud ICME's, the IMF is enhanced and rotates through a large angle (*Klein and Burlaga*, 1982). ICME's can travel at velocities exceeding 2000 km/s, allowing them to arrive at earth just 20 hours after leaving the Sun. CIRs are generally slower, around 800 km/s, and produce fewer very large geomagnetic storms compared to ICME's, but they tend to last longer than ICME driven storms and are often associated with a geo-effect magnetic cloud. ICME's are sometimes accompanied by solar flares, that can greatly enhance the X-Ray and EUV irradiance.

1.5.1 Storm Effects

A number of quintessential electrodynamic features of the M-I system contribute to space weather effects during geomagnetic storms, two of which are Sub-auroral Polarization Streams (SAPS) (*Foster and Burke*, 2002; *Foster*, 2002) and sub-auroral ion drifts (SAID) (*Spiro et al.*, 1978; *Anderson et al.*, 1991, 1993). SAIDs are narrow regions ($\sim 1^{\circ}$) of westward drifts with highly variable velocities that sometimes exceed 5000 m/s, corresponding to an electric field of approximately 250 mV/m (*Erickson et al.*, 2002). Occurring about 80% of the time in the pre-midnight sector (*Anderson et al.*, 2001), SAPS are the broader and more permanent feature of westward convection. They are located equator-ward of the auroral oval usually between dusk and midnight, but can extend well towards the noon and post-midnight sectors. SAPS are an important ionospheric phenomenon because they relate to a number of ionospheric features including, but not limited to, mid-latitude density troughs (*Muldrew*, 1965; *Middleton et al.*, 2008; *Yang et al.*, 2016), Storm Enhanced Densities (SEDs) (*Huba and Sazykin*, 2014), and plasmaspheric plumes (e.g. *Spiro et al.*, 1978; *Anderson et al.*, 1991; *Foster and Burke*, 2002; *Zou et al.*, 2013; *Foster et al.*, 2014). Eastward electric fields during geomagnetic storms can almost eliminate the equatorial F-layer, by lifting it so high that the plasma falls down along magnetic field lines into the mid-latitude ionosphere (*Greenspan et al.*, 1991; *Basu et al.*, 2001). Dayside plasma is often extended through the cusp and into the polar cap during times of enhanced convection electric fields. This is known as a Tongue of Ionization (TOI) (*Sato and Rourke*, 1964; *Knudsen*, 1974; *Thomas et al.*, 2013). Sudden ionosphere disturbances also occur during solar flares when photoionization increases from enhanced solar irradiance (*Donnelly*, 1967).

Many of these features are at least partially studied through their relationship with TEC, the height integrated electron density in the ionosphere. TEC observations have become prevalent with the widespread use of GPS. GPS can determine TEC

by measuring the difference in transit times of two radio frequencies (1575.42 MHz and 1227.60 MHz) between a transmitting GPS satellite and the receiver (*Mannucci et al.*, 1998). The relative precision of TEC provided by GPS measurements is on the order of 0.01 TECU with an absolute accuracy of 1-3 TECU (*Mannucci et al.*, 1998; *Tsurutani*, 2004), where 1 TECU = 10^{16} electrons m^{-2}.

There are variations in TEC by season (*Wright*, 1963; *Tsurutani*, 2004; *Mannucci*, 2005; *Mendillo et al.*, 2005; *Adimula et al.*, 2016), latitude (*Liu et al.*, 2009b), local time (*Scherliess et al.*, 2008), and the solar irradiance and activity level (*Fejer et al.*, 1979; *Forbes et al.*, 2000; *Liu et al.*, 2009a). Energetic particles from the solar wind and other geomagnetic events constitute another important source of TEC, especially at higher latitudes (*Buonsanto*, 1999; *Fuller-Rowell et al.*, 2006; *Mendillo*, 2006; *Tsurutani et al.*, 2009; *Zhu and Ridley*, 2014).

Geomagnetic storms can also profoundly affect the thermosphere. As magnetospheric convection intensifies, joule heating increases the temperature of the high latitude thermosphere. This causes the thermosphere to expand and increases the drag on low altitude satellites (*Bruinsma et al.*, 2006; *Zhou et al.*, 2009). The accuracy of accelerometer derived thermospheric densities and winds has improved in recent years (e.g. *Sutton et al.*, 2007; *Sutton*, 2009), making it possible to examine the disturbed and quiescent state of the thermosphere. For example, *Ritter et al.* (2010) found that the polar thermospheric density increased by 4-15% during substorms, depending on the level of geomagnetic activity. The variable energy input during storms also leads to the creation of wave structures known as Traveling Atmospheric Disturbances (TADs) (*Richmond and Matsushita*, 1975; *Lu et al.*, 2014). These waves can travel at 1-2 km/s and are dissipated via collisions with ions. This is one way in which energy is transferred from the polar regions to mid-latitudes, and even the opposite polar hemisphere, as will be seen in Chapter III.

1.5.2 Outstanding Questions

This Chapter has described the most fundamental properties and dynamics of the geospace environment. Given this information, there are a number of open questions still to be pursued. The response of the M-I-T system to solar forcing is dependent on multiple time and location scales. Furthermore, current numerical models have many limitations that need to be evaluated, improved, and validated with observations. As such, a major goal of the work in this thesis is to answer the following questions.

- What are the differences, strengths, and weaknesses of current and previous numerical models developed to simulate geomagnetic storms in the upper atmosphere and inner magnetosphere?

- What is the dependence of model configuration on storm time simulation results? Which models capture the relevant physics most precisely as compared to observations?

- How does the description of electron scattering in the inner magnetosphere influence the ability of coupled models to capture the electrodynamic feedback loop between the ionosphere and the magnetosphere?

- How is the response of the upper atmosphere to geomagnetic storms dependent on the universal time of storm onset? Furthermore, what are the factors leading to this dependence? Are they asymmetrical between hemispheres?

- What is the seasonal variation of the ionospheric response to storms in terms of TEC? What are the primary processes behind this seasonal variation in each hemisphere at different latitudes and longitudes?

1.5.3 Outline

The questions introduced in Section 1.5.2 are investigated in the following Chapters. Chapter II presents a brief history of numerical models of the upper atmosphere and inner magnetosphere. It also describes a new contribution to a ring current model in which the auroral description was improved. Chapter III presents a thermospheric modeling effort to elucidate the universal time effect of the thermosphere to solar wind electric field changes. Chapter IV describes a model comparison and validation effort between two of the leading I-T models and GPS TEC. This study focused on discovering the biases of each model based on local time and latitude in terms of TEC the entire year of 2010, so as to study seasonal effects as well. The study in Chapter V used the new model configuration to investigate the electrodynamic impact of various descriptions of the diffuse aurora for multiple geomagnetic storms. Chapter VI simulated the upper atmosphere during one storm with a wide variety of high latitude particle precipitation and electric field models. The hypothetical scenario of the storm occurring at different seasons was investigated considering hemispheric asymmetry and universal time dependencies. Finally, Chapter VII concludes by summarizing the overall findings of this research, as well as suggests numerous ideas for future work to advance the scientific communities understanding of the M-I-T system.

CHAPTER II

Methodology

Numerical models are an invaluable resource for researchers because the geospace environment is so vast and difficult to observe. The first ever space physics model was developed in 1931 by Sydney Chapman (*Chapman*, 1931). Since then, models have become increasingly sophisticated through the implementation of increasing numbers of observations, a better understanding of the fundamental physics, and advances in computing power.

Numerical models are either empirical or physics based. Empirical models are generally very quick to run and give solutions based on statistical fits to previous observations. For example, one of the most widely used empirical models for the thermosphere is the Mass Spectrometer and Incoherent Scatter (MSIS) model (*Hedin*, 1983, 1987, 1991). MSIS provides for the temperature and density of the thermosphere based on solar flux and geomagnetic activity level. A similar model exists for the ionosphere called the International Reference Ionosphere (IRI) (*Rawer et al.*, 1978; *Bilitza*, 2001). Shortcomings of these models are that they are time invariant and their accuracy is highly variable. IRI, for example, has been shown to have errors in its electron density calculations by up to 50% (*Themens et al.*, 2014). However, the models are frequently used because of their efficiency and ability to represent the upper atmosphere reasonably well during nominal conditions. Time dependent physics

based models regularly employ them to specify initial and boundary conditions.

2.1 I-T Models

The first of the self-consistent physics models for the upper atmosphere was the Thermosphere General Circulation Model (TGCM) (*Dickinson et al.*, 1981). The model used MSIS to specify the initial conditions, assumed hydrostatic equilibrium, and included heating only from solar radiation and auroral precipitation. The model was then advanced to include interactions with the ionosphere, as well as an improved auroral zone that included the two-cell convection pattern from an empirical model. This was known as the Thermosphere Ionosphere General Circulation Model (TIGCM) (*Roble and Ridley*, 1987; *Roble et al.*, 1987). The need for self-consisntent electrodynamic coupling between the ionosphere and thermosphere was addressed a few years later in the creation of the Thermosphere Ionosphere Electrodynamics General Circulation Model (TIEGCM) (*Richmond*, 1992), a model frequently used today. This model is able to simulate the motion of both the ions and the neutrals by incorporating electric fields imposed by neutral winds up to 65° latitude. The next model upgrade came in the form of coupling with the mesosphere and upper stratosphere in Thermosphere Ionosphere Mesosphere Electrodynamics General Circulation Model (TIMEGCM) (*Roble and Ridley*, 1994). The lower boundary of the model was extended from 97 km in TIEGCM to 30 km. This model is often used today, especially for looking at the influence of tides and gravity waves on the upper atmosphere. It has a pressure based coordinate system and assumes hydrostatic equilibrium.

The next extension of TIGCM was the Thermosphere Ionosphere Nested Grid (TING) model (*Wang et al.*, 1999, 2004), which used nested grids in latitude and longitude. This allowed the model resolution to vary within the simulation domain, which provided an invaluable resource for researchers to study either small scale

structures or focus on a particular region.

Created separately from TIGCM and TING, was the Coupled Thermosphere-Ionosphere-Plasmasphere Electrodynamics (CTIPe) model (*Fuller-Rowell et al.*, 1980, 1988; *Millward et al.*, 1996). This first principles model included the plasmasphere by modeling the ionosphere along field lines to higher altitudes. This model used a coordinate system based on atmospheric pressure like TIEGCM, but had a Eulerian framework where magnetic field lines were fixed in location.

Another I-T model, and the one primarily used in Chapters III, IV, and VI, is the Global Ionosphere-Thermosphere Model (GITM) (*Ridley et al.*, 2006). A 3-dimensional model, GITM differs from the other I-T models in a number of ways; (1) it has an adjustable resolution, (2) the grid in latitude and altitude is non-uniform, (3) it does not assume hydrostatic equilibrium, (4) it does not assume local chemical equilibrium, (5) the user has the ability to choose from a wide range of auroral and high latitude electric field models, and (6) a realistic or ideal magnetic field can be used. Each of the studies mentioned above uses some or all of these features, making GITM an ideal choice.

GITM is a fully parallel code, meaning that the simulation domain is split into blocks so that many processors can run the model simultaneously and exchange information at each time step. The thermosphere is solved for in terms of eight different species including O, O_2, N_2, $N(^2D)$, $N(^2P)$, $N(^4S)$, He, and NO. The ionospheric species are $O^+(^4S)$, $O^+(^2D)$, $O^+(^2P)$, O_2^+, N^+, N_2^+, and NO^+. For all of these ion and neutral species, GITM solves the full continuity, momentum, and energy equations. The vertical and horizontal advection is treated separately because strong vertical gradients can arise in the non-hydrostatic solution. In the horizontal direction, the mass density is the sum of species densities:

$$\rho = \sum_s M_s N_s, \tag{2.1}$$

where M_s is the molecular mass of the species s, and N is the number density. A normalized neutral temperature, $\Gamma = \rho/p$, is used because to simply the energy equation. p here is the total neutral pressure. The continuity equation is then

$$\frac{\partial N_s}{\partial t} + N_s \nabla \cdot \mathbf{u} + \mathbf{u} \cdot \nabla N_s = 0, \tag{2.2}$$

where t is time and $\mathbf{u}$ is the neutral velocity. The momentum is

$$\frac{\partial \mathbf{u}}{\partial t} + \mathbf{u} \cdot \nabla \mathbf{u} + \nabla \Gamma + \frac{\Gamma}{\rho} \nabla \rho = 0, \tag{2.3}$$

and the energy equation is

$$\frac{\partial \Gamma}{\partial t} + \mathbf{u} \cdot \nabla \mathbf{\Gamma} + (\gamma - 1)\Gamma \nabla \cdot \mathbf{u} = 0, \tag{2.4}$$

where γ is the ratio of the specific heat at constant pressure over constant volume. In the case of the vertical direction, the natural logarithm of ρ and N_s are used instead, and the vertical advection is solved individually for each species because of diverging scale heights above the homopause.

2.1.1 Inputs and Drivers

One of GITM's greatest strengths is its ability to use many different models for high-latitude electrodynamics and precipitation. The most common electrodynamic models used are the Assimilative Mapping of Ionospheric Electrodynamics (AMIE) (*Richmond*, 1992), the Weimer models (*Weimer*, 1996, 2005), an empirical model based on AMIE (*Ridley et al.*, 2000), as well as the SWMF (*Tóth et al.*, 2005), which includes electric potentials from a global magnetosphere model (*Powell et al.*, 1999). Particle precipitation patterns from the *Fuller-Rowell and Evans* (1987c), *Hardy et al.* (1987), Ovation SME (*Mitchell et al.*, 2013), or Ovation Prime (*Newell et al.*, 2009).

Other I-T models have also been coupled with global magnetosphere models. One such example of this is the Coupled Magnetosphere-Ionosphere-Thermosphere (CMIT) model (*Wiltberger et al.*, 2004; *Wang et al.*, 2004, 2008). CMIT was created using TIEGCM and the Lyon-Fedder-Mobarry (LFM) global magnetosphere code (*Lyon et al.*, 2004) using the Magnetosphere-Ionosphere Coupler/Solver (MIX) coupler module (*Merkin and Lyon*, 2010). LFM is able to solve for plasma pressure, velocity, density, and magnetic field in the magnetosphere using ideal Magnetohydrodynamics (MHD). MIX uses conductances from TIEGCM to specify the electric potential at the inner boundary of LFM. TIEGCM is passed auroral precipitation and magnetospheric electric field parameters from LFM. This two-way coupled model allows the magnetosphere and ionosphere/thermosphere to influence each other dynamically.

A shortcoming of global magnetospheric MHD models is that they are unable to reproduce the fundamental physics in regions of high magnetic field strength (within approximately 2.5 R_e), as well as for high energy particles that experience plasma motions outside the definition of ideal MHD. As such, the ring current is often modeled using a dedicated kinetic model.

This thesis describes a contribution made to GITM by one way coupling a kinetic ring current model to it. The ring current provides both the energy flux and average energy of the aurora as well as electric potentials below 67° latitude. This is described in Section 2.2.

I-T models also require a specification of the solar EUV radiation. It is difficult to measure this quantity from the ground because of atmospheric absorption, but it was found that the radio flux at a frequency of 10.7 cm correlates extremely well with EUV flux. Since this is easily measurable from the ground, a frequently used model is EUV Flux Model for Aeronomic Calculations (EUVAC), which defines the EUV from daily and 81 day averaged values of $F_{10.7}$ (*Richards et al.*, 1994). Another common

empirical model is the Flare Irradiance Spectral Model (FISM) (*Chamberlin et al.*, 2007), which was created more recently based on an increasing number of observations of EUV flux itself.

2.2 Ring Current Models

Models of the ring current date back to the early 1970's (*Wolf*, 1970; *Harel et al.*, 1981; *Wolf et al.*, 1982; *Kistler et al.*, 1989; *Chen et al.*, 1993; *Fok et al.*, 1993; *Jordanova et al.*, 1996). These studies produced two core models, the Rice Convection Model (RCM) and the Ring Current Atmosphere Interaction Model (RAM). A wide spectrum of more sophisticated models were then built on top of these, including RCM with a self-consistent magnetic field (*Toffoletto et al.*, 2003b), RCM-Equilibrium (RCM-E) (*Lemon et al.*, 2004; *Chen et al.*, 2015), Comprehensive Ring Current Model (CRCM) (*Fok et al.*, 2001), Comprehensive Inner Magnetosphere-Ionosphere Model (CIMI) (*Fok et al.*, 2014), RAM with self-consistent magnetic field (RAM-SCB) (*Zaharia et al.*, 2008, 2010; *Jordanova et al.*, 2008), and the Hot Electron Ion Drift Integrator (HEIDI) (*Liemohn et al.*, 2001b; *Ilie et al.*, 2012).

The primary difference between RAM and RCM, is that RCM treats the plasma as multiple fluids, where RAM is a kinetic model that solves for the phase space density on a grid that extends onto velocity space as well as location space. Furthermore, RCM generally assumed isotropic pitch angle distributions, whereas RAM allows any pitch angle distribution. Earlier versions of RCM computed electric fields consistent with the particle distribution in the magnetosphere, whereas RAM used empirical models. The idea behind CRCM was to combine the self-consistent electric field from RCM with the ability for particles to be anisotropic. CIMI coupled the Radiation Belt Electron (RBE) model to CRCM. HEIDI is a direct extension of RAM that used the AMIE and Magnetic Boundary Index (MBI) (*Gussenhoven et al.*, 1981) techniques. AMIE uses the CPCP to produce the convection electric field. MBI is an

approximation of the equatorward edge of the auroral oval mapped to local midnight, which provides an activity dependence on the magnetospheric electric field. HEIDI was also updated to include the Dynamic Global Core Plasma Model (DGCPM) (*Liemohn et al.*, 2004). All ring current models generally require a magnetic field model, a conductance model, as well as plasma distributions to both initialize the model and provide the outer boundary condition.

Since depressions in the Earth's magnetic field from ring current intensification influence the gradient curvature drift of ring current particles (*Ebihara and Ejiri*, 2000), many models now have a self-consistent description of the magnetic field as well. This was the motivation leading to RAM-SCB, RCM-E, and one of the latest version of HEIDI (*Ilie et al.*, 2012), which allow the magnetic field strength to change self-consistently with the particle distributions in the ring current.

Encompassing all of the M-I electrodynamic feedback physics in a self-consistent manner has been a longstanding challenge in the ring current modeling community. The earliest models used plasma sheet convective electric fields driven by analytical models such as Volland-Stern (*Volland*, 1973; *Stern*, 1975), or empirically derived potentials from, for example, the Weimer models (*Weimer*, 1996, 2001, 2005), resulting in many studies about the storm-time inner magnetospheric plasma (e.g. *Fok and Moore*, 1997; *Liemohn et al.*, 2001b; *Kozyra et al.*, 2002; *Jordanova*, 2003; *Chen et al.*, 2003). The need for a self-consistent electric field was then addressed by including some description of the ionospheric conductance (*Wolf et al.*, 1982; *Toffoletto et al.*, 2003a; *Fok et al.*, 2001; *Ridley and Liemohn*, 2002).

2.2.1 HEIDI

The model that was developed and used in Chapters V, and VI is the HEIDI model (*Liemohn et al.*, 2004). HEIDI is based on RAM (*Fok et al.*, 1993, 1995; *Jordanova et al.*, 1996), and solves the time-dependent Boltzmann equation for the phase space

density of H^+, O^+, He^+, and e^-. The model is gyration and bounce averaged such that the grid lies on the equatorial plane. The phase space distribution function $Q(R_0, \phi, E, \mu_0, t)$, is solved for using the kinetic equation,

$$\frac{\partial Q}{\partial t} + \frac{1}{R_0^2}\frac{\partial}{\partial R_0}\Big(R_0^2\Big\langle\frac{dR_0}{dt}\Big\rangle Q\Big) + \frac{\partial}{\partial \phi}\Big(\Big\langle\frac{d\phi}{d\phi}\Big\rangle Q\Big) + \frac{1}{\sqrt{E}}\frac{\partial}{\partial E}\Big(\sqrt{E}\Big\langle\frac{\partial E}{\partial t}\Big\rangle Q\Big) + \frac{1}{h(\mu_0)\mu_0}\frac{\partial}{\partial \mu_0} \cdot\Big(h(\mu_0)\mu_0\Big\langle\frac{d\mu_0}{dt}\Big\rangle Q\Big) = \Big\langle\frac{\delta Q}{\delta t}\Big\rangle_{collisions}, \tag{2.5}$$

where R_0 is the radial distance of the particle, ϕ is the longitude in magnetic coordinates, E is the kinetic energy, and $\mu_0 = \cos\,\alpha_0$, where α_0 is the pitch angle. This equation includes pitch angle scattering and energy loss from Coulomb collisions with thermal plasma, charge exchange, precipitation to the upper atmosphere, collisionless drifts, as well as plasma flow through the dayside outer boundary (*Liemohn et al.*, 2010; *Ilie et al.*, 2012). The energy range of the species varies from a few eV to hundreds of keV. The radial domain of HEIDI is 2 to 6.6 R_e, the location of geosynchronous orbit. Input here is given by observed particle fluxes by the Multiple-Particle Analyzer (MPA) (*McComas et al.*, 1993) and Synchronous Orbiting Particle Analyzer (SOPA) (*Belian et al.*, 1992) instruments from Los Alamos National Laboratory (LANL). The composition of the particles in the plasma sheet is assumed to have a Kp dependence and is derived using the empirical Young relationships provided by *Young et al.* (1982). HEIDI can be run with a static dipole magnetic field, or self-consistently within the SWMF (*Ilie et al.*, 2012, 2015).

Similar to GITM, one of HEIDI's strengths is its ability to use a variety of electric field models. These include Volland-Stern (*Volland*, 1973; *Stern*, 1975), the modified McIlwain E5D model (*McIlwain*, 1986; *Liemohn et al.*, 2001b), and a self-consistent electric field using the Ridley Ionosphere Model (RIM) (*Ridley and Liemohn*, 2002; *Ridley et al.*, 2004a), which uses an idealized auroral conductance relationship with

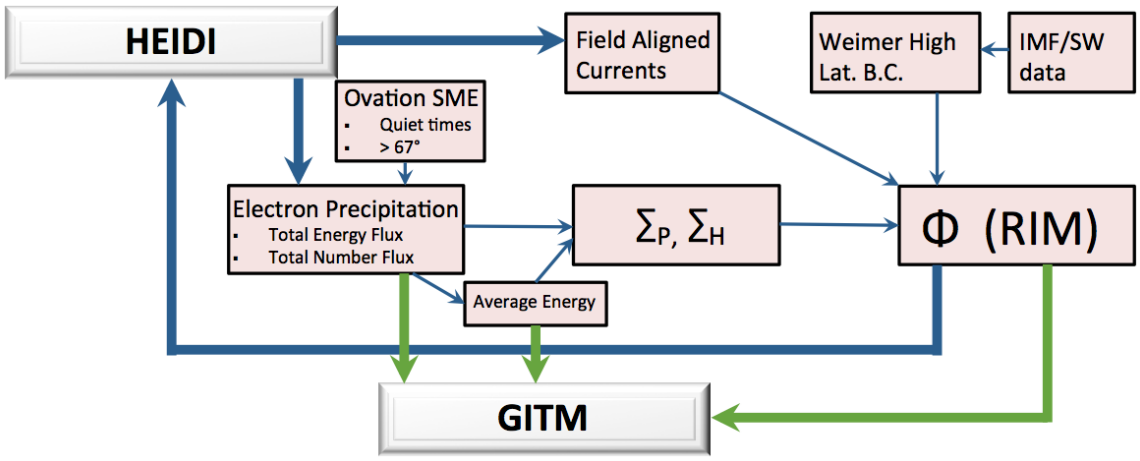

Figure 2.1: Schematics of the new self-consistent aurora and one-way coupling between the ring current solver, HEIDI, and the ionosphere/thermosphere model, GITM

FACs. This self-consistent electric field is limited in that it does not include the self-consistent coupling between particle precipitation and electric fields in both the ionosphere and magnetosphere.

2.2.2 Self-Consistent Aurora Model Contribution

I expanded on the model from *Ridley and Liemohn* (2002) by using the diffuse aurora produced by electron scattering as the primary source for conductance instead of a relationship with the FACs.

A schematic of the model configuration is shown in Figure 2.1. The Magnetosphere-Ionosphere (M-I) system is described by a number of models working together in an ad-hoc framework. First, ion and electron distributions in the inner magnetosphere are solved for using HEIDI. This version of HEIDI uses a static dipole magnetic field.

The electrons scattered into the loss cone by HEIDI were used to calculate iono-

spheric conductances using the formulation by *Robinson et al.* (1987):

$$\begin{aligned} \Sigma_P &= \frac{40\overline{E}}{16+\overline{E}^2}\phi_E^{1/2} \\ \frac{\Sigma_H}{\Sigma_P} &= 0.45(\overline{E})^{0.85} \end{aligned} \tag{2.6}$$

where Σ_H and Σ_P are the Hall and Pedersen conductances, $\overline{E}$ is the average energy in keV and ϕ_E is the energy flux in ergs cm^{-2} s^{-1}. *Kaeppler et al.* (2015) recently used incoherent scatter radar observations to verify the Robinson et al. formulas, finding good agreement with Pedersen conductance. They also updated the relation to be even more accurate for Hall conductances, which could be used in future studies.

Since the outer boundary of HEIDI is at geosynchronous orbit, the self-consistent coupling could only occur below the footprint of the magnetic field lines there, at 67° magnetic latitude. Empirical models were used poleward of this boundary to complete the coupling. Driven by the SuperMAG Auroral Electrojet index (*Newell and Gjerloev*, 2011), the Ovation SME model (*Mitchell et al.*, 2013) gave a smooth and relatively accurate description of the aurora. The Weimer electric potential model (*Weimer*, 2005) was also used to specify the electric potential above the 67° boundary and was driven by the upstream solar wind conditions observed by the ACE spacecraft (*McComas et al.*, 1998; *Smith et al.*, 1998).

The inclusion of these empirical models created sharp boundaries between self-consistently calculated values and the empirical models. As such, a smoothing was applied so that erroneous electric field intensification's did not arise along this boundary. Furthermore, the magnetospheric origin of the aurora often resides tailward of geosynchronous orbit. The Ovation model was solely used during these times for a more realistic auroral specification in the ionosphere. As the hemispheric power produced by HEIDI increased, the contribution of the Ovation aurora was decreased linearly until only the self-consistent version remained. The self-consistent contri-

bution began when the HEIDI hemispheric power reached 10 GW and the Ovation contribution decreased to 0 GW when the total hemispheric power reached 40 GW.

In addition to the Hall and Pedersen conductances, the region 2 FACs were passed to RIM to solve for the electric potentials below 67°. The FACs were calculated numerically from local pressures in HEIDI (*Liemohn et al.*, 2001a).

Given the FAC ($J_{\parallel}$), the height-integrated Hall and Pedersen conductivity tensor $\overline{\Sigma}$ and the magnetic dip angle I, the electric potential, ϕ, may be found by solving

$$\bigtriangledown \cdot (-\overline{\Sigma} \bigtriangledown \phi) = J_{\parallel} \sin I. \tag{2.7}$$

This equation implies that when FACs flow into regions of lower conductivity, the electric field must increase to ensure current continuity. The electric potentials were then passed back to HEIDI to drive the convective electric field in the ring current. This completed the self-consistent electric field model in HEIDI. The plasma populations of the HEIDI simulations were initialized by those of a previous simulation under nominal solar wind and magnetosphere conditions. All of the simulations were run for a period of at least 24 hours before storm onset to remove erroneous contributions from this initial condition.

A limitation of the model was not including proton precipitation in the conductance calculations. The conductance produced by their precipitation in the subauroral region has been found to be on the order of several mhos (*Galand and Richmond*, 2001; *Zou et al.*, 2014). Conductance resulting from precipitating hot ions has also been shown to distort the potential pattern (*Khazanov et al.*, 2003). Our model may therefore have underestimated the conductance in this region, potentially leading to stronger electric fields mapping back to the magnetosphere. Furthermore, the model did not include contributions from discrete auroral arcs or direct injections from the magnetosphere such as in the cusp region. While the majority of the con-

ductance still comes from the diffuse electron aurora in a statistical sense (*Robinson et al.*, 1987), these types of precipitation should be included in the future for a more accurate description.

The model presented here is currently one-way coupled with GITM (*Ridley et al.*, 2006), which can be used to integrate the thermosphere in to the system. In the future, the self-consistent aurora from this version of HEIDI will be merged with the other version of HEIDI with a self-consistent magnetic field (*Ilie et al.*, 2012) coupled with the SWMF (*Tóth et al.*, 2005, 2012; *Ilie et al.*, 2015).

The next 4 Chapters are related projects with the following basic descriptions:

1. Use GITM to determine if the time of day of geomagnetic activity influences the impact of the event on the upper atmosphere.

2. Investigate the seasonal and hemispheric asymmetry in TEC using year long simulations of GITM and TIEGCM

3. Use the new self-consistent aurora feature to HEIDI to explore the impact of the efficiency of pitch angle scattering on the electrodynamic coupling between the upper atmosphere and magnetosphere.

4. Compare HEIDI and other high latitude drivers of GITM on the influence to other high-latitude drivers on storm time ionospheric phenomenon.

CHAPTER III

Universal Time Effect in the Response of the Thermosphere to Electric Field Changes

3.1 Introduction

Understanding the thermospheric response to energy input is important for the practical reason that as energy is added to the system, the thermosphere expands and causes more drag on low altitude satellites (*Bruinsma et al.*, 2006; *Zhou et al.*, 2009). The accuracy of accelerometer derived thermospheric densities and winds has improved in recent years (e.g. *Sutton et al.*, 2007; *Sutton*, 2009), making it possible to examine the disturbed and quiescent state of the thermosphere. Satellite observations have also unveiled seasonal and local time dependence of the thermospheric density (*Hedin and Carignan*, 1985; *Bruinsma et al.*, 2006; *Rentz and Lühr*, 2008; *Müller et al.*, 2009).

The influence of magnetospheric electric fields on the thermosphere is intricately tied to the plasma motion, as well as the density and velocity of the neutrals. Therefore magnetospheric electric fields are a crucial process when considering any possible UT effects. The thermospheric energy balance is strongly coupled to the ionosphere through the difference between ion and neutral velocities. The time-scale of velocity changes in the ions is significantly shorter than in the neutrals (*Vasylinas*, 2005). This

means that the ion flows across the field-lines are relatively weakly controlled by the neutrals (*Deng et al.*, 1991; *Odom et al.*, 1997), but the neutral flows across the field lines are more strongly controlled by the ion flows (*Deng*, 2006; *Conde and Smith*, 1995; *Mikkelsen et al.*, 1981). Consequently, the magnetic field direction is important for controlling both the ion flows and the neutral winds. In addition, the component of the neutral wind along the magnetic field can strongly control the structure of the ionosphere - when the magnetic field is oriented between the horizontal and vertical directions, neutral winds can push plasma along the field lines (*Bramley and Young*, 1968; *Burrell et al.*, 2012, 2013), causing the height of the F_2 peak to move up or down, depending on the structure of the wind and magnetic field (*Hedin and Mayr*, 1973; *Rishbeth et al.*, 1978; *Rishbeth and Mendillo*, 2001; *Muella et al.*, 2010).

Regions of energetic particle precipitation roughly vary in accordance with convection and potential patterns (*Foster et al.*, 1986; *Singh et al.*, 2013; *Mitchell et al.*, 2013), the location of which are heavily influenced by the location of the Earth's geomagnetic pole. This fact combined with the tilt and offset of the geomagnetic pole from the geographic pole suggests that the response of the ionosphere/thermosphere system to impulsive events may be strongly dependent upon the time of the event, because the Earth's geomagnetic field rotates through the Sun-fixed coordinate system. When the geomagnetic pole is in sunlight, there is more ion production in regions of strong electric potential, such as the throat. In this case, the Joule heating that results from a difference in the ion and neutral velocities may be stronger. Therefore, the thermospheric response to solar wind and Universal Time (UT). Because the geomagnetic pole is offset from the Earth's rotational axis, the magnetospheric energy is deposited in different locations relative to the solar terminator. Such UT modulation may be larger in the southern hemisphere, because the greater separation between geographic and geomagnetic poles (*Fuller-Rowell et al.*, 1988) causes the geomagnetic pole to be at lower solar zenith angles during the day and higher solar zenith angles

at night.

It is well known that the magnetospheric activity level is dependent upon the time of day and season, because of the tilt of the geomagnetic pole away from Earth's rotation axis (*Russell and McPherron*, 1973). This so-called Russell-McPherron effect occurs because if one takes the nominal IMF as being in a Parker spiral (i.e., B_y being roughly opposite of B_x, and B_z being approximately zero) and the field is transformed from GSE to GSM coordinates in which the Z-axis is oriented in the plane of the magnetic field axis, instead of the equatorial plane of the sun, GSM B_z gains some magnitude from GSE B_y. This means that there will be time periods of negative GSM B_z when the IMF is actually a pure Parker spiral in GSE coordinates, and implies that there may be a larger amount of activity for nominal solar wind and IMF conditions during the equinoxes when this geometry maximizes (*Russell and McPherron*, 1973; *Liou et al.*, 2001).

In addition to the Russell-McPherron effect, seasonal variations have also been found to be caused by variations in the angle between the geomagnetic dipole axis and the solar wind flow direction (*Cliver et al.*, 2000). Furthermore, UT variations as a result of magnetosphere-solar wind coupling have been reproduced in numerical model simulations, primarily through changes in the magnetic reconnection process (*Cnossen et al.*, 2012b). In this study, we primarily examined what the thermospheric effects are due to the same change in high-latitude drivers, but at different times of the day. While these effects are influenced by the tilt of the dipole, this study examined the ramifications of the northern and southern geomagnetic poles being at different solar local times, and what this means for ionosphere/thermosphere coupling, rather than the magnetosphere/solar wind coupling.

Longitudinal variations in the strength of Earth's magnetic field strength can also contribute to UT variations (*Förster and Cnossen*, 2013; *Cnossen et al.*, 2012b). The magnetic field magnitudes are shown for each hemisphere in Figure 3.1. Each plot

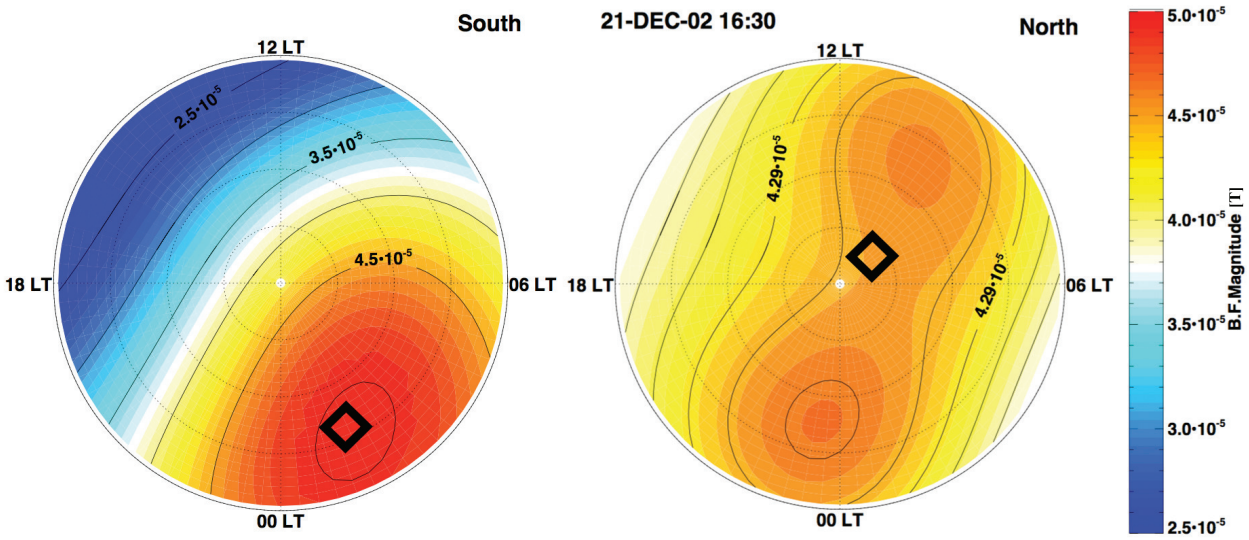

Figure 3.1: Magnetic field (B.F.) magnitude in the northern and southern hemispheres on the left and right, respectively. The diamond is location of the geomagnetic pole.

shows the magnitude at 1700 UT poleward of 50° latitude at 590 *km* altitude. The two peak structure in the northern hemisphere differs greatly in comparison to the larger single peak structure in the southern hemisphere. One can imagine these structures rotating in local time throughout the day. This rotation alters the local magnetic field strength on the dayside, causing significant changes in the electric current and ion drift in the ionosphere, as well as ion drag in the thermosphere (*Rees and Fuller-Rowell*, 1989). The magnetic field strength has also been found to alter the height F_2 peak of the ionosphere (*Cnossen and Richmond*, 2012; *Sojka and Schunk*, 1997), which could translate into a UT dependence based on the longitudinal variation described in Figure 3.1. Longitudinal variations in the electron density have also been found recently. Zonal winds were found to be responsible for up to 80% of the longitudinal variations in electron density during equinox in a series of GITM simulations (*Wang et al.*, 2015). Additionally, the ionosphere response to storms in the American sector in the afternoon was found to be larger in terms of total plasma content (*Immel and Mannucci*, 2013; *Garner et al.*, 2010).

The effect of a weaker dipole on the ionosphere/thermosphere system was inves-

tigated recently by *Cnossen et al.* (2011). By reducing Earth's dipole moment by 25% in their simulations, they found that Joule heating power (Joule heating integrated both hemispherically and in height) was increased by a minimum of 13% in the northern hemisphere summer, and a maximum of 30% for March equinox in the southern hemisphere. Since the potential pattern rotates with the geomagnetic pole, the average magnetic field strength in the throat region of the potential pattern varies throughout the day.

The idea of a UT dependence in the ionosphere/thermosphere system is not new. Numerical simulations to investigate how magnetospheric activity can produce a UT effect in a global thermospheric circulation model were done decades ago (*Roble et al.*, 1982; *Fesen et al.*, 1995). These early studies found that maximum perturbations in each hemisphere occur 12 hours offset from each other. *Fuller-Rowell et al.* (1994) also performed numerical simulations using a coupled ionosphere/thermosphere model where they found the atmospheric response to depend on the longitude of the geomagnetic pole. Despite the interest over the last few decades, the particular mechanics of this UT dependence and the magnitude of its effects are still not completely understood. This study aims to improve that understanding by looking at changes in thermospheric temperature, as well as neutral and electron densities caused by an idealized change in the interplanetary magnetic field.

3.2 Technique

This study used GITM, a model that is described in detail by *Ridley et al.* (2006). It is a three dimensional model that solves the continuity, momentum, and energy equations with realistic source terms in a spherical coordinate system. A primary difference between GITM and other ionosphere/thermosphere models is that GITM uses an altitude grid, instead of pressure, which facilitates the ability to develop non-hydrostatic solutions. GITM was run with a resolution of 2.5° latitude by 5°

longitude with a stretched altitude, resolving the vertical scales to approximately 1/3 of a scale height. Idealized simulations were used to obtain an understanding and quantifiable estimate of how important UT effects are for the response of the ionosphere/thermosphere system to impulsive events.

GITM was run for 48 hours prior to any changes in the drivers to eliminate any transient influence of the initial conditions. 23 simulations were then continued from the start-up simulation and run for 24 hours from March 21^{st} 0000 UT. 22 of these simulations were disturbed by changing the high latitude electric potential for 70 minutes. This was accomplished by using the *Weimer* (2005) electric potential model, and altering the IMF B_z component (in GSM coordinates) from $-2\,nT$ to $-10\,nT$ linearly over ten minutes, holding the IMF B_z constant at $-10\,nT$ for 50 minutes, then linearly changing the IMF B_z back to $-2\,nT$ over ten minutes. IMF B_y and B_x were held at zero.

It is important to note that the use of the Weimer empirical electric potential model implicitly includes the UT variations resulting from solar wind/magnetosphere coupling, due to the tilt angle dependence. To illustrate this, the CPCP for the baseline equinox simulation is plotted in Figure 3.2. The CPCP is calculated by taking the difference between the maximum and minimum electric potentials in each hemisphere. The plot shows a UT variation in both hemispheres. However, since the amplitude of this variation is only about 2 kV, the overall effect in the thermosphere response will be minimal relative to the magnitude of the idealized energy input event. The perturbed CPCP reaches values of about 160 kV (not shown), so the UT variation only comprises a couple of percent of the large perturbation.

There were no changes in any other solar wind drivers, auroral specifications, or EUV inputs. The $F_{10.7}$ for this series of runs was fixed at $100\,sfu$ (solar flux units), while the auroral hemispheric power was held constant at $20\,GW$. While it is relatively unphysical to have no change in aurora with a strong change in the ionospheric electric

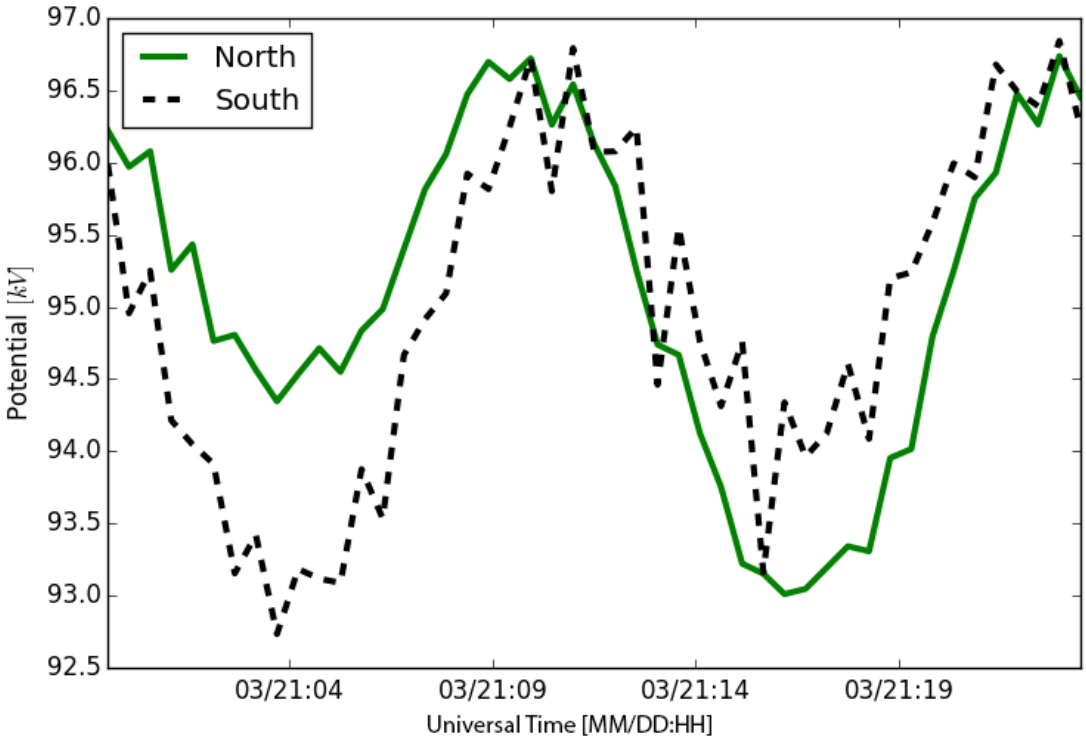

Figure 3.2: Cross polar cap potential produced by the *Weimer* (2005) electric potential model for the baseline case at equinox with an IMF B_z of $-2\,nT$.

field, it could be viewed as a time period of steady magnetospheric convection in which a substorm does not occur (*DeJong et al.*, 2008; *DeJong*, 2014; *Newell et al.*, 2010). The only difference between the 22 different runs was the time in which the change in IMF B_z occurred - each run was offset by one hour from the previous run. In other words, run 1 had the start of the IMF transition start occurring at 0100 UT and the perturbation ending at 0210 UT, run 2 had the transition occurring at 0200 UT and ending at 0310 UT, and so on. The 23$^{\text{rd}}$ simulation had no IMF change at all and was the reference simulation. The IGRF was used in all simulations, except when noted. Since the IGRF model was used, effects from magnetic field strength and tilt angle variations with longitude are expected. In a second series of 23 runs, the magnetic field was set to a pure dipole in which the magnetic and geographic

axes were aligned. These simulations serve to eliminate both the tilt angle effect and longitudinal variations in magnetic field strength. The MSIS model (*Hedin*, 1991) was used as a lower boundary at 97 km, which also introduced atmospheric tides to the simulation results as well.

3.3 Results and Discussion

Figures 3.3 and 3.4 show simulation results of the temperature and winds in the northern and southern hemispheres from two of the runs (the 0600 UT and 1700 UT change times) during and after the period of the electric potential perturbation. These plots show the difference between the perturbed run and the baseline case, which was run with a constant IMF Bz. or the purposes of this discussion, time (t) 0 min refers to the onset time of the perturbation for a particular run, with subsequent times indicating the number of minutes after the onset of the perturbation. While all of the patterns for the same time are very roughly similar to each other, the hemispheres and simulations where the geomagnetic pole (indicated by a diamond on each plot) is on the same side of the terminator when the electric field change occurred show stronger congruency. Since these simulations were run at equinox, the terminator lies along the line from 0600 UT to 1800 UT, with the day side being on the top half of each plot. The difference between the daytime and nighttime response can be seen by comparing either the 1700 UT north and 0600 UT south plots (central two columns, in which the geomagnetic pole was on the dayside) or the 0600 UT north and 1700 UT south plots (outer two columns, in which the geomagnetic pole was on the nightside). At t=30 (first row), the neutral winds were enhanced in all simulations. Each plot shows a two cell convection pattern, which is similar to the ion convection at the time (not shown). In addition, the temperature had increased in each simulation with a somewhat similar pattern. This is the general pattern that one expects from a Joule heating enhancement in the high latitude region (e.g. *Thayer*, 1998; *Zhang et al.*,

2005; *Immel et al.*, 2006; *Deng and Ridley*, 2007).

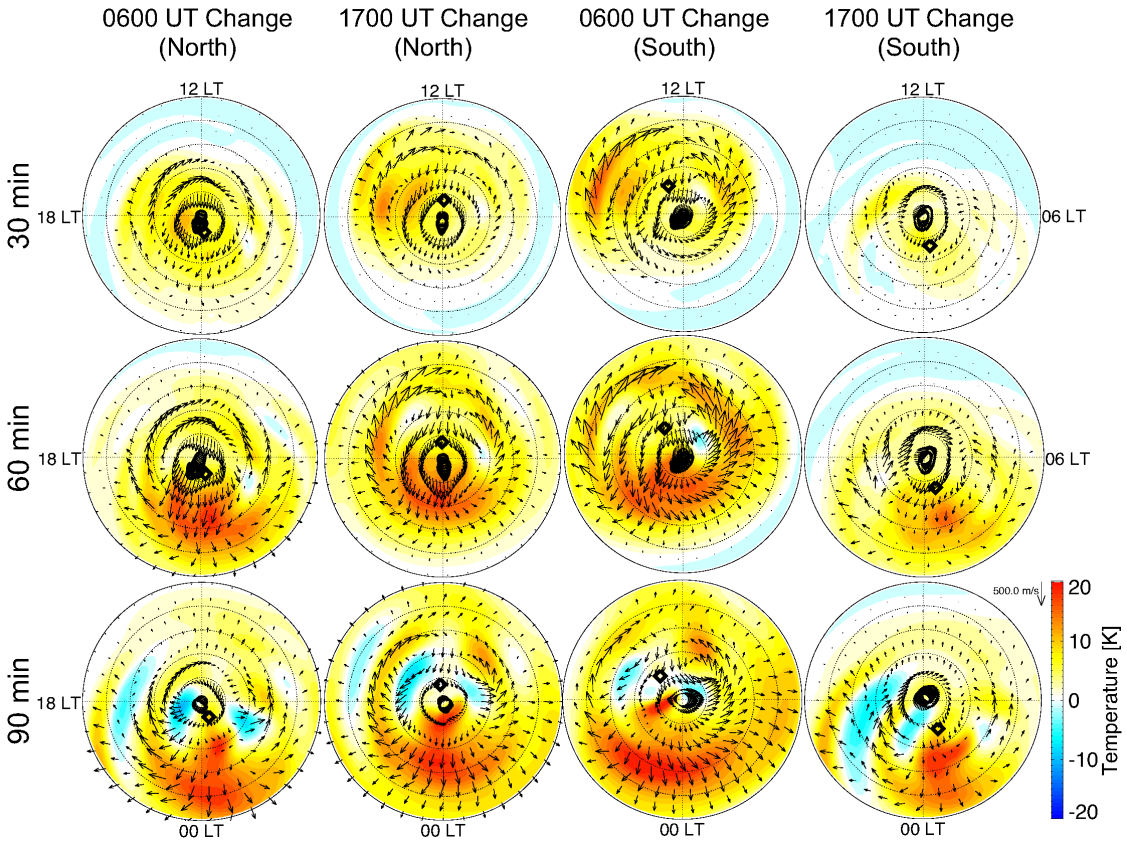

Figure 3.3: Contours of the thermospheric temperature percentage difference between the run with a perturbation and the run without the perturbation plotted under the absolute difference in the neutral wind at 404 *km* altitude. The plots in the left and right two columns show the northern and southern hemisphere responses, respectively. Within each pair, the left plot shows results in which the electric field change started at 0600 UT, and the right plot for 1700 UT. The center of the plot is the geographic north pole, while the outer ring represents 40° latitude. The grid spacing is 10°. The top of the plot indicates noon, while the right side indicates dawn. The geomagnetic pole position is indicated by the diamond. The rows show t=30, 60, and 90 minutes after the start of the change.

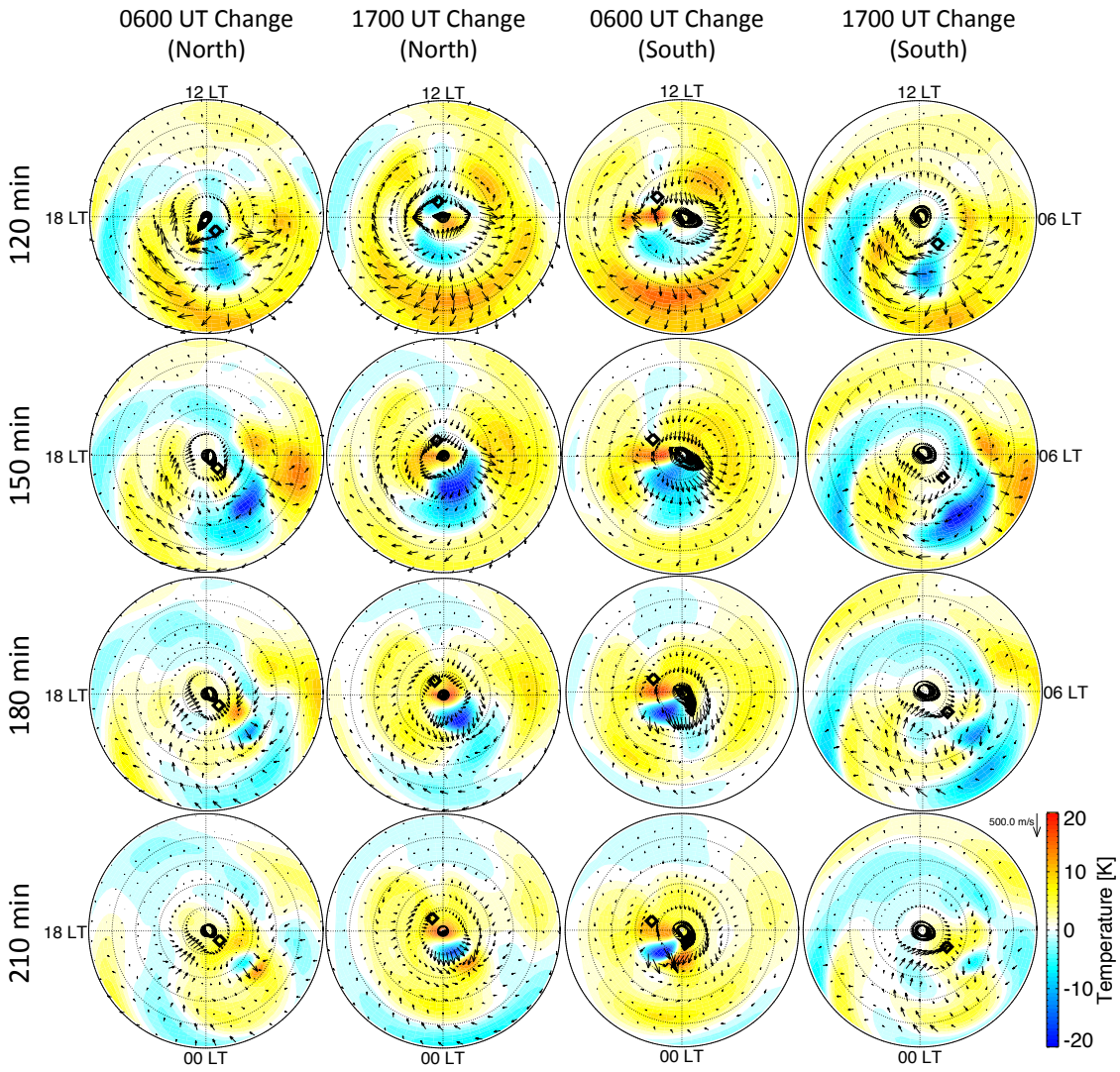

Figure 3.4: Figure 3.3 continued. The rows are 120, 150, 180, and 210 minutes after the start of the electric field change.

In each of the time-series, the thermosphere heated up when the electric field increase was applied (at t=30 and t=60), and then cooled down afterwards (from t=90 onward). The cooling completed a clear wave-like structure that propagated away from the polar region, which can be observed by following a single hemispheric simulation through Figures 3.3 and 3.4. For example, in the second and third columns, there was a temperature peak on the nightside at 65° latitude at t=90. This peak moved to 55° latitude by t=120 and 45° latitude at t=150 on the nightside. This roughly corresponds to a wave speed of 620 ms^{-1}, while the sound speed was close to 875 ms^{-1}. Previous model results have found the phase speed of this global wind surge to be about 600 ms^{-1} as well (*Fuller-Rowell et al.*, 1994). Associated with this wave were equatorward perturbations in the winds in excess of 200 ms^{-1}. These perturbed winds lasted until t=120, when they started decreasing and rotating in the westward direction, as one might expect due to the Coriolis force. By 210 minutes after the start of the enhancement, the temperature had decreased over almost the entire polar region and the large equatorward winds had less than half of their peak perturbed values.

On the dayside in the inner columns, the temperature increased from the pole to 50° at 30 minutes. It then expanded to below 40° latitude before 60 minutes. At that time, there was a significant equatorward flow perturbation on the dayside at low latitudes, while there was little equatorward flow perturbation on the nightside at such low latitudes. The equatorward flow on the dayside decreased rapidly and by t=120, the main flow was poleward near noon, due to the residual ion drag driven by the two-cell convection pattern. This two-cell pattern remained for at least two hours after the electric field enhancement had ended, although it became quite distorted as it rotated with the planet.

When the enhancement happened while the magnetic field was on the night side (the outer two columns), the initial perturbation was more confined and was smaller

in magnitude. Additionally, the disturbance did not extend on to the dayside nearly as much as the nightside. Also, the resulting wind perturbations were also much weaker than when the enhancement occurred while the geomagnetic pole was on the dayside.

The effects on the thermospheric mass density were also explored, though they are not shown. At 404 km, the general behavior of the simulated density was very similar to the behavior observed in the temperature plots in Figures 3.3 and 3.4, though the impact was more severe. While the temperature scale went up to 25% at 404 km altitude, the mass density scale went up to about 100%, indicating that the heating occurred significantly lower than 404 km and that the atmosphere was being lifted by the heating that occurred (*Deng et al.*, 2013).

It should be noted that some of the differences between the hemispheres in Figures 3.3 and 3.4 may be attributed to plotting in the geographic coordinate system, while the driving is controlled in the magnetic coordinate system. The following figures show a more hemispherically integrated perspective, but it is still possible that some hemispheric asymmetries appear from displaying results geographically, when many of the physical processes at hand are more oriented towards a magnetic coordinate system. While switching to a geomagnetic system may change the structuring of the peaks and valleys, it would not change the magnitude of the changes.

The plots in Figure 3.5 show the average temperature poleward of 45° geographic latitude for the northern and southern hemispheres, plotted on the left and right respectively. The black line shows the unperturbed baseline simulation, while the 22 colored lines show the results of the 22 simulations where the electric field perturbation started at 0100, 0200, 0300, ..., 2200 UT, and started to end at 0200, 0300, 0400, ..., 23 UT00. The get darker with the time of the perturbation. Five altitudes are plotted, starting at 128 km altitude at the top and going to 590 km on the bottom. If a single color trace is followed, the heating during the IMF enhancement is observed,

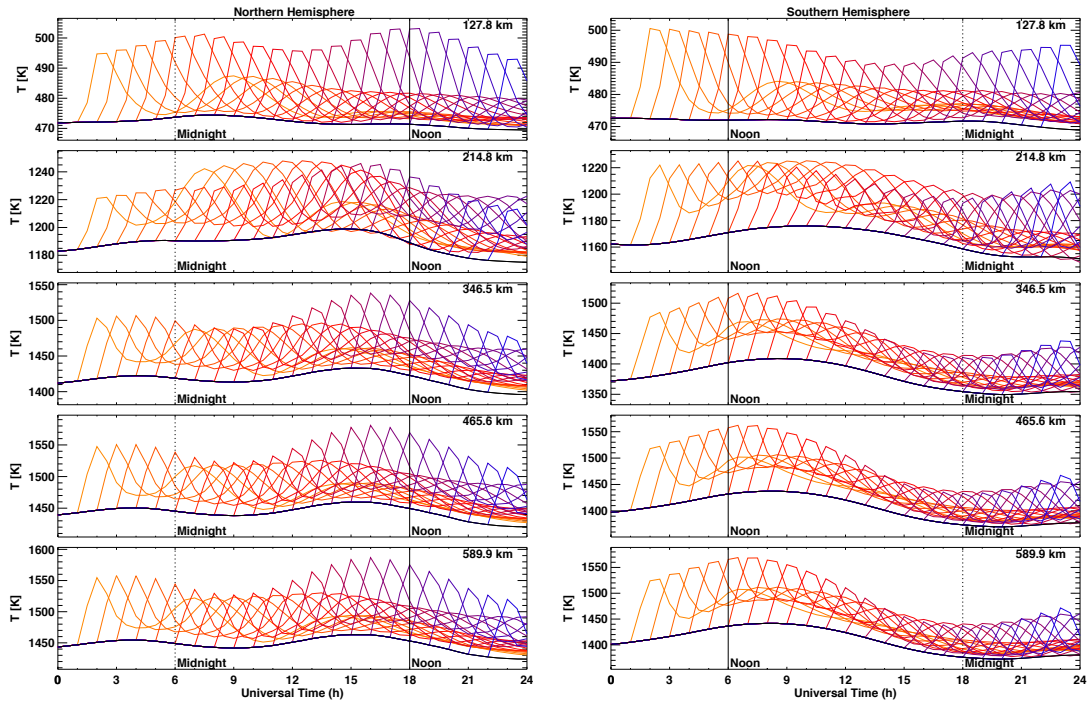

Figure 3.5: The average thermospheric temperature poleward of 45° latitude for the northern and southern hemispheres on the left and right, respectively. Five different altitudes are shown, with the lowest altitude in the topmost row and the highest altitude at the bottom of the figure. 23 different simulations are presented at each altitude. The unperturbed simulation is shown as a black line, while the colored lines represent the 22 simulations in which there was a 70 minute electric field perturbation. In each hemisphere, the time in which the geomagnetic pole is at noon solar local time is indicated as a solid vertical line, while the time in which the geomagnetic pole is at midnight is indicated by a dashed vertical line. Note that the y-axis scale for the southern hemisphere is slightly smaller.

encompassing the changes shown in Figures 3.3 and 3.4. The temperature is observed to increase rapidly during the perturbation in IMF, peaking at one hour, which is the time when the IMF started to recover back to its nominal value. The thermosphere then rapidly cooled. A minimum in temperature was reached around 4.5 hours after the start of the enhancement. Shortly after this, the gravity wave (or travelling atmospheric disturbance) from the opposite hemisphere entered the polar region and the temperature started to increase again, warming to a point just a few degrees cooler than the highest temperature peak. The secondary peak temperature was reached

about 9 hours after the start of the electric field enhancement. This is consistent with a wave propagating at 620 ms^{-1}, as discussed earlier (i.e., it traveled roughly from pole to pole in nine hours). All of the traces have similar behavior - a quick rise, slower decay and secondary maximum about nine hours later, though this is only visible for the first few simulations. The temperature oscillated for the rest of the simulation, but overall trended towards the background simulation temperature.

The magnitude of the perturbations in Figure 3.5 is dependent on the altitude and the time of day. The largest temperature increases at each altitude spanned $31K$ at 126 km, to $122K$ at 590 km. Comparing temperature enhancements that occurred when the geomagnetic pole was closer to noon to those when the geomagnetic pole was closer to midnight suggests a dependence on UT. For example, at 590 km in the southern hemisphere, the temperature increased by $129K$ when the geomagnetic pole was near noon, but only $68K$ when the pole was near midnight. In the northern hemisphere, the UT variation was smaller, with the maximum perturbation at 590 km of $122K$, and the minimum perturbation of $86K$.

The averaged high-latitude mass density perturbation was also dependent upon the UT at which the electric field enhancement occurred (Figure 3.6). This was true at all altitudes and in both hemispheres, but was more apparent in the southern hemisphere. For example, at 590 km in the southern hemisphere, the density increase was 1.1×10^{-13} $kg\ m^{-3}$ when the geomagnetic pole was near midnight and 2.0×10^{-13} $kg\ m^{-3}$ when it was near noon. In the northern hemisphere the difference was slightly less. The maximum perturbation was the same as in the southern hemisphere, but the minimum perturbation reached 1.3×10^{-13} $kg\ m^{-3}$.

The behavior seen in the simulations is easier to understand if the percentage differences between the perturbed and unperturbed simulation are explored, as shown in Figure 3.7. The figure shows the mass density perturbation values divided by the unperturbed simulation values, or $\rho = 100(\rho_p - \rho_u)/\rho_u$, where the mass density, ρ,

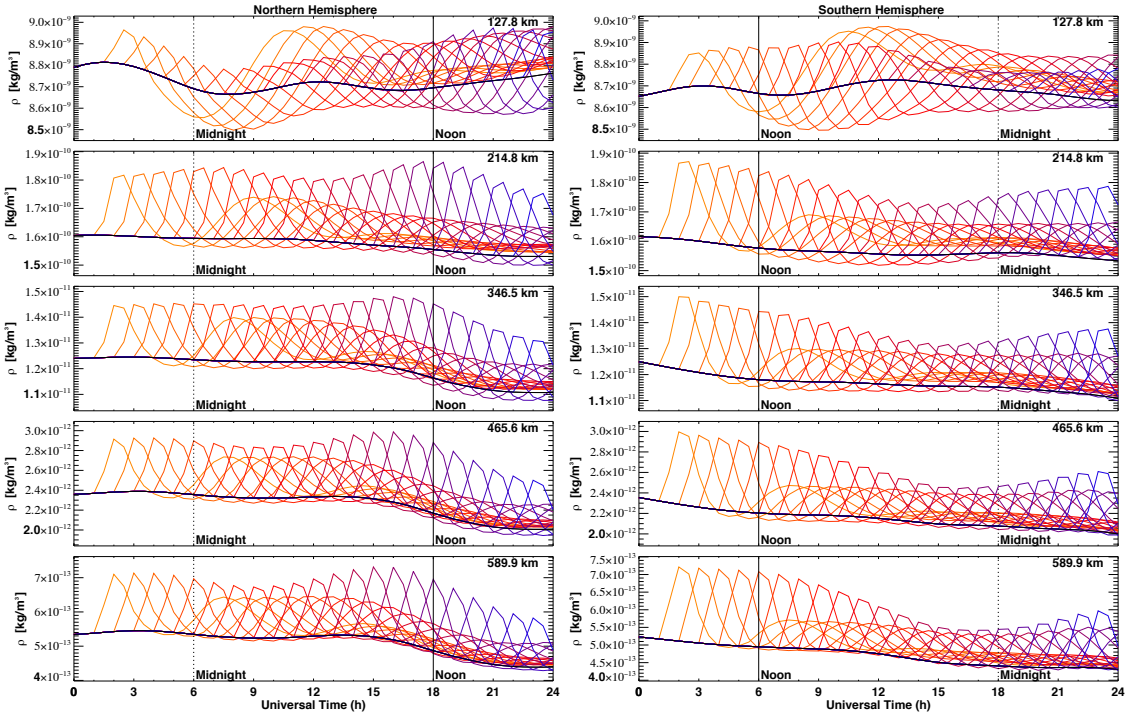

Figure 3.6: The same as Figure 3.5 but for the thermospheric mass density.

is the value shown in each line, ρ_p is the value of the perturbed simulation (colored lines in Figure 3.6), and ρ_u is the mass density of the unperturbed run (black lines in Figure 3.6). Mass densities below the unperturbed simulation (negative percentage changes) resulted from the mass density collapsing after the perturbation ended, leading to the natural negative well of a gravity wave.

At high altitudes in the northern hemisphere, there was a weak increase in density (30% at 590 km) when the perturbation occurred in the first half of the day (in terms of UT) when the geomagnetic pole was on the nightside, but a more prominent increase (42% at 590 km) when the perturbation occurred later in the day when the geomagnetic pole was on the dayside. For the southern hemisphere, the larger perturbations occurred earlier in the day, with a 43% change occurring when the geomagnetic pole was near noon and a 23% change occurring when it was near midnight. At 215 km, 347 km, and 466 km, the structure of the differences remained the same, but the magnitude of the change increased with altitude. The noon-midnight

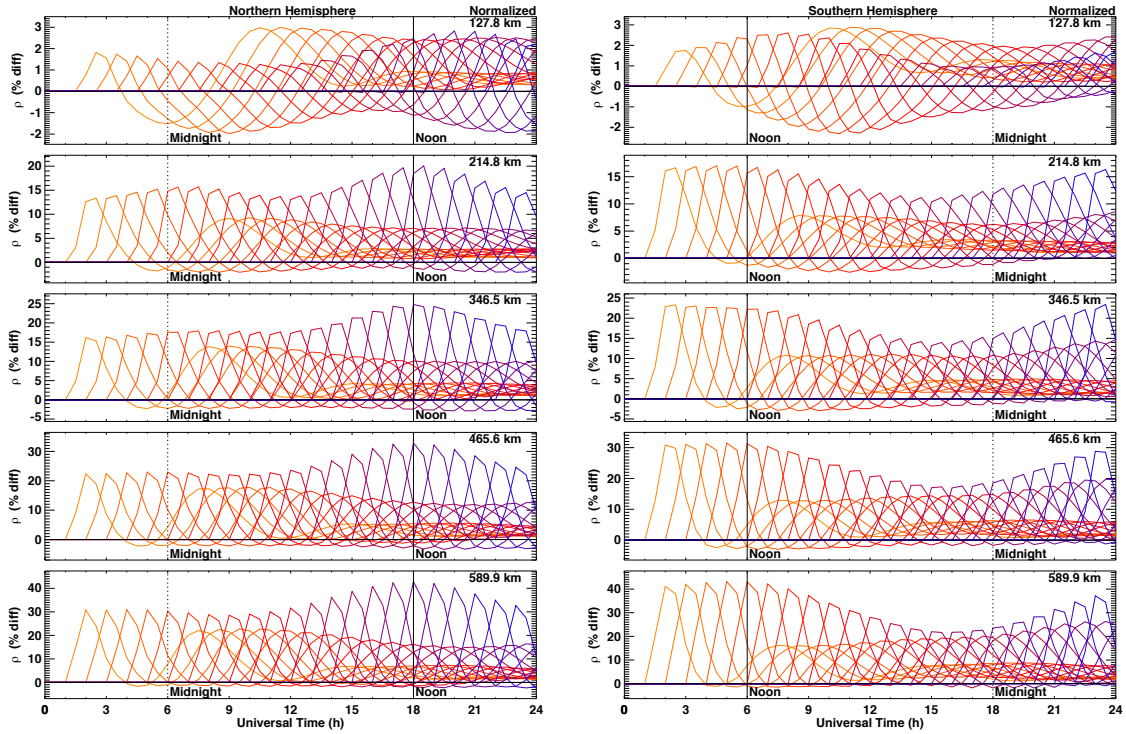

Figure 3.7: The thermospheric mass density perturbation as shown in Figure 3.6, but shown as percentage differences to the unperturbed simulation. Note that the y-axis scale for the southern hemisphere is slightly smaller at the 214 and 346 km altitudes.

difference shrank from 18% at 590 km to 4% at 215 km. In other words, the density perturbations were larger at higher altitudes when the geomagnetic pole was closer to noon.

The behavior at the lowest altitude was different than at the higher altitudes. The secondary peak in the wave structure at 128 km altitude was much stronger in both hemispheres. These peaks were often nearly 50% greater in the simulations near midnight. The magnitude by which this peak exceeded the initial perturbation was larger in the northern hemisphere by 0.5%. Interestingly, at 128 km altitude in the northern hemisphere, the perturbations around 1000 UT were primarily reductions, while around 2000 UT, the perturbations almost always increased. In the southern hemisphere at 128 km altitude, a similar behavior was observed, but the reductions took place towards the middle of the day, while the largest increases also tended to

occur during the same time-frame. Note that the percentage change at low altitudes was extremely small compared to the response at higher altitudes (1-3% versus about 20-45%, respectively).

Variations in the trends in the lower and upper thermospheric mass density response may be due to different effects. For example, at lower altitudes, the tides may play a role (*Groves and Forbes*, 1984; *Fesen et al.*, 1986). At 120 km, the thermosphere is still dominated by tides from the lower atmosphere, while by 200 km, the thermosphere is more decoupled from the lower atmosphere tidal structures (*Groves and Forbes*, 1984). It should be noted that even at F region heights, lower atmosphere tidal structures can still have important effects (*Immel et al.*, 2006). The perturbations caused by the IMF changes may have acted in or out of phase with the natural tidal structures. Additionally, oscillations generated by thermospheric winds below 200 km have been found to interact with lower atmospheric tides (*Müller-Wodarg et al.*, 2001). This interaction could modify the interference of the perturbation with the tidal structures. The prevalence of these tides in the GITM simulations are investigated further in Figure 3.9. Further, the Joule heating energy is typically deposited at altitudes between 110 and 150 km (*Deng et al.*, 2011; *Huang et al.*, 2012). Therefore, the gradient in pressure may have decreased at the 128 km altitude slice, possibly causing downward flow, which would decrease the density.

Figure 3.8 shows the local time variation of the averaged maximum thermospheric mass density perturbation over the polar region at the end of the IMF perturbation for both the southern and northern hemispheres. The lines in the left plots were derived by finding the maxima of the initial perturbations in the percentage change of the mass density as shown in Figure 3.7 (i.e., tracing from peak to peak). The lines were then shifted to correspond to the local time of the geomagnetic pole in each hemisphere. The dotted segments in each curve represent missing simulations (i.e., IMF changes at 2300 and 0000 UT), which were filled in using a spline interpolation.

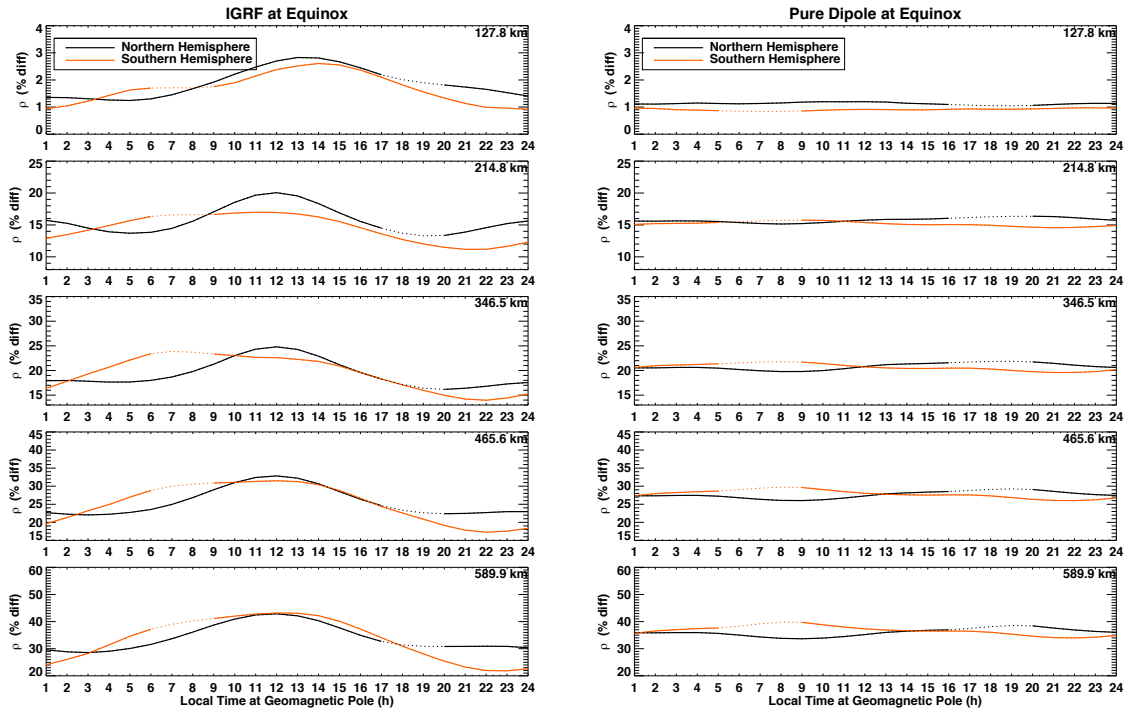

Figure 3.8: Normalized maxima of the thermospheric mass density for the IGRF case on the left and a pure dipole on the right. At each altitude, the red lines show the southern hemisphere and the black lines show the northern hemisphere. The dotted portions of the curves represent interpolated values.

The left plots in Figure 3.8 were derived directly from Figure 3.7, while the right plots were derived by re-running all of the simulations using an ideal dipole that was aligned with the rotation axis of the Earth.

A strong local time dependence in the density response was seen in each hemisphere at all altitudes in the IGRF case. At most altitudes, the peak in density in each hemisphere corresponded to the time when the geomagnetic pole in that hemisphere was closest to noon, while the minimum occurred when the pole was close to midnight. The peaks for the southern hemisphere were broader than in the northern hemisphere, especially on the morning side. The density perturbation in the southern hemisphere was weaker from 1900-0200 local time, but was stronger from 0400-0900 local time. The weaker reaction at night may have been caused by the larger offset between the geographic and geomagnetic poles in the southern hemisphere. If this

	Max %		Min %		Mean %	
Altitude $[km]$	**N**	**S**	**N**	**S**	**N**	**S**
127.8	2.83	2.61	1.24	0.92	1.89	1.68
214.8	20.05	16.99	13.27	11.18	15.69	14.45
346.6	24.80	23.52	16.17	13.97	19.28	19.45
465.6	32.84	31.49	22.05	17.27	25.61	25.20
589.9	42.86	43.16	28.57	21.85	34.05	33.35

Table 3.1: Synopsis of the thermospheric density mass density increases at March equinox from Figure 3.8. The table shows the maximum, minimum, and mean percentage change at each altitude.

were true, one would expect a larger reaction at noon, which did not happen. It could be that the strength of the magnetic field or some other longitudinally dependent process could cause this difference, which is explored in more detail below. The magnitude of the percentage differences in mass density changes with altitude. Table **??** shows an overview of the maximum, minimum, and mean percentage changes at each altitude for the IGRF case shown in the left panel of Figure 3.8. Magnitudes range from a 1-3% increase at 128 km to a 22-43% increase at 590 km.

In the pure dipole case, shown in the right panel of Figure 3.8, the northern and southern hemisphere density perturbations do not alter significantly with local time. This is what was expected during equinox for a dipole aligned with the rotation axis of the Earth, since there was no tilt or offset to create an asymmetry by which the UT of electric field perturbation would make a difference. Note that since the geomagnetic and geographic poles are at the same location in the centered/pure dipole plots, the time here does not exactly correspond to a local time at the geomagnetic pole. The local time shown in the x-axis for these plots was calculated from the longitude of the geomagnetic pole in the IGRF simulations. This aligns the same universal times with the other plots for better comparison. The difference between hemispheres may be attributed to tides, slight variations in the background thermosphere when the perturbation occurred, and a slight UT dependence in the *Weimer* (2005) model, or a combination of these influences. To investigate this, the pure dipole case was

re-run with MSIS tides removed as well as a 0° tilt specified for the potential model. Shown in Figure 3.9, this decreased the UT dependence at higher altitudes. The remaining dependence could be due to the short 2 day start-up time in all of the simulations, though we expect this to account for no more than a few percent of it. The simulations with the perturbations induced at the end of the day were introduced to an ionosphere/thermosphere system that was a couple percent closer to steady state than the previous simulations. This interpretation is supported by the behavior of the baseline simulation from the run without tides or tilt shown in the right panel of Figure 3.9. At higher altitudes, the baseline simulation increases to a point before reaching steady state just after 1200 UT. However, Figure 3.12 will later show that this cannot fully explain the remaining UT dependence shown here. Interestingly, the times that the northern (1700-2400 UT) and southern (0500-1100 UT) hemispheres had the strongest perturbations in the dipole simulations were the same times that the strongest perturbations were seen in the IGRF simulations. Other studies have shown that the neutral wind response follows a similar response in each hemisphere during these times (*Förster and Cnossen*, 2013).

The previous series of runs were done for equinox conditions, but Figure 3.10 shows the same simulation results for the 22 simulations as shown in Figure 3.8 (left), but conducted for June (left) and December (right) solstice conditions. These simulations were run using the IGRF. In these simulations, the winter hemisphere had larger perturbations compared to the summer hemisphere case when the pole was near noon and a smaller perturbation when the pole was near midnight. During the solstice, the winter hemisphere showed a strong dependence of the thermospheric response to the local time of the pole, while summertime in both hemispheres appeared to dampen the UT dependence in the mass density response to energy input. This seasonal dependence can be seen when comparing the northern hemisphere in the June and December simulations. In December, the largest perturbation in the northern

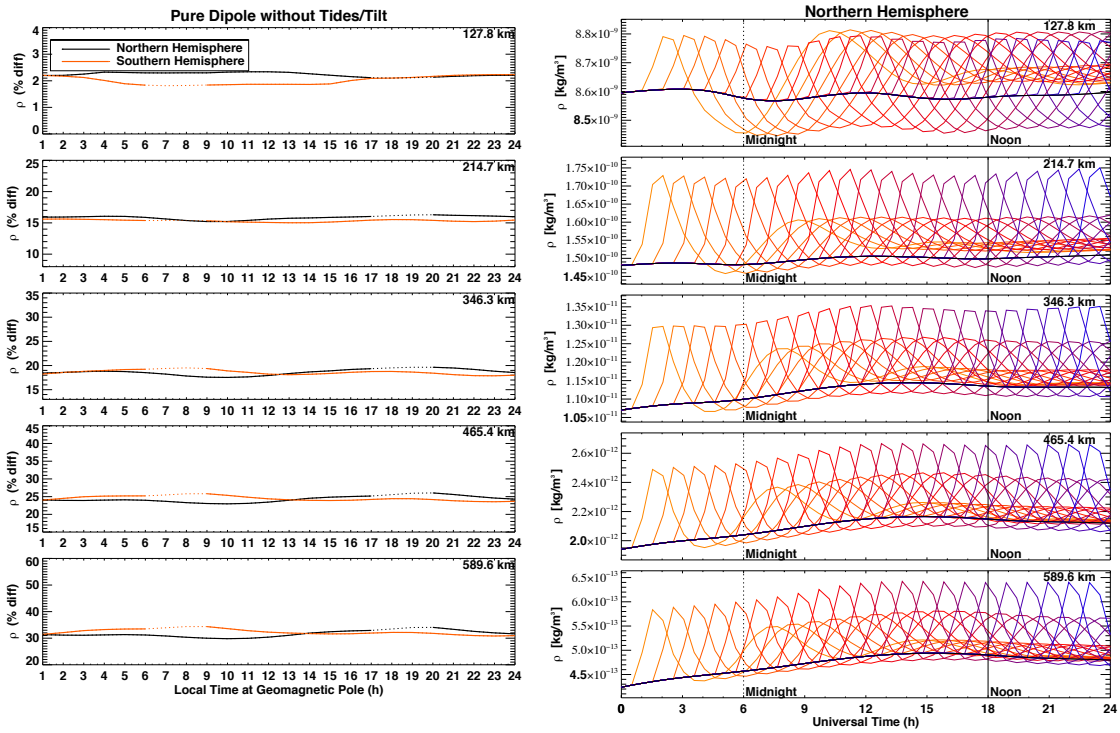

Figure 3.9: The left panel shows the normalized maxima of the thermospheric mass density in a pure dipole simulation without tides or any tilt in the *Weimer* (2005) potential model. At each altitude, the red lines show the southern hemisphere and the black lines show the northern hemisphere. The right panel shows the mean density of the same simulations.

hemisphere occurred near noon, while in June, the response was nearly semi-diurnal. The summer perturbations also had a small magnitude, peaking with nearly the same response at noon and midnight. This may be because the electron density variation that the pole is subjected to during the summer is smaller than at equinox or in the winter.

The summer signature in the southern hemisphere was not symmetric around noon as it was in the northern hemisphere. At altitudes above 200 km, the density perturbations were largest near 0500 Local Time (LT), and smallest near 1900 LT. Note that part of these asymmetries are due to the tilt angle dependence in the electric potential model, but that only accounts for a small percentage of the electric field variation throughout the day as seen in Figure 3.2. Furthermore, a relatively larger

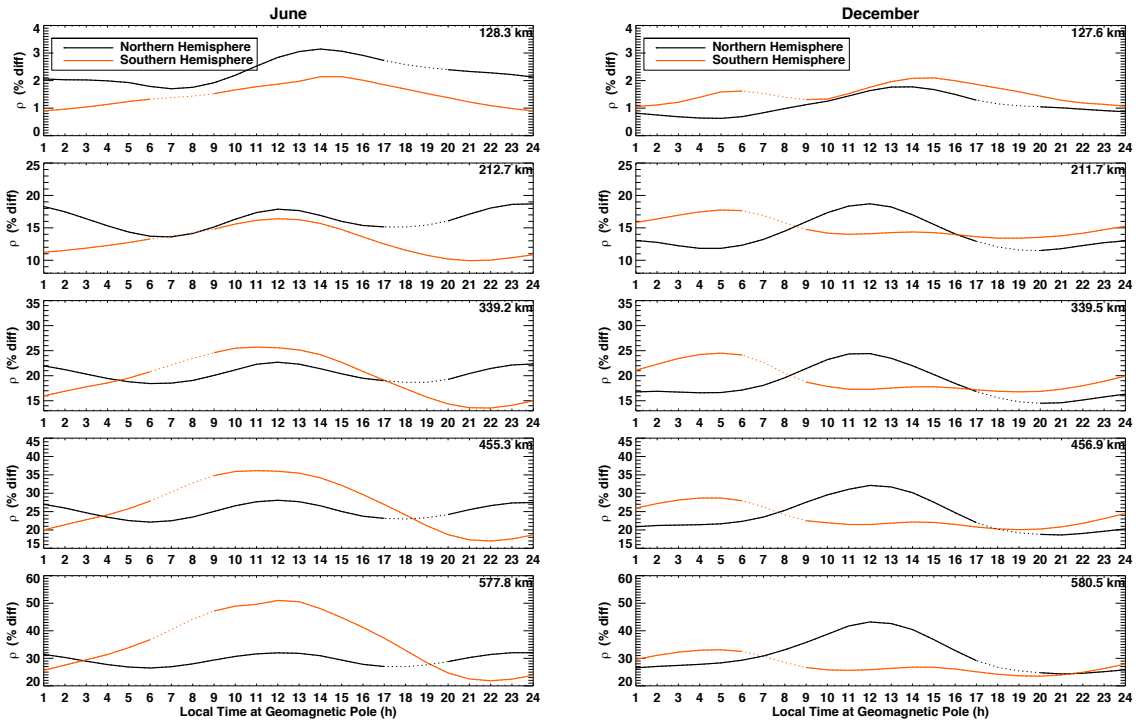

Figure 3.10: Normalized maxima of the thermospheric mass density for the June case and December case on the left and right, respectively. Both of these used the IGRF. At each altitude, the red lines show the southern hemisphere and the black lines show the northern hemisphere.

maximum to minimum difference in the perturbations existed in the southern hemisphere winter in comparison to northern hemisphere winter. Table **??** summarizes the maximum percentage changes from Figure 3.10. The magnitude of the differences of the maxima compared with equinox conditions in Table **??** are within 3% of each other, but the southern hemisphere winter showed increasing divergence from the northern hemisphere winter as a function of altitude. There was a nearly 8% larger response at 590 *km* in the southern hemisphere. *A et al.* (2012a) also found that the thermosphere density enhancements following a geomagnetic storm were greater in the southern polar region, but only during vernal equinox. They noted that this may be explained by a weaker magnetic field, allowing for stronger ion flows and subsequent Joule heating.

These results raise an interesting question regarding the seasonal dependence of

	June Max %		Dec Max %	
Altitude [km]	**N**	**S**	**N**	**S**
127.8	3.14	2.14	1.77	2.10
214.8	18.70	16.42	18.71	17.76
346.6	22.69	25.71	24.42	24.51
465.6	28.08	36.14	32.13	28.69
589.9	32.04	51.01	43.21	33.10

Table 3.2: Synopsis of the maximum thermospheric density mass density increases at June and December from Figure 3.10.

the response of the thermosphere to electric field enhancements. If we expect the increased electron density in the summer polar cap to drive a stronger response in the temperature and neutral mass density, then why did the winter hemisphere show a stronger percentage change in Figure 3.10? The answer to this is partly revealed by looking at the absolute differences in Figure 3.11. In December, altitudes above 340 km show a large absolute difference in the summer hemisphere for all local times. The larger percentage change in the winter hemisphere was therefore due to a less dense background thermosphere, not to a larger absolute change. However, the June results behave differently at similar altitudes. Here the summer hemisphere's response is only larger when the geomagnetic pole is near local midnight. The winter hemisphere's difference is just as large as the summer's when the southern geomagnetic pole is pointed towards the sun.

These asymmetries may be attributed to the larger diurnal change in the local magnetic field intensity. Figure 3.1 indicates that the structure of the magnetic field in the southern hemisphere lends itself to a potential pattern with a more varied background magnetic field strength throughout the day.

Another way to explain the hemispheric asymmetry in the reaction is through the diurnal variation of the mean electron density in each hemisphere. Figure 3.12 shows the mean electron density above 50° magnetic latitude at an altitude of 346 km plotted against the local time of the geomagnetic pole for the 4 baseline simulations of

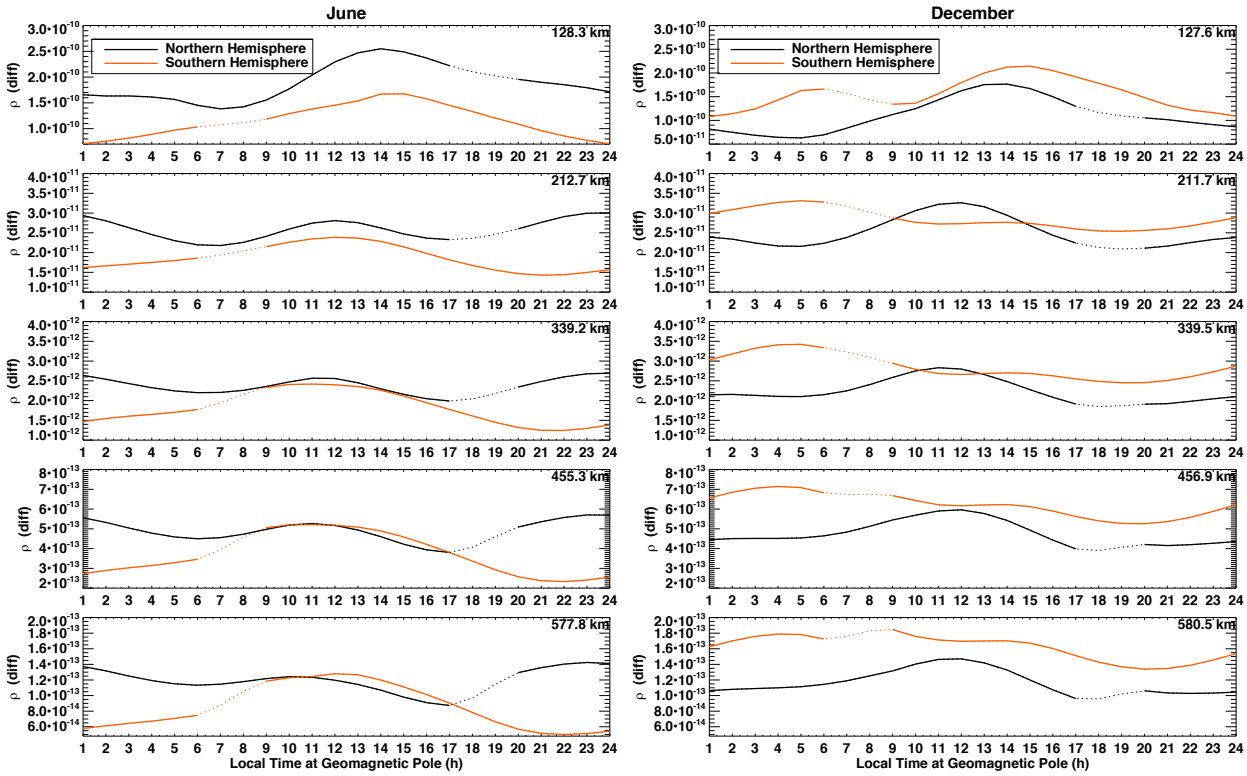

Figure 3.11: Absolute differences between the maxima of the perturbation and baseline simulations of the thermospheric mass density change for the June case and December case on the left and right, respectively. Both of these used the IGRF. At each altitude, the red lines show the southern hemisphere and the black lines show the northern hemisphere.

each of the major run sets presented in this paper, as well as 2 additional simulations to investigate the importance of tides in the UT variation. Note that the plots in the top row have a jump in the electron density occurring around 1800 LT in the northern hemisphere and 0600 LT in the southern hemisphere. This corresponds to the change from the end of one day to the start of the same day 24 hours earlier, which indicates that these simulations are not fully in steady state. The first is the March equinox case using the IGRF magnetic field configuration in plot a. Here the electron density is more variable in the southern hemisphere. When the local time at the geomagnetic pole is closest to noon, the electron density in the southern hemisphere is greater than the northern hemisphere, but near midnight it is smaller.

The degree of flatness in the peak surrounding local noon in the southern hemisphere resembles the neutral density peaks in Figure 3.8 above 200 km. Plot f of Figure 3.12 shows that the simulation with a centered dipole magnetic field configuration without atmospheric tides has no difference between hemispheres in electron density at all, which was expected. However, there is still a very small diurnal variation in both hemispheres, which may be due to a boundary condition or model parameter that has a UT dependence not fully considered here. Interestingly, it appears that the introduction of tides in the model causes the simulation to take longer to reach steady state, as Plots d and f of Figure 3.12 have almost no jump, but Plots a-c, and e of Figure 3.12 do.

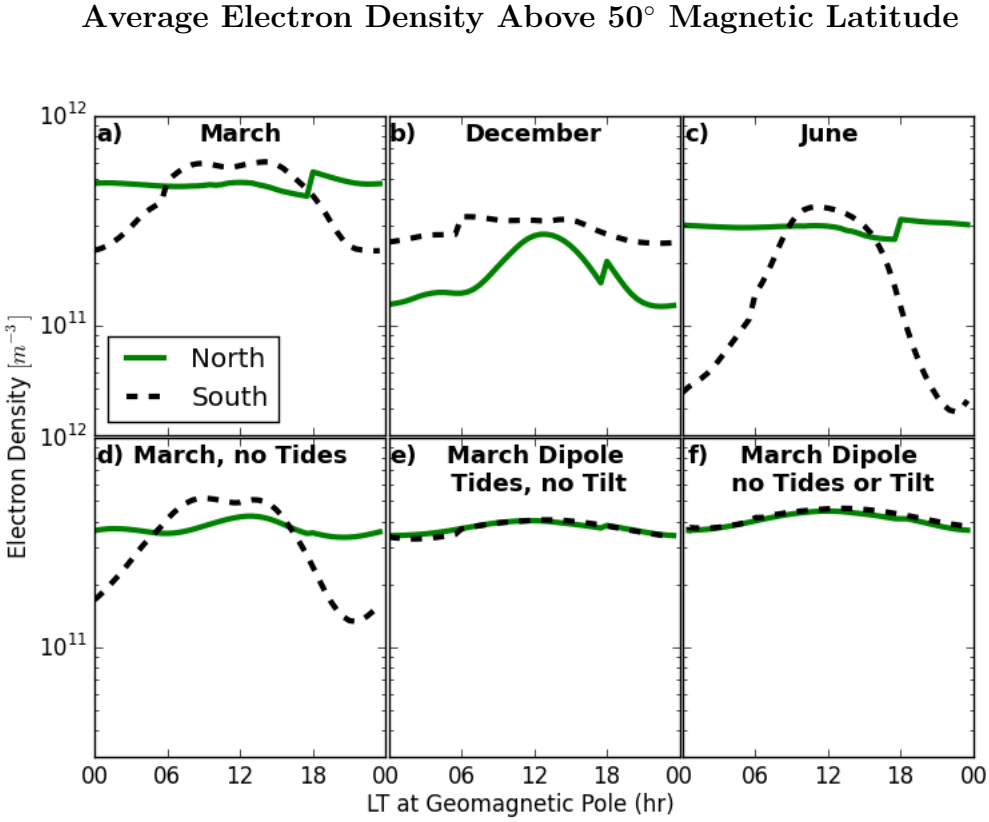

Figure 3.12: The electron density at 346 km altitude averaged above 50° magnetic latitude plotted against the local time at the geomagnetic pole for both hemispheres. The simulations plotted are the same as the baseline case of each simulation set. The northern hemisphere is given by the solid green line, and the southern hemisphere by the dashed black line.

The electron density results from the solstices are shown in Plots b and c of Figure 3.12. The winter hemisphere was characterized by a more prominent diurnal variation in electron density. In the southern hemisphere winter (dashed curve in Plot c of Figure 3.12), this effect was especially pronounced as the electron density reached a higher maximum and lower minimum than the northern hemisphere winter (solid line Plot b of Figure 3.12). This result has also been observed in topside electron density data from the Defense Meteorological Satellite Program (DMSP) (*Garner et al.*, 2010). The southern hemisphere winter electron density was also more symmetric around noon, similar to the neutral density simulations in Figure 3.10. The electron density was nearly identical for each hemisphere in the summer, implying that as more of the hemisphere is covered in sunlight, the UT dependence from the other factors is dampened.

The simulations in Plot d of Figure 3.12 are the same as Plot a of Figure 3.12, but with tides removed. The northern hemisphere electron density UT variation became more pronounced without tides. In the southern hemisphere, the slopes near dawn and dusk steepened, but the UT variation was relatively unchanged otherwise. Adding tides to the centered dipole simulations (Plot e of Figure 3.12) did not affect the electron density results very much at all. The only noticeable difference is due to the tides simulation taking longer to reach steady state.

By comparing Figures 3.10 and 3.12, a relationship between the mass and electron density variations can be understood. Since the geomagnetic pole in the southern hemisphere is more offset, the amplitude of the variations in mass density and electron density are larger than they are in the northern hemisphere. The longitudinal dependence in the magnetic field strength and declination angle is also visible in the electron density plots by the shape of the variation in the winter hemisphere. These structures are mirrored in the density peaks from Figure 3.10. The equinox case displays a similar correspondence, as the southern hemisphere peak lasts for a similar

duration as the largest neutral density enhancements.

These results are also consistent with the absolute differences in the winter hemisphere's in Figure 3.11 above 340 km. The June plot on the left reveals that when the geomagnetic pole is pointed towards the sun, there is a nearly equal response in neutral mass density. However, near local midnight, the southern hemisphere response is much smaller. This behavior corresponds to the variation in local time of the geomagnetic pole in the electron density in Plot c of Figure 3.12. Near 1200 LT, the electron density is larger than the northern hemisphere, but then drops off by an order of magnitude near 0000 LT. Furthermore, at higher altitudes, the December results show that the smaller variation in electron density leads to a smaller response in the northern hemisphere winter.

In summary, the solstice simulations show: a) the winter hemisphere has a larger UT variation, with a stronger perturbation at noon and a weaker perturbation at midnight; b) the southern hemisphere winter has larger variation than the northern hemisphere winter; and c) semi-diurnal variations observed in the summer solstice have different phases between the northern and southern hemispheres, likely due to hemispheric asymmetries in the longitudinal variations in Earth's magnetic field strength.

Plots d and e of Figure 3.12 indicate that tides play a less important role than the tilt in the Weimer model and magnetic field asymmetries. Tides do not seem to affect the electron densities as much since Plot f (no tides and no tilt) is nearly identical in shape and magnitude to Plot e (with tides and no tilt). Furthermore, Plot d (without tides) differs from plot a only in that the simulation reached steady state quicker, and that the UT variation in the northern hemisphere is slightly more pronounced.

The UT variation from the Weimer model is still present, but shown to be no more than a couple percent of the variation from the discussion of Figure 3.2. The series of simulations can not differentiate between the influence of the magnetic field

magnitude and the dependence on magnetic field declination angle, or separate any longitudinal dependence on neutral winds. These effects will have to be studied in subsequent research.

3.4 Summary and Conclusions

The Earth's magnetic field is roughly dipolar in configuration, but is tilted and offset in relation to the rotation axis. This means that as the Earth spins, the geomagnetic poles change local time. In the northern hemisphere, the geomagnetic pole is in Canada, so it is pointed most toward the sun around 1800 UT, while in the southern hemisphere, the pole is located off the coast of Antarctica, close to Australia, and is pointed most towards the sun around 0600 UT.

In equinox conditions around 1800 UT in the northern hemisphere, ion production rates at the geomagnetic pole due to solar EUV are maximized. This means that the majority of the ion convection pattern will be in sunlight. Conversely, around 0600 UT in the northern hemisphere, the ionization at the geomagnetic pole will be minimized, thereby reducing the ion density throughout the ion convection pattern. The thermospheric neutral gas heating rate due to friction between the ions and the neutrals is directly dependent on the electron density (*Deng and Ridley*, 2005, 2007; *Codrescu et al.*, 1995). It is therefore expected that when there is increased ionization, there would be increased thermospheric heating, which was observed in the idealized simulations described above. In conclusion, it was found that:

- The thermospheric heating due to an ion convection increase was greater when the geomagnetic pole was pointed towards the sun than when it was pointed away from the sun, during winter and equinox conditions.
- The winter hemisphere displayed a stronger overall response to solar wind electric field perturbations in the percentage change in the neutral mass density,

than the summer hemisphere. This variability was caused by the winter hemisphere having a larger variation in the polar-cap electron density than the summer hemisphere, and is consistent with previous observations (e.g. *Hedin and Carignan*, 1985; *A et al.*, 2012a).

- Longitudinal variations in Earth's magnetic field strength and declination angle are secondary factors in the UT variation in both the thermosphere and the ionosphere.

- The larger offset of the geomagnetic pole in the southern hemisphere leads to a larger UT variation compared to the northern hemisphere.

These results imply that ionospheric and thermospheric models, including those which predict satellite drag, should incorporate UT and seasonal dependencies. They should also take into account the hemispheric asymmetries described above. Further research is needed to quantify these effects during real storms. The physical processes behind the influence of the magnetic field structure in the UT variations have yet to be uncovered and should also be explored in more detail.

CHAPTER IV

A Year Long Comparison of GPS TEC and Global Ionosphere-Thermosphere models

An important application of global ionosphere-thermosphere (IT) models is in understanding and predicting the TEC in the upper atmosphere. This is critical for the practical reasons that gradients in TEC lead to GPS signal degradation and scintillation of high frequency radio signals (*Pi et al.*, 1997; *Vladimer et al.*, 1999; *Jakowski et al.*, 2005; *Afraimovich et al.*, 2009). The advent of global TEC maps (*Mannucci et al.*, 1998; *Rideout and Coster*, 2006) has afforded global modelers the ability to perform large scale data-model comparisons. Additionally, many studies have advocated the use of data assimilation to improve numerical models of the ionosphere (*Hajj et al.*, 2004; *Wang et al.*, 2004; *Schunk and Nagy*, 2004; *Schunk et al.*, 2005; *Scherliess et al.*, 2008; *Chen et al.*, 2016; *Chartier et al.*, 2016). The purpose of this study was to investigate the performance of two models in comparison with GPS TEC data for the entire year of 2010. Results were compared for a variety of temporal and regional scales in both magnetic and geographic coordinates. In doing so, the capabilities of two different modeling approaches were quantified to highlight strengths and areas of bias in terms of TEC. *Shim et al.* (2012) performed a thorough analysis of a number of IT models in response to 9 different events. This Chapter expands on that study by focusing on just two models during an entire year

of predominately quiet times. The two models used in this study were the TIEGCM (*Roble et al.*, 1988; *Richmond*, 1992; *Qian et al.*, 2013) and the GITM (*Ridley et al.*, 2006). The most relevant differences and model configurations used in this study are described in Section 4.1. Relevant sources and losses of the ionosphere are described in 1.2

4.1 Model and Data Description

GITM and TIE-GCM are parallel, 3-dimensional, time dependent codes that solve the fully coupled momentum, energy, and continuity equations for both neutral and ion species. Both are described in more detail in Section 2.1. For this study, electron precipitation in both models was provided by *Fuller-Rowell and Evans* (1987a) and electric potentials were specified by *Weimer* (2005), driven by the upstream solar wind conditions observed from the ACE spacecraft (*McComas et al.*, 1998; *Smith et al.*, 1998). Both TIE-GCM and GITM were run for the entire year of 2010 with an output cadence of 30 minutes.

The temperature and density of the thermosphere at the lower boundary of GITM (95-100 km) was specified by the MSIS model (*Hedin*, 1983, 1987, 1991). As such, seasonal variations, diurnal and semi-diurnal migrating tides were empirically included in GITM's lower boundary. The horizontal wind patterns at the boundary were specified by the Horizontal Wind Model (*Drob et al.*, 2008). The FISM (*Chamberlin et al.*, 2007) defined the solar EUV flux. GITM was run with a resolution of 1.0° latitude by 4.0° longitude with a stretched altitude grid, resolving the vertical scales to approximately 1/3 of a scale height.

The TIE-GCM simulation had a resolution of 2.5° latitude by 2.5° longitude with 4 grid points per scale height. Daily and 81 day averaged $F_{10.7}$ were used to specify the solar EUV flux in accordance with the EUVAC model (*Richards et al.*, 1994). Since photoionization is a primary source of TEC, the change in EUV flux model could

be important. *Peterson et al.* (2009) showed that the EUVAC model prescribed a slightly higher solar irradiance power than the data through which the FISM model was based. It is therefore expected that TEC from photoionization will be larger in TIE-GCM. The difference between the two models is much greater during solar flares (*Strickland et al.*, 2007), but this shouldn't have effected the primarily quiet time results shown here.

The neutral temperature at the lower boundary of TIE-GCM was fixed at 181K, with a constant density. Both migrating and non-migrating tides were included in TIE-GCM as specified by The Global Scale Wave Model (GSWM) (*Hagan and Forbes*, 2002, 2003). Since the tides are partly a result of solar EUV forcing, seasonal and local time variations exist within the GSWM. Some of the differences in results between the two models throughout the day and/or year may therefore be attributed to the different lower boundary conditions. Since each model is highly dependent on it's inputs and drivers (e.g. *Liuzzo et al.*, 2015), the results in this paper represent what occurred during typical model runs.

Model results were compared to ground-based GPS receiver data provided by the Madrigal database at MIT Haystack Observatory (*Rideout and Coster*, 2006). Vertical TEC was used as it provides the best estimate of TEC distributions in the ionosphere based on slant-path TEC measurements (*Mannucci et al.*, 1998). The relative precision of TEC provided by GPS measurements is on the order of 0.01 TECU with an absolute accuracy of 1-3 TEC-Unit, where 1 TECU = $10^{16}[e/m^2]$ (TECU) (*Mannucci et al.*, 1998; *Tsurutani*, 2004). In each model comparison, the TEC was calculated by integrating the electron density over all altitudes. Corresponding values were then interpolated to the times and locations of the GPS observations. The small contribution of electrons to the TEC in the region above the model boundaries were ignored. Furthermore, the oscillating upper boundary of TIE-GCM may have lead to a difference in the height of integration compared to GITM. This was also neglected,

since the density of electrons above 500 km is generally an order of magnitude less than the F2 peak (*Schunk and Nagy*, 2004). The primary metrics used to evaluate the models were RMSE and PE. These parameters are well described in *Shim et al.* (2012). Note that a PE of 1 indicates a perfect prediction, 0 means that the model accuracy was on par with the variance of the observations, and negative values indicate that RMSE was larger than the variance of the observations. If the PE is negative, simply taking the average of the observations would have given a better prediction of the TEC than the model.

4.2 Results

Plots C-G in Figure 4.1 show the GITM results in blue, TIE-GCM in red, and observations in black for the entire year of 2010. Plots A and B show the $F_{10.7}$ and Dst indices for reference. All of the values in this figure are daily averages. The $F_{10.7}$ values in plot A resemble the characteristic 27-day rotation of the sun, but this period is not reflected in either the observations or the models. While $F_{10.7}$ has been shown to be a very good proxy for EUV flux on long time scales (*Wintoft*, 2011), a variation of 15 $W/m^2/Hz$ between solar rotations was not enough to drive significant changes in average daily TEC values.

2010 was a relatively quiet year in terms of solar activity. The average daily Dst dropped below -40 nT only 5 times. Some of the larger spikes in the northern hemisphere GITM TEC correspond with these days, but not in the GPS measurements. The TEC spikes in GITM occurred on the first day of the month in the summer hemisphere as a result of numerical error produced by restarting the simulation on a monthly basis. TIE-GCM had smaller increases in TEC in the southern mid-latitudes, which did agree with observations. GITM over-responded to geomagnetic storms in terms of TEC in the northern hemisphere, but not the southern.

TIE-GCM consistently under-predicted the TEC at all latitudes and seasons, ex-

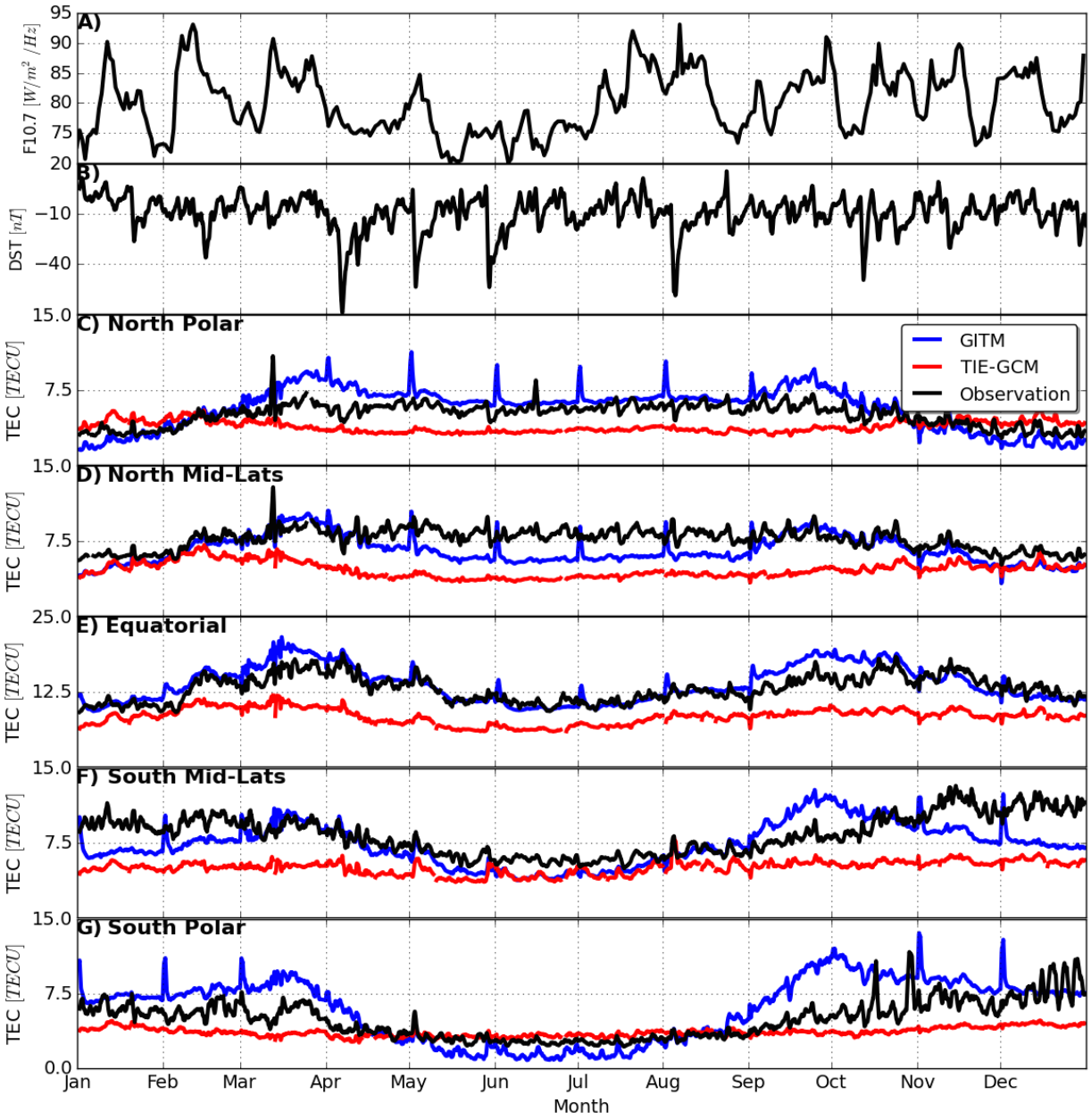

Figure 4.1: $F_{10.7}$ and Dst in the first two rows followed by daily averages of the TEC in 5 different regions in plots C-G. GITM results are plotted in blue, TIE-GCM in red, and observations in black. Note that the scale in the equatorial region in plot E goes to 25 TECU instead of 15. Each plot represents a 30° bin in geographic latitude. Plot C represents latitudes from 60° to 90°, plot D from 30° to 59° to degrees, and so on.

cept for the polar winters. This is contrasted with an under-prediction by GITM during these times as is evident in December and January of plot C. Here, TIE-GCM was 1.09 TECU above observations, but GITM was below by 1.14 TECU. For the months of May through July, the southern hemisphere winter, plot G shows that GITM was 1.29 TECU lower than observations, while TIE-GCM was only 0.64 TECU higher. Contributing factors to these results include differences between the models in the EUV flux model, chemistry, upper boundary conditions, and neutral winds. The seasonal biases of each model are further investigated in the following sections.

The GITM TEC increased significantly at all latitudes during the month of September, especially in the southern hemisphere. While this does correspond to an increase in F10.7, the same could be said about other months such as July where the GITM TEC stayed relatively constant at all latitudes. A similar, but less pronounced increase occurs in GITM during March, suggesting that this feature may be related to equinox conditions. This has been reproduced before in a version of TIE-GCM that included lower atmosphere dynamics (*Mendillo et al.*, 2002) which were postulated to be related to vertical drifts imposed by neutral winds instead of composition changes in the thermosphere.

There was more TEC near equinoxes than solstices in both the GITM and GPS observations. These semiannual variations in low and mid-latitudes have been observed before and are related to thermospheric temperature and density, as well as the peak F2-layer height and electron density, hmF2 and NmF2, all of which peak near equinox (*Rishbeth and Mendillo*, 2001; *Rishbeth*, 2004). The ability for GITM to capture this variation is possibly related to the use of MSIS (*Hedin*, 1987) for the lower boundary condition of the thermosphere. *Hedin* (1987) reported that the model has a minimum in atomic oxygen and molecular nitrogen in July, and a maximum in October at equatorial latitudes. Furthermore, the semiannual variation in MSIS is stronger in the southern hemisphere for oxygen, but stronger in the northern hemisphere for

	GITM		TIE-GCM	
	RMSE	PE	RMSE	PE
North Polar	1.38	-0.55	1.92	-2.10
North Mid-Lats	1.60	-1.41	3.36	-9.94
Equatorial	1.80	0.32	4.90	-3.94
South Mid-Lats	2.13	-0.18	3.68	-2.52
South Polar	2.31	-0.53	1.99	-0.17
All	1.84	-0.47	3.17	-3.73

Table 4.1: RMSEin TECU and PE for GITM and TIE-GCM versus GPS TEC observations. The values are taken from daily averages for the entire year of 2010.

molecular nitrogen. Since oxygen is the main constituent of the thermosphere above a certain altitude, photoionization of more oxygen should lead to more TEC in the southern hemisphere, which is what happened in GITM. Additionally, a stronger semiannual variation of N_2 in the northern hemisphere will decrease the O/N_2 ratio compared to the southern hemisphere, which will dampen the variation there. This is another characteristic seen in plots C and G of Figure 4.1.

The results from Figure 4.1 are quantified in Table 4.1 using the RMSE and PE metrics. Each metric is shown by geographic latitude, as well as for the entire globe in the final row. Interestingly, GITM's RMSE was smallest in the northern hemisphere polar region and then increased in an almost perfectly linear fashion as the domain moved towards the southern pole. This suggests that the model parameters in GITM may be over-fitted to the northern hemisphere. A separate but distinct pattern emerged in the TIE-GCM results where the RMSE was lowest near the poles and increased towards the equator. Since the dominating physical processes in the polar regions are the same, TIE-GCM may have captured the physics related to TEC consistently better in the polar regions than at the equator.

The PE of GITM for both models was negative at all latitude bins, except for GITM in the equatorial region. These results indicate that, even though each model produced TEC with an RMSE of less than a few TECU, simply taking the mean of the

observations would provide a better prediction of the globally averaged TEC during quiet times than either model in most cases. It should be noted that the PE for TIE-GCM, GITM, and other models was found to be worse during quiet times than during storms, presumably because an increase in the variance of observations decreases the PE (*Shim et al.*, 2012). Additionally, both models had a significantly worse PE in the northern mid-latitudes, approximately 3 times worse than any other latitude region. Perhaps this is expected, since physics from both the polar and equatorial regions are important here. This trend was not true in the southern mid-latitudes and will be investigated further in Section 4.2.2

In the polar regions, coupling with the magnetosphere and solar wind dominates the movement of both the plasma and the neutrals in the upper atmosphere. As such, it makes sense to investigate each model's TEC results also in terms of MLT. Additionally, viewing the TEC in magnetic coordinates ensures the equatorial anomaly stays within the equatorial latitude bin.

4.2.1 MLT and Seasonal Dependence

Figure 4.2 shows the TEC variation in MLT averaged over the different solstice and equinox months. This data was also averaged over magnetic latitude, such that this represents a global average of the TEC. The blue and red solid lines represent the GITM and TIE-GCM results respectively, while the dashed black line is the GPS observations. The RMSE error is displayed in the bottom left corner of each plot. In all cases, TIE-GCM under predicted the observations, with RMSE's ranging from 2.1 TECU in December, to 4.2 TECU in September. GITM's results were much more varied. During the solstice months, GITM also under predicted the TEC, except in the dawn sector. During the equinox months, GITM consistently over predicted the TEC by up to 4 TECU on the dayside. The RMSE was the same for both equinox months at 3.1 TECU.

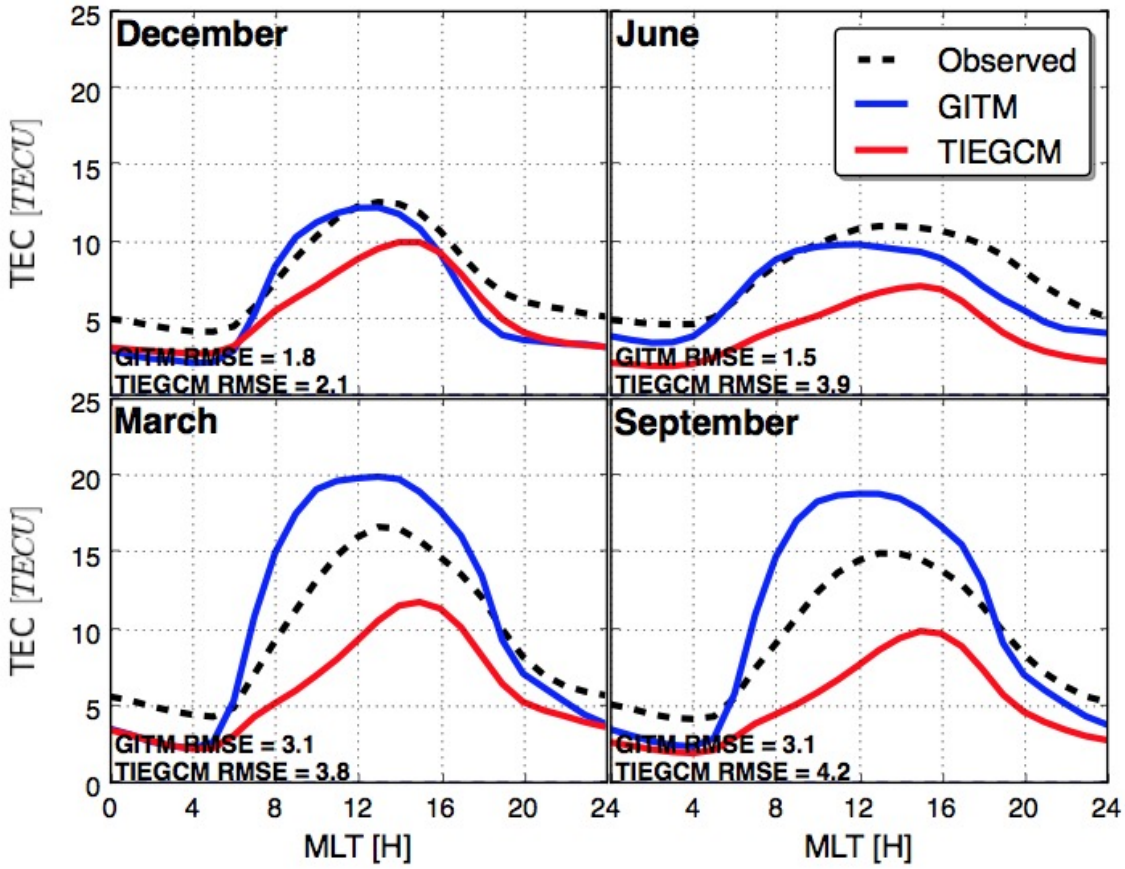

Figure 4.2: TEC in TECU versus MLT for both solstices at the top and equinoxes at the bottom. The results were averaged over the entire month and all latitudes for each plot. GITM is represented by blue, TIE-GCM by red, and GPS observations by the dashed black line. The RMSE for each model is displayed in the bottom left of each plot.

The June and December plots in Figure 4.2 reveal how much hemispheric asymmetry effects globally averaged TEC. If plasma production was solely due to photoionization, these plots would have been very similar. However, there was a flattening of the post noon TEC peak in both the models and the observations in June, the northern hemisphere summer. Furthermore, the maximum of this peak was 1.5 TECU less than in December. This phenomenon has been widely observed and is known as the F_2 layer annual asymmetry. It has been attributed to a combination of neutral composition changes (*Mendillo et al.*, 2005), influence of the lower atmosphere (*Rishbeth*,

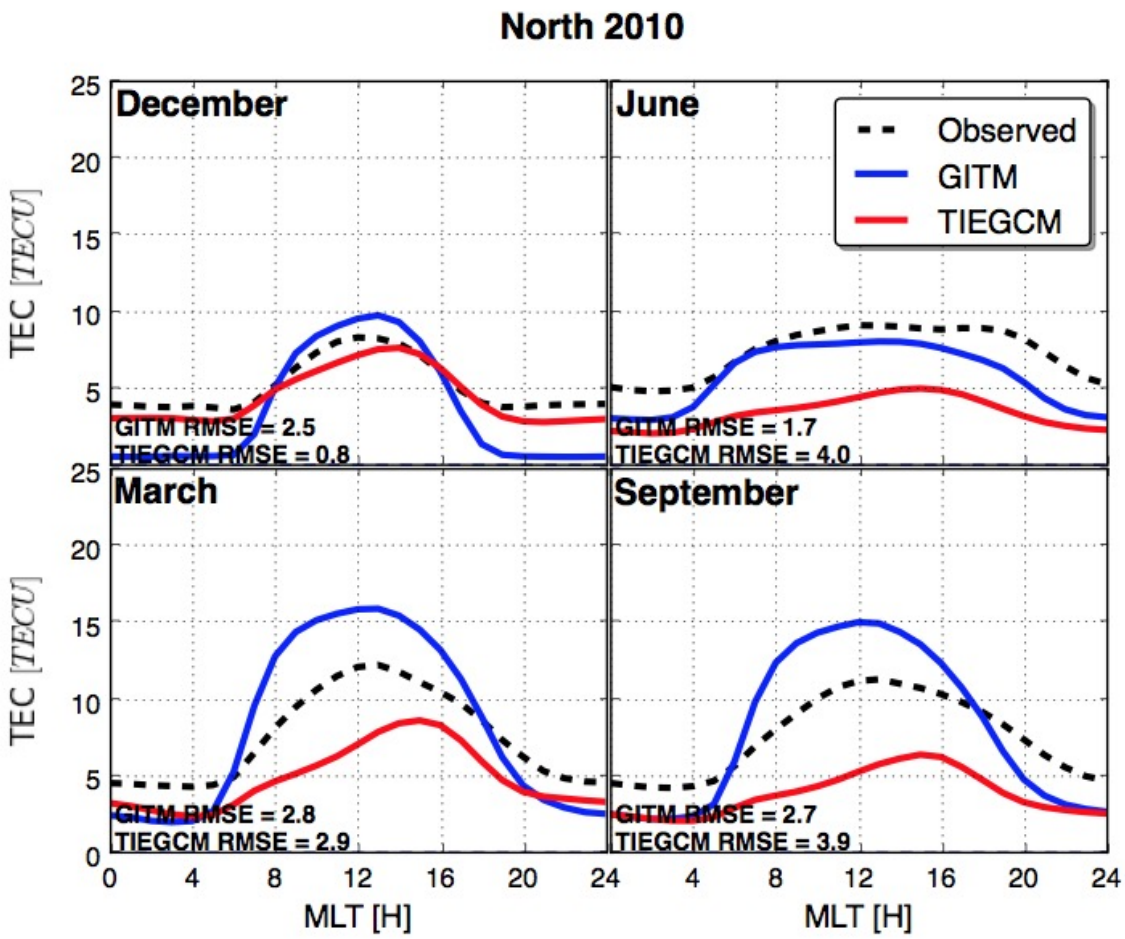

Figure 4.3: The same as Figure 4.2, but for magnetic latitudes greater than 30° in the northern hemisphere.

2006), and the separation of the geographic and geomagnetic axes combined with the change in distance from the sun (*Zeng and Horwitz*, 2008). The broader peak in the northern hemisphere resembles the structure of the magnetic field strength. Since the dynamics of the hemisphere in which most of the electrons reside dominates this plot, it is possible that the magnetic field structure was controlling the globally averaged TEC. The difference between hemispheres is likely subdued since the largest contributor of TEC is the equatorial region. To investigate this further, Figures 4.3, 4.4 and 4.5 show the same parameters split into latitudinal regions. Figure 4.3 represents all magnetic latitudes above 30° in the northern hemisphere, such that the midlatitudes and polar regions from Figure 4.1 are merged. Figure 4.4 is the same except for in

the southern hemisphere and Figure 4.5 is the equatorial region, from -30° to 30° latitude.

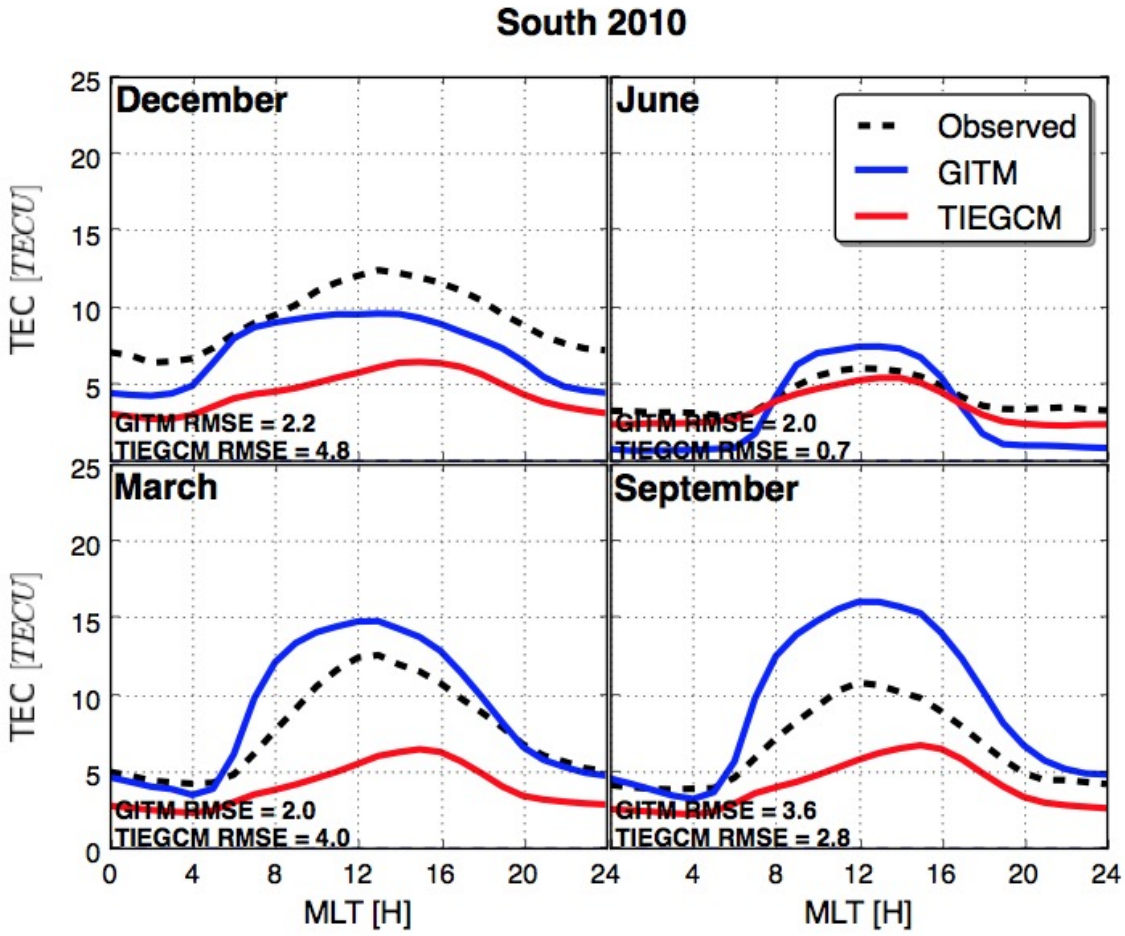

Figure 4.4: The same as Figure 4.3, but for magnetic latitudes greater than 30° in the southern hemisphere.

Comparing Figures 4.3 and 4.4, a few notable differences arise both from model to model, and in the observations themselves. Starting with the observations during the solstices in the top row, the southern hemisphere TEC maximum varied from 12.5 TECU in December to 6 TECU in June, but stayed relatively constant between solstices at 8-9 TECU in the northern hemisphere. TIE-GCM performed very well in both winter hemisphere's with an RMSE of less than 1 TECU in both cases. GITM's RMSE ranged from 1.7 TECU to 2.5 TECU, performing much better on the dayside than the nightside in every case. In fact, GITM had almost no TEC on the nightside

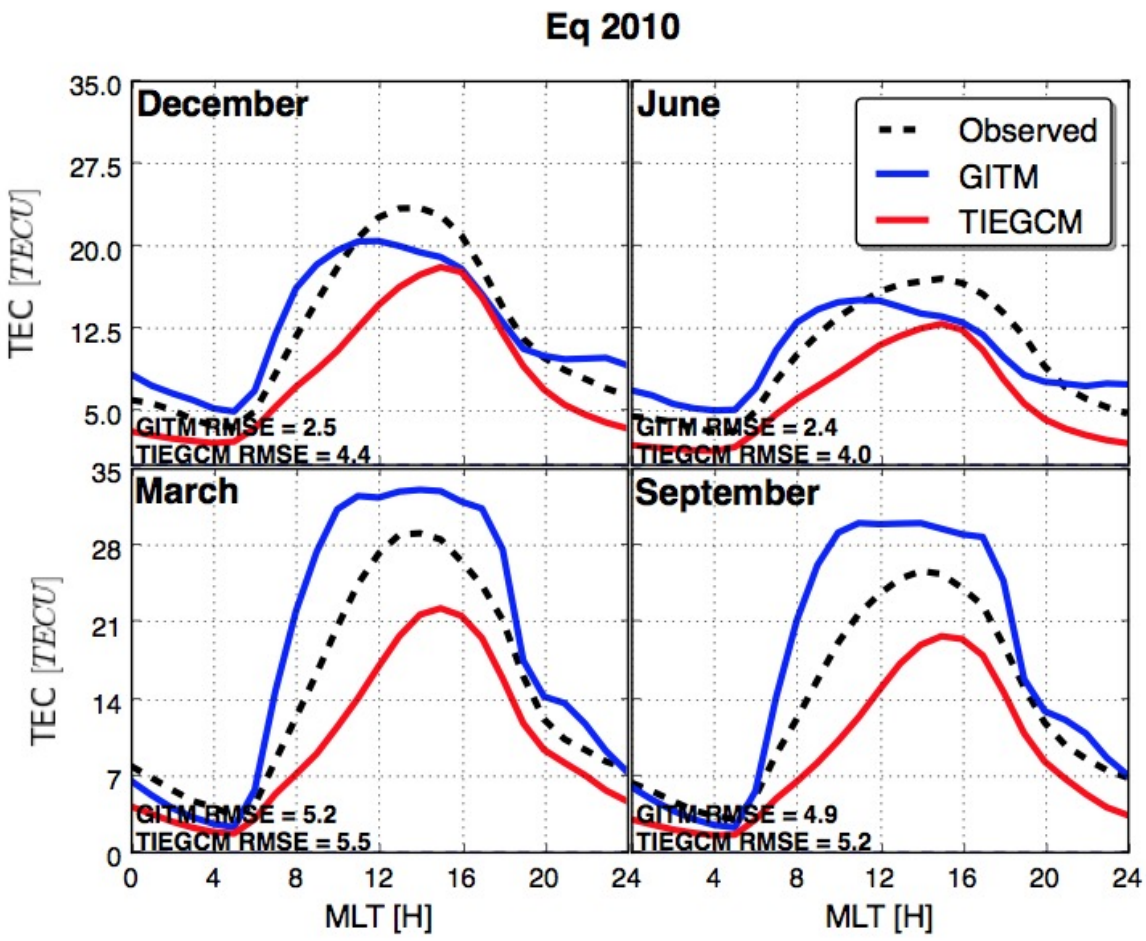

Figure 4.5: The same as Figures 4.3 and 4.4, but for magnetic latitudes between -30° and 30°.

in the winter hemisphere. This is contrasted with TIE-GCM which had 3.5 TECU on the nightside during the summer and 3 TECU during the winter. The lack of nightside TEC in GITM is because the model does not include plasmaspheric drainage back to the ionosphere during the night time (*Lunt et al.*, 1999; *Yizengaw et al.*, 2008), unlike TIEGCM. The observations during both summer hemispheres indicated that TEC persists longer after dusk in the northern hemisphere. While both models did produce an elongated TEC peak, they began decreasing around 16 MLT, compared to the observed 19 MLT.

Both models performed measurably worse in the equatorial region, shown in Figure 4.5. At the peak, GITM overestimated the TEC by 2-5 TECU and TIE-GCM

underestimated it by 4-7 TECU, though its peak was shifted by 3 MLT like during the solstice months. Also during the solstices, GITM had a TEC peak on the dawn-side near 9 MLT. To elucidate this and the other features described in this section, detailed contour plots are shown in Section 4.2.2.

4.2.2 TEC Maps

A more detailed view of the TEC is required to uncover reasons why the models may have the particular biases described in the previous sections. For the June solstice, Figures 4.6, 4.7, and 4.8 show TEC maps for GPS observations, GITM, and TIE-GCM, respectively. In each figure, the northern and southern hemispheres are shown poleward of 60° latitude in the left and right dial plots, respectively. TEC for the entire planet verses local time is shown in the rectangle plot, separated by the same latitude bins as Figure 4.1. These figures were averaged over the entire month of June to, in a sense, dampen the signal to noise ratio of the plots, Since they are in local time coordinates, any longitudinal features were also erased which helps to compensate for the sparse data over oceans. Viewing the entire month allowed patterns to emerge rather than possible transient structures that may have existed on the actual solstice. All of the results were taken at the vertical TEC locations and the averaging and plots were made exactly the same way with the data and models.

The structure of the GPS TEC in the polar region of the northern hemisphere in Figure 4.6 was different than expected considering just photoionization alone, since one might expect that the electron density would decrease from the dayside to the nightside in accordance with the solar zenith angle. The TEC wrapped around the globe extensively, creating a TEC hole between 70° and 80° from 21-02 LT. The TEC hole was likely created by the $\mathbf{E} \times \mathbf{B}$ ion drift transporting plasma downwards along magnetic lines on the nightside into a region of higher neutral density where recombination rates are faster (*Deng*, 2006). The equatorial anomaly (*Appleton*,

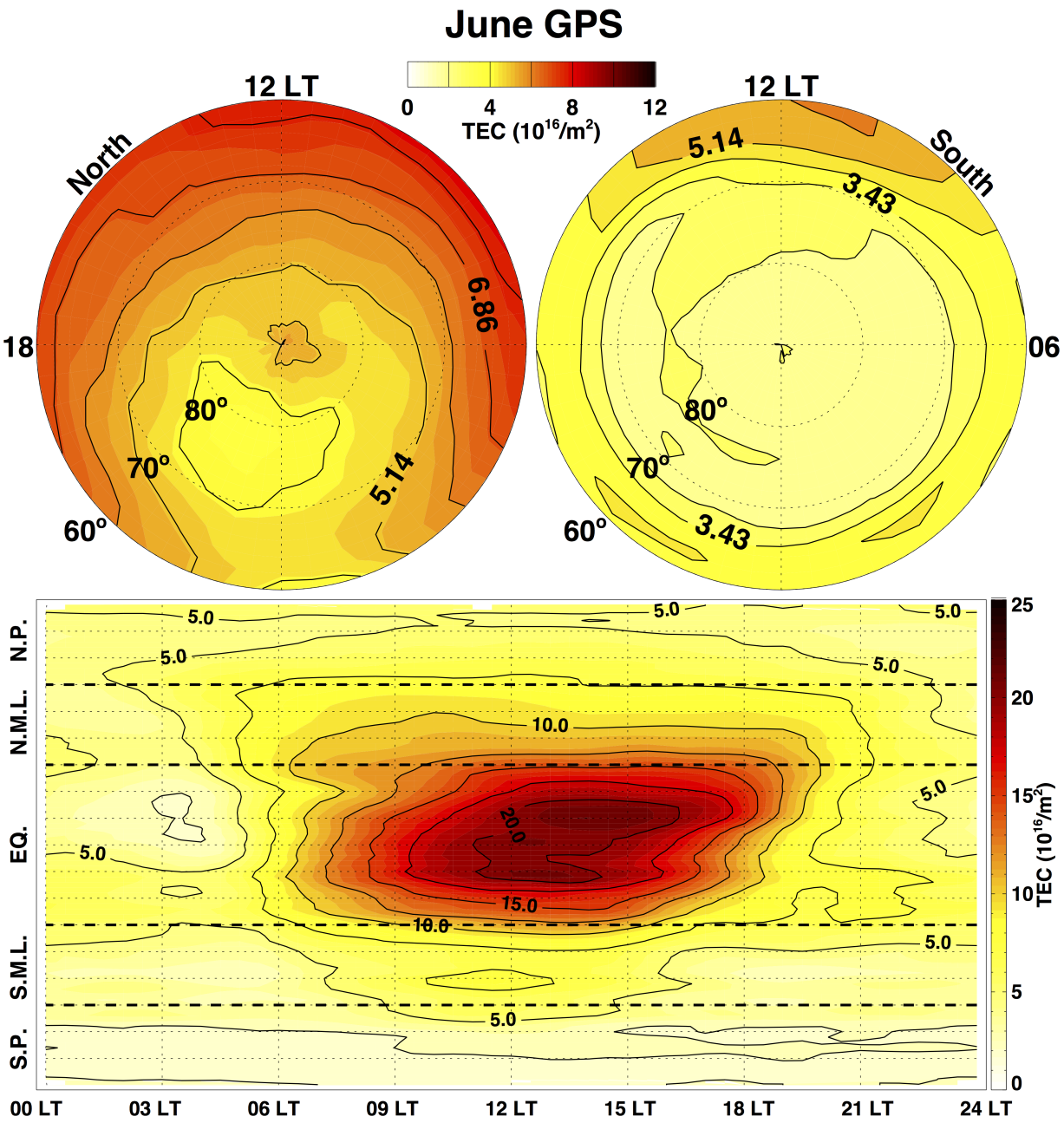

Figure 4.6: Global view of TEC for GPS observations averaged over the month of June, 2010. The dial plots are the northern (left) and southern (right) hemisphere's poleward of 60°. The rectangle plot is divided into the same latitude bins as Figure 4.1. Note that this Figure is now in local time and geographic latitude instead of magnetic coordinates. The scale of the polar plots is half that of the rectangle plot.

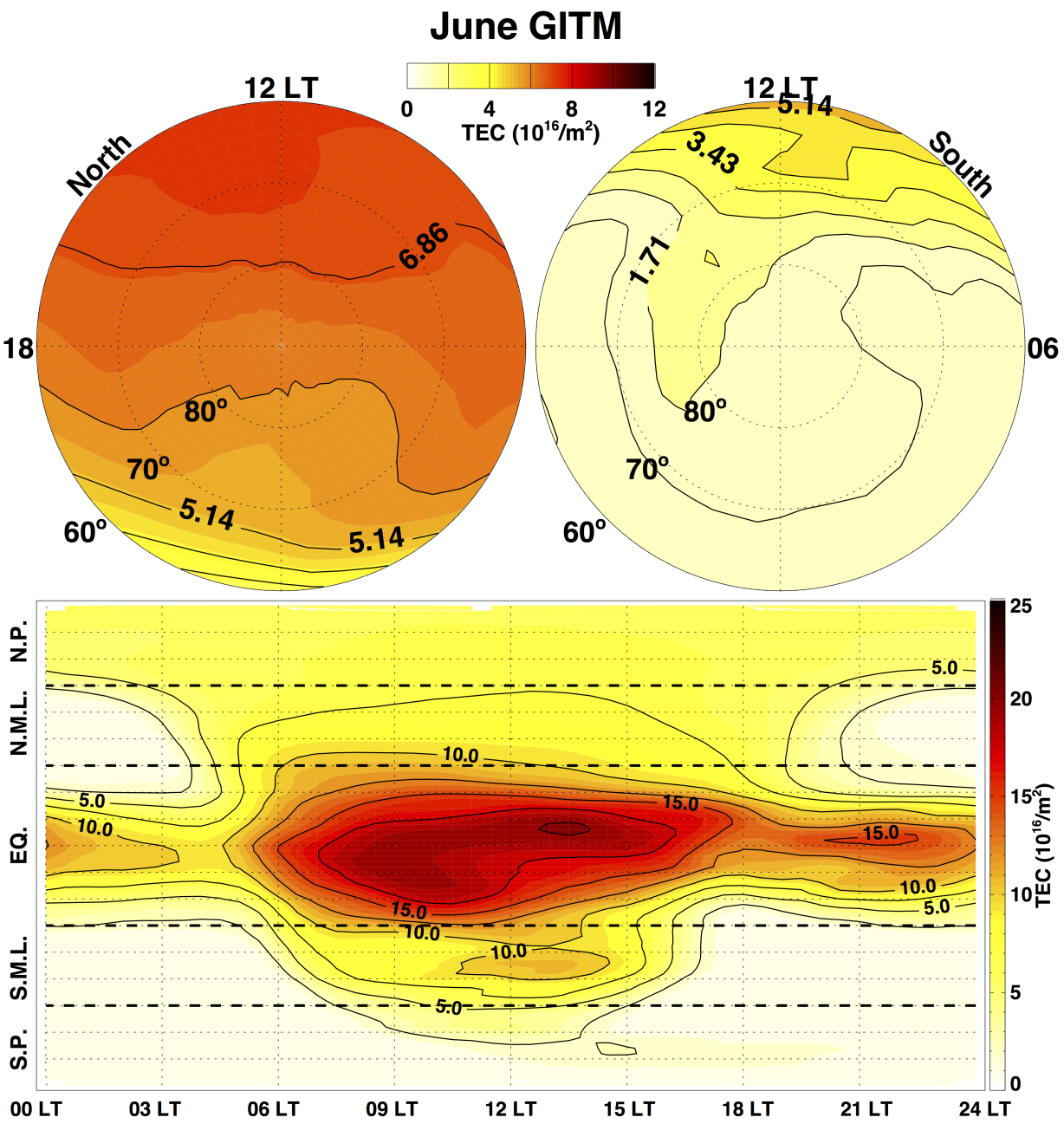

Figure 4.7: The same as Figure 4.6, except for the GITM simulation results.

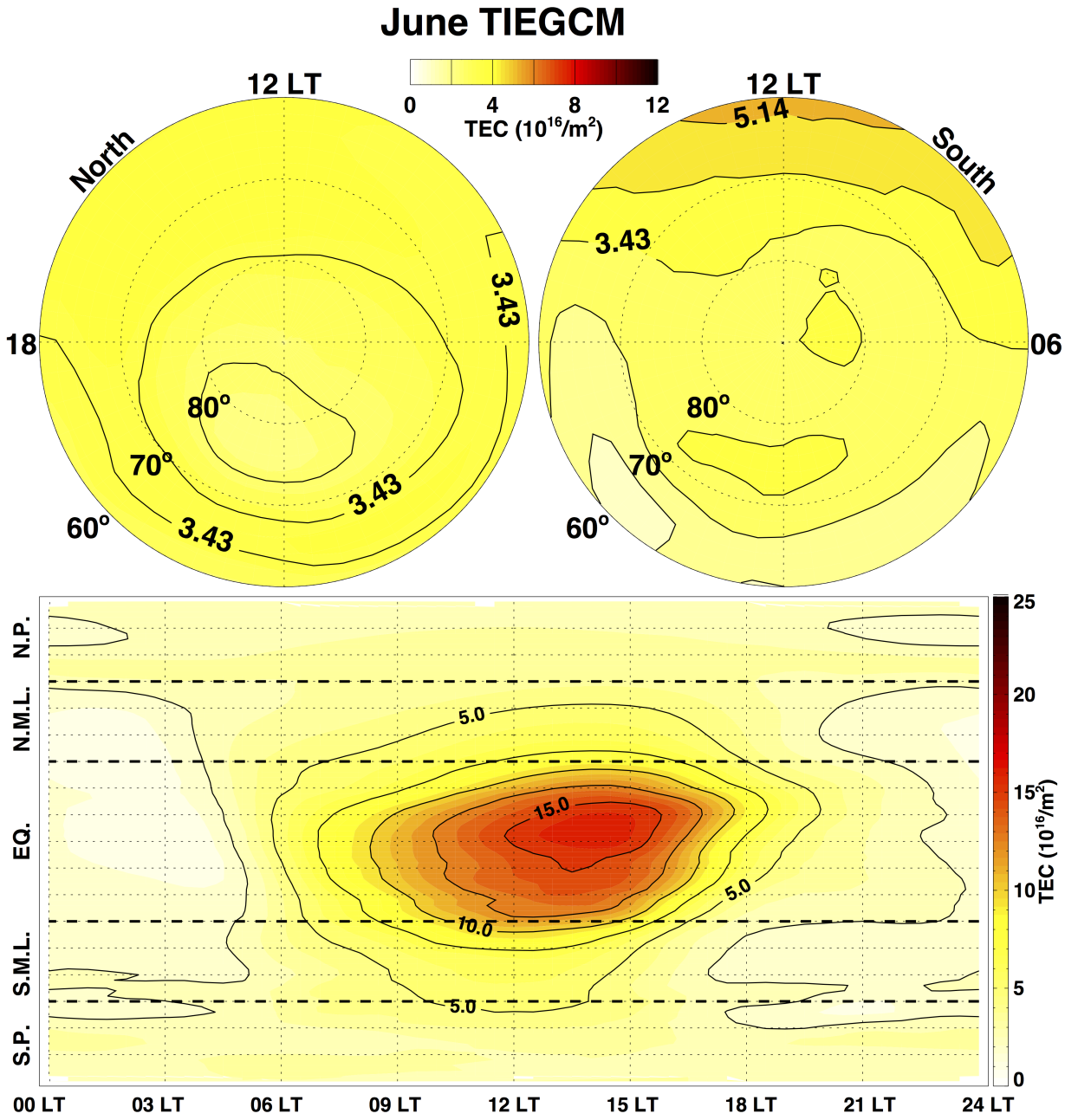

Figure 4.8: The same as Figures 4.6 and 4.7, except for the TIE-GCM simulation results.

1946) is visible by the TEC maxima at +/- 10° from 12-15 LT. However, the four peak ionospheric equatorial anomaly (*Immel et al.*, 2006; *Scherliess et al.*, 2008) was not observed.

The TEC in the northern polar latitudes in the GITM simulation was stratified across the polar cap predominately in accordance with solar zenith angle dependent photoionozation. The upper left plot in Figure 4.7 shows that the TEC steadily decreased from about 10 TECU at 12 LT to 4 TECU at 00 LT at 60°. The TEC hole in the polar cap was not reproduced, possibly indicating that there was a divergence between actual and simulated neutral winds here. The polar winter hemisphere was similarly stratified on the dayside, but a TEC bulge persisted towards the duskward nightside, similar to the observations. This may have resulted from interactions with the ionospheric convection pattern, neutral winds, or a number of other processes (*Zou et al.*, 2013).

The dayside equatorial TEC maximum did not spread into the midlatitudes nearly as much as the GPS measurements. For example, the GITM TEC dropped to 50% of its peak value by 28° latitude at 12 LT. This is contrasted with nearly 40° in the GPS TEC. Furthermore, there was a deep TEC minimum on the nightside at mid-latitudes which likely corresponded to the lack of plasmaspheric refilling in the model. This also occurred in the southern hemisphere mid and polar latitudes. However, many electrons persisted in the nightside ionosphere in GITM in the equatorial region. The equatorial anomaly in GITM is exceedingly efficient at lifting plasma in this region, possibly resulting in the nightside enhancement as well as the faster decline in TEC towards mid-latitudes. Additionally, tidal variations in the equatorial region are visible in Figure 4.7. A TEC bulge associated with the seasonal anomaly discussed in Section 6.2 was also produced near 13 LT between 40° and 50°.

TEC in the TIE-GCM simulation had a different structure than either GITM or the GPS observations. Shown in Figure 4.8 for the same time period, the TEC in both

polar regions was nearly uniform around 3.5 TECU. While some processes sustained the polar winter TEC, a TEC decrease in the polar cap did not evolve. The model also reproduced the known seasonal anomaly, but to a broader extent than GITM. An equatorial anomaly was not as present in the TIE-GCM results, but the single TEC maximum in the equatorial region was positioned closer to the observations between 12 and 15 LT at 5° latitude in the northern hemisphere, whereas GITM had a broad TEC maximum from dawn to dusk. Except for the southern polar region, the nightside TEC in the TIE-GCM simulation was also smaller than observations, but to a lesser extent than GITM.

Both models reproduced the structure of the GPS TEC observations relatively well during March. Figures 4.9, 4.10, and 4.11 show contour plots of the TEC averaged over the month for the observations, GITM, and TIE-GCM respectively. Note that compared to the June figures, the maximum scales are increased to 50 TECU in the rectangle plot and 25 TECU in the polar plots, except for the TIE-GCM figure which are 25 and 12 TECU. TIE-GCM had less TEC during this month so the smaller scale allows for a better structural analysis.

The GPS observations had at least 4 distinguishing features. The first is that the most TEC resided between 12-15 LT from -8° to -15° latitude. This is presumably due to the equatorial anomaly combined with the transition from the southern hemisphere summer. In September, this peak occurred in the northern hemisphere (not shown). TIE-GCM matched the longitudes of the maximum, but peaked closer to the equator, with longitudinally narrow TEC enhancements from the equatorial anomaly. GITM peaked much later in the day, from 14-17 LT, as well as in the northern hemisphere near 5° latitude.

The second feature is that there was an extension of the equatorial TEC into the dusk side, extending from 15-00 LT. The observations were characterized by what looks like diffusion from 17-20 LT as well two extensions at 0° and -9° that are most

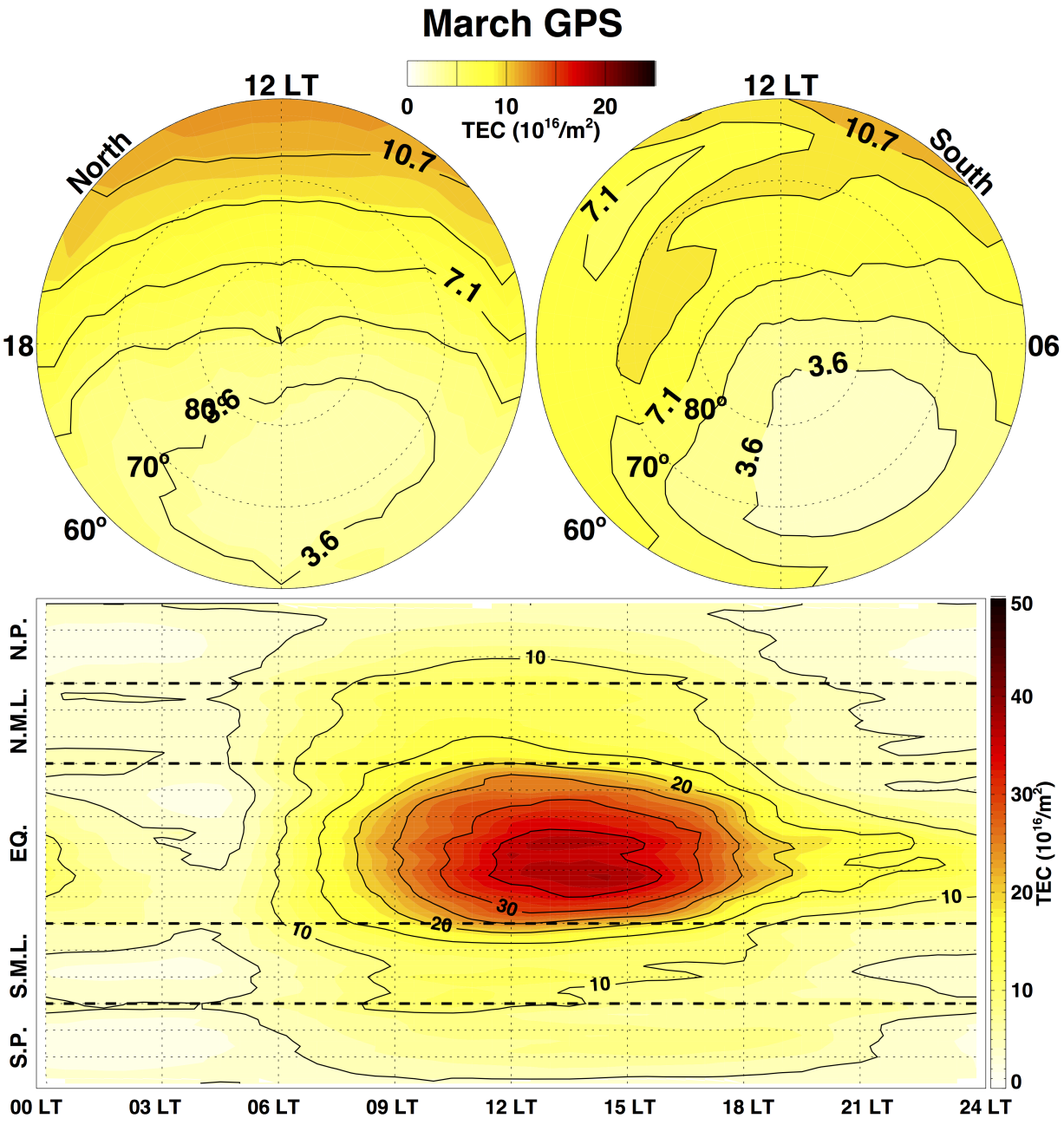

Figure 4.9: TEC for the GPS results averaged over March of 2010. Note that the scales are higher than the June figures.

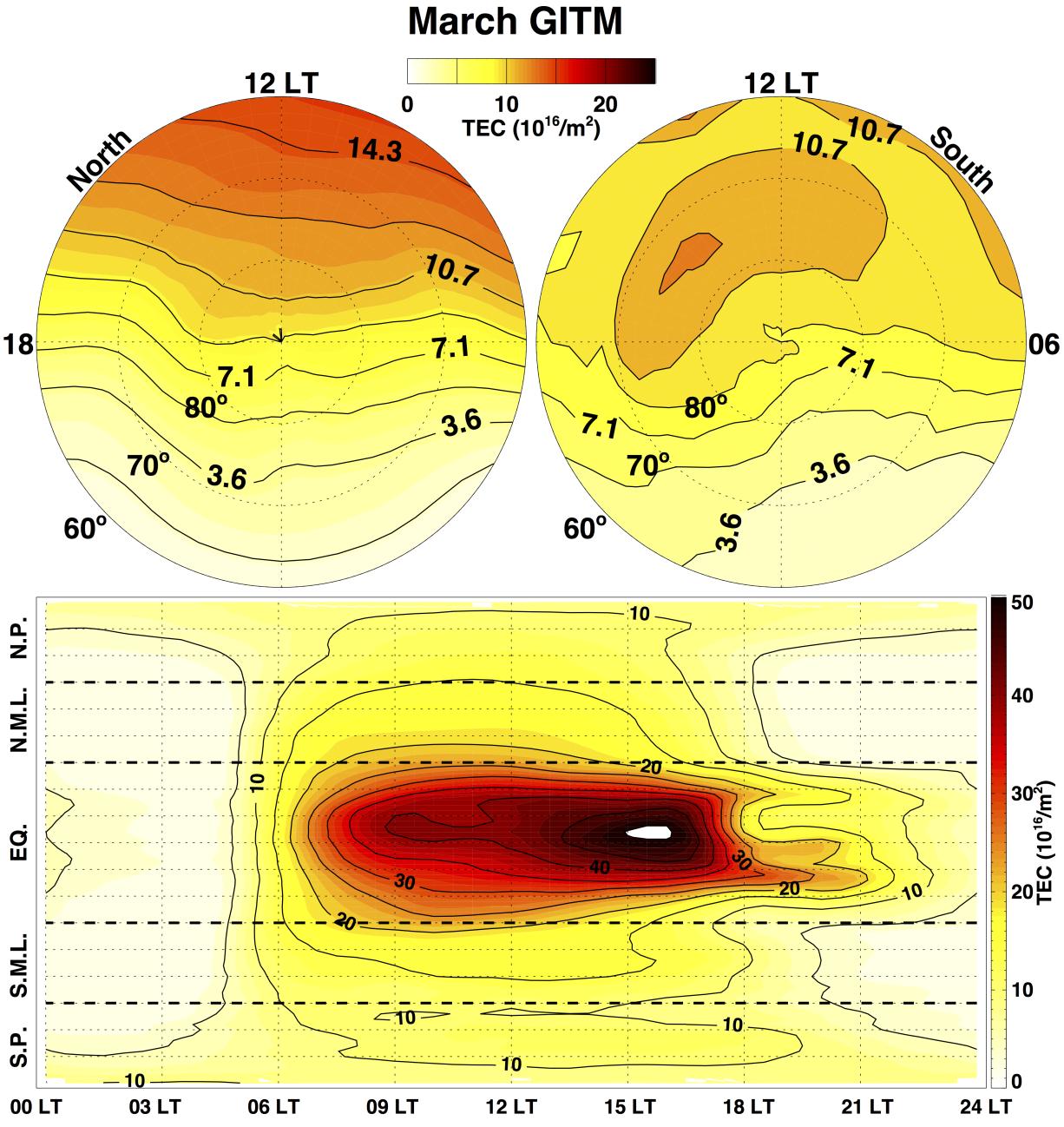

Figure 4.10: The same as Figure 4.9, except for the GITM results.

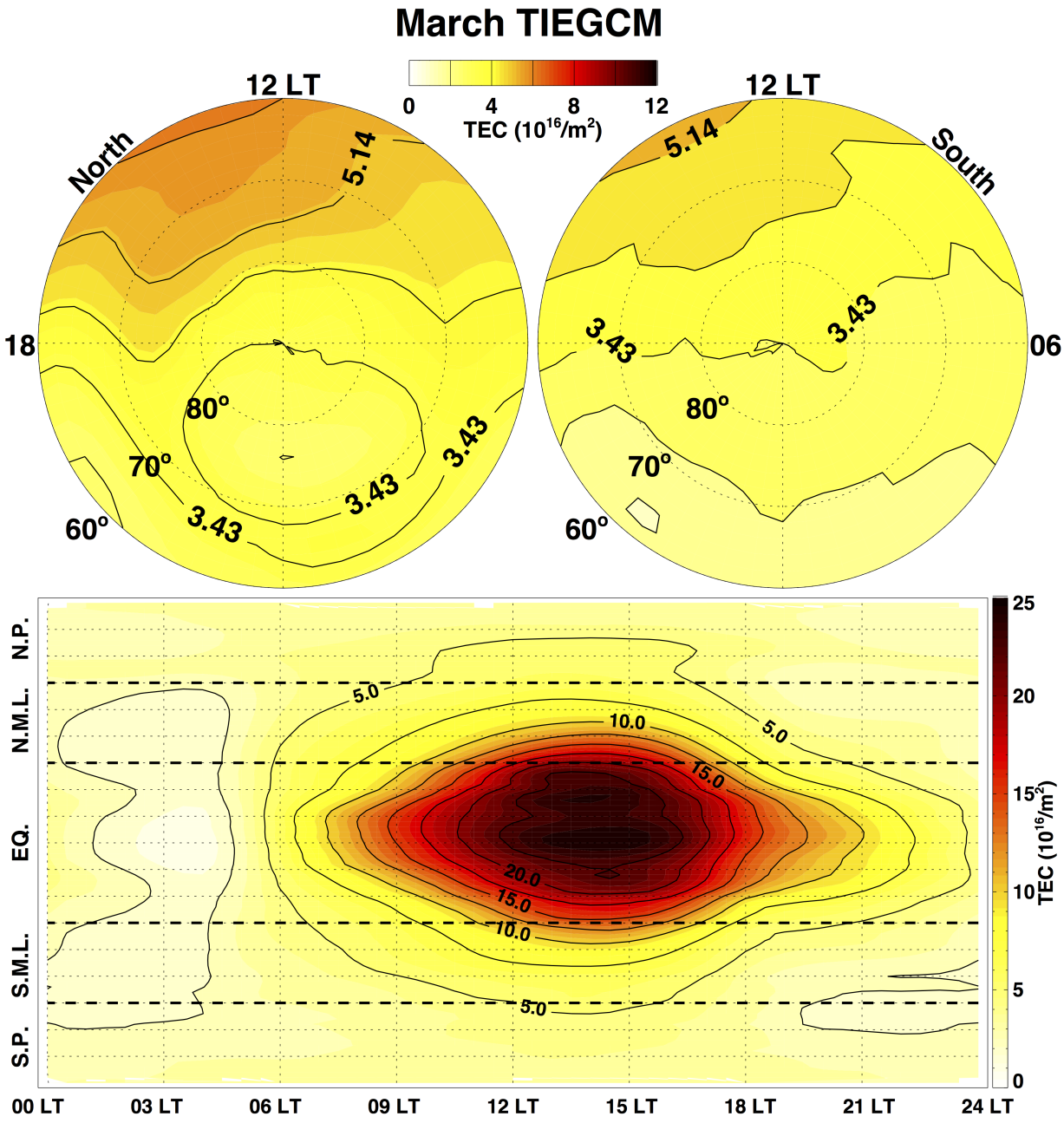

Figure 4.11: TEC for the TIE-GCM results averaged over March of 2010. Note that the scales are half that of Figure 4.10

visible by the contour lines from 21-23 LT. TIE-GCM captured the diffusive like structure very well, but missed the smaller scale extensions. The opposite was true of the GITM results, where the even more TEC extended towards the dusk side, especially in the southern hemisphere.

There were a couple of interesting features in the southern polar hemisphere in the GPS and GITM results. The third feature is a TEC hole from 00-04 LT between 65° and 85° latitude in the GPS observations. This phenomenon was also present in the September southern hemisphere results (not shown), suggesting it is a hemispheric asymmetry effect and not seasonal. Neither of the models reproduced this TEC depletion. Finally, GPS measured a TEC enhancement extending from 11 LT past 18 LT between 67° and 78° latitude, which looks like an extension of pre-noon, midlatitude TEC which may have been caught in the ionospheric convection pattern, similar to a tongue of ionization. GITM produced this enhancement, but to a much wider latitudinal extent.

Contour plots for the December and September months are not shown primarily because they were similar and/or lacked significant features. In December, the structure of the GITM and TIE-GCM simulations were very similar to June with the hemispheres reversed. Both models had more TEC in December compared to June as per Figure 4.1 and Table 4.1.

4.3 Summary and Conclusions

This study presented a year long analysis of GPS TEC observations compared with model results from TIE-GCM and GITM during 2010. A number of seasonal and local time biases were revealed in the models in addition to some phenomenon that neither model captured. The main findings are described below.

- For the simulation settings described in Section 4.1, TIE-GCM under-predicted

the TEC during all seasons and latitudes except for polar winters whereas GITM primarily over-predicted the TEC. This resulted from a number of factors including chemistry, upper boundary conditions, neutral winds, and EUV flux models.

- GITM performed best in the northern hemisphere with decreasing accuracy towards the south pole. Since model development is often focused on the northern hemisphere due to data availability, this result suggests that GITM may be over-fitted to the northern hemisphere. The smaller sample size of observations in the southern hemisphere or larger offset of the geomagnetic pole may have also contributed to this bias. TIE-GCM preformed best in the polar regions with decreasing accuracy towards the equator primarily due to less TEC near the subsolar point combined with a weaker equatorial anomaly.

- The GPS measurements revealed TEC holes in the north hemisphere summer nightside, as well as the southern polar region during both equinoxes likely due to $\mathbf{E} \times \mathbf{B}$ drift pushing plasma down magnetic field lines to altitudes with more neutrals available for recombination.

- Except the equatorial region, GITM had almost no TEC on the nightside since the model does not include plasmaspheric refilling processes. The equatorial anomaly in GITM was very strong and contributed to TEC persisting on the duskside after being lifted to high altitudes. The equatorial anomaly was very weak or not present in TIE-GCM, but the TEC values near midnight were consistent with observations.

Future research projects should take these biases into consideration and use the model that best represents the time or region of interest. While this study focused primarily on quiet time TEC comparison, readers interested in storm time comparisons between I-T models can refer to *Shim et al.* (2012). These results also demonstrate

that although the current models do a reasonably good job reproducing the magnitude and structure of the TEC throughout the course of a year, they still require more development as is evident by the relatively low RMSE values on the order of 1-4 TECU, but negative prediction efficiencies. These results were highly dependent on choice of high latitude drivers, EUV flux model, and ill-constrained input parameters specified in the input files like photoelectron heating efficiency as well as eddy diffusion and thermal conductivity coefficients.

CHAPTER V

The Effect of Ring Current Electron Scattering Rates on Magnetosphere-Ionosphere Coupling

This simulation study investigated the electrodynamic impact of varying descriptions of the diffuse aurora on the magnetosphere-ionosphere (M-I) system. Pitch angle diffusion caused by waves in the inner magnetosphere is the primary source term for the diffuse aurora, especially during storm time. The magnetic local time (MLT) and storm dependent electrodynamic impacts of the diffuse aurora were analyzed using a comparison between a new self-consistent version of the Hot Electron Ion Drift Integrator (HEIDI) with varying electron scattering rates and real geomagnetic storm events. The results were compared with Dst and hemispheric power indices, as well as auroral electron flux and cross-track plasma velocity observations. It was found that changing the maximum lifetime of electrons in the ring current by 2-6 hours can alter electric fields in the nightside ionosphere by up to 26%. The lifetime also strongly influenced the location of the aurora, but the model generally produced aurora equatorward of observations.

The ring current carries the majority of the energy density and plasma pressure in the magnetosphere. Protons are the main contributor to this due to their long lifetimes. The timescale for protons can be measured in days, where electrons may last only minutes or hours depending on L-shell and energy (*Chen et al.*, 2015).

Despite this, the storm time electron ring current has been found to constitute up to 25% of the ring current energy density (*Frank*, 1967; *Liu et al.*, 2005; *Jordanova and Miyoshi*, 2005).

Recent plasma sheet particle and wave observations have shown that pitch angle diffusion is not strong everywhere (*Schumaker et al.*, 1989; *Gough et al.*, 1979; *Belmont et al.*, 1983; *Roeder and Koons*, 1989; *Meredith et al.*, 1999, 2000). Simulations with only strong pitch angle diffusion have also demonstrated too high of a scattering rate in this limit (*Chen and Schulz*, 2001; *Chen et al.*, 2005, 2015). In light of this, models were developed where the pitch angle diffusion transitions from strong to weak closer to the Earth (*Chen and Schulz*, 2001; *Chen et al.*, 2005), but without dependence on geomagnetic activity. Chorus wave scattering electron lifetimes were then parametrized on the dayside and nightside which varied by energy, geocentric distance, as well as the Kp index (*Gu et al.*, 2012; *Orlova and Shprits*, 2014). Plasmaspheric hiss electron losses were similarly parametrized by *Orlova and Shprits* (2014) and *Orlova et al.* (2016).

Plasma injection to the ring current from ionospheric outflow has also been shown to influence electrodynamics in the M-I system (*Winglee et al.*, 2002; *Yu and Ridley*, 2013; *Ilie et al.*, 2015; *Welling et al.*, 2015b). Simulation studies have revealed that heavy ion outflow can create stronger azimuthal pressure gradients in the ring current, leading to FAC intensification that further enhances the electric fields and subsequent outflow (*Kronberg et al.*, 2014; *Welling et al.*, 2015a). Completely describing these processes would require a global ionosphere/thermosphere model that is fully (two-way) coupled to a kinetic inner magnetosphere model. For the magnetosphere, this coupling would also mean a more accurate calculation of the electric field, since ionosphere/thermosphere chemistry and transport can greatly affect conductances (*Deng et al.*, 1991; *Peymirat*, 2002; *Garner et al.*, 2007). For the ionosphere, the coupling would improve the description of the aurora and electric fields driven by the inner

magnetosphere, leading to a more accurate model of ionosphere/thermosphere morphology. While this study ignores these effects, they should be included in future model developments.

Yu et al. (2016) compared a diffusion coefficient method (*Jordanova et al.*, 2008) to the electron lifetime loss method described here. They developed the Ring current-Atmosphere interaction Model with Self-Consistent Magnetic field (RAM-SCB) (*Jordanova and Miyoshi*, 2005; *Zaharia et al.*, 2010) to include both loss methods and investigated their effect on electron dynamics and M-I coupling. For a particular storm, they found that the diffusion coefficient method better agreed with observed precipitation fluxes.

In this study, the MLT and storm dependent electrodynamic impacts of the diffuse aurora were investigated using a comparison between the Hot Electron Ion Drift Integrator (HEIDI) model (*Liemohn et al.*, 2001a, 2005, 2006) with varying electron lifetimes and auroral observations. While previous studies have focused on the magnetospheric repercussions of the improved M-I electrodynamics, the emphasis here was on the ionospheric electric fields and aurora for the electron lifetime loss method only. These modeling efforts are a first step towards coupling with a global ionosphere-thermosphere model.

5.1 Methodology

HEIDI was run for 4 different storms, each with 4 scattering rate descriptions, for a total of 16 simulations. The basis of the loss model used originates directly from the work of *Chen and Schulz* (2001); *Chen et al.* (2005) and *Schulz* (1974). The model is such that the loss rate, $\overline{\lambda}(\varphi)$, transitions from strong to weak pitch-angle diffusion by

$$\overline{\lambda}(\varphi, R, E) = \frac{\lambda(\varphi, R, E)}{1 + \lambda(\varphi, R, E)\tau}, \tag{5.1}$$

where τ is the lifetime against strong diffusion, φ is the MLT, and λ is the scattering rate as a function of MLT (φ), energy (E), and geocentric distance (R) (*Chen et al.*, 2005). Note that this relationship does not include a dependence on magnetic activity, which can change the location of the plasmapause (*Moldwin et al.*, 2002; *Katus et al.*, 2015) and scattering from enhanced wave amplitudes (*Meredith et al.*, 2004; *Miyoshi et al.*, 2006).

As *Chen et al.* (2005) demonstrated, the resulting lifetimes increase as particles move towards the Earth. This contrasts that of strong diffusion, where the lifetimes become increasingly short at low L-shells. In fact, the lifetimes increase so much in the weak diffusion limit that the loss is too little when compared with observations at geosynchronous orbit (*Chen et al.*, 2015). To remedy this, an upper limit, τ_{max} was introduced to the scattering rates. For this study, τ_{max} was set to 8 hours, 4 hours, and 2 hours. Additionally, an energy dependent functional form was used where the lifetime in hours was given by,

$$\tau_{max} = 10(E)^{-0.5}, \tag{5.2}$$

where E is the particle energy in KeV. This formula was derived by comparing HEIDI electron fluxes at geosynchronous orbit to observations for different τ_{max} values. While the other τ_{max} values were arbitrarily chosen, the purpose of this was to demonstrate the importance of the electron scattering rate description on the ability of the model to reproduce auroral observations.

A test simulation with strong scattering everywhere was also done for each storm. In this case, the electrons were lost so quickly and close to the outer boundary that they did not have the chance to gain energy adiabatically by moving towards the Earth into a region of higher magnetic field strength. The result of this was an extremely low energy flux throughout the domain. These simulations resulted in the

#	Time (UT)	Dst	Type
1	2002/08/21 0700	-106	CME
2	2003/08/18 1600	-148	CME
3	2003/07/12 0600	-105	CIR
4	2005/08/31 1600	-131	CIR

Table 5.1: Synopsis of geomagnetic storm events simulated.

model defaulting to empirical results, so they are not shown in this paper.

To get a better understanding of the influence of the scattering rates, the model was run for 4 different storms. The storms were chosen to vary in strength and type, all while ensuring data availability. These include two co-rotating interaction regions (CIR) storms and two coronal mass ejection (CME) events. The storms were identified using the extensive list compiled by *Zhang et al.* (2007) of all the storms during solar cycle 23 in which the Dst dropped below -100 nT. A synopsis of the storms is given in Table 5.1. One weaker and one stronger storm was chosen for each type. The season was kept constant, as well as the UT of the main phase between storms of similar strength.

5.2 Results

5.2.1 Dst

The strength of the ring current is often measured using the disturbance storm time (Dst) index, which is calculated from the reduction of Earth's magnetic field observed at low-latitude magnetometers (*Sugiura et al.*, 1991). In this study, the results are compared to the Dst^* index from both the Kyoto World Data Center and the United States Geological Survey (USGS) (*Love and Gannon*, 2009; *Gannon and Love*, 2011). The Dst^* index more accurately describes the storm time ring current by removing from the Dst index the contributions from the magnetopause current, induced currents in the conducting Earth, and the quiet time ring current (*Ebihara*

and Ejiri, 1998; *Kozyra et al.*, 1998; *Liemohn et al.*, 2001b; *Katus et al.*, 2015). The model calculates Dst^* using the Dessler-Parker-Sckopke relationship (*Dessler and Parker*, 1959; *Sckopke*, 1966) given by

$$Dst^* = -3.98 \times 10^{-30} E_{RC} \tag{5.3}$$

where E_{RC} is the total modeled ring current energy in KeV and Dst^* is in nT.

A comparison of the Dst^* for all of the simulations is shown in Figure 5.1. The dashed black and purple lines represent the observed values. The dark grey line, with the strongest Dst^*_{min}, is an additional run performed using the empirically driven model with the Volland-Stern (V-S) electric field (*Volland*, 1973; *Stern*, 1975). The remaining colored lines correspond to the results of simulations using different electron loss rate descriptions.

The self-consistent version of HEIDI produced a smaller Dst^* drop with little variation of the results between simulations using different τ_{max} values. This was to be expected, as electrons generally constitute a small percentage of the ring current energy density (*Frank*, 1967; *Liu et al.*, 2005; *Jordanova and Miyoshi*, 2005). There is no difference between these runs before the storms, since the aurora during this time was derived from the same empirical model. Storm B was the only storm with a notable difference in the Dst^*. Here the Dst^*_{min} was -94 nT for a τ_{max} of 2 hours, -83 nT for the energy dependent τ_{max}, -74 nT for a τ_{max} of 8 hours, and -72 for a τ_{max} of 4 hours. While the Dst^* was underestimated by an average of about 20 nT during the main phase of the storm, the magnitude was captured better throughout the main phase of storms A and B. However, the simulations of storms C and D missed the minimum by over 40 nT. In storms B and D, the self-consistent runs were more accurate in the timing of the minimum peak in Dst^*, but then recovered at a slower rate than the observations. While more storms would need to be run to determine if the model updates improve the Dst^* results, these simulations demonstrate that this

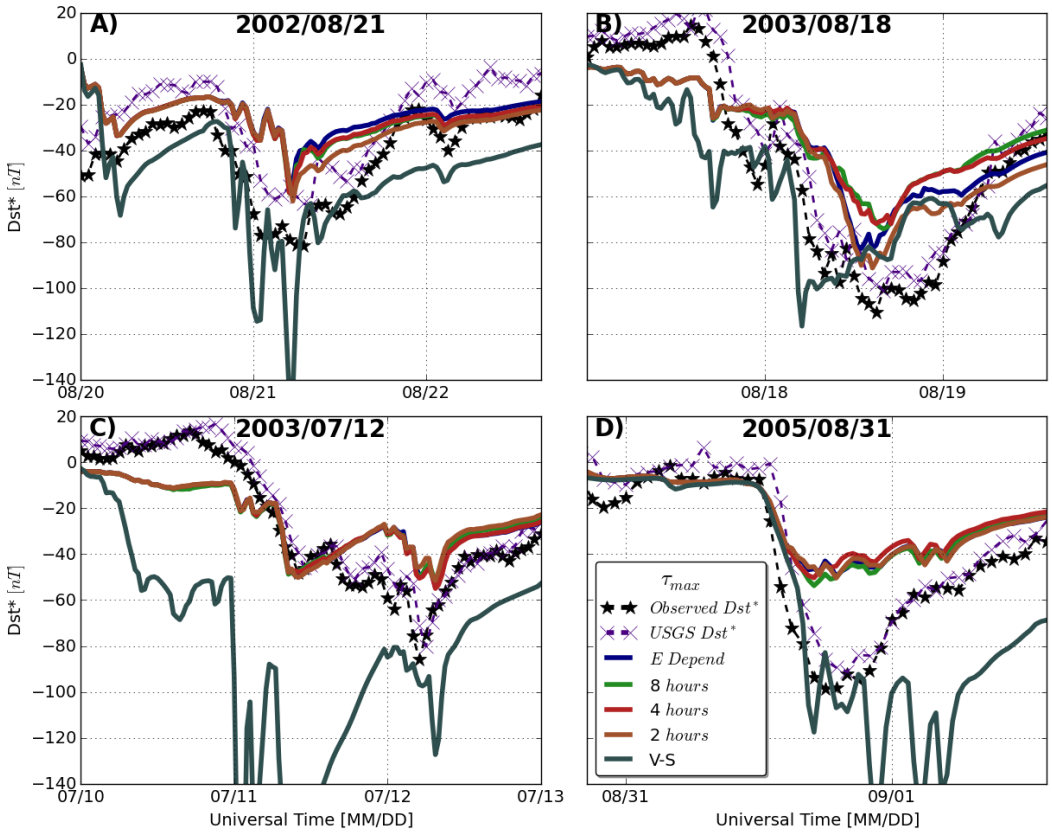

Figure 5.1: Dst* data-model comparison for all 4 storms and all simulations. The dashed black and purple lines show the Kyoto Dst* and USGS Dst* respectively. The dark grey line is the Volland-Stern run. The blue, green, red, and brown lines show the energy dependent, 8 hour, 4 hour, and 2 hour τ_{max} runs.

model version performs reasonably well at capturing Dst^* compared to the model driven by V-S.

5.2.2 Auroral Location and Strength

The location and strength of the simulated aurora was compared to Global Ultra-Violet Imager (GUVI) data from the Thermosphere, Ionosphere, Mesosphere Energetics and Dynamics (TIMED) satellite (*Paxton et al.*, 1999, 2004; *Christensen*, 2003). From a circular orbit of 625 km, GUVI's far-ultraviolet (115 to 180 nm) scanning

imaging spectrograph provided horizon-to-horizon images of the aurora. The width of single disk scan is 11.8 degrees.

Figure 5.2 shows an example comparison. In the upper left corner, Figure 8a shows the simulated electron flux. The time of this plot was chosen to be near the middle of the satellite pass, indicated both by the diagonal time stamp as well as the vertical black line in Figure 8c. Figure 8b shows GUVI data for the 15:48 UT during the August 21st, 2002 storm. The starting position is indicated near dusk. Figure 8c shows the electron total energy flux averaged over the horizon to horizon swath width for the pass. The dashed black line indicates the GUVI swath averaged energy flux. The HEIDI electron flux was interpolated and averaged similarly for each time. The simulated aurora was slightly poleward of the measured aurora in the 21-03 MLT sector, but close to the same position in the 18-21 MLT sector. However, the strength of the aurora in the 18-21 MLT sector was smaller than the observations. This was a common theme among all of the comparisons, suggesting a shortcoming of the model in this region. A similar issue of the dusk side aurora was reported in *Chen et al.* (2015), likely due to a shortage of observations of very-low-frequency (VLF) waves by the SCATHA satellite, upon which the loss model was built (*Chen et al.*, 2005).

Programmatically determining the location of the diffuse aurora in both the data and model was difficult due to superposition of the discrete aurora and the presence of multiple auroral bands. To ensure an accurate comparison, each comparison between HEIDI and GUVI passes were analyzed by hand for all of the storm and τ_{max} combinations. The downside of the data model comparison using satellite data was that not every minute of model output could be compared. However, it was found that the location and strength of the HEIDI aurora did not vary significantly in the 20 or so minutes of a satellite pass. The only orbits considered were those where HEIDI was entirely in self-consistent mode. More specifically, the comparison was only done when the self-consistently calculated hemispheric power was greater than

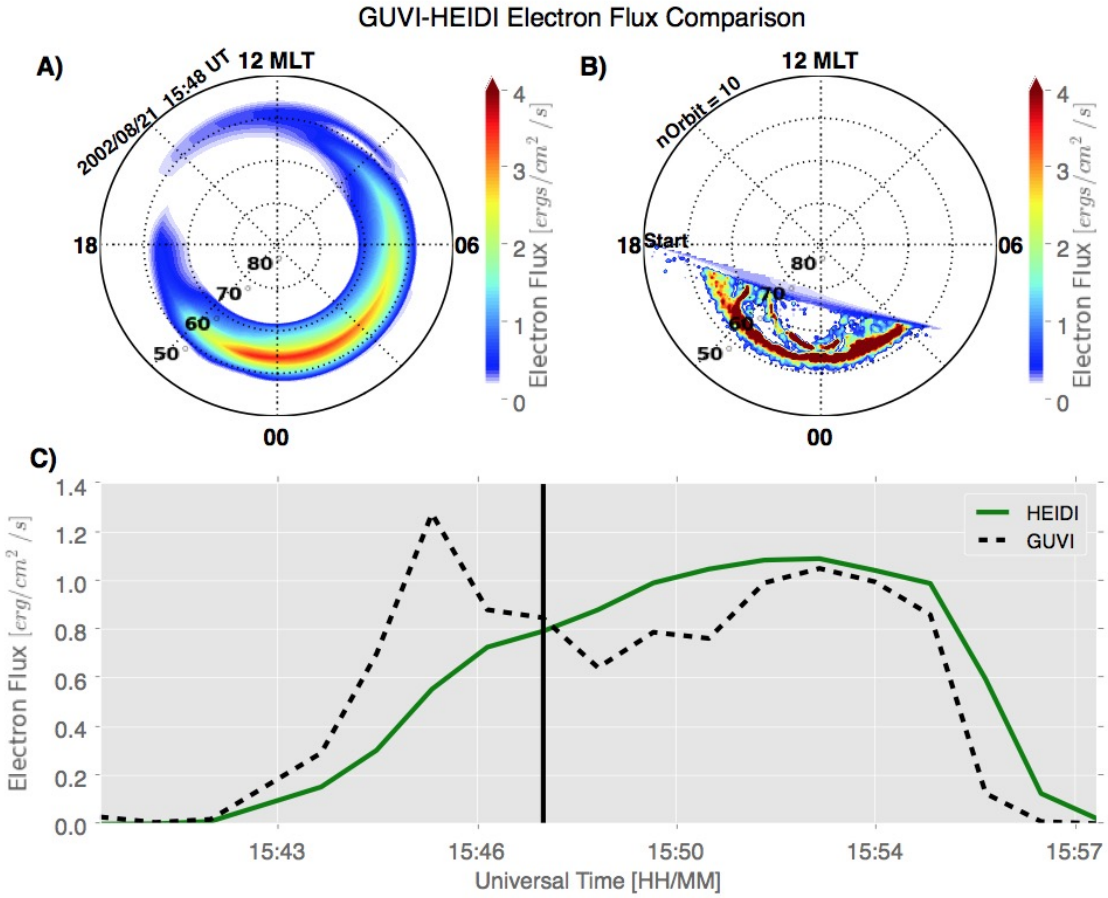

Figure 5.2: This snapshot compares the HEIDI electron flux in plot A to the GUVI observed aurora in plot B for the August 21st, 2002 storm with a τ_{max} of 2 hours. The dashed black line in plot C shows 30 second bins of the average GUVI electron flux per swath. The solid green line are the HEIDI values interpolated to those times and regions. The vertical black bar in plot C is the time at which plot A is drawn.

10 GW. The analysis was further constrained to the northern hemisphere, since the electrodynamics were solved only in this hemisphere.

The location and strength of the diffuse aurora was compared in 3 hour MLT sectors, starting from 00 MLT. Discrete auroral arcs were not separately accounted for and comparisons were only recorded in MLT bins where GUVI data existed for more than 50% of the region. The process was defined as follows:

- Define the location of the HEIDI and GUVI aurora as the center of the auroral band with the most total energy flux
- Interpolate the simulated total energy flux to the locations of the GUVI measurements, averaged over times within ± 15 seconds of the model output.
- Define the strength of the HEIDI and GUVI aurora as the average of the total energy flux in each MLT bin

Figure 5.2 was recreated for each storm, each simulation, and each satellite pass. For each of these, the location of the aurora was recorded from plots like Figures 8a and 8b in each MLT sector where GUVI data was available. Furthermore, the modeled and observed strengths in each sector with GUVI data were recorded. In total, over 600 comparisons were made, the results of which are shown in Figure 5.3.

Figure 5.3 quantifies the ability of the models with different τ_{max} values to capture gross features in the auroral observations. The coloring of each sector is the average difference between the total electron flux in HEIDI and GUVI. The yellow dots are the average location of the aurora in each MLT sector. The black lines, dashed for GUVI, are spline interpolations between the points to create a semi-realistic auroral oval to make comparisons easier. In plot A, the $\tau_{max} = 2$ hour simulation results were dropped in the 15-18 sector because there were no times with GUVI observations where the model produced an aurora in that sector for this value of τ_{max}.

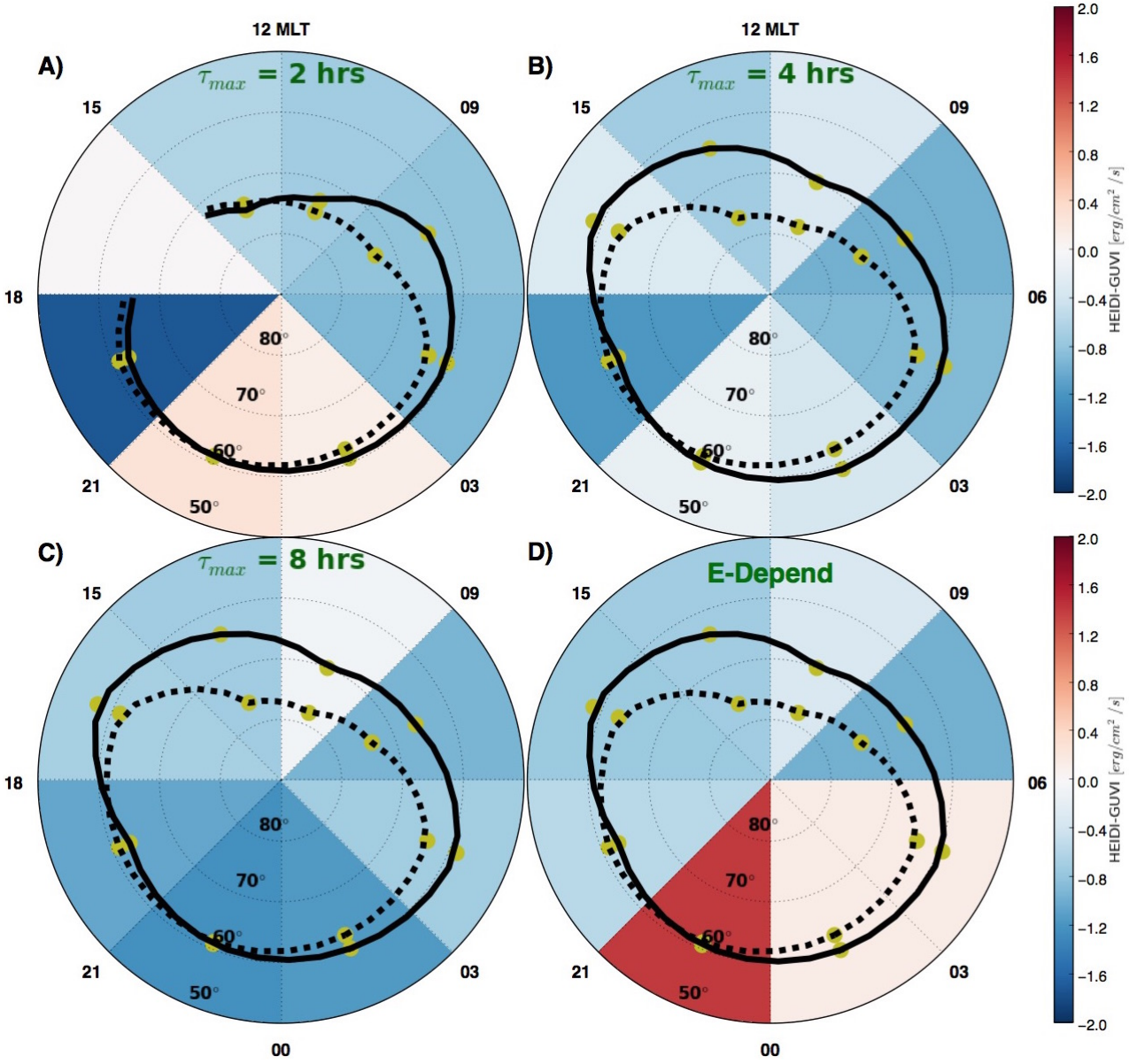

Figure 5.3: Comparison of the strength and location of the aurora between HEIDI and GUVI for each τ_{max} for all storms and times. The colors represent the average difference between HEIDI and GUVI in each sector, blue meaning HEIDI was smaller, red meaning larger. The yellow dots are the average location of the aurora. These are connected by solid black lines for HEIDI and dashed black lines for GUVI. These lines were created with spline interpolations.

The location of the aurora in all four simulation sets shared a similar feature. The difference between the oval locations was very little in the 18-00 MLT sectors, but then increased more and more towards the dayside. This suggests that as electrons drifted towards dawn, they moved too far towards the Earth before being scattering at lower L-shells, and thus lower latitudes. The locations of the auroral ovals of the HEIDI simulations were nearly identical for the 4 hour, 8 hour, and energy dependent cases. The two hour case was vastly different, owing to the fact that 2 hours was not enough time for the electrons to drift as far as 09 MLT. A promising result was the 2 hour case from 09-15 MLT, where the location matched much better than the other cases.

The effects of the lifetimes are perhaps more visible in the strength results which are indicated by the colors in Figure 5.3. When compared with the $\tau_{max} = 8$ hour runs in plot C, the $\tau_{max} = 2$ runs in plot A had a stronger aurora in the 21-03 MLT sectors, but weaker in the 03-18 MLT region. Looking at the 21-00 MLT sector, the $\tau_{max} = 2$ hour case over-predicted the strength of the aurora by 0.4 ergs cm^{-2} s^{-1}, but the $\tau_{max} = 8$ case under-predicted by 1.4 ergs cm^{-2} s^{-1}. On the other side of the planet, in the 09-12 MLT sector, the results were flipped, with the $\tau_{max} = 2$ case under-predicting by 0.9 ergs cm^{-2} s^{-1} and the $\tau_{max} = 8$ case being nearly equal to the GUVI observations. The differences in the $\tau_{max} = 4$ case were a meld between the $\tau_{max} = 2$ and $\tau_{max} = 8$, as expected. It is interesting that the latitude of the HEIDI aurora is unchanged in plots B-D. This suggests that the conductance changes resulting from this aurora were not enough to significantly alter the convection electric field. If that were the case, the extent to which electrons penetrate to lower L-shells would have been dependent on τ_{max}. The energy dependent case is unique in that the electron flux is greater than the other simulations on the entire nightside, from 18-06 MLT, but despite this some of the lower energy particles still circumnavigated the planet well past magnetic noon.

There are a couple important points to take away from this analysis. The first is that the pitch angle diffusion time limit greatly influenced the strength of the aurora in all MLT sectors. The second is that it only appears to have changed the location of the aurora in the $\tau_{max} = 2$ hour case. It should be noted that the results presented here are an average of all 4 storms, and that the response of each individual storm is quite different, as was demonstrated in the Dst^* results in Section 5.2.1. Conductance and electric potential results for individual storms are presented in Section 5.2.4, and Section 5.2.5 investigates what difference the conductance made on the ability of the model to reproduce realistic self-consistent electric fields.

5.2.3 Hemispheric Power

The hemispheric power (HP) is the total area integrated particle energy deposited into a hemisphere (*Fuller-Rowell and Evans*, 1987a). This quantity provides an initial large-scale metric for the amount of aurora produced by the model. Figure 5.4 shows a data-model comparison of HP for each storm and simulation in the northern hemisphere.

The HP for storm A matched reasonably well with observations, with all simulations tracking the approximate running average of the POES data for the majority of the storm time. Notice that the maximum diffusion lifetime near the beginning and end of the simulation had no effect on the HP at all. This is an indication that the auroral oval was outside of the HEIDI boundary during these times, and that the Ovation aurora was being used here. A curious result of the simulations in plot A is that the 4 hour τ_{max} produced more hemispheric power than the others for the first half of the storm. This is likely related to the energy dependent nature of the HP itself. As particles drift towards the Earth, they gain energy adiabatically due to the increasing magnetic field strength. In this case, the amount of electron flux diffusing into the loss cone was balanced by this energy enhancement. With a minimum Dst^* of

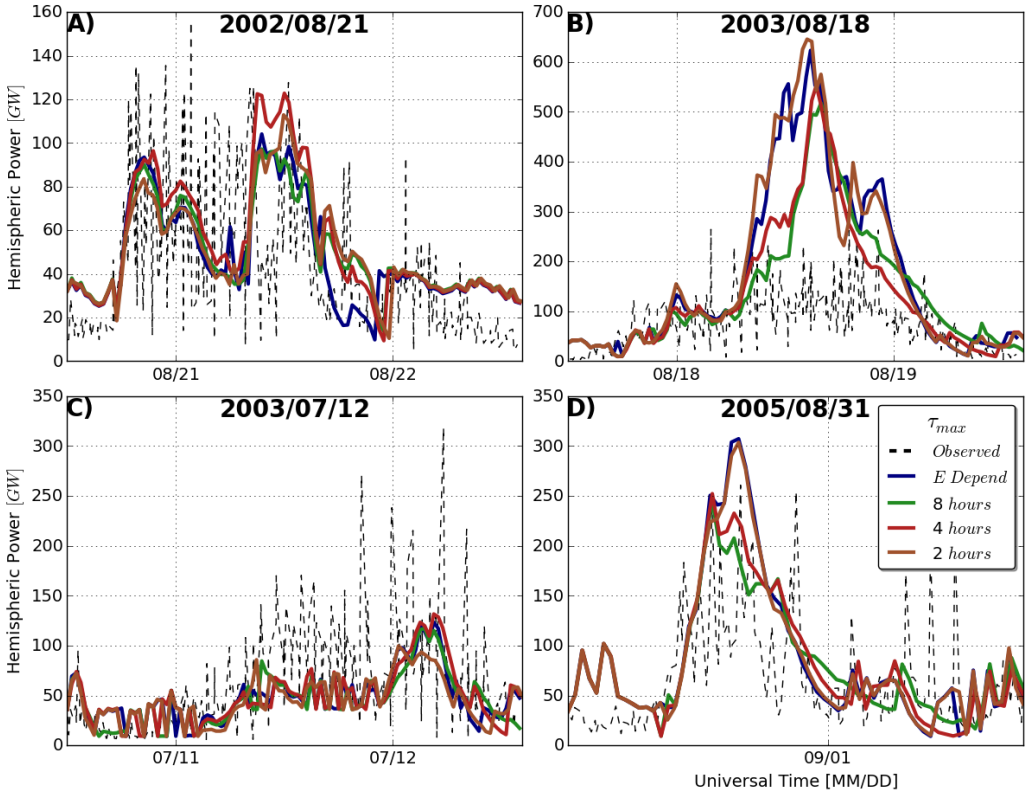

Figure 5.4: Hemispheric power comparison for all 4 storms and τ_{max} values. The dashed black lines are the observations derived from NOAA POES satellites measurements. The blue, green, red, and brown lines show the energy dependent, 8 hour, 4 hour, and 2 hour τ_{max} runs. Times when all the colored lines are on top of each other indicate when only Ovation SME was used to specify the aurora.

-106 nT and maximum observed hemispheric power of just over 100 GW, the relative weakness of this storm suggests slower convection in the inner magnetosphere. As a result, the electrons move towards the Earth more slowly, and are more likely to be lost at a lower characteristic energy, resulting in less HP. The 4 hour τ_{max} simulation kept electrons around long enough for their energy to increase, but not too long as to prohibit their loss, as seen in the green line of the 8 hour simulation during the middle of the simulation. This conclusion is further supported by the energy dependent τ_{max}. Since the lower energy electrons were lost more slowly in this case, the fact the blue

line HP was smaller for much of the storm suggests that the characteristic energies of the electrons were indeed low for this storm.

A more expected result comes from storm B. The POES HP was vastly overestimated by the model in this case, but the large response helped to exaggerate the τ_{max} differences. There are two important features to notice here. The first is that the shorter lifetimes produced significantly more aurora at the beginning of the storm. Around noon of August 18th, the $\tau_{max} = 2$ hour simulation produced 500 GW, but the $\tau_{max} = 8$ hour simulation produced only 200 GW, since electrons were allowed to persist longer in the latter case. The second feature to notice is the time shift of the response. The $\tau_{max} = 8$ hour simulation peaked 2 hours later than the $\tau_{max} = 2$ hour simulation, and was 120 GW less.

Figure 3c shows a case where the model under-predicted observations. There was little difference in magnitude between these simulations, but the timing of auroral enhancements were still shifted from each other albeit by time frames of under an hour. There are two factors that explain why HEIDI underestimated the HP in Figure 3c, but overestimated it in Figure 3b. The first is the outer boundary condition where electron flux observations were greater at geosynchronous orbit for storm 2. The second is the adiabatic heating of the electrons as they move closer to Earth. The electrons reached lower L-shells in Figure 3b, causing the energy and subsequent HP to increase. This was most likely driven by stronger convection electric fields for storm B.

Figure 3d is a good example of how shorter maximum lifetimes could produce more aurora initially, but less later. The $\tau_{max} = 2$ hour simulation had 100 GW more at its peak than the 8 hour simulation, but 30 GW less 12 hours later. All of the simulations in this case came close to the right values in addition to capturing the timings of HP increase well. These results suggest that the maximum diffusion lifetime had consequences on both the magnitude and timing of auroral enhancements

produced by the model, but they were inconsistent between storms.

5.2.4 Conductance and Potentials

The conductivity and its gradients produced by the aurora are a primary factor in controlling the ionospheric electrodynamics in terms of ring current coupling (*Nopper and Carovillano*, 1978; *Vasyliunas*, 1970). As equation 2.6 suggests, the average energy and electron flux of the aurora are essential to the description of the conductivity and therefore the height integrated conductance. This section highlights the differences in the time evolution in the conductances for each τ_{max}, and explores how that influenced the electric fields that drive plasma in the ionosphere-magnetosphere feedback system. For this analysis, the focus was on the August 18th, 2003 storm because the differences between simulations was greatest.

The auroral electron energy fluxes during four different times during the main phase of the storm are displayed in Figure 5.5. There were large differences between the different simulations (columns) at each time during the storm (rows). In the top row, early in the main phase, the aurora gained strength from the higher to lower τ_{max}. This is because during the beginning of the storm, few electrons had time to reach the maximum lifetime of the higher τ_{max} values, so they did not precipitate into the atmosphere. As the storm progressed, the simulations with a higher τ_{max} had much more wrapping of the aurora around towards the dayside. This was caused by the ability of longer lifetime electrons to $\mathbf{E} \times \mathbf{B}$ drift and gradient curvature drift towards the dawn and noon sectors. Complementary to this was a weaker aurora on the nightside for those cases. Since electrons drift towards the Earth across the entire nightside, there are large differences from about 21 MLT to the dawnside.

Figure 5.6 shows the Pedersen conductance for the same times and simulations as the energy flux results from Figure 5.5. The Pedersen conductance was calculated using the energy flux and average energy of precipitating electrons as described in

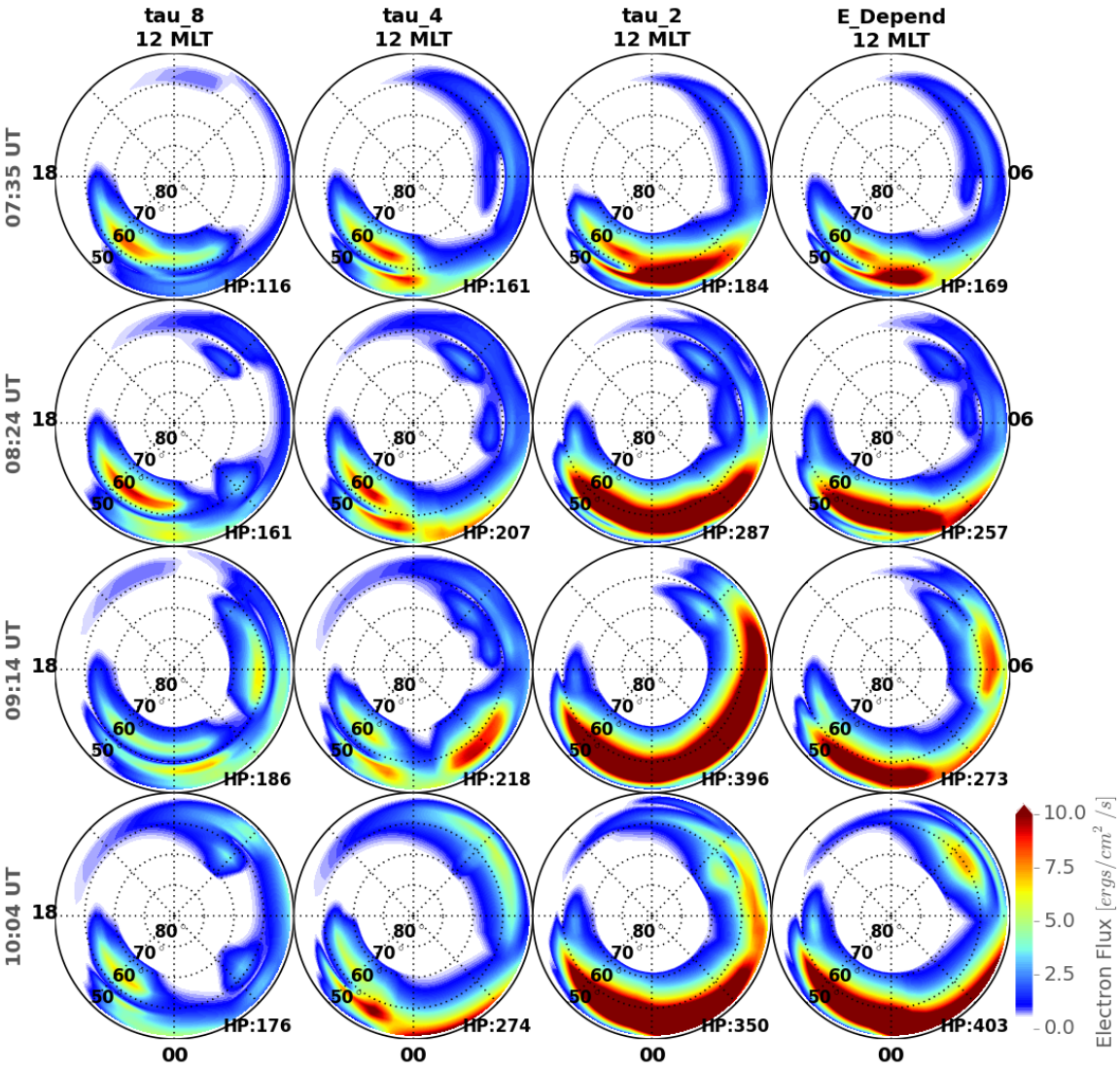

Figure 5.5: Energy fluxes in $erg/cm^2/s$ for each τ_{max} during the August 18th, 2003 storm. Each row is a different time during the main phase of the storm. The first column is for a $\tau_{max} = 8$ hours , the second for $\tau_{max} = 4$ hours, the third for $\tau_{max} = 2$ hours, and the fourth for the energy dependent τ_{max}. Each subfigure is plotted in magnetic coordinates, with 12 MLT at the top. The bounding magnetic latitude is 50°. The hemispheric power is shown in the bottom right of each subplot.

Chapter II, as well as a dayside driven conductance described by *Moen and Brekke* (1993). While there were some regions where the auroral Pedersen conductance was stronger than the dayside conductance, the conductance produced by photoionization is generally larger than conductance from the aurora. In addition, because of the summer conditions where the dayside solar EUV dominated the conductance pattern, weaker electric fields and stronger field aligned currents would be expected (*Cnossen and Richmond*, 2012; *Cnossen and Förster*, 2016), as well as weaker responses to geomagnetic storms (*A et al.*, 2012a; *Perlongo and Ridley*, 2016). Since all of the storms chosen for this study were during the northern hemisphere summer, the amount of electrons making it beyond 06 MLT had little effect on the total Pedersen conductance on the dayside in any of the different simulations. In fact, there were almost no differences between simulations from 12-18 MLT.

An assumption of the Robinson formula is that the electron precipitation is Maxwellian in form, causing a peak in Pedersen conductance at an average energy of 4 keV, assuming a constant energy flux. As such, the conductances in Figure 5.6 don't necessarily correspond to the largest energy fluxes in Figure 5.5. This can particularly be seen at 9:14 UT in the $\tau_{max} = 4$ simulation, where the energy flux is greater towards dawn, but the conductance is largest towards dusk. In addition to this, the scattering rate, λ_ϕ, in equation 5.1 is dependent on the electron energy, MLT, and L-shell (*Chen et al.*, 2005). Consequently, the average energy of the precipitating particles changed significantly between τ_{max} values. In the energy dependent case, higher average energies in the magnetospheric electrons resulted in shorter electron lifetimes, leading to a similar response as the $\tau_{max} = 2$ hour simulation. Throughout the storm, the larger nightside energy fluxes in the 2 hour case produced more Pedersen conductance there. In general, the conductance on the dawn side was significantly larger for the $\tau_{max} = 2$ hour case.

Figure 5.7 shows the total electric field strength for the same times as Figures 5.5

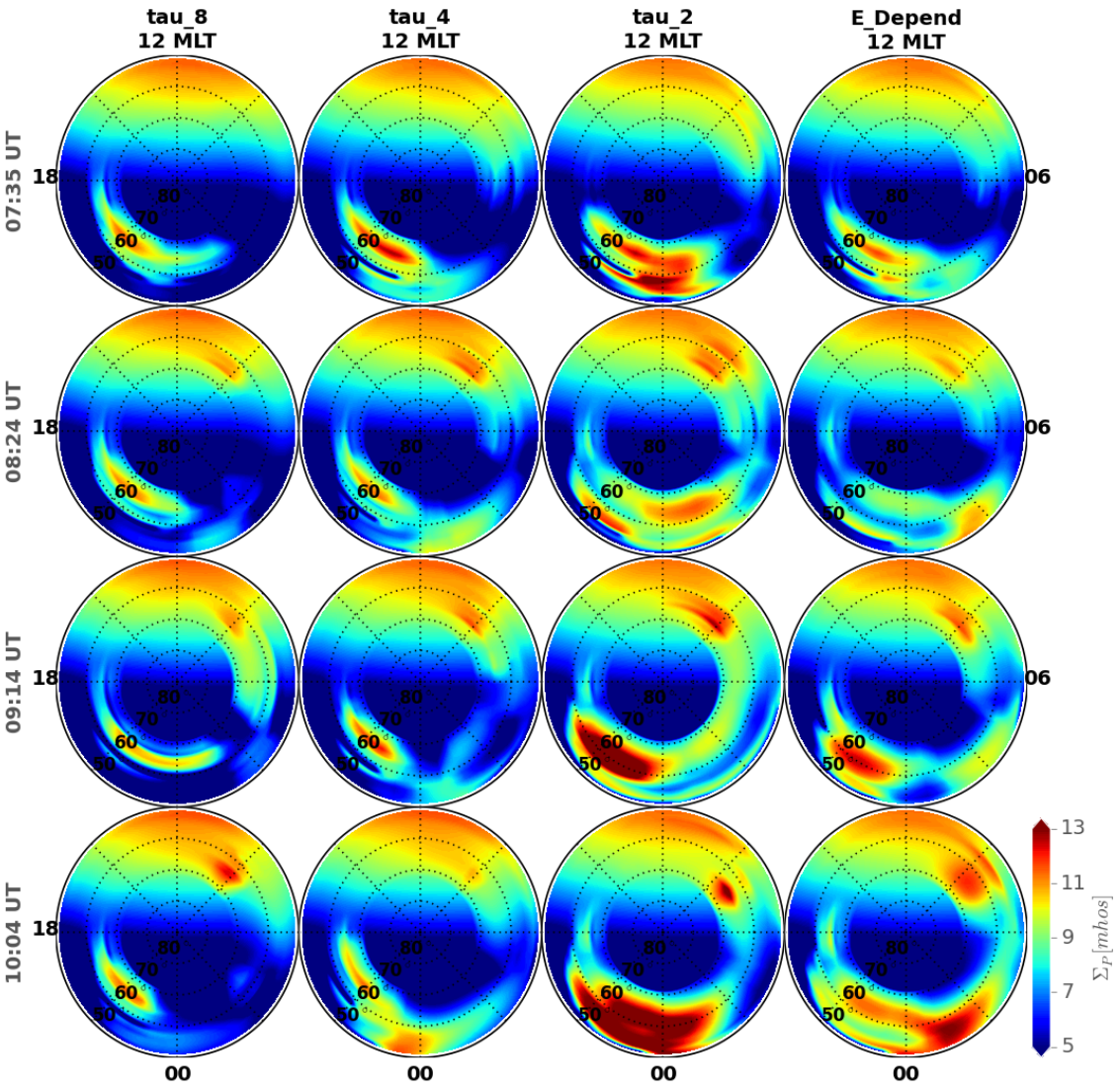

Figure 5.6: Total Pedersen conductance, including solar and auroral sources for each τ_{max} during the August 18th, 2003 storm in the same format as Figure 5.5.

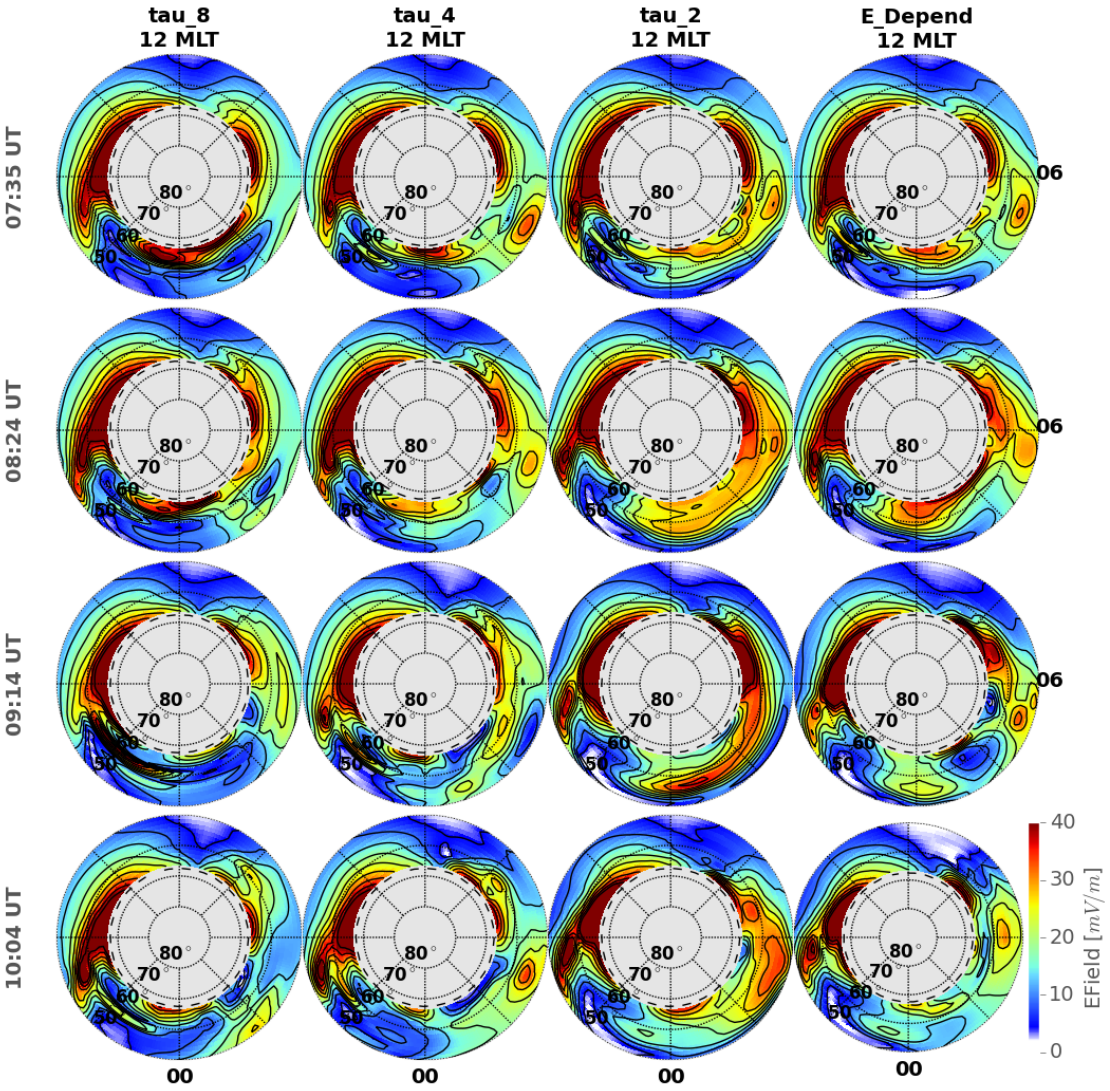

Figure 5.7: Total electric field magnitude for each τ_{max} during the August 18th, 2003 storm. The dashed line represents the outer boundary of HEIDI. Poleward of this boundary the potentials were described by the Weimer electric potential model.

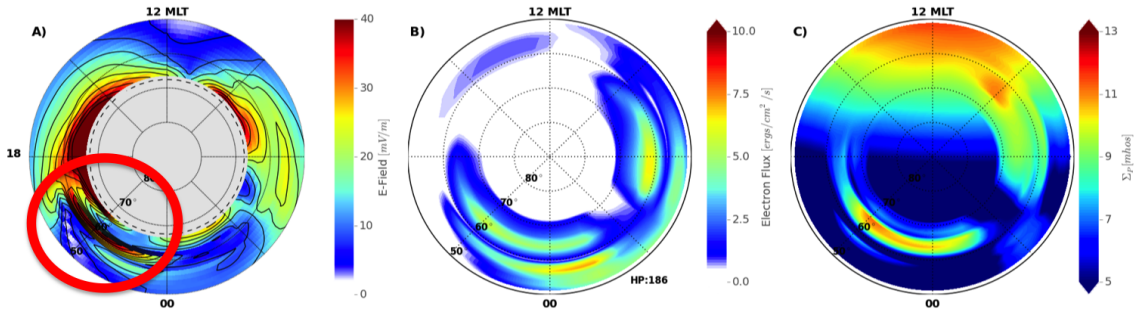

Figure 5.8: Expanded electric field (A), electron flux (B), and Pedersen conductance (C) plots from August 18th, 2003 at 9:14 UT. All 3 plots are from the $\tau_{max} = 8$ hour simulation case. The red circle highlights the SAPS feature.

and 5.6. The black dashed line represents the boundary between the self-consistent calculations and the Weimer potentials, which are not shown, since they are the same in all τ cases. The electric fields on the dayside were relatively unchanged between the different simulations since the dayside total conductances were very similar to each other. Vastly different structures were seen on the nightside though, which were dependent on the scattering rate. In the $\tau_{max} = 8$ and 4 hour simulations, a strong and narrow electric field, associated with a sub-auroral polarization stream (SAPS), developed in the 19-24 MLT region equatorward of the main auroral oval, but poleward of a detached auroral feature from 09:14 UT to 10:04 UT. This feature is highlighted in Figure 5.8, which shows the SAPS as well as the electron flux and Pedersen conductance for the $\tau_{max} = 8$ hour case at 9:14 UT. The conductance was greater than 10 mhos at the center of the main auroral band in the region just poleward of the SAPS. Equatorward of that was a narrow band of less than 5 mho conductance. Further equatorward was an increase in Pedersen conductance to ~9 mho. This structure tended to confine the strong electric field channel to the narrow band between the primary and secondary conductance peaks. When this secondary peak did not exist, such as in the $\tau_{max} = 2$ hour simulation case, a SAPS channel did not appear, but a penetration electric field extended much further equatorward. This is consistent with modeling efforts which have shown that an increase in ionospheric

conductance reduces the shielding and therefore results in further inward transport of the ring current plasma and a stronger ring current (*Ebihara et al.*, 2004; *Zheng et al.*, 2008). Figures 5.7-5.8 demonstrate that τ_{max} had a significant impact on the structure of the conductance patterns, which lead to major changes in the electric fields.

Figure 5.9 quantifies these results by averaging the ionospheric electric field strength, Pedersen conductivity, and FAC both in time and longitudinally. The left column shows each variable versus magnetic latitude averaged over 18-21 MLT. The right column is the same, but for 21-03 MLT. An average was then taken over all times during August 18th, 2003. These MLT regions were chosen because the electron scattering rates diverged mostly eastward of 21 MLT. Furthermore, most electric field plots showed SAPS developing in the 18-21 MLT region in the $\tau_{max} = 8$ and 4 hour simulations.

The electric fields for 18-21 MLT in Figure 7a show the high latitude electric field decreasing towards lower magnetic latitudes until about 54°, where there was an enhancement in the $\tau_{max} = 8$ and 4 hour simulations. In this region the Pedersen conductance in Figure 7c was generally low, so these electric fields can be attributed to SAPS. There was little difference in this region in conductance due to the characteristics of the electron scattering model used, except that the 2 hour case was slightly higher. The electric field was 2.1 mV/m less in this case compared to the average of the other simulations.

The behavior of the FAC current in Figure 7e also varied for each τ_{max}. This was expected since each τ_{max} drives different conductances, which leads to different electric fields, which then map back to the ring current, changing the convection electric field which drives the ion convection. This then changes the azimuthal pressure gradients in the ring current, which drive FACs. Since so many processes occur between the conductance differences from the electron scattering rates and the FAC changes near

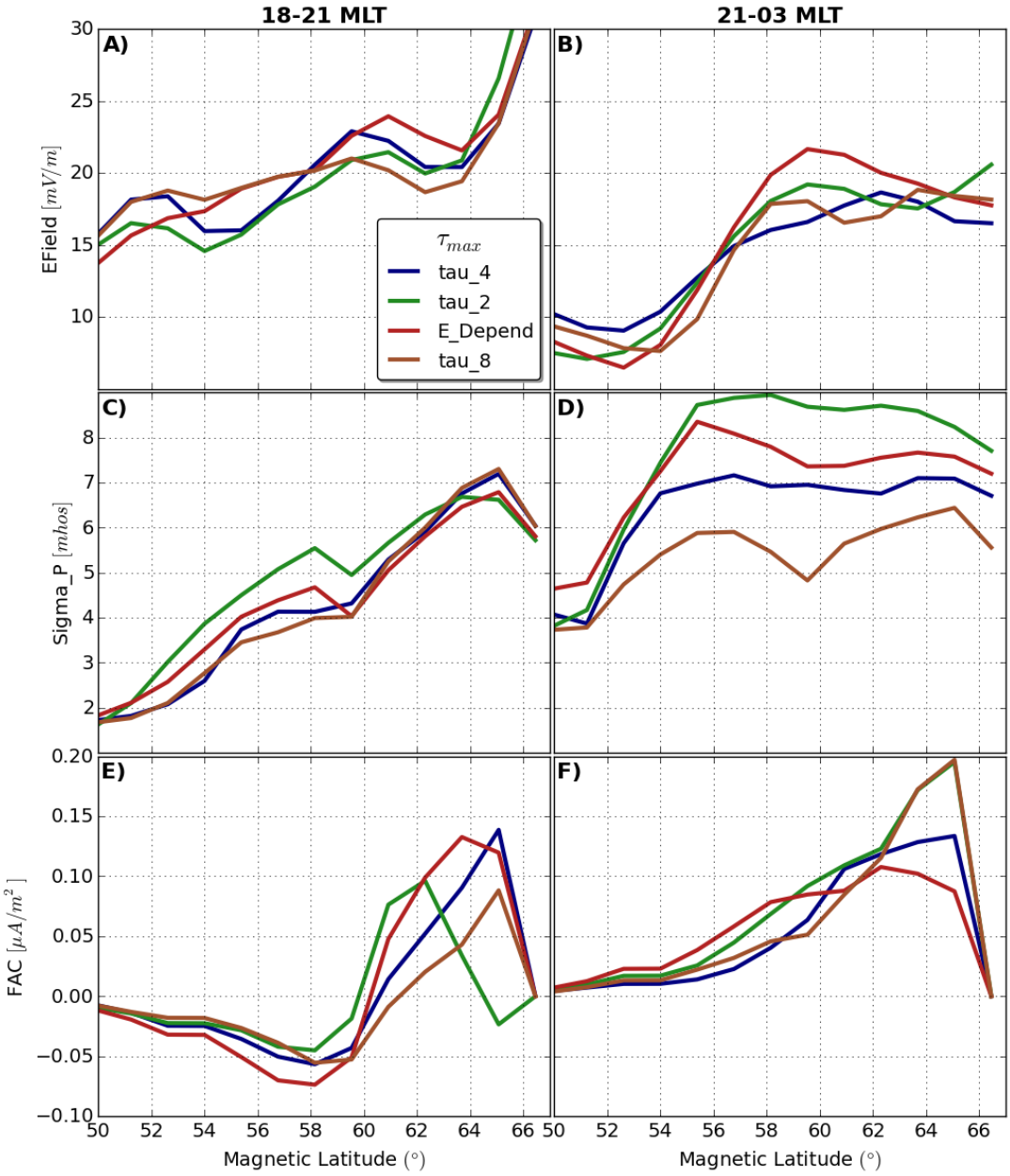

Figure 5.9: The electric field strength, Pedersen conductivity, and FAC for each τ_{max} in the top, middle, and bottom rows respectively. Each parameter is averaged over 18-21 MLT in the left column and 21-03 MLT in the right column. The results are further averaged over all times during the main phase of the August 18th, 2003 storm.

the end of the feedback loop, it is impossible to draw causal relationships from this. However, treating the rest of the ring current like a black box, the FAC plots do demonstrate that changes of just 10% in the ionospheric electric fields can alter the position and magnitude of subsequent FAC by at least 50%, as was the case between the energy dependent and $\tau_{max} = 8$ and 2 hour simulations in Figure 7f. Furthermore, the location of the peak of the FAC in Figure 7e moved 3 degrees equatorward when the electric field was an average of 2.8 mV/m less in the 2 hour verses the energy dependent simulation, but this shift was not seen in the other simulations where the electric field was also decreased.

The Pedersen conductance in the 21-03 MLT region in Figure 7d were much more stratified than the dusk results in Figure 7c. This is congruent with the auroral locations presented in Section 5.2.2 for all storms: The 2 hour simulation had the most conductance, followed by the energy dependent, 4 hour, and 8 hour simulations. The two simulations with the larger conductances had higher electric fields within the auroral zone, while Equation 2.7 implies that lower conductivity leads to higher electric field[s], these averages show that a higher total conductance in a region can lead to larger electric fields in the same general area. The FAC equatorward of the strong electric field shows these two simulations as having the largest FAC's also, which may contribute to the strong electric fields, despite the strong conductance. The strong electric fields may further be a result of the structure in the aurora. When the aurora is enhanced among multiple bands created by the energy dependence in the loss model, it is more likely that strong electric fields will develop around them, as seen in Figure 5.7. Figure 7b shows that the electric field can vary from 21-03 MLT between 16 mV/m and 22 mV/m between the 4 hour and energy dependent simulations at 60°. In other words, the auroral zone experienced a 26% larger electric field when averaged over the entire storm in these longitudes. This demonstrates how significant the effects of changing the maximum lifetime of electrons in the ring

current has in self-consistent M-I models.

A major shortcoming of the model at this time is the amount of smoothing that is needed to be done for numerical stability given the resolution of the model. It is expected that this smoothing produces artificially small electric fields due to the flattened conductance gradients. Furthermore, any small-scale structures in electron precipitation or the subsequent electrodynamics are indiscernible. The effects of these limitations are explored further in section 5.2.5, but first the simulations are compared to different data sets.

5.2.5 Ionospheric Electric Fields

Data from the Defense Meteorological Satellites Program (DMSP) (*Hardy*, 1984; *Rich and Hairston*, 1994; *Hairston et al.*, 1998) was used to compare the modeled electric field results for each storm. Unfortunately, a full MLT analysis like in Section 5.2.2 could not be performed because there were not enough times when GUVI observations overlapped DMSP satellite tracks. The lack of discrete aurora in the model further complicated such an analysis since it was not possible to discern electric fields resulting from conductance produced by discrete or diffuse aurora. For these reasons, only a couple examples are shown in Figures 5.10 and 5.11 to demonstrate the model's electric field results.

Figure 5.10 demonstrates a time during the August 21st, 2002 storm when the GUVI observations matched very well in both strength and magnitude near 20 MLT, where DMSP took measurements. While the magnitude of the velocity in Figure 10e matched relatively well with a root-mean-square-error (RMSE) of about 200 m/s, the small scale structure of the aurora seen in red was completely missed. This was unsurprising since the resolution of the electrodynamics model was 2.8° in longitude and 1.8° in latitude. Furthermore, the smoothing done to merge with the Weimer potentials poleward of the boundary made it difficult, if not impossible, to model

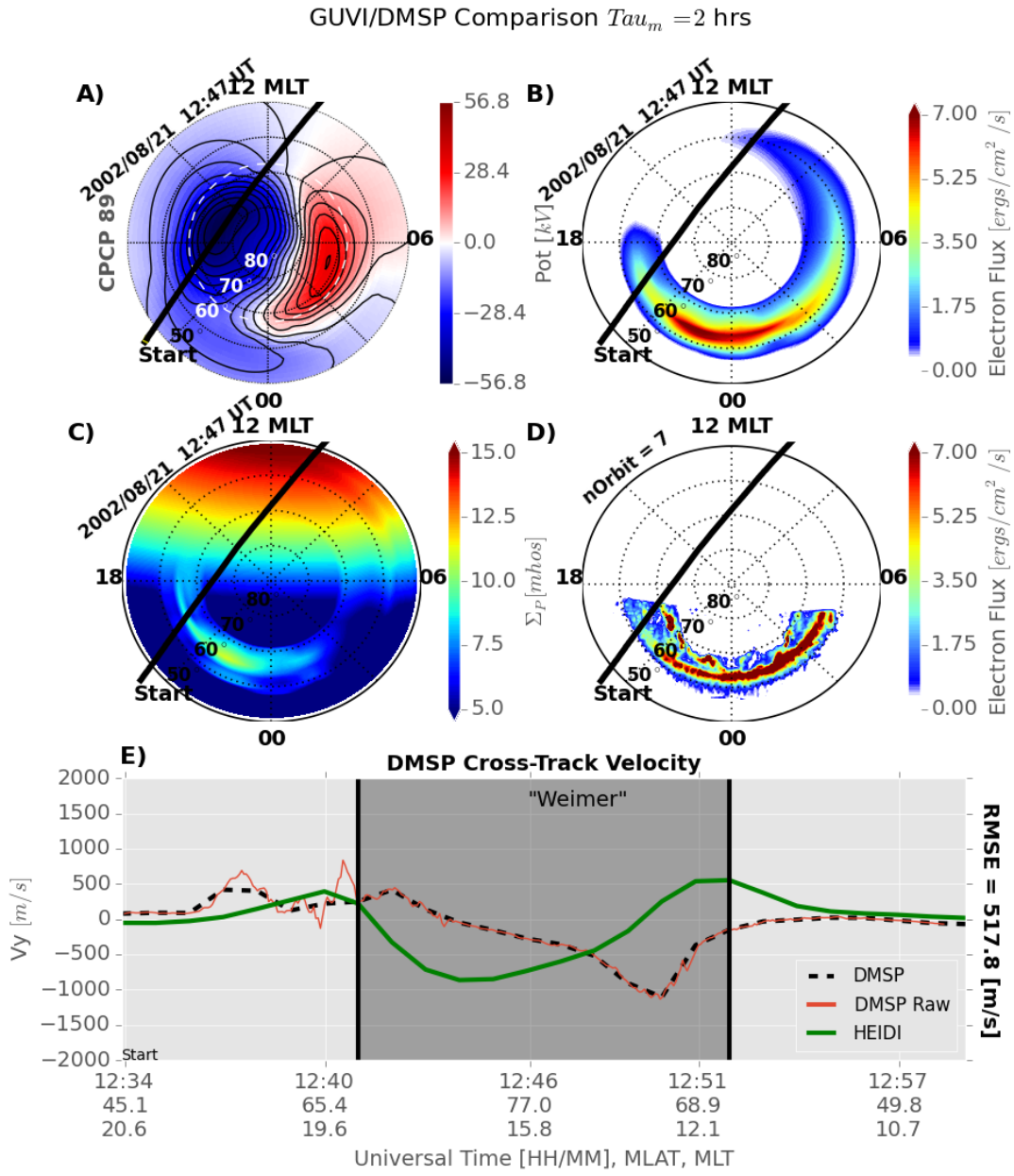

Figure 5.10: (A) the HEIDI electric potentials, (B) electron flux, and (C) Pedersen conductivity during the August 21st, 2002 storm for a $\tau_{max} = 2$ hours. (D) the GUVI auroral observations. The over-plotted black lines are the DMSP orbit paths. (E) The dashed black line is the cross track plasma velocity of DMSP at the HEIDI 1 min output interval; the green line is the equivalent V_y for HEIDI interpolated to the DMSP location; and the dark grey shaded region indicates poleward of the 67° HEIDI boundary. The red line is the high resolution raw DMSP data.

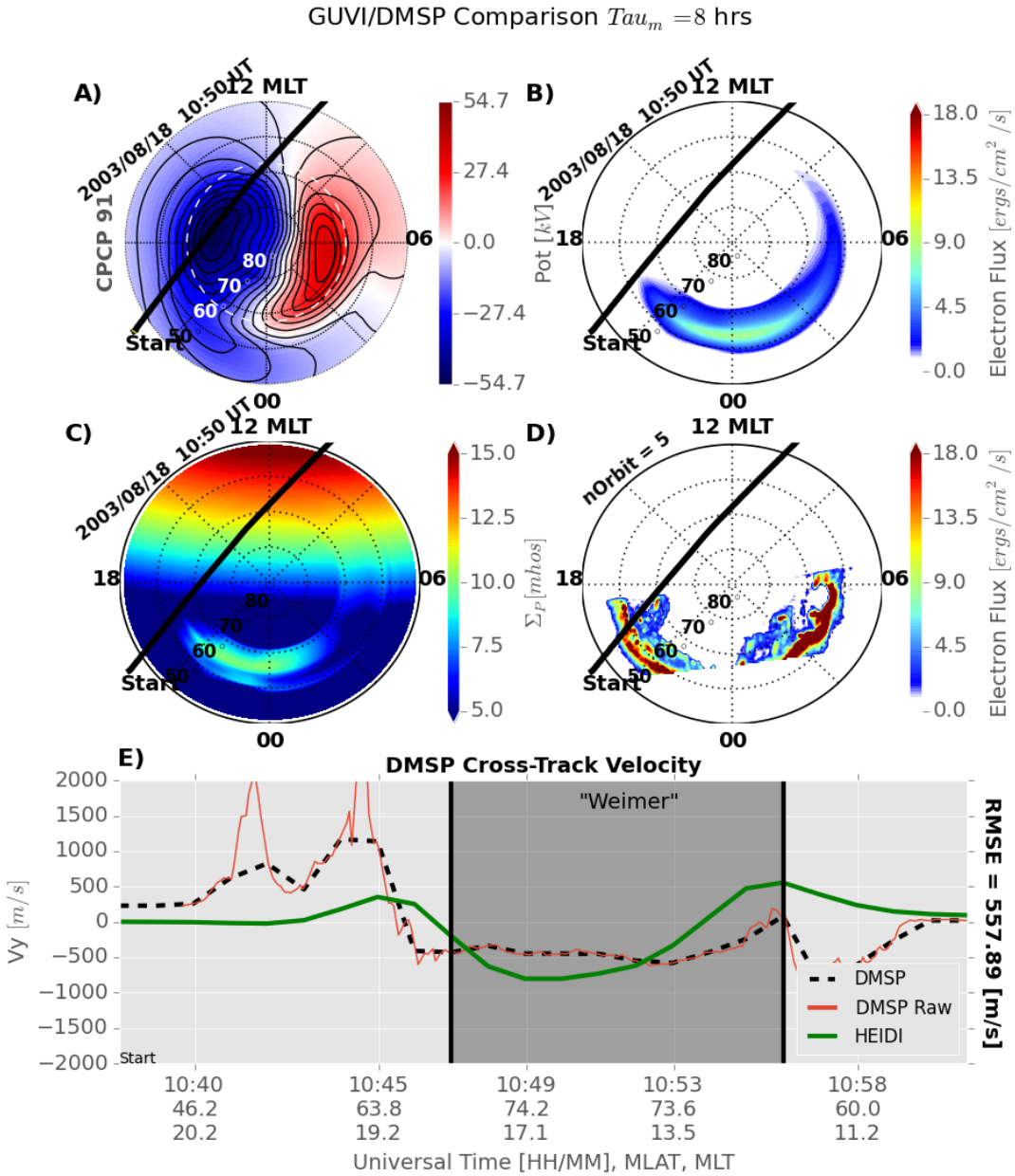

Figure 5.11: The same as Figure 5.10, but for a τ_{max} of 8 hours during the August 18th, 2003 storm.

small-scale electric fields properly here. Small-scale electric fields associated with discrete aurora are also missing from the model at this time. Figure 5.11 shows a time where HEIDI completely missed a large auroral enhancement. DMSP observed velocities over 2000 m/s both equatorward and poleward of the auroral oval, while HEIDI predicted a maximum velocity of just 420 m/s on the poleward side. Furthermore, the velocity was much slower for the entire flyby of the 18-21 MLT region.

The point of these figures is primarily to show how important the scattering rate, and subsequent conductances can be to accurately capturing the overall strength of the electric fields in the ionosphere. They also show that when the auroral strength and location matches observations, the model does reasonably capture the gross electric field strength.

In the future, data providing boundary conditions for much more recent storms will become available and allow the model to be run and compared with data from a plethora of electric field measurements, including the Super Dual Auroral Radar Network (SuperDARN) (*Greenwald et al.*, 1995), and incoherent scatter radars; as well as auroral imagery from the SSUSI instrument on DMSP.

5.3 Discussion and Summary

In recent years, there has been a push for magnetosphere-ionosphere-thermosphere models to become fully coupled and self-consistent. This study advanced one link in that chain by creating a version of HEIDI that computes both electric fields and auroral precipitation self-consistently with auroral precipitation. This is an updated version of HEIDI. In the previous version, the aurora was quite idealized, and was driven by a simple relationship with the FACs (*Ridley and Liemohn*, 2002; *Liemohn et al.*, 2004). The new version of the model used a much more complex description of the aurora and compared better to Dst^* than HEIDI with a Volland-Stern electric field (*Volland*, 1973; *Stern*, 1975), but comparisons between observation and model results

of aurora and ionospheric electric fields varied greatly. The hemispheric power plots and aggregate analysis of the HEIDI and GUVI aurora demonstrate the importance of running models for a wide variety of events and parameters, the maximum diffusive scattering lifetime in this case.

This study imposed an upper limit on the electron scattering rates defined by the *Chen et al.* (2005) loss model, which was found to produce exceedingly long lifetimes at low L-shells (*Chen et al.*, 2015). This parameter, τ_{max}, was shown to have significant impacts on the strength and location of the simulated aurora, as well as the electrodynamic system. It was found that a limit of $\tau_{max} = 2$ hours produced the best agreement with the location of the aurora observed by GUVI, but $\tau_{max} = 4$ hours agreed best with the total energy flux averaged over all sectors. In the $\tau_{max} = 2$ hours case, the strength of the aurora was increased in the 21-03 MLT sector, but fewer electrons drifted around the Earth and precipitated on the dayside, especially in the 09-12 MLT sector. The total energy flux produced by the different τ_{max} values were consistent with the idea that a smaller τ_{max} should produce more aurora on the nightside and less on the dayside.

Furthermore, average differences in ionospheric conductances of just a few mhos between τ_{max} simulations led to more than a 25% change in electric field strength in the 21-03 MLT region. While not shown systematically, it was observed that times when the aurora match observations, the electric fields in the ionosphere were on par with measurements from DMSP.

If τ_{max} had such a large effect on electric fields, then the $\mathbf{E} \times \mathbf{B}$ drift speeds of the electrons should have also differed between simulations. However, the location of the simulated aurora stayed relatively constant between the different τ_{max} values. This is evident in Figure 5.5 where the choice of τ_{max} altered the longitudinal extent of the energy flux to a much larger degree than in latitude. If the $\mathbf{E} \times \mathbf{B}$ drift speed were smaller for a particular τ_{max}, the electrons should have precipitated at larger L-shells

and higher latitudes. While it appears this occurred for the $\tau_{max} = 2$ hour simulation in many of the MLT sectors of plot A in Figure 5.2, Figure 5.9 showed that it did not have a consistently smaller electric field than the other τ_{max} values in the 21-03 MLT sector. Since this is the sector where the strength of the aurora differed the most from the $\tau_{max} = 4$ and $\tau_{max} = 8$ simulations, this mechanism does not explain the improvement in auroral locations on the nightside or dayside of the $\tau_{max} = 2$ hour simulation. It also indicates that the large scale convection electric field was not greatly influenced by τ_{max}. Furthermore, changes in the convection electric field brought on by the inclusion of ionospheric electrodynamics are responsible for altering the rate of the ion outflow through the dayside magnetopause, a process determined to be the primary loss mechanism for the ions in this model (*Liemohn et al.*, 1999). If the outflow rate of the ions was altered between τ_{max} simulations, there would have been greater difference in Dst^*.

Another way that τ_{max} could effect the location of the diffuse aurora is by changing the characteristic energy of the electron population that reach a given MLT sector. Higher energy particles will gradient-curvature drift at larger L-shells and thus precipitate at higher latitudes. τ_{max} also puts a limit on the distance that cold plasma can gradient-curvature drift before being lost to the thermosphere. The higher latitude dayside aurora in the $\tau_{max} = 2$ hours case could result from these two factors. The cold electrons were lost before they were able to drift past 09 MLT, but the higher energy electrons persisted at larger L-shells until 15 MLT. Despite the better match for $\tau_{max} = 2$ hours, HEIDI produced an aurora 5-10° equatorward of the GUVI observations for all τ_{max} from 00 to 12 MLT, perhaps due to the relatively close outer-boundary of geosynchronous orbit, or lower plasma average energies than reality. Further research should be done to identify if this is a common bias in the HEIDI model and, if so, determine the cause of it.

The choice in τ_{max} was shown to alter the simulation's ability to reproduce auro-

ral features by a large degree. While the arbitrarily chosen $\tau_{max} = 2$ hour simulation matched the location of the aurora the best, all of the simulations presented here demonstrate the importance of understanding the electron loss rates in the ring current. Since small deviations in the upper limit of the scattering rates were shown to have a large effect on the electrodynamic results, any uncertainty in this parameter is a major hindrance to the accuracy of M-I coupled models. This offers a cautionary tale in ring current modeling. Moving from more empirically driven models to self-consistent frameworks adds complexity that could make the results less predictive until each parameter is modeled accurately. For example, running HEIDI in self-consistent mode puts significantly more pressure on the electron scattering model to be correct because of the electrodynamic feedback loop. As a result, times when the scattering diverges from observations may result in a much worse off solution than empirical versions. Transitioning to self-consistent models should therefore be done keeping the assumptions and errors of all components between models in mind.

CHAPTER VI

Seasonal and High-Latitude Driver Influence on Ionospheric Morphology

Investigating space weather phenomena is difficult considering that the geomagnetic activity level varies significantly with season, as was seen in Chapters III and IV. In this paper, these effects are taken as a given and the difference in the upper atmosphere's response to the same solar wind and IMF drivers for each solstice. A number of other studies have looked at seasonal and hemispheric asymmetry in the I-T system. *Cnossen and Förster* (2016) used the CMIT model (*Wiltberger et al.*, 2004; *Wang et al.*, 2004, 2008) to investigate hemispheric asymmetry in reference to solar cycle on seasonal influence during geomagnetically quiet times and found that neutral wind speeds were always larger in the summer hemisphere. *Förster and Cnossen* (2013) used the same model during March equinox and found significant hemispheric asymmetry in the neutral winds and plasma drift. This chapter explores the possibility that these asymmetries also influence the storm time TEC response.

Despite numerous storm time I-T simulations of TEC phenomenon, there remain very few that incorporate a coupled ring current model as a high latitude driver. The RCM (*Wolf et al.*, 1982; *Toffoletto et al.*, 2003a) was coupled with the National Research Laboratory (NRL) ionosphere-plasmasphere model (SAMI3) (*Huba et al.*, 2000; *Huba and Joyce*, 2010; *Krall and Huba*, 2013) to demonstrate the the electrodynamic

coupling between the ring current and ionosphere influences SED formation (*Huba and Sazykin*, 2014). SAMI3-RCM uses empirical relationships for the thermosphere and does not include contributions of ring current precipitation to the electrodynamic coupling like in the HEIDI-GITM coupling presented here.

This study is unique in that it focuses on a particular geomagnetic storm simulated with a wide variety of high-latitude input drivers, including a ring current model with self-consistent particle precipitation and electric fields. The storm inputs were shifted to investigate the seasonal differences between the M-I-T coupled response. Simulation results for the actual event were compared against GPS TEC measurements and CHAllenging Minisatellite Payload (CHAMP) neutral densities.

6.1 Methodology

An ensemble of simulations were done to elucidate the effects of high latitude drivers on the seasonal and regional storm time response of the I-T system. Every simulation was done using the Global Ionosphere-Thermosphere Model (GITM), which is a parallel, 3-dimensional, time dependent code that solves the fully coupled momentum, energy, and continuity equations for both neutral and ion species. GITM uses a fixed altitude grid from 100 km to 600 km that allows for nonhydrostatic solutions to develop in the vertical momentum equation. The temperature and density of the thermosphere at the lower boundary (95-100 km) were specified by the MSIS model (*Hedin*, 1983, 1987, 1991). The horizontal wind patterns at the boundary were specified by the Horizontal Wind Model (*Drob et al.*, 2008). The FISM (*Chamberlin et al.*, 2007) defined the EUV flux. GITM was run with a resolution of 1.0° latitude by 4.0° longitude with a stretched altitude grid, resolving the vertical scales to approximately 1/3 of a scale height.

Four different combinations of high latitude drivers were used that varied in their specifications of the electric potential and aurora, consisting of the average energy and

	Sim1 (WFR)	**Sim2 (WOV)**	**Sim3 (SWMF)**	**Sim4 (HEIDI)**
Electric Potential	Weimer 2005	Weimer 2005	BATSRUS RCM	Weimer2005/ HEIDI
Aurora	Fuller-Rowell	Ovation SME	BATSRUS RCM	OvationSME/ HEIDI

Table 6.1: Overview of the high latitude electric potential and auroral precipitation models used.

energy flux. Table 6.1 provides a reference for each simulation. The first used the *Weimer* (2005) electric potential model driven by the upstream solar wind conditions observed from the ACE spacecraft (*McComas et al.*, 1998; *Smith et al.*, 1998) in conjunction with aurora described by *Fuller-Rowell and Evans* (1987b). A second type of simulation was done with the Weimer model, but with the Ovation SME (*Mitchell et al.*, 2013) auroral precipitation model driven by the SuperMAG Auroral Electrojet index (*Newell and Gjerloev*, 2011). The Fuller-Rowell auroral model consists of ten pre-defined auroral descriptions dependent on activity level, where Ovation SME has a dynamic auroral strength but static location. The third type of simulation was done using the SWMF (*Tóth et al.*, 2005, 2012) through the Community Coordinated Modeling Center (CCMC). The Block Adaptive Tree Solar wind Roe-type Upwind Scheme (BATS-R-US) MHD code (*Powell et al.*, 1999) was chosen to simulate the global magnetosphere (*Ridley and Liemohn*, 2002; *Welling and Zaharia*, 2012), and the RCM was used for the inner magnetosphere particle code (*Wolf*, 1970; *Wolf et al.*, 1982; *Toffoletto et al.*, 2003b; *Ridley et al.*, 2004b). RCM changes the plasma pressure in the inner magnetosphere altering the field aligned currents and ionospheric electric fields. The ionospheric potential solution and aurora from BATSRUS was taken as the driver for GITM in this case. These runs were available on CCMC. The fourth simulation type used the HEIDI model (*Liemohn et al.*, 2001a, 2005, 2006) to specify both the electric potentials and electron precipitation below 67°. Weimer and

Ovation SME were used poleward of this. HEIDI was recently updated to include a self-consistent electric field using electron loss due to wave scattering in the inner magnetosphere *(Perlongo et al.,2017)*. Consequently, both the HEIDI and SWMF models allow for a dynamic auroral precipitation pattern to develop. The HEIDI model is also described in Chapter II. The northern hemisphere drivers from HEIDI and the SWMF were mirrored to the southern hemisphere in the GITM simulations to study the effect the response of each hemisphere to identical inputs. The SWMF simulations were run from the start of August 19th, 2002 to eliminate erroneous contributions from initial conditions. Results from the HEIDI simulations are not shown until the 20th, 14 hours before storm onset because geosynchronous satellite data was not available before the start of the 20th to drive the HEIDI model. This is not a problem for the remainder of the run because, as was shown in *Kozyra et al.* (2002), the IMF B_z reversal is very efficient at removing influence from the initial condition and concluded that the pre-conditioning of the inner magnetosphere is not necessary for eventual ring current development.

Additional baseline simulations were done using the Weimer and Fuller-Rowell models, but with nominal solar wind input conditions of V_{sw} = 400 km/s, V_n = 5 cm^{-3}, and 0 nT for all IMF components. The hemispheric power was set to a quiet time value of 20 GW for these simulations. The purpose of the baseline simulations was to provide a reference point for the perturbations in the storm time simulations. In other words, they reveal what the upper atmosphere may have looked like during each time period had a storm not occurred.

The August 20th, 2002 storm was chosen considering data availability needed to drive the ring current model. *Perlongo et al. (2017)* showed that HEIDI performed best in terms of hemispheric power for this storm compared to three other storms in that study. This storm was a result of an ICME whose sheath and magnetic cloud impacted Earth's magnetic field as identified by *Zhang et al.* (2007) in their

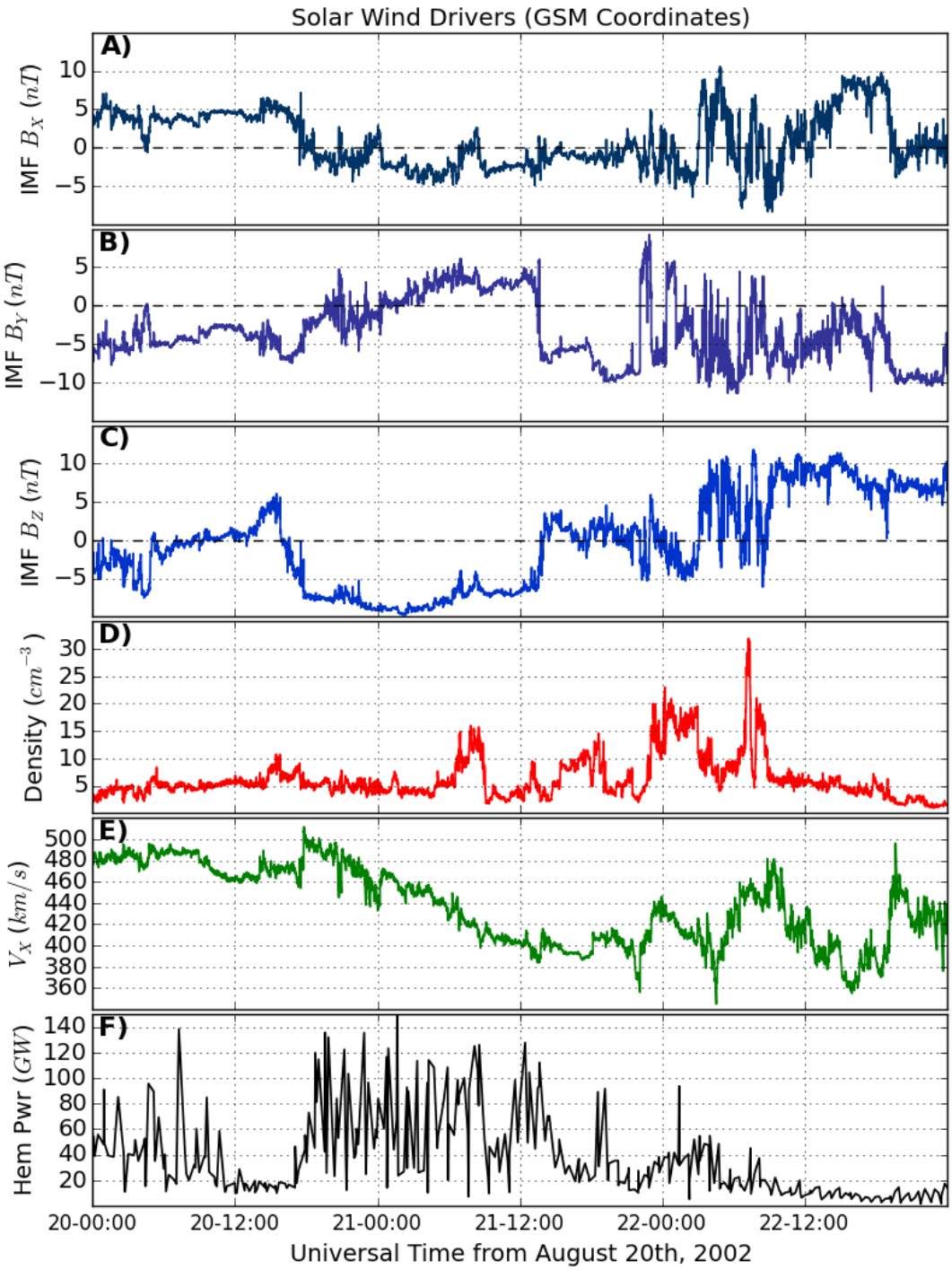

Figure 6.1: IMF, solar wind, and hemispheric power for August 20-23, 2002. Subplots A-F show IMF Bx (A), B_y (B), B_z (C), solar wind density (D) and velocity (E), as well as the hemispheric power (F).

catalog of storms during solar cycle 23 in which the disturbed storm time index (Dst) dropped below -100 nT. Figure 6.1 shows the IMF in plots A-C, solar wind parameters in plots D-E observed by the ACE spacecraft (*McComas et al.*, 1998; *Smith et al.*, 1998), and Hemispheric Power (HP) in plot F for the entire simulation time period. The storm was characterized by a rotation in IMF B_z extending from 15 UT on August 20th to 14 UT on the 21st. IMF B_y shifted from about -5 nT to +5 nT during this time period. The solar wind velocity and density were at nearly nominal values. The velocity decreased from 500 to 400 km/s and the density stayed between 5 and 10 cm^{-3} except for a 3 hour increase to 15 cm^{-3} near the end of the storm. The HP in plot F was the total area-integrated particle energy deposited into the northern hemisphere (*Fuller-Rowell and Evans*, 1987a) as derived from NOAA Polar Orbiting Environment Sensors (POES) satellites measurements. This plot shows that the hemispheric power varied between 20 and 120 GW throughout the course of the storm, indicating an active auroral oval. After simulating this storm which each type of driver in Table 6.1, all of the input files were shifted to each of solstices and equinoxes to investigate the theoretical effect of the same drivers applied to an I-T system in each season.

6.2 Results

6.2.1 Real Event

Figure 6.2 provides a first look at the simulation results with a comparison of neutral densities with the CHAMP (*Reigber et al.*, 2002) satellite. The simulation results were interpolated to the time and location of CHAMP at approximately 400 km. Each of the simulations behaved quite differently, even WFR and WOV, which were both driven by Weimer electric potentials. These two simulations diverged after the main 14 UT on August 21st, with Weimer producing mass densities over

	WFR	WOV	SWMF	HEIDI
North Polar	0.42	0.50	0.44	0.57
North Mid-Lats	0.89	1.15	0.81	1.15
Equatorial	0.29	0.22	0.21	0.14
South Mid-Lats	0.42	0.35	0.28	0.29
South Polar	0.39	0.41	0.46	0.39
All	0.45	0.48	0.40	0.45

Table 6.2: Normalized Root mean-square error (NRMSE) for GITM versus GPS TEC observations. The columns are the simulations for each driver; (1) Weimer potentials and Fuller-Rowell aurora, (2) Weimer potentials and Ovation SME aurora, (3) the SWMF with BATSRUS and RCM, and (4) HEIDI.

$1.0 \times 10^{-12} kg/m^3$ larger than the CHAMP observations. This increase is explained by stronger auroral precipitation in the WFR which led to more Joule heating and lifting of the thermosphere compared to WOV. However, WFR and WOV did much better than the SWMF and HEIDI runs for the first two days. SWMF had smaller mass densities than the baseline simulations before the storm during August 20th and after the storm on August 22nd. There was a 35% difference at the CHAMP mass density peak between the WOV and SWMF high-latitude drivers, which had largest and smallest responses respectively. Since ionospheric density is strongly influenced by the neutral density in the thermosphere, it may be reasonable to expect that the SWMF and HEIDI simulations would have had a greater ionospheric response because the mass density was lower than WFR and WOV at CHAMP locations.

Model results were also compared to ground-based GPS receiver data provided by the Madrigal database at MIT Haystack Observatory (*Rideout and Coster*, 2006). Vertical TEC was used as it provides the best estimate of TEC distributions in the ionosphere based on slant-path TEC measurements (*Mannucci et al.*, 1998). The relative precision of TEC provided by GPS measurements is on the order of 0.01 TECU with an absolute accuracy of 1-3 TECU (*Mannucci et al.*, 1998; *Tsurutani*, 2004), where 1 TECU = 10^{16} electrons m^{-2}. In each model comparison, the total

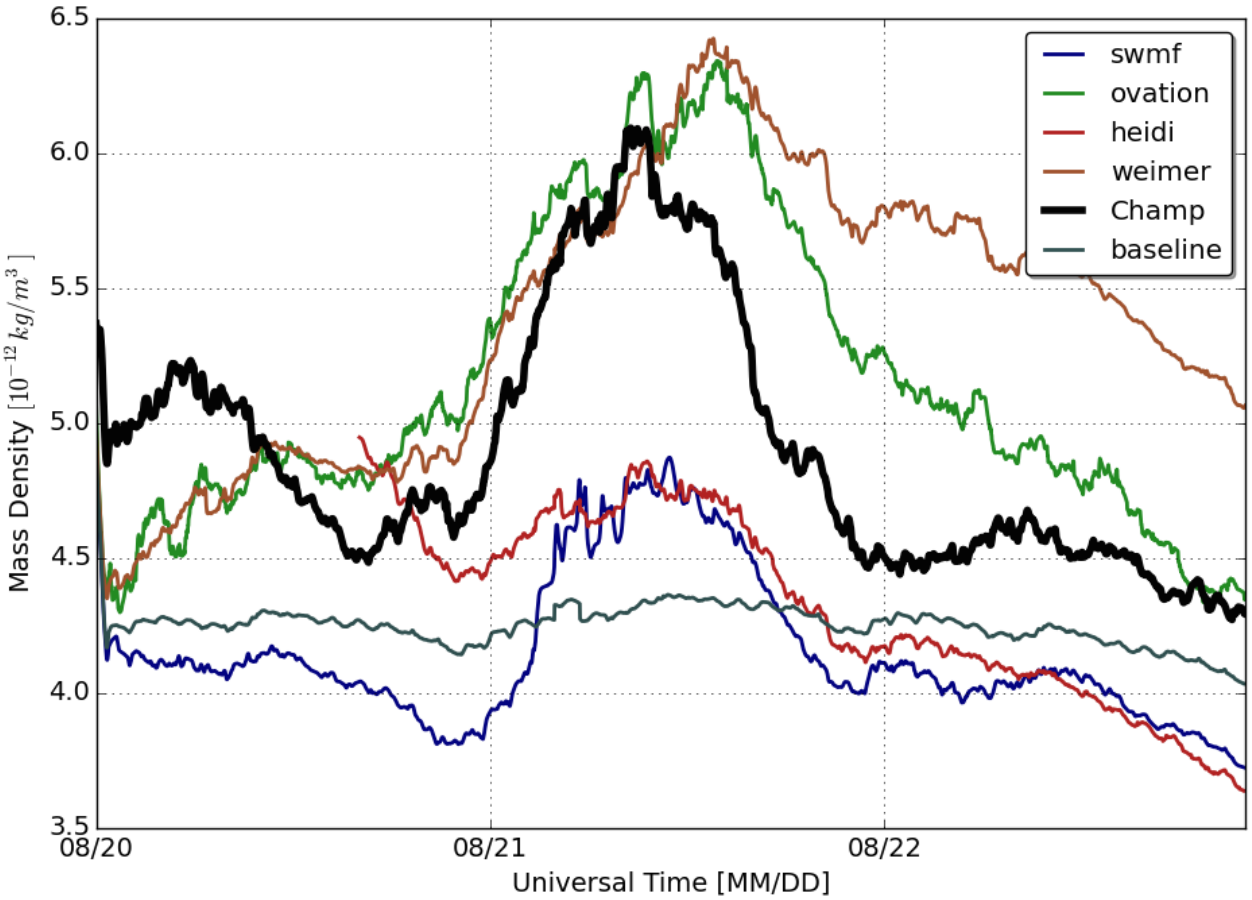

Figure 6.2: Comparison of CHAMP neutral densities with GITM for multiple high-latitude drivers during the August 20th, 2002 storm. The observations are in black, the baseline in grey, and the various drivers are colored accordingly.

electron content was calculated by integrating the electron density over all altitudes.

Figure 6.3 shows a comparison between GPS TEC observations and each type of GITM simulation described in Table 6.1. The results were averaged over all longitudes and split into 30° latitudinal bins, except the equatorial region in Figure 2C, which extends from 30° to -30°. The time period is same as Figure 6.1. The HEIDI simulation begins 14 hours later than the others due to data limitations at geosynchronous orbit that provides the outer boundary condition for HEIDI. The Normalized Root-Mean Square Error (NRMSE) for each simulation/region is shown in Table 6.2. An NRMSE of zero would mean a perfect prediction and infinity for an infinitely bad prediction. A score of 1 means that the model has the same predictive power as a persistance forecast with an amplitude equal to the mean of the observations.

In the northern polar hemisphere, the GITM TEC was relatively equal between high-latitude drivers at a nearly constant 10 TECU. All of the simulations missed an observed TEC increase to over 15 TECU in the latter half of August 20th resulting in NRMSEs between 0.42 and 0.57. The simulations under-predicted the observations in the northern mid-latitudes more substantially. NRMSEs for the entire time period were near 1.0. Since the baseline simulation TEC is nearly identical to the others, it is clear that there was essentially no storm-time TEC response in the summer hemisphere simulations. While a subdued response is expected here because of larger O/N_2 ratios, this effect appears to be more dominant in the model than in reality.

The high-latitude driver description created significantly more variance in the TEC response at equatorial and southern latitudes. Beginning at 15 UT on August 20th, the simulations began to diverge. In the equatorial region there was a 59% difference between WFR and SWMF simulations 24 hours later. The WFR and WOV simulations produced more TEC than the baseline, but SWMF and HEIDI predicted a negative ionospheric storm. HEIDI performed the best in this region, with an NRMSE of 0.14. Figures 6.3D and 6.3E show that all of the simulations

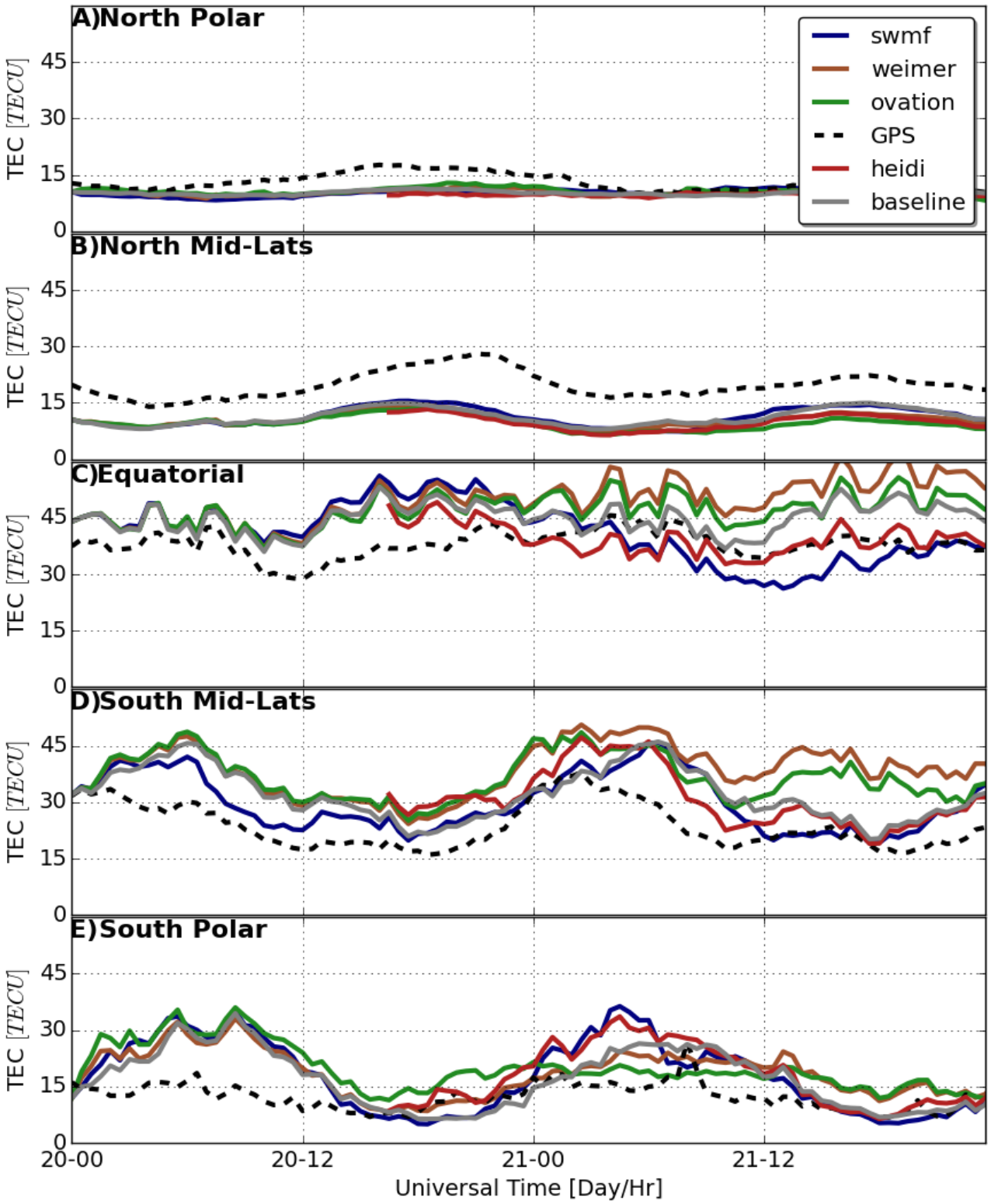

Figure 6.3: GPS TEC vs GITM with 4 different drivers in 5 latitude regions in plots A-G. Note that the scale in the polar regions goes from 0 to 50 TECU instead of 0 to 90 TECU. Each plot represents a 30° bin in geographic latitude. Plot A represents latitudes from 60° to 90°, plot B from 30° to 59° to degrees, and so on.

over-predicted the GPS observations in the southern hemisphere. In the southern polar region, the models predicted over 30 TECU when the GPS average was only 15 TECU. Note that in Figure 6.3E the SWMF and HEIDI simulations had the largest TEC during the main phase of the storm, which is consistent with the CHAMP results from Figure 6.2. Figure 6.3 demonstrates that the choice of high-latitude driver makes a bigger impact on the TEC simulation results depending on how large the response of the model is to the storm in any particular region. It also shows the heavily asymmetrical nature of the upper atmospheric response to this storm, which will be highlighted in the seasonal simulations shown in Section 6.2.2.

6.2.2 Seasonal Effects

As described in Section 6.1, the storm drivers were shifted to the solstice and equinox months to investigate the response of the ionosphere to identical forcing, but with different background conditions associated with the seasons. An initial view of the TEC response is shown in Figure 6.4. Each subplot represents a particular hemisphere and month, such that the summer hemispheres are in Figures 6.4A and 6.4B and the winter hemispheres in 6.4C and 6.4D. The TEC was averaged over all longitudes poleward of 60° in the given hemisphere. Note that the HEIDI simulation results do not begin until 14 UT on the first day of the simulations.

The summer hemispheres showed nearly no storm-time response at all, with only a slight deviation from the baseline case in the SH summer. This is unsurprising since it is well known that the ratio between atomic oxygen and molecular nitrogen (O/N_2) is much smaller in the summer hemisphere (*Hedin et al.*, 1974; *Jacchia*, 1974; *Mayr et al.*, 1978; *Strickland et al.*, 2004; *Qian et al.*, 2009), primarily due to upwelling of the heavier N_2 during the summer (*Burns et al.*, 1989; *Rishbeth*, 1998). When O/N_2 is small, electron loss to chemical recombination with N_2 dominates and the TEC is reduced. Figure 6.5 verifies that GITM reproduces this phenomenon. O/N_2

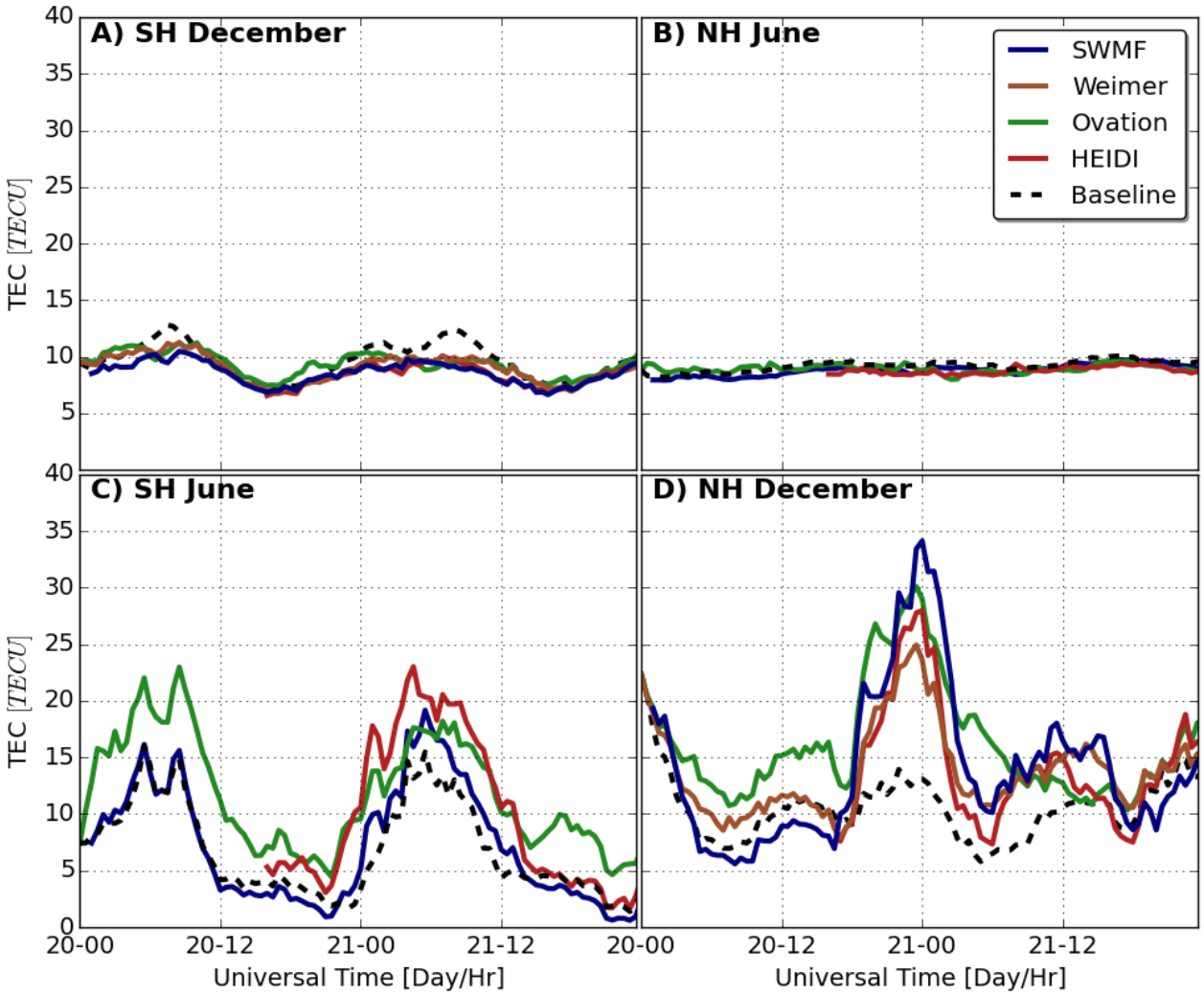

Figure 6.4: GITM TEC averaged over all longitudes above 60 degrees latitude for A) Southern hemisphere December, B) Northern hemisphere June, C) Southern hemisphere June, and D) Northern hemisphere December. The colored lines represent the simulations with GITM run by various high-latitude drivers and the black dashed line is the baseline simulation.

from the baseline simulations are shown with summer on the top and winter on the bottom. The ratio was calculated by integrating from the top of the simulation domain down to the altitude where $[N_2] = 1 \times 10^{22}$ cm^{-3}. This value was determined through comparisons with O/N_2 ratios from observations by the Global Ultraviolet Imager (GUVI) on the Thermosphere Ionosphere Mesosphere Energetics Dynamics (TIMED) satellite (*Paxton et al.*, 1999, 2004; *Christensen*, 2003). In both seasons, a large gradient gradient in O/N_2 was produced between hemispheres. There was also an asymmetry in the nightside O/N_2 with the NH summer having a ratio 0.2 higher than the SH summer poleward of 20°. Hemispheric asymmetries in O/N_2 have been shown to be caused by the differences in magnetic field structure and offset of the geographic and geomagnetic poles (*Qian et al.*, 2016).

High-latitude driver choice had a more significant impact on the ionosphere's response during the winter for both hemispheres. Figure 6.4C shows that the average TEC increased from 15 TECU in the baseline case to up to 23 TECU in the HEIDI simulation on the 21st. However, the largest response for all high-latitude specifications occurred during the NH winter in Figure 6.4D. At 18 UT, the baseline simulation TEC was 13 TECU. Storm-time values during this time ranged from 24 TECU for WFR to 34 TECU for SWMF. For SWMF, the average TEC difference between the baseline and GITM was 13 TECU larger in the NH winter. It is clear that some hemispheric asymmetry was driving this difference since all 4 simulations were approximately twice as geo-effective in the NH winter versus the SH winter.

Figure 6.6 depicts the storm time dynamics contributing to this asymmetric response in the NH winter. The WOV, SWMF, and HEIDI simulations are shown for four different times. The first two times, 14 UT and 16 UT, are just before the main phase of the storm. The TEC is contoured under the convection pattern shown by the black lines. The equipotential lines are the same in every plot with an interval of 6 kV within a range of -50 to 50 kV. The cross polar cap potential (CPCP) is

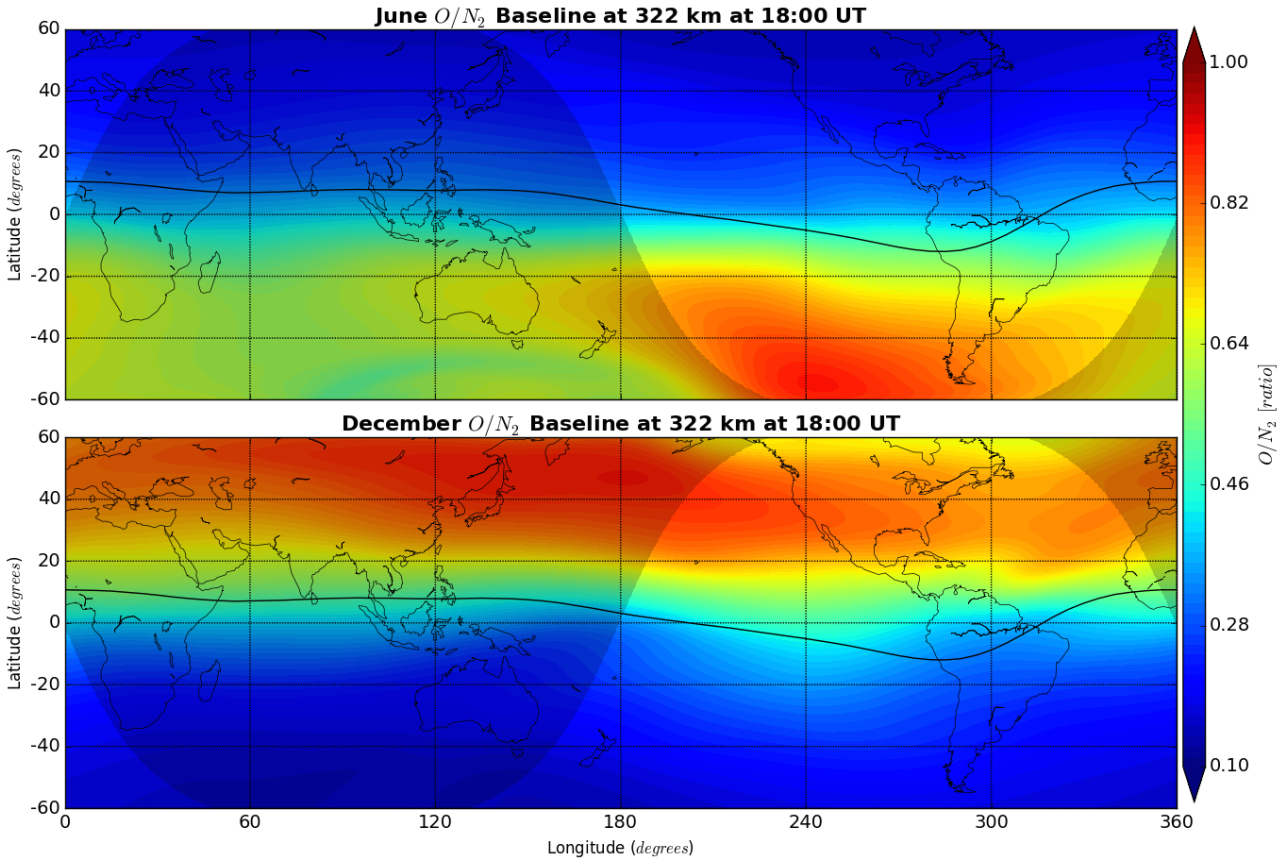

Figure 6.5: GITM O/N_2 for the baseline simulation. June solstice is at the top and December at the bottom. The geomagnetic equator is indicated by the solid black line.

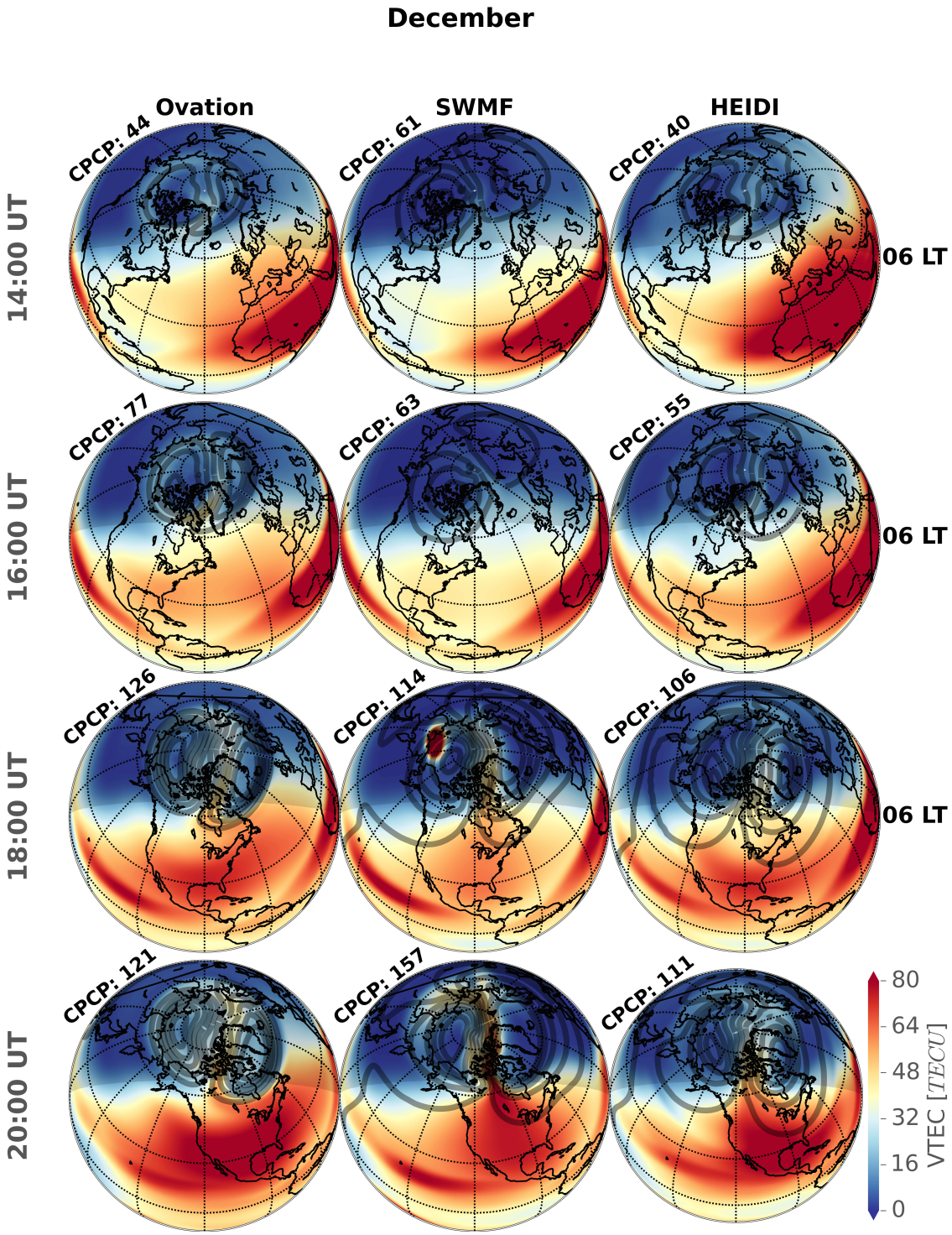

Figure 6.6: GITM TEC under electric potential contour lines for the Ovation, SWMF, and HEIDI simulations for December in the NH. The first two rows are before storm onset and the last two are during the main phase. All of the figures have been rotated such that local noon is at the center. The cross polar cap potential is given in the top left corner of each subplot and the shaded region depicts the nightside.

given in the top left corner of each subplot. Each plot was shifted such that the solar terminator stays in the same location. The nightside is denoted by the shaded region.

A feature of every simulation was the strengthening of the electric potential pattern as the storm developed between 16 UT and 18 UT. However, the extent to which the electric field penetrated to mid-latitudes varied between simulations and was not necessarily correlated with CPCP. The penetration electric field is important for the development of tongues of ionization's (TOIs) because the $\mathbf{E} \times \mathbf{B}$ drift can push plasma up magnetic lines to higher altitudes in the thermosphere where less recombination occurs. At 18 UT, a TOI developed in all 3 simulations as plasma was lifted at the mid-latitudes and moved into the polar cap following the anti-sunward convection pattern. The TOI was weakest in the WOV case despite the strongest CPCP because of a comparably weak penetration electric field. The CPCP for HEIDI was 106 kV at 18 UT compared to 126 kV for WOV, but the potential pattern extended 20° further equatorward down to 36° in HEIDI. As Figure 6.4 shows, SWMF had the highest average TEC above 60° latitude for this time period. This is evident in these figures by the combination of a strong CPCP and penetration electric field. Another important feature in Figure 6.6 is the SEDs that appeared over the American sector around storm onset. These SEDs provided a large seed population of plasma that was entrained in the convection pattern and then created a strong TOI. What appears to be a polar cap patch was produced around 18 UT only in the SWMF simulation, but this was a numerical error produced by the model at the geographic pole.

The question remains: Why was the TEC perturbation much larger in the NH winter than the SH winter? Figure 6.7 is identical to Figure 6.6 except it shows the SH in June. The SWMF comparison is not one to one since the inputs were created using the SWMF which ran at each season independently, therefore producing different potential patterns in June compared to December. The convection patterns for HEIDI and WOV are identical to those in December, but mirrored to the SH.

The CPCP produced by SWMF in this case was considerably lower than December, barely exceeding 60 kV at 20 UT. As a result, no major storm-time effects were seen in this simulation. However, the same can be said about HEIDI and WOV at 18 UT. Comparison with Figure 6.6 shows that there are 2 major factors contributing to less geo-effective SH winter. The first is that the convection patterns overlapped considerably less with the dayside. The potential pattern in WOV never encountered the daylight and the SWMF pattern penetrated less broadly in latitude and longitude compared to the NH December. This happened because of the greater tilt of the geomagnetic pole in the southern hemisphere combined with the UT of storm onset. At 18 UT, the geomagnetic pole was closest to the anti-sunward side of Antarctica, increasing the distance between the convection pattern and the dayside. This is contrasted with the NH December, where the geomagnetic pole near Eastern Canada was much closer to the dayside at storm onset. The second factor causing a weaker TEC response in the SH winter was a much smaller mid-latitude seed population. The TEC between 30° and 60° latitude was about 20 TECU on the dayside of the SH winter at 18 UT, compared to 52 TECU on the dayside of the NH winter. With much less plasma to entrain within the convection pattern, the TOI that developed by 20 UT in the HEIDI simulation was considerably weaker than its NH winter counterpart.

The larger electron seed population in the NH winter was a feature of the baseline simulation and unrelated to storm-time effects. This is evident in Figure 6.8, which shows the baseline TEC for June at the top and December at the bottom at 18 UT on the 20th of each month. A TEC bulge of over 60 TECU developed over the southern United States in December. Nothing similar occurred in the SH winter. This feature does not appear to be associated with the equatorial anomaly, as the bulge is disconnected from that feature. Both plots show that GITM is able to reproduce some of the 4-peak structure within the equatorial anomaly (*Immel et al.*, 2009) with the inclusion of atmospheric tides provided by MSIS at the lower boundary of the

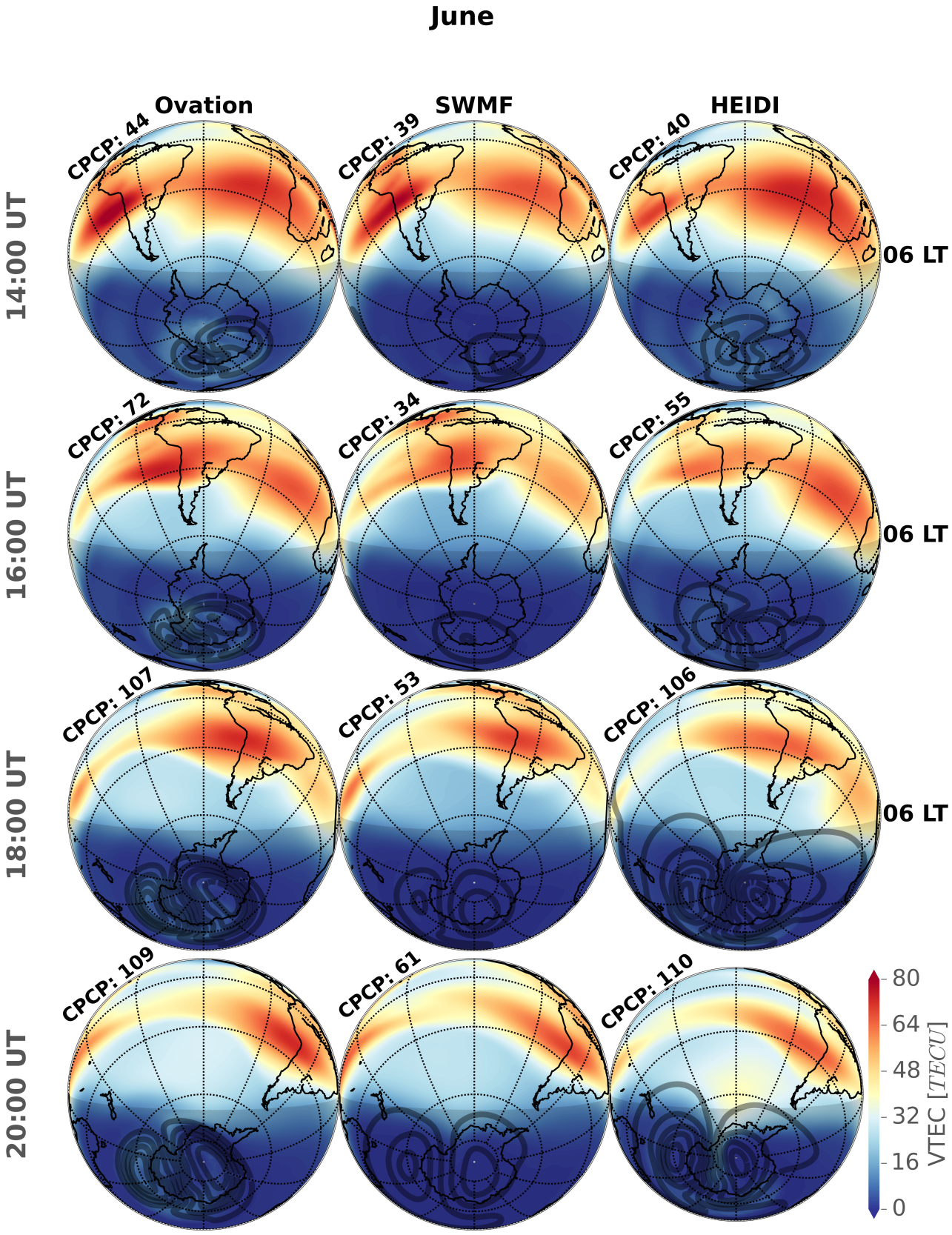

Figure 6.7: The same as Figure 6.6, but for June in the SH.

model.

Neutral winds can be very effective at pushing plasma up and down magnetic field lines, thereby contributing to fluctuations in TEC. Figure 6.9 shows that the TEC bulge in the baseline simulation in Figure 6.8 results from the dynamics of neutral winds interacting with Earth's magnetic field. The vectors in this Figure represent the horizontal neutral winds, but the contour is only the vertical component along the magnetic field lines resulting from those neutral winds. Generally speaking, equatorward neutral winds push plasma up field lines, and poleward winds push plasma down field lines. Furthermore, pressure gradient forces primarily create neutral winds that are oriented away from the subsolar point and from the summer to winter hemisphere. Since all of the simulations in this study were done during solar maximum in 2002, the EUV flux at the subsolar point is quite large and appears to have dominated over the summer to winter flow because neutral wind vectors in the mid-latitudes on the dayside were pointed away from the subsolar point and towards the winter hemisphere.

The light red color between 240° and 300° longitude just north of the magnetic pole in the NH December plot indicates that neutral winds were pushing plasma up field lines in that location, contributing to the TEC enhancement from Figure 6.8. There were some eastward pointing neutral winds in this location that were pointed towards the geomagnetic equator that is indicated by the solid black line. This resulted in upward neutral winds in the NH winter. The SH winter in the top plot had much stronger neutral winds directed away from the geomagnetic equator at mid-latitudes resulting in downward directed ion flows, reducing the mid-latitude TEC in the SH winter. This asymmetrical neutral wind structure was therefore integral in the development of SEDs and a strong TOI seen in the northern hemisphere in Figure 6.6.

While the penetration electric field is an important factor contributing to storm

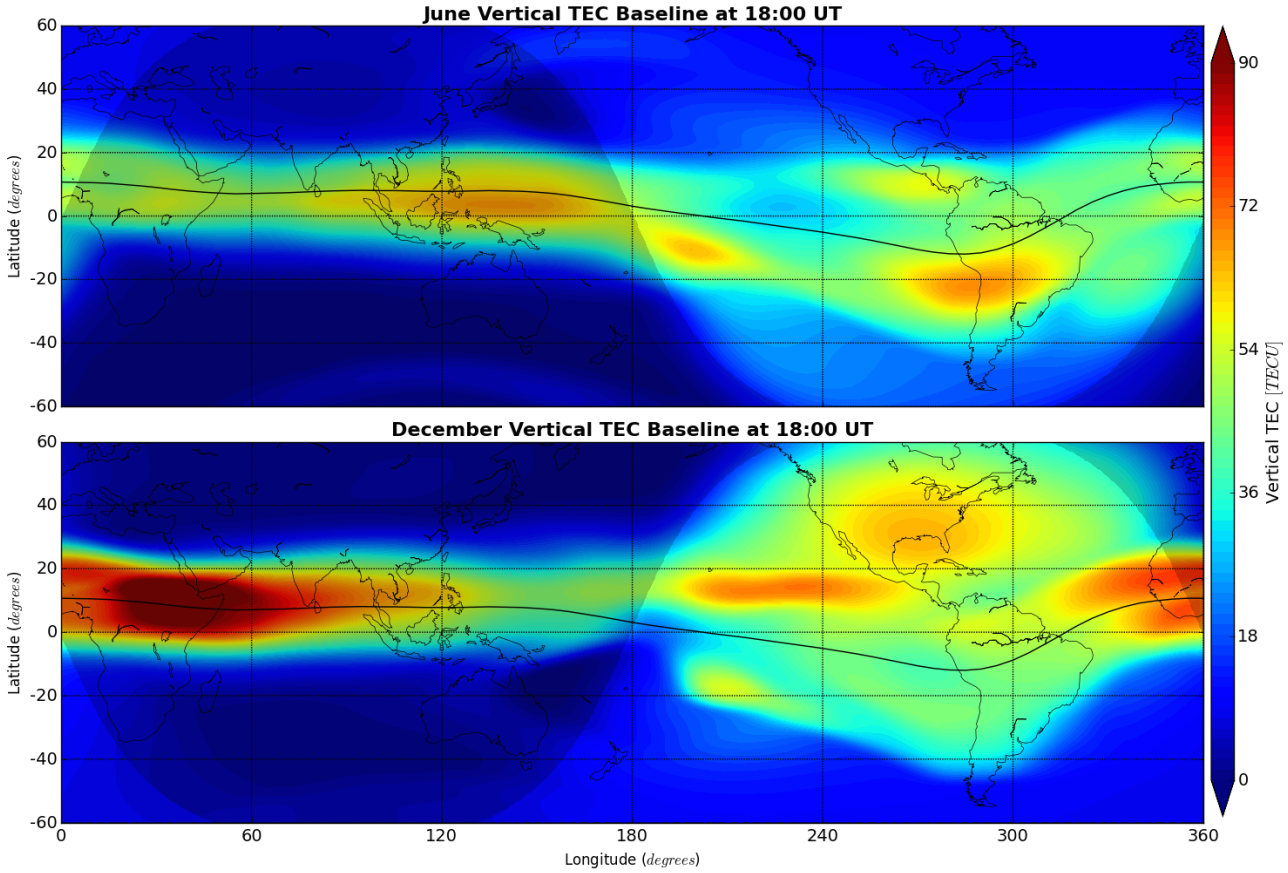

Figure 6.8: GITM Vertical TEC for the baseline simulation. June solstice is at the top and December at the bottom. The geomagnetic equator is indicated by the solid black line.

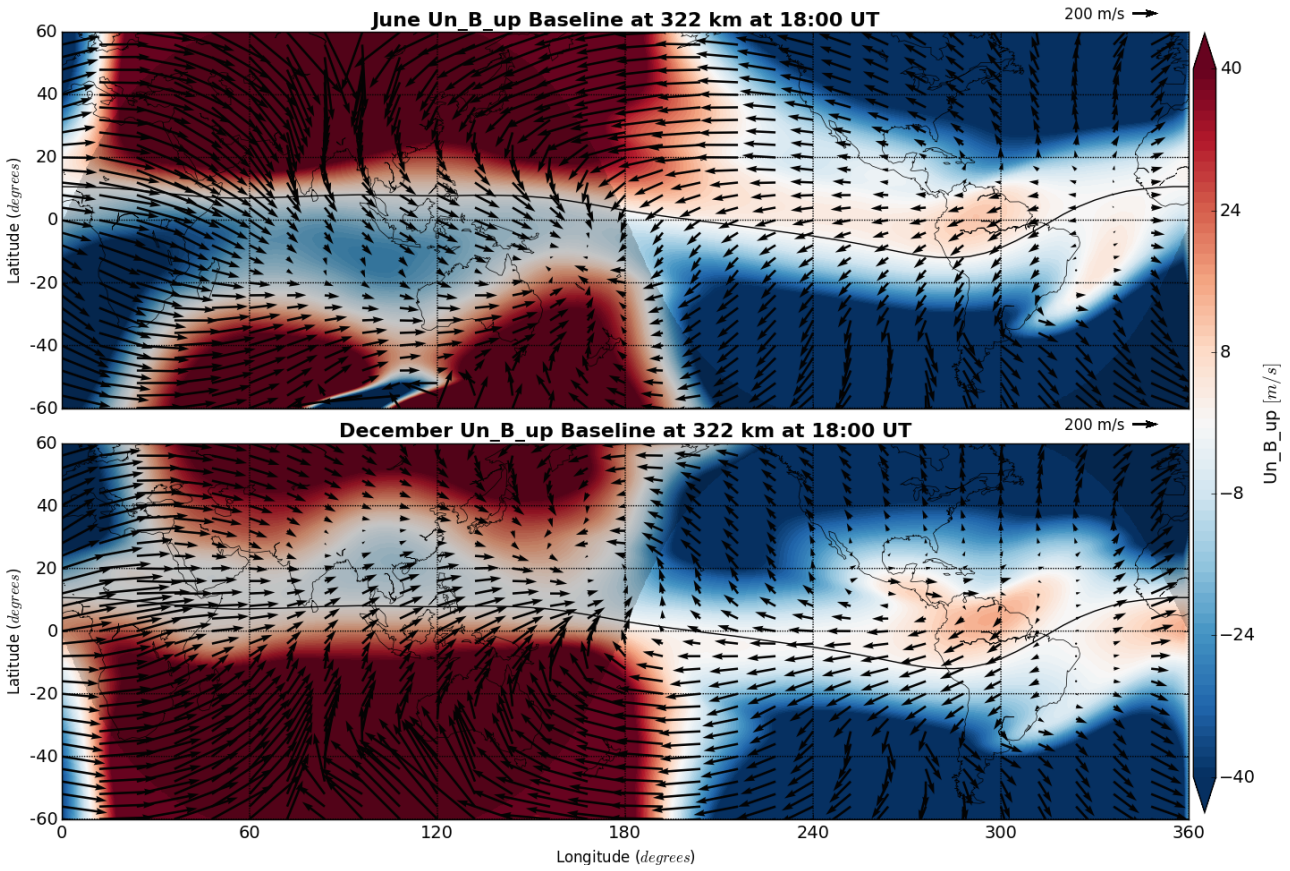

Figure 6.9: GITM neutral winds for the baseline simulation. The vectors are the horizontal neutral winds and the contour is the vertical neutral wind component along magnetic field lines. June solstice is at the top and December at the bottom. The geomagnetic equator is indicated by the solid black line.

time TEC phenomenon, there are a number of other sources and sinks of electron density that could be contributing to the strength of the SEDs and TOI observed in Figures 6.6 and 6.7. Figures 6.10 and 6.11 display a number of these for the HEIDI simulation, which produced a much weaker TOI in the SH winter. Each subplot contains the values for HEIDI storm simulation subtracted by the baseline simulations, thereby depicting the storm time perturbations.

The process forming the TOI is visible in the NH December plots in Figure 6.6. The enhanced convection pattern between 21 and 12 LT pushed plasma up field lines as seen in the vertical ion velocity in Figure 10E. Along this track, the electron tem-

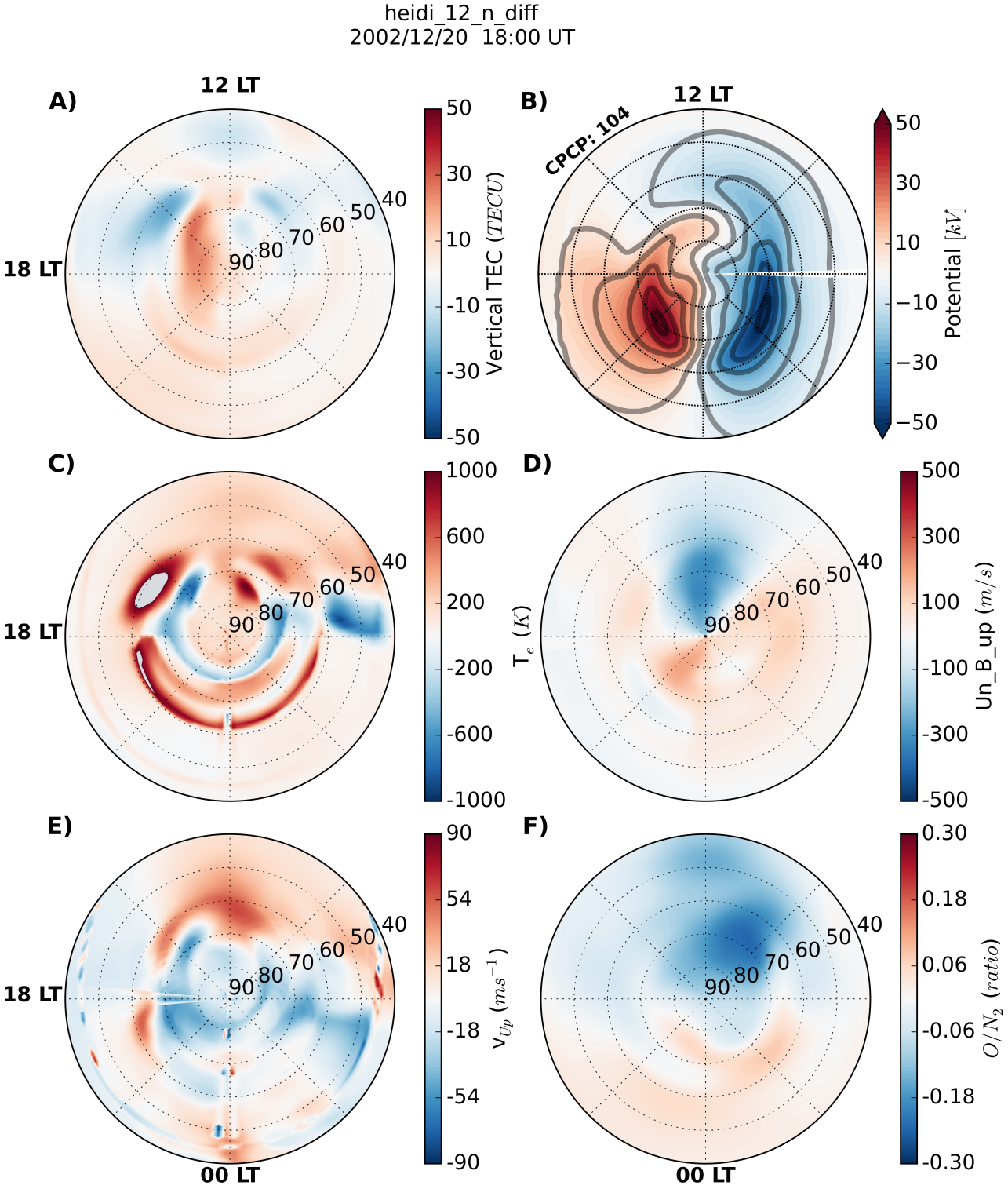

Figure 6.10: Differences between the HEIDI NH December simulation and the baseline run for 6 different quantities at 18 UT on the December 20th. The plots represent: A) vertical TEC, B) electric potential, C) electron temperature, D) vertical component of the neutral wind along magnetic field lines, E) vertical ion velocity, F) O/N_2 ratio.

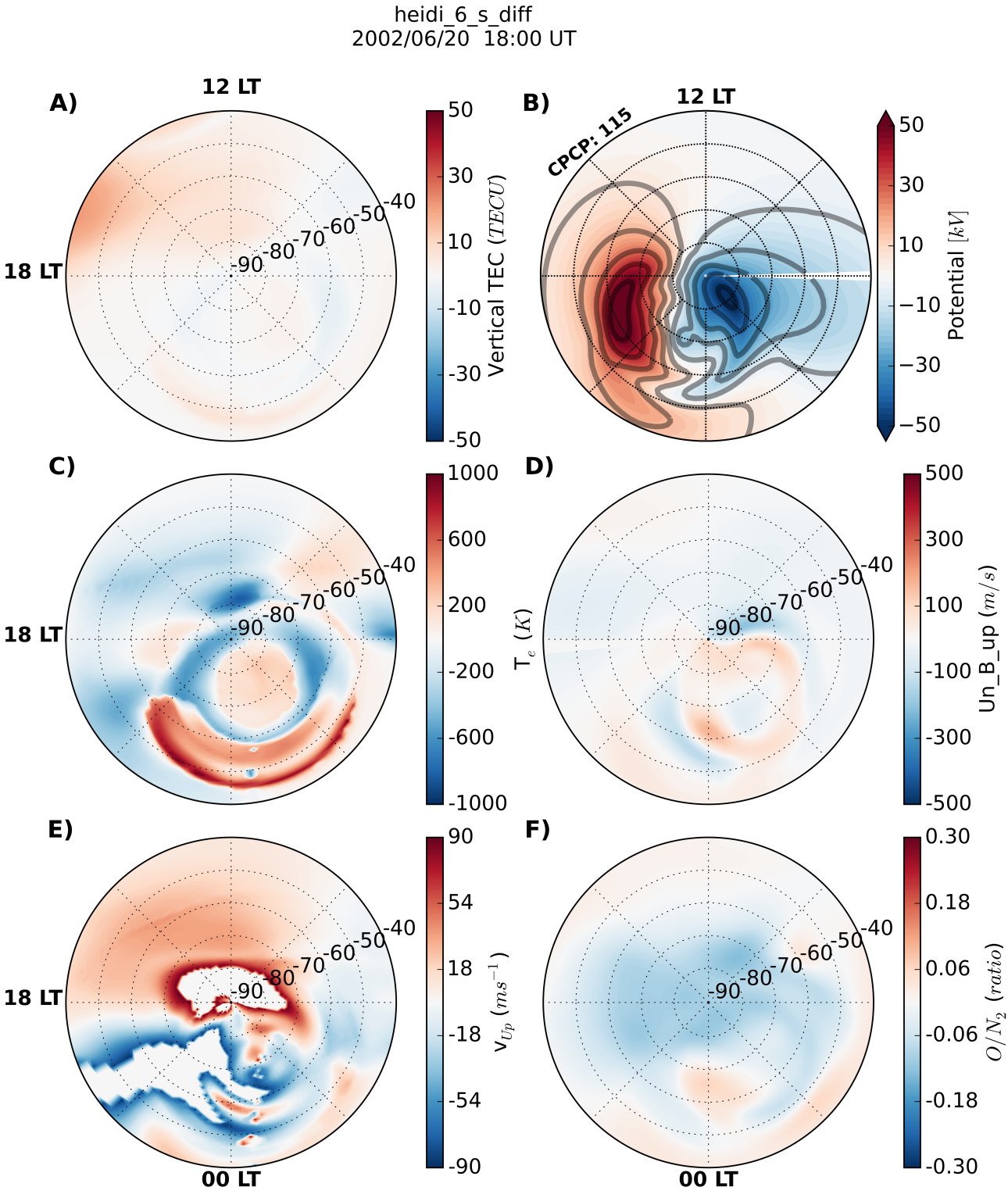

Figure 6.11: The same as Figure 6.10, but for the SH in June.

perature in Figure 6.10C increased by over 1000K higher than the baseline simulation, coinciding with an electron density trough region straddling 15 LT at 60° latitude in Figure 6.10A. As the convection turned poleward near 12 LT, the $\mathbf{E} \times \mathbf{B}$ drift pulled the lifted plasma from the mid-latitudes over the polar cap creating the TOI. The increased convection through the throat region accelerated the neutral winds towards the pole, due to the increased ion drag, creating a downward wind seen in Figure 6.10D. Simultaneously, Joule heating associated with this process lifted the thermosphere and decreased the O/N_2 ratio in Figure 6.10F. The last two processes served to reduce the strength of the TOI.

This is contrasted with the SH June results in Figure 6.11. Only a minor TEC increase of about 15 TECU occurred between 12 and 18 LT in Figure 6.11A. No channel of increased convection, vertical ion velocity, or electron temperature increase is evident in Figures 6.11A, 6.011C, and 6.11E. The weaker TOI appeared as there was still some vertical ion velocity on the dayside from the convection pattern. Neutral winds were not accelerated on the dayside towards the polar cap, and the subsequent Joule heating was less on the mid-latitude dayside, possibly related to the small O/N_2 ratio in Figure 6.11F compared to 6.10F. The electron temperature and vertical ion velocity changes associated with the auroral oval were lied on the nightside where the baseline TEC in Figure 6.8 was very low. Consequently, there was almost no TEC change from the baseline simulation on the nightside in Figure 6.11A.

6.3 Discussion and Conclusions

The impact of solar storms on the Earth's upper atmosphere is dependent on more than the solar wind dynamic pressure and the strength and orientation of the IMF. The season and UT at which the storm occurs has been shown to have an impact on TEC, as well as thermospheric densities and temperatures (*Förster and Cnossen*, 2013; *Cnossen et al.*, 2012b; *Perlongo and Ridley*, 2016; *Cnossen and*

Förster, 2016; *Laundal et al.*, 2016). Furthermore, there is often an asymmetric response between hemispheres (*Cnossen et al.*, 2011, 2012a; *A et al.*, 2012b). This study investigated the reasons for these variations with a systematic modeling effort. A global ionosphere-thermosphere model, GITM (*Ridley et al.*, 2006), was run with a variety of high-latitude drivers, some driven by empirical models and others by physics-based magnetosphere codes. These are summarized in Table 6.1. An ICME that occurred on August 20th, 2002 was run for each model configuration. The inputs were then shifted to the solstices to highlight the effect of identical solar inputs on model results for both hemispheres in the summer and winter.

The results for the real event were compared to CHAMP neutral density measurements as well as ground based GPS TEC measurements. The GITM neutral densities along CHAMP's satellite track varied by up to 35% between simulations. Most GITM simulations showed a strong response to the storm, similar to CHAMP, but there was a large variance between the simulation results with some drivers causing an under prediction, and others having too slow of a recovery. The Weimer driven simulations overestimated CHAMP densities, but SWMF and HEIDI driven runs consistently underestimated them. None of the GITM runs produced a considerable TEC response in the NH, with all of them underestimating the GPS TEC observations there. The SH results showed that the variation between high-latitude driver results was negatively correlated with the magnitude of the TEC in the baseline run. The SWMF and HEIDI runs produced the largest TEC in the SH polar region with an average TEC double that of the observations.

The hemispheric asymmetry seen in TEC response for the actual event was more clearly defined in the solstice results. A hotter thermosphere in the summer led to low O/N_2 ratios resulting in effectively no storm-time TEC response in the polar regions of either hemisphere. This confirms the results of *Adimula et al.* (2016), where they hypothesized that O/N_2 ratios caused a similar variation in seasonal GPS TEC

observations. Seasonal variations in neutral wind patterns have also been known to introduce regional dependence on TEC storm effects by changing the height of the F_2 peak (*Prölss*, 1980, 1987; *Fuller-Rowell et al.*, 1994). Positive storm effects have been observed to be more prevalent during the winter (*Rishbeth*, 1998; *Thomas et al.*, 2016), agreeing with the simulations presented here.

For all model configurations, the TEC response to the storm was larger in the NH winter than the SH winter. First, a TEC bulge developed in the mid-latitudes of the NH winter in the American sector as a result of neutral winds pushing plasma upwards along magnetic fields, which provided a seed population for the TOI. The origin of the electron density enhancement over North America was not a storm-time effect, as it was also produced in the baseline simulation. The declination angle of the magnetic field changes from positive to negative in the east-west direction here, a property which has found to cause a longitudinal asymmetry in the ability of neutral winds to push plasma up and down field lines (*Zhang et al.*, 2012; *Zhao et al.*, 2013). Since the seed population regulated the response of the storm-time ionosphere, these results reinforce the findings of *Sojka et al.* (2012), who found that the neutral winds could potentially have as large an influence on the TEC response as electric fields.

Given the seed population, a penetration electric field extended into the dayside mid-latitudes to produce SEDs and entrain the plasma within the convection pattern, creating a TOI. This process was predicated on the ability of a penetration electric field to reach sufficiently low latitudes, which did not occur in the Weimer simulations or in the SH winter simulations, except for the HEIDI run. This is because the geomagnetic pole was much further from the dayside in the SH winter. The SH pole is tilted further away from the geographic pole than in the NH, so the UT of storm onset has a large influence on how much penetration electric field reached mid-latitudes in the SH. Additionally, the electric potential model had a large influence on the TEC response because of the strength and penetration of the resulting electric

fields. The Weimer model does not include penetration electric fields, so a weaker or non-existent TOI was expected. However, the inclusion of the ring current in the SWMF and HEIDI simulations allows for penetration electric fields to develop, increasing the ability of those models to accurately represent the physical processes that generate SEDs and TOIs.

This research has demonstrated that the storm time ionosphere is heavily dependent on the season and UT of storm onset. The most geo-effective storm occurred in the NH winter with a main phase onset time such that the American sector was on the dayside. Additionally, it has highlighted the variance in model results between high-latitude electric field and auroral input configurations.

CHAPTER VII

Conclusions

This dissertation described and investigated some of the fundamental processes behind the dynamics of the M-I-T system. Each chapter focused on hemispheric asymmetries, as well as seasonal, local time, and latitudinal dependencies.

First, using a large set of idealized GITM simulations with varied season and magnetic field configurations, that study found that the local time of the magnetic pole plays a key role in the thermospheric response. It further found that UT effects are greater in the southern hemisphere. These effects include larger thermospheric perturbations in density and temperature when the geomagnetic pole was pointed towards the sun. It also found that longitudinal variations in Earth's magnetic field, caused by the tilt and offset of the magnetic pole, influence the magnitude of the UT variations.

Chapter IV provided a reference and analysis of how two leading global ionosphere models, GITM and TIEGCM, were able to reproduce ground based GPS TEC observations. The models were run for the entire year of 2010 and the results were tabulated into regional and MLT bins. It was found that GITM had a propensity to overestimate the TEC while the opposite was true of TIEGCM. It was also found that the accuracy of GITM was best in the northern polar region and decreased almost linearly towards the south pole, suggesting that the model may be over-fitted

to the northern hemisphere. TIEGCM compared best at the poles and worst near the equator by the equatorial anomaly. The results also identified a TEC hole in the northern hemisphere summer nightside in the GPS observations, the processes of which should be studied further. This project is useful for researchers deciding which model to use. Their choice may be influenced by which model performed better in the region they are interested in.

Momentarily moving away from the upper atmosphere, Chapter V presented a project using the new HEIDI ring current model configuration described in Chapter II. The focus of this study was on the electrodynamic feedback between the ionosphere and the diffuse aurora created by electron scattering by plasma waves in the inner magnetosphere. Running four different geomagnetic storms revealed that the scattering rate description had a large impact on the total amount of aurora, hemispheric power, as well as the location and strength of the aurora and subsequent ionospheric electric fields. While the study did find a cutoff to the maximum lifetime of an electron in the inner magnetosphere that was most agreeable with auroral observations, it highlighted that the electric field results are currently insufficient to reasonably supplant empirical models as the go-to source for high-latitude electric potentials and electron precipitation in global I-T models. The coupling does, however, provide a basis for further model development to improve the sophistication of coupled models in the coming years.

The ensemble simulations presented in Chapter VI were a culmination of the previous research projects. GITM was driven by the new version of HEIDI among other high-latitude drivers to investigate the UT and seasonal dependence of model results. The study also compared GPS TEC and CHAMP neutral density observations for an actual storm event, finding large variations in results between drivers and latitude. The primary research findings were related to the hemispheric and seasonal asymmetries in storm-time TEC simulation results, given identical solar forcing. Small

O/N_2 ratios in the summer suppress storm time TEC enhancements because of the lifted thermosphere that increases recombination rates in the F-region ionosphere. The solstice results were asymmetric, with the northern hemisphere winter having a larger TEC response than the southern hemisphere. It was found that this resulted from a combination of the UT of storm onset in conjunction with the further offset of the geomagnetic pole in the southern hemisphere. Additionally, neutral winds acted to push mid-latitude plasma in the northern hemisphere American sector to higher altitudes in the winter than its South American counterpart. This contributed to a larger seed population for the growth of SEDs and TOI's.

Overall, the research presented in this thesis has advanced two major goals outlined in Chapter I. First, it has advanced a numerical model of the ring current that can be further developed and used to improve our understanding of the interactions between the ionosphere and magnetosphere. Secondly, the time and spatial dependency of the geospace response to solar forcing was investigated through a series of concentrated modeling efforts. Despite the advancements detailed above, there are still numerous open questions and potential research projects, some of which are outlined below.

7.1 Future work

The research in this thesis was designed such that future researchers can take the tools and ideas that were developed and use them to advance research of related geospace phenomenon. The following is a list of ideas and projects that are suitable continuations of the research presented in this thesis.

1. The analysis of the thermosphere in response to idealized storms occurring at different UT's was just that: idealized. The ideas presented in Chapter III should be taken and applied to real storm events and properly compared to

observations of the thermosphere and ionosphere including, but not limited to, GPS TEC, incoherent scatter radar, ionosondes, and in-situ satellite measurements of thermospheric temperature and density. Combined with the seasonal results from Chapter VI, it would be interesting to identify times and days where space weather effects are more likely to occur based on the predisposition of the upper atmosphere to respond more or less to solar forcing.

2. Longitudinal variations were also hypothesized in Chapter III to be of importance for UT variations, but the processes behind this were not fully investigated. A research project devoted to understanding how the magnetic field structure lends to neutral and electron density profiles would be useful. As shown in Chapter VI, vertical neutral winds can redistribute plasma according to the magnetic field configuration which in turn can enhance or reduce the geo-effectiveness of a solar storm.

3. The 2010 TEC comparisons with GITM and TIEGCM presented in Chapter IV provide a launch point for any number of developments for either model. For example, there was a clear deficiency in the mid-latitude nightside of GITM to reproduce GPS TEC observations. A description of plasmaspheric refilling should be added to the code for it to be more realistic in this region. TIEGCM performed best near the polar regions and worse towards the equator, seemingly due to a weaker equatorial anomaly that should also be addressed.

4. The study using HEIDI to investigate the effect of electron scattering rates on the location and strength of the aurora and its relationship to electrodynamic coupling between the ring current and upper atmosphere presented in Chapter V raised pertinent questions for future coupled models. Since the scattering rate was found to have such a large impact on the electrodynamics, models need to improve their description of this parameter. There are new parametrization's

based on Van Allen probes data by *Orlova et al.* (2016) that should be implemented.

5. The HEIDI model in particular is segmented between versions that have different capabilities. The self-consistent auroral model developed in Chapter II should be merged with the version in the SWMF that contains an arbitrary magnetic field strength, as that has been shown to be of great importance for ring current dynamics. After this is complete, adding a description of discrete aurora in HEIDI may greatly improve the electric field comparisons.

6. The storm-time TEC results from the ensemble of simulations were only compared for the solstice months. As described in Chapter III, many researchers have identified considerable differences in the upper atmosphere's response to storms between the equinoxes as well. These simulations were completed as well and should be analyzed more thoroughly. Additionally, this project only considered one storm event that was shifted to each season. Perhaps choosing only one high-latitude driver and running a wide variety of storms among different seasons could confirm the results from this project. Even more high-latitude drivers could also be considered, including AMIE.

In conclusion, the M-I-T is a vast and inter-dynamic system that produces an important, but challenging research area. Space weather is an increasingly crucial phenomenon to predict as it has costly and even potentially deadly consequences. The research in this thesis advances our knowledge needed to predict and mitigate space weather, but an incredible amount of work remains. The future work described above provides a potential starting place for future researchers to continue improving our understanding of this unique and interesting domain.

BIBLIOGRAPHY

BIBLIOGRAPHY

A, E., A. J. Ridley, D. Zhang, and Z. Xiao (2012a), Analyzing the hemispheric asymmetry in the thermospheric density response to geomagnetic storms, *Journal of Geophysical Research*, *117*(A8), A08,317, doi:10.1029/2011JA017259.

A, E., A. J. Ridley, D. Zhang, and Z. Xiao (2012b), Analyzing the hemispheric asymmetry in the thermospheric density response to geomagnetic storms, *Journal of Geophysical Research: Space Physics*, *117*(A8), n/a–n/a, doi:10.1029/2011JA017259.

Adimula, I. A., O. A. Oladipo, and S. J. Adebiyi (2016), Latitudinal and Seasonal Investigations of Storm-Time TEC Variation, *Pure and Applied Geophysics*, *173*(7), 2521–2533, doi:10.1007/s00024-016-1291-2.

Afraimovich, E., E. Astafyeva, V. Demyanov, and I. Gamayunov (2009), Mid-latitude amplitude scintillation of GPS signals and GPS performance slips, *Advances in Space Research*, *43*(6), 964–972, doi:10.1016/j.asr.2008.09.015.

Albert, J. M. (1994), Quasi-linear pitch angle diffusion coefficients: Retaining high harmonics, *Journal of Geophysical Research*, *99*(A12), 23,741, doi:10.1029/94JA02345.

Anderson, P. C., R. A. Heelis, and W. B. Hanson (1991), The ionospheric signatures of rapid subauroral ion drifts, *Journal of Geophysical Research*, *96*(A4), 5785, doi:10.1029/90JA02651.

Anderson, P. C., W. B. Hanson, R. A. Heelis, J. D. Craven, D. N. Baker, and L. A. Frank (1993), A proposed production model of rapid subauroral ion drifts and their relationship to substorm evolution, *Journal of Geophysical Research*, *98*(A4), 6069, doi:10.1029/92JA01975.

Anderson, P. C., D. L. Carpenter, K. Tsuruda, T. Mukai, and F. J. Rich (2001), Multisatellite observations of rapid subauroral ion drifts (SAID), *Journal of Geophysical Research*, *106*(A12), 29,585, doi:10.1029/2001JA000128.

Appleton, E. V. (1946), Two Anomalies in the Ionosphere, *Nature*, *157*(3995), 691–691, doi:10.1038/157691a0.

Basu, S., et al. (2001), Ionospheric effects of major magnetic storms during the International Space Weather Period of September and October 1999: GPS observations,

VHF/UHF scintillations, and in situ density structures at middle and equatorial latitudes, *Journal of Geophysical Research: Space Physics*, *106*(A12), 30,389–30,413, doi:10.1029/2001JA001116.

Belian, R. D., G. R. Gisler, T. Cayton, and R. Christensen (1992), High- Z energetic particles at geosynchronous orbit during the Great Solar Proton Event Series of October 1989, *Journal of Geophysical Research*, *97*(A11), 16,897, doi:10.1029/92JA01139.

Belmont, G., D. Fontaine, and P. Canu (1983), Are equatorial electron cyclotron waves responsible for diffuse auroral electron precipitation?, *Journal of Geophysical Research: Space Physics*, *88*(A11), 9163–9170, doi:10.1029/JA088iA11p09163.

Bilitza, D. (2001), International Reference Ionosphere 2000, *Radio Science*, *36*(2), 261–275, doi:10.1029/2000RS002432.

Blanc, M., and A. Richmond (1980), The ionospheric disturbance dynamo, *Journal of Geophysical Research*, *85*(A4), 1669, doi:10.1029/JA085iA04p01669.

Bramley, E., and M. Young (1968), Winds and electromagnetic drifts in the equatorial F2-region, *Journal of Atmospheric and Terrestrial Physics*, *30*(1), 99–111, doi:10.1016/0021-9169(68)90044-5.

Broun, J. (1848), Observations in magnetism and meteorology made at Makerstoun in Scotland, *Trans. R. Soc. Edinburgh*, *18*(401).

Bruinsma, S., J. M. Forbes, R. S. Nerem, and X. Zhang (2006), Thermosphere density response to the 2021 November 2003 solar and geomagnetic storm from CHAMP and GRACE accelerometer data, *Journal of Geophysical Research*, *111*(A6), A06,303, doi:10.1029/2005JA011284.

Buonsanto, M. (1999), Ionospheric Storms A Review, *Space Science Reviews*, *88*(3/4), 563–601, doi:10.1023/A:1005107532631.

Burke, W. J. (2007), Penetration electric fields: A VollandStern approach, *Journal of Atmospheric and Solar-Terrestrial Physics*, *69*(10-11), 1114–1126, doi:10.1016/j.jastp.2006.09.013.

Burns, A. G., T. L. Killeen, and R. G. Roble (1989), Processes responsible for the compositional structure of the thermosphere, *Journal of Geophysical Research*, *94*(A4), 3670, doi:10.1029/JA094iA04p03670.

Burrell, A. G., R. A. Heelis, and R. A. Stoneback (2012), Equatorial longitude and local time variations of topside magnetic field-aligned ion drifts at solar minimum, *Journal of Geophysical Research*, *117*(A4), A04,304, doi:10.1029/2011JA017264.

Burrell, A. G., R. A. Heelis, and A. Ridley (2013), Daytime altitude variations of the equatorial, topside magnetic field-aligned ion transport at solar minimum, *Journal of Geophysical Research: Space Physics*, *118*(6), 3568–3575, doi:10.1002/jgra.50284.

Chamberlin, P. C., T. N. Woods, and F. G. Eparvier (2007), Flare Irradiance Spectral Model (FISM): Daily component algorithms and results, *Space Weather*, *5*(7), n/a–n/a, doi:10.1029/2007SW000316.

Chapman, S. (1931), The absorption and dissociative or ionizing effect of monochromatic radiation in an atmosphere on a rotating earth, *Proceedings of the Physical Society*, *43*(1), 26–45, doi:10.1088/0959-5309/43/1/305.

Chartier, A. T., et al. (2016), Ionospheric data assimilation and forecasting during storms, *Journal of Geophysical Research: Space Physics*, *121*(1), 764–778, doi:10.1002/2014JA020799.

Chen, C. H., C. H. Lin, T. Matsuo, W. H. Chen, I. T. Lee, J. Y. Liu, J. T. Lin, and C. T. Hsu (2016), Ionospheric data assimilation with thermosphere-ionosphere-electrodynamics general circulation model and GPS-TEC during geomagnetic storm conditions, *Journal of Geophysical Research: Space Physics*, *121*(6), 5708–5722, doi:10.1002/2015JA021787.

Chen, M. W., and M. Schulz (2001), Simulations of diffuse aurora with plasma sheet electrons in pitch angle diffusion less than everywhere strong, *Journal of Geophysical Research: Space Physics*, *106*(A12), 28,949–28,966, doi:10.1029/2001JA000138.

Chen, M. W., M. Schulz, L. R. Lyons, and D. J. Gorney (1993), Stormtime transport of ring current and radiation belt ions, *Journal of Geophysical Research: Space Physics*, *98*(A3), 3835–3849, doi:10.1029/92JA02608.

Chen, M. W., M. Schulz, G. Lu, and L. R. Lyons (2003), Quasi-steady drift paths in a model magnetosphere with AMIE electric field: Implications for ring current formation, *Journal of Geophysical Research: Space Physics*, *108*(A5), doi:10.1029/2002JA009584.

Chen, M. W., M. Schulz, P. C. Anderson, G. Lu, G. Germany, and M. Wüest (2005), Storm time distributions of diffuse auroral electron energy and X-ray flux: Comparison of drift-loss simulations with observations, *Journal of Geophysical Research*, *110*(A3), A03,210, doi:10.1029/2004JA010725.

Chen, M. W., C. L. Lemon, T. B. Guild, A. M. Keesee, A. Lui, J. Goldstein, J. V. Rodriguez, and P. C. Anderson (2015), Effects of modeled ionospheric conductance and electron loss on self-consistent ring current simulations during the 5-7 April 2010 storm, *Journal of Geophysical Research: Space Physics*, *120*(7), 5355–5376, doi:10.1002/2015JA021285.

Christensen, A. B. (2003), Initial observations with the Global Ultraviolet Imager (GUVI) in the NASA TIMED satellite mission, *Journal of Geophysical Research*, *108*(A12), 1451, doi:10.1029/2003JA009918.

Cliver, E. W., Y. Kamide, and A. G. Ling (2000), Mountains versus valleys: Semiannual variation of geomagnetic activity, *Journal of Geophysical Research*, *105*(A2), 2413, doi:10.1029/1999JA900439.

Cnossen, I., and M. Förster (2016), North-ncessouth asymmetries in the polar thermosphere-ionosphere system: Solar cycle and seasonal influe, *Journal of Geophysical Research: Space Physics*, *121*(1), 612–627, doi:10.1002/2015JA021750.

Cnossen, I., and A. D. Richmond (2012), How changes in the tilt angle of the geomagnetic dipole affect the coupled magnetosphere-ionosphere-thermosphere system, *Journal of Geophysical Research*, *117*(A10), A10,317, doi:10.1029/2012JA018056.

Cnossen, I., A. D. Richmond, M. Wiltberger, W. Wang, and P. Schmitt (2011), The response of the coupled magnetosphere-ionosphere-thermosphere system to a 25% reduction in the dipole moment of the Earth's magnetic field, *Journal of Geophysical Research*, *116*(A12), A12,304, doi:10.1029/2011JA017063.

Cnossen, I., A. D. Richmond, and M. Wiltberger (2012a), The dependence of the coupled magnetosphere-ionosphere-thermosphere system on the Earth's magnetic dipole moment, *Journal of Geophysical Research: Space Physics*, *117*(5), n/a–n/a, doi:10.1029/2012JA017555.

Cnossen, I., M. Wiltberger, and J. E. Ouellette (2012b), The effects of seasonal and diurnal variations in the Earth's magnetic dipole orientation on solar windmagnetosphere-ionosphere coupling, *Journal of Geophysical Research*, *117*(A11), A11,211, doi:10.1029/2012JA017825.

Codrescu, M. V., T. J. Fuller-Rowell, and J. C. Foster (1995), On the importance of E-field variability for Joule heating in the high-latitude thermosphere, *Geophysical Research Letters*, *22*(17), 2393–2396, doi:10.1029/95GL01909.

Conde, M., and R. W. Smith (1995), Mapping thermospheric winds in the auroral zone, *Geophysical Research Letters*, *22*(22), 3019–3022, doi:10.1029/95GL02437.

Cowley, S. W. H. (2000), Magnetosphere-ionosphere interactions: A tutorial review, pp. 91–106, American Geophysical Union, doi:10.1029/GM118p0091.

Daglis, I., G. Balasis, N. Ganushkina, F.-A. Metallinou, M. Palmroth, R. Pirjola, and I. Tsagouri (2009), Investigating dynamic coupling in geospace through the combined use of modeling, simulations and data analysis, *Acta Geophysica*, *57*(1), doi:10.2478/s11600-008-0055-5.

DeJong, A. D. (2014), Steady magnetospheric convection events: How much does steadiness matter?, *Journal of Geophysical Research: Space Physics*, *119*(6), 4389–4399, doi:10.1002/2013JA019220.

DeJong, A. D., A. J. Ridley, and C. R. Clauer (2008), Balanced reconnection intervals: four case studies, *Annales Geophysicae*, *26*(12), 3897–3912, doi:10.5194/angeo-26-3897-2008.

Deng, W., T. L. Killeen, A. G. Burns, and R. G. Roble (1991), The flywheel effect: Ionospheric currents after a geomagnetic storm, *Geophysical Research Letters*, *18*(10), 1845–1848, doi:10.1029/91GL02081.

Deng, Y., and A. J. Ridley (2007), Possible reasons for underestimating Joule heating in global models: E field variability, spatial resolution, and vertical velocity, *Journal of Geophysical Research*, *112*(A9), A09,308, doi:10.1029/2006JA012006.

Deng, Y., T. J. Fuller-Rowell, R. A. Akmaev, and A. J. Ridley (2011), Impact of the altitudinal Joule heating distribution on the thermosphere, *Journal of Geophysical Research: Space Physics*, *116*(A5), 313, doi:10.1029/2010JA016019.

Deng, Y., T. J. Fuller-Rowell, A. J. Ridley, D. Knipp, and R. E. Lopez (2013), Theoretical study: Influence of different energy sources on the cusp neutral density enhancement, *Journal of Geophysical Research: Space Physics*, *118*(5), 2340–2349, doi:10.1002/jgra.50197.

Deng, . (2006), Examining the high latitude thermosphere and ionosphere using a global model, *ProQuest Dissertations And Theses; Thesis (Ph.D.)–University of Michigan*.

Deng, ., and . Ridley (2005), Ionospheric positive and negative storm phases: Dependence on the vertical ion transport, tongue of ionization and neutral advection, *American Geophysical Union*.

Dessler, A. J., and E. N. Parker (1959), Hydromagnetic theory of geomagnetic storms, *Journal of Geophysical Research*, *64*(12), 2239–2252, doi:10.1029/JZ064i012p02239.

Dickinson, R. E., E. C. Ridley, and R. G. Roble (1981), A three-dimensional general circulation model of the thermosphere, *Journal of Geophysical Research*, *86*(A3), 1499, doi:10.1029/JA086iA03p01499.

Donnelly, R. F. (1967), The solar flare radiations responsible for sudden frequency deviations, *Journal of Geophysical Research*, *72*(21), 5247–5256, doi:10.1029/JZ072i021p05247.

Drob, D. P., et al. (2008), An empirical model of the Earth's horizontal wind fields: HWM07, *Journal of Geophysical Research: Space Physics*, *113*(A12), n/a–n/a, doi:10.1029/2008JA013668.

Dungey, J. (1961), Interplanetary Magnetic Field and the Auroral Zones, *Physical Review Letters*, *6*(2), 47–48, doi:10.1103/PhysRevLett.6.47.

Ebihara, Y., and M. Ejiri (1998), Modeling of solar wind control of the ring current buildup: A case study of the magnetic storms in April 1997, *Geophysical Research Letters*, *25*(20), 3751–3754, doi:10.1029/1998GL900006.

Ebihara, Y., and M. Ejiri (2000), Simulation study on fundamental properties of the storm-time ring current, *Journal of Geophysical Research: Space Physics*, *105*(A7), 15,843–15,859, doi:10.1029/1999JA900493.

Ebihara, Y., M. Fok, R. A. Wolf, T. J. Immel, and T. E. Moore (2004), Influence of ionosphere conductivity on the ring current, *Journal of Geophysical Research*, *109*(A8), A08,205, doi:10.1029/2003JA010351.

Erickson, P. J., J. C. Foster, and J. M. Holt (2002), Inferred electric field variability in the polarization jet from Millstone Hill E region coherent scatter observations, *Radio Science*, *37*(2), 11–1–11–14, doi:10.1029/2000RS002531.

Fejer, B., D. Farley, R. Woodman, and C. Calderon (1979), Dependence of equatorial F region vertical drifts on season and solar cycle, *Journal of Geophysical Research*, *84*(A10), 5792, doi:10.1029/JA084iA10p05792.

Fesen, C. G., R. E. Dickinson, and R. G. Roble (1986), Simulation of the thermospheric tides at equinox with the National Center for Atmospheric Research Thermospheric General Circulation Model, *Journal of Geophysical Research*, *91*(A4), 4471, doi:10.1029/JA091iA04p04471.

Fesen, C. G., R. G. Roble, and M.-L. Duboin (1995), Simulations of seasonal and geomagnetic activity effects at Saint Santin, *Journal of Geophysical Research*, *100*(A11), 21,397, doi:10.1029/95JA01211.

Finlay, C. C., et al. (2010), International Geomagnetic Reference Field: the eleventh generation, *Geophysical Journal International*, *183*(3), 1216–1230, doi:10.1111/j.1365-246X.2010.04804.x.

Fok, M.-C., and T. E. Moore (1997), Ring current modeling in a realistic magnetic field configuration, *Geophysical Research Letters*, *24*(14), 1775–1778, doi:10.1029/97GL01255.

Fok, M. C., J. U. Kozyra, A. F. Nagy, C. E. Rasmussen, and G. V. Khazanov (1993), Decay of equatorial ring current ions and associated aeronomical consequences, *Journal of Geophysical Research: Space Physics*, *98*(A11), 19,381–19,393, doi:10.1029/93JA01848.

Fok, M.-C., T. E. Moore, J. U. Kozyra, G. C. Ho, and D. C. Hamilton (1995), Three-Dimensional Ring Current Decay Model, *Journal of Geophysical Research*, *100*(A6), 9619, doi:10.1029/94JA03029.

Fok, M.-C., R. A. Wolf, R. W. Spiro, and T. E. Moore (2001), Comprehensive computational model of Earth's ring current, *Journal of Geophysical Research: Space Physics*, *106*(A5), 8417–8424, doi:10.1029/2000JA000235.

Fok, M.-C., N. Y. Buzulukova, S.-H. Chen, A. Glocer, T. Nagai, P. Valek, and J. D. Perez (2014), The Comprehensive Inner Magnetosphere-Ionosphere Model, *Journal of Geophysical Research: Space Physics*, *119*(9), 7522–7540, doi:10.1002/2014JA020239.

Forbes, J. M. (1996), Planetary Waves in the Thermosphere-Ionosphere System., *Journal of geomagnetism and geoelectricity*, *48*(1), 91–98, doi:10.5636/jgg.48.91.

Forbes, J. M., S. E. Palo, and X. Zhang (2000), Variability of the ionosphere, *Journal of Atmospheric and Solar-Terrestrial Physics*, *62*(8), 685–693, doi:10.1016/S1364-6826(00)00029-8.

Förster, M., and I. Cnossen (2013), Upper atmosphere differences between northern and southern high latitudes: The role of magnetic field asymmetry, *Journal of Geophysical Research: Space Physics*, *118*(9), 5951–5966, doi:10.1002/jgra.50554.

Förster, M., and S. Haaland (2015), Interhemispheric differences in ionospheric convection: Cluster EDI observations revisited, *Journal of Geophysical Research: Space Physics*, *120*(7), 5805–5823, doi:10.1002/2014JA020774.

Foster, J. C. (2002), Average characteristics and activity dependence of the subauroral polarization stream, *Journal of Geophysical Research*, *107*(A12), 1475, doi:10.1029/2002JA009409.

Foster, J. C., and W. J. Burke (2002), SAPS: A new categorization for sub-auroral electric fields, *Eos, Transactions American Geophysical Union*, *83*(36), 393, doi:10.1029/2002EO000289.

Foster, J. C., J. M. Holt, R. G. Musgrove, and D. S. Evans (1986), Ionospheric convection associated with discrete levels of particle precipitation, *Geophysical Research Letters*, *13*(7), 656–659, doi:10.1029/GL013i007p00656.

Foster, J. C., P. J. Erickson, A. J. Coster, S. Thaller, J. Tao, J. R. Wygant, and J. W. Bonnell (2014), Storm time observations of plasmasphere erosion flux in the magnetosphere and ionosphere, *Geophysical Research Letters*, *41*(3), 762–768, doi:10.1002/2013GL059124.

Frank, L. A. (1967), On the extraterrestrial ring current during geomagnetic storms, *Journal of Geophysical Research*, *72*(15), 3753–3767, doi:10.1029/JZ072i015p03753.

Fuller-Rowell, T., M. Codrescu, C. Minter, and D. Strickland (2006), Application of thermospheric general circulation models for space weather operations, *Advances in Space Research*, *37*(2), 401–408, doi:10.1016/j.asr.2005.12.020.

Fuller-Rowell, T. J., and D. S. Evans (1987a), Height-integrated Pedersen and Hall conductivity patterns inferred from the TIROS-NOAA satellite data, *Journal of Geophysical Research*, *92*(A7), 7606, doi:10.1029/JA092iA07p07606.

Fuller-Rowell, T. J., and D. S. Evans (1987b), Height-integrated Pedersen and Hall conductivity patterns inferred from the TIROS-NOAA satellite data, *Journal of Geophysical Research*, *92*(A7), 7606, doi:10.1029/JA092iA07p07606.

Fuller-Rowell, T. J., and D. S. Evans (1987c), Height-integrated Pedersen and Hall conductivity patterns inferred from the TIROS-NOAA satellite data, *Journal of Geophysical Research*, *92*(A7), 7606, doi:10.1029/JA092iA07p07606.

Fuller-Rowell, T. J., D. Rees, T. J. Fuller-Rowell, and D. Rees (1980), A Three-Dimensional Time-Dependent Global Model of the Thermosphere, *Journal of the Atmospheric Sciences*, *37*(11), 2545–2567, doi:10.1175/1520-0469(1980)037¡2545:ATDTDG¿2.0.CO;2.

Fuller-Rowell, T. J., D. Rees, S. Quegan, R. J. Moffett, and G. J. Bailey (1988), Simulations of the seasonal and universal time variations of the high-latitude thermosphere and ionosphere using a coupled, three-dimensional, model, *Pure and Applied Geophysics PAGEOPH*, *127*(2-3), 189–217, doi:10.1007/BF00879811.

Fuller-Rowell, T. J., M. V. Codrescu, R. J. Moffett, and S. Quegan (1994), Response of the thermosphere and ionosphere to geomagnetic storms, *Journal of Geophysical Research*, *99*(A3), 3893, doi:10.1029/93JA02015.

Galand, M., and A. D. Richmond (2001), Ionospheric electrical conductances produced by auroral proton precipitation, *Journal of Geophysical Research: Space Physics*, *106*(A1), 117–125, doi:10.1029/1999JA002001.

Gannon, J., and J. Love (2011), USGS 1-min Dst index, *Journal of Atmospheric and Solar-Terrestrial Physics*, *73*(2-3), 323–334, doi:10.1016/j.jastp.2010.02.013.

Gardiner, W. G. (1969), Origin of the Term Ionosphere, *Nature*, *224*(5224), 1096–1096, doi:10.1038/2241096a0.

Garner, T., G. Crowley, and R. Wolf (2007), The impact of stormtime changes in the non-auroral conductance upon the low- and mid-latitude electric field, *Journal of Atmospheric and Solar-Terrestrial Physics*, *69*(10), 1200–1212, doi:10.1016/j.jastp.2006.09.010.

Garner, T. W., B. T. Taylor, T. L. Gaussiran, W. R. Coley, M. R. Hairston, and F. J. Rich (2010), Statistical behavior of the topside electron density as determined from DMSP observations: A probabilistic climatology, *Journal of Geophysical Research*, *115*(A7), A07,306, doi:10.1029/2009JA014695.

Gold, T. (1959), Motions in the magnetosphere of the Earth, *Journal of Geophysical Research*, *64*(9), 1219–1224, doi:10.1029/JZ064i009p01219.

Goncharenko, L. P., J. L. Chau, H.-L. Liu, and A. J. Coster (2010), Unexpected connections between the stratosphere and ionosphere, *Geophysical Research Letters*, *37*(10), n/a–n/a, doi:10.1029/2010GL043125.

Gough, M. P., P. J. Christiansen, G. Martelli, and E. J. Gershuny (1979), Interaction of electrostatic waves with warm electrons at the geomagnetic equator, *Nature*, *279*(5713), 515–517, doi:10.1038/279515a0.

Greenspan, M. E., C. E. Rasmussen, W. J. Burke, and M. A. Abdu (1991), Equatorial density depletions observed at 840 km during the great magnetic storm of March 1989, *Journal of Geophysical Research: Space Physics*, *96*(A8), 13,931–13,942, doi:10.1029/91JA01264.

Greenwald, R. A., et al. (1995), DARN/SuperDARN, *Space Science Reviews*, *71*(1-4), 761–796, doi:10.1007/BF00751350.

Groves, G., and J. M. Forbes (1984), Equinox tidal heating of the upper atmosphere, *Planetary and Space Science*, *32*(4), 447–456, doi:10.1016/0032-0633(84)90124-7.

Gu, X., Y. Y. Shprits, and B. Ni (2012), Parameterized lifetime of radiation belt electrons interacting with lower-band and upper-band oblique chorus waves, *Geophysical Research Letters*, *39*(15), doi:10.1029/2012GL052519.

Gussenhoven, M. S., D. A. Hardy, and W. J. Burke (1981), DMSP/F2 electron observations of equatorward auroral boundaries and their relationship to magnetospheric electric fields, *Journal of Geophysical Research*, *86*(A2), 768, doi:10.1029/JA086iA02p00768.

Hagan, M. E., and J. M. Forbes (2002), Migrating and nonmigrating diurnal tides in the middle and upper atmosphere excited by tropospheric latent heat release, *Journal of Geophysical Research*, *107*(D24), 4754, doi:10.1029/2001JD001236.

Hagan, M. E., and J. M. Forbes (2003), Migrating and nonmigrating semidiurnal tides in the upper atmosphere excited by tropospheric latent heat release, *Journal of Geophysical Research: Space Physics*, *108*(A2), doi:10.1029/2002JA009466.

Hairston, M. R., R. A. Heelis, and F. J. Rich (1998), Analysis of the ionospheric cross polar cap potential drop using DMSP data during the National Space Weather Program study period, *Journal of Geophysical Research: Space Physics*, *103*(A11), 26,337–26,347, doi:10.1029/97JA03241.

Hajj, G. A., B. D. Wilson, C. Wang, X. Pi, and I. G. Rosen (2004), Data assimilation of ground GPS total electron content into a physics-based ionospheric model by use of the Kalman filter, *Radio Science*, *39*(1), n/a–n/a, doi:10.1029/2002RS002859.

Hardy, D. A. (1984), Precipitating electron and ion detectors (SSJ/4) for the block 5D/flights 6-10 DMSP satellites: calibration and data presentation, *Rep. AFGL-TR-84-0317*.

Hardy, D. A., M. S. Gussenhoven, R. Raistrick, and W. J. McNeil (1987), Statistical and functional representations of the pattern of auroral energy flux, number flux, and conductivity, *Journal of Geophysical Research*, *92*(A11), 12,275, doi:10.1029/JA092iA11p12275.

Harel, M., R. A. Wolf, R. W. Spiro, P. H. Reiff, C.-K. Chen, W. J. Burke, F. J. Rich, and M. Smiddy (1981), Quantitative simulation of a magnetospheric substorm 2. Comparison with observations, *Journal of Geophysical Research*, *86*(A4), 2242, doi:10.1029/JA086iA04p02242.

Hedin, A. E. (1983), A Revised thermospheric model based on mass spectrometer and incoherent scatter data: MSIS-83, *Journal of Geophysical Research*, *88*(A12), 10,170, doi:10.1029/JA088iA12p10170.

Hedin, A. E. (1987), MSIS-86 Thermospheric Model, *Journal of Geophysical Research*, *92*(A5), 4649, doi:10.1029/JA092iA05p04649.

Hedin, A. E. (1991), Extension of the MSIS Thermosphere Model into the middle and lower atmosphere, *Journal of Geophysical Research*, *96*(A2), 1159, doi:10.1029/90JA02125.

Hedin, A. E., and G. R. Carignan (1985), Morphology of thermospheric composition variations in the quiet polar thermosphere from Dynamics Explorer measurements, *Journal of Geophysical Research*, *90*(A6), 5269, doi:10.1029/JA090iA06p05269.

Hedin, A. E., and H. G. Mayr (1973), Magnetic control of the near equatorial neutral thermosphere, *Journal of Geophysical Research*, *78*(10), 1688–1691, doi:10.1029/JA078i010p01688.

Hedin, A. E., H. G. Mayr, C. A. Reber, N. W. Spencer, and G. R. Carignan (1974), Empirical model of global thermospheric temperature and composition based on data from the Ogo 6 quadrupole mass spectrometer, *Journal of Geophysical Research*, *79*(1), 215–225, doi:10.1029/JA079i001p00215.

Heelis, R. A., J. K. Lowell, and R. W. Spiro (1982), A model of the high-latitude ionospheric convection pattern, *Journal of Geophysical Research*, *87*(A8), 6339, doi:10.1029/JA087iA08p06339.

Huang, Y., A. D. Richmond, Y. Deng, and R. Roble (2012), Height distribution of Joule heating and its influence on the thermosphere, *Journal of Geophysical Research*, *117*(A8), A08,334, doi:10.1029/2012JA017885.

Huba, J. D., and G. Joyce (2010), Global modeling of equatorial plasma bubbles, *Geophysical Research Letters*, *37*(17), n/a–n/a, doi:10.1029/2010GL044281.

Huba, J. D., and S. Sazykin (2014), Storm time ionosphere and plasmasphere structuring: SAMI3-RCM simulation of the 31 March 2001 geomagnetic storm, *Geophysical Research Letters*, *41*(23), 8208–8214, doi:10.1002/2014GL062110.

Huba, J. D., G. Joyce, and J. A. Fedder (2000), Sami2 is Another Model of the Ionosphere (SAMI2): A new low-latitude ionosphere model, *Journal of Geophysical Research: Space Physics*, *105*(A10), 23,035–23,053, doi:10.1029/2000JA000035.

Ilie, R., M. W. Liemohn, G. Toth, and R. M. Skoug (2012), Kinetic model of the inner magnetosphere with arbitrary magnetic field, *Journal of Geophysical Research: Space Physics*, *117*(A4), n/a–n/a, doi:10.1029/2011JA017189.

Ilie, R., M. W. Liemohn, G. Toth, N. Yu Ganushkina, and L. K. S. Daldorff (2015), Assessing the role of oxygen on ring current formation and evolution through numerical experiments, *Journal of Geophysical Research: Space Physics*, *120*(6), 4656–4668, doi:10.1002/2015JA021157.

Immel, T. J. (2005), Global storm time plasma redistribution imaged from the ground and space, *Geophysical Research Letters*, *32*(3), L03,107, doi: 10.1029/2004GL021120.

Immel, T. J., and A. J. Mannucci (2013), Ionospheric redistribution during geomagnetic storms, *Journal of Geophysical Research: Space Physics*, *118*(12), 7928–7939, doi:10.1002/2013JA018919.

Immel, T. J., G. Crowley, C. L. Hackert, J. D. Craven, and R. G. Roble (2006), Effect of IMF B y on thermospheric composition at high and middle latitudes: 2. Data comparisons, *Journal of Geophysical Research*, *111*(A10), A10,312, doi: 10.1029/2005JA011372.

Immel, T. J., S. L. England, X. Zhang, J. M. Forbes, and R. DeMajistre (2009), Upward propagating tidal effects across the E- and F-regions of the ionosphere, *Earth, Planets and Space*, *61*(4), 505–512, doi:10.1186/BF03353167.

Jacchia, L. G. (1974), Variations in thermospheric composition: A model based on mass spectrometer and satellite drag data, *Journal of Geophysical Research*, *79*(13), 1923–1927, doi:10.1029/JA079i013p01923.

Jakowski, N., V. Wilken, S. Schlueter, S. Stankov, and S. Heise (2005), Ionospheric space weather effects monitored by simultaneous ground and space based GNSS signals, *Journal of Atmospheric and Solar-Terrestrial Physics*, *67*(12), 1074–1084, doi:10.1016/j.jastp.2005.02.023.

Johnson, C. Y. (1966), Ionospheric composition and density from 90 to 1200 kilometers at solar minimum, *Journal of Geophysical Research*, *71*(1), 330–332, doi: 10.1029/JZ071i001p00330.

Jordanova, V. K. (2003), Ring current asymmetry from global simulations using a high-resolution electric field model, *Journal of Geophysical Research*, *108*(A12), 1443, doi:10.1029/2003JA009993.

Jordanova, V. K., and Y. Miyoshi (2005), Relativistic model of ring current and radiation belt ions and electrons: Initial results, *Geophysical Research Letters*, *32*(14), n/a–n/a, doi:10.1029/2005GL023020.

Jordanova, V. K., L. M. Kistler, J. U. Kozyra, G. V. Khazanov, and A. F. Nagy (1996), Collisional losses of ring current ions, *Journal of Geophysical Research*, *101*(A1), 111, doi:10.1029/95JA02000.

Jordanova, V. K., J. Albert, and Y. Miyoshi (2008), Relativistic electron precipitation by EMIC waves from self-consistent global simulations, *Journal of Geophysical Research: Space Physics*, *113*(A3), n/a–n/a, doi:10.1029/2008JA013239.

Kaeppler, S. R., D. L. Hampton, M. J. Nicolls, A. Strømme, S. C. Solomon, J. H. Hecht, and M. G. Conde (2015), An investigation comparing ground-based techniques that quantify auroral electron flux and conductance, *Journal of Geophysical Research: Space Physics*, *120*(10), 9038–9056, doi:10.1002/2015JA021396.

Katus, R. M., M. W. Liemohn, E. L. Ionides, R. Ilie, D. Welling, and L. K. Sarno-Smith (2015), Statistical analysis of the geomagnetic response to different solar wind drivers and the dependence on storm intensity, *Journal of Geophysical Research: Space Physics*, *120*(1), 310–327, doi:10.1002/2014JA020712.

Kennel, C. F. (1969), Consequences of a magnetospheric plasma, *Reviews of Geophysics*, *7*(1, 2), 379, doi:10.1029/RG007i001p00379.

Khazanov, G. V., M. W. Liemohn, T. S. Newman, M. Fok, and R. W. Spiro (2003), Self-consistent magnetosphere-ionosphere coupling: Theoretical studies, *Journal of Geophysical Research*, *108*(A3), 1122, doi:10.1029/2002JA009624.

Kistler, L. M., F. M. Ipavich, D. C. Hamilton, G. Gloeckler, B. Wilken, G. Kremser, and W. Stüdemann (1989), Energy spectra of the major ion species in the ring current during geomagnetic storms, *Journal of Geophysical Research*, *94*(A4), 3579, doi:10.1029/JA094iA04p03579.

Klein, L. W., and L. F. Burlaga (1982), Interplanetary magnetic clouds At 1 AU, *Journal of Geophysical Research*, *87*(A2), 613, doi:10.1029/JA087iA02p00613.

Knudsen, W. C. (1974), Magnetospheric convection and the high-latitude F ₂ ionosphere, *Journal of Geophysical Research*, *79*(7), 1046–1055, doi:10.1029/JA079i007p01046.

Kozyra, J. U., M.-C. Fok, E. R. Sanchez, D. S. Evans, D. C. Hamilton, and A. F. Nagy (1998), The role of precipitation losses in producing the rapid early recovery phase of the Great Magnetic Storm of February 1986, *Journal of Geophysical Research*, *103*(A4), 6801, doi:10.1029/97JA03330.

Kozyra, J. U., M. W. Liemohn, C. R. Clauer, A. J. Ridley, M. F. Thomsen, J. E. Borovsky, J. L. Roeder, V. K. Jordanova, and W. D. Gonzalez (2002), Multi-step Dst development and ring current composition changes during the 4-6 June 1991 magnetic storm, *Journal of Geophysical Research: Space Physics*, *107*(A8), SMP 33–1–SMP 33–22, doi:10.1029/2001JA000023.

Krall, J., and J. D. Huba (2013), SAMI3 simulation of plasmasphere refilling, *Geophysical Research Letters*, *40*(11), 2484–2488, doi:10.1002/grl.50458.

Kronberg, E. A., et al. (2014), Circulation of Heavy Ions and Their Dynamical Effects in the Magnetosphere: Recent Observations and Models, *Space Science Reviews*, *184*(1-4), 173–235, doi:10.1007/s11214-014-0104-0.

Lanzerotti, L. J., K. LaFleur, C. G. Maclennan, and D. W. Maurer (1998), Geosynchronous spacecraft charging in January 1997, *Geophysical Research Letters*, *25*(15), 2967–2970, doi:10.1029/98GL00987.

Laundal, K. M., I. Cnossen, S. E. Milan, S. E. Haaland, J. Coxon, N. M. Pedatella, M. Förster, and J. P. Reistad (2016), NorthSouth Asymmetries in Earth's Magnetic Field, *Space Science Reviews*, pp. 1–33, doi:10.1007/s11214-016-0273-0.

Le, G., C. T. Russell, and K. Takahashi (2004), Morphology of the ring current derived from magnetic field observations, *Annales Geophysicae*, *22*(4), 1267–1295, doi:10.5194/angeo-22-1267-2004.

Lemon, C., R. A. Wolf, T. W. Hill, S. Sazykin, R. W. Spiro, F. R. Toffoletto, J. Birn, and M. Hesse (2004), Magnetic storm ring current injection modeled with the Rice Convection Model and a self-consistent magnetic field, *Geophysical Research Letters*, *31*(21), n/a–n/a, doi:10.1029/2004GL020914.

Liemohn, M. W., J. U. Kozyra, V. K. Jordanova, G. V. Khazanov, M. F. Thomsen, and T. E. Cayton (1999), Analysis of early phase ring current recovery mechanisms during geomagnetic storms, *Geophysical Research Letters*, *26*(18), 2845–2848, doi:10.1029/1999GL900611.

Liemohn, M. W., J. U. Kozyra, C. R. Clauer, and A. J. Ridley (2001a), Computational analysis of the near-Earth magnetospheric current system during two-phase decay storms, *Journal of Geophysical Research*, *106*(A12), 29,531, doi:10.1029/2001JA000045.

Liemohn, M. W., J. U. Kozyra, M. F. Thomsen, J. L. Roeder, G. Lu, J. E. Borovsky, and T. E. Cayton (2001b), Dominant role of the asymmetric ring current in producing the stormtime Dst *, *Journal of Geophysical Research*, *106*(A6), 10,883, doi:10.1029/2000JA000326.

Liemohn, M. W., A. J. Ridley, D. L. Gallagher, D. M. Ober, and J. U. Kozyra (2004), Dependence of plasmaspheric morphology on the electric field description during the recovery phase of the 17 April 2002 magnetic storm, *Journal of Geophysical Research*, *109*(A3), A03,209, doi:10.1029/2003JA010304.

Liemohn, M. W., A. J. Ridley, P. C. Brandt, D. L. Gallagher, J. U. Kozyra, D. M. Ober, D. G. Mitchell, E. C. Roelof, and R. DeMajistre (2005), Parametric analysis of nightside conductance effects on inner magnetospheric dynamics for the 17 April 2002 storm, *Journal of Geophysical Research*, *110*(A12), A12S22, doi:10.1029/2005JA011109.

Liemohn, M. W., A. J. Ridley, J. U. Kozyra, D. L. Gallagher, M. F. Thomsen, M. G. Henderson, M. H. Denton, P. C. Brandt, and J. Goldstein (2006), Analyzing electric field morphology through data-model comparisons of the Geospace Environment Modeling Inner Magnetosphere/Storm Assessment Challenge events, *Journal of Geophysical Research*, *111*(A11), A11S11, doi:10.1029/2006JA011700.

Liemohn, M. W., M. Jazowski, J. U. Kozyra, N. Ganushkina, M. F. Thomsen, and J. E. Borovsky (2010), CIR versus CME drivers of the ring current during intense magnetic storms, *Proceedings of the Royal Society A: Mathematical, Physical and Engineering Sciences*, *466*(2123), 3305–3328, doi:10.1098/rspa.2010.0075.

Liou, K., P. T. Newell, D. G. Sibeck, C.-I. Meng, M. Brittnacher, and G. Parks (2001), Observation of IMF and seasonal effects in the location of auroral substorm onset, *Journal of Geophysical Research*, *106*(A4), 5799, doi:10.1029/2000JA003001.

Liu, L., W. Wan, B. Ning, and M.-L. Zhang (2009a), Climatology of the mean total electron content derived from GPS global ionospheric maps, *Journal of Geophysical Research: Space Physics*, *114*(A6), n/a–n/a, doi:10.1029/2009JA014244.

Liu, L., B. Zhao, W. Wan, B. Ning, M.-L. Zhang, and M. He (2009b), Seasonal variations of the ionospheric electron densities retrieved from Constellation Observing System for Meteorology, Ionosphere, and Climate mission radio occultation measurements, *Journal of Geophysical Research: Space Physics*, *114*(A2), n/a–n/a, doi:10.1029/2008JA013819.

Liu, S., M. W. Chen, J. L. Roeder, L. R. Lyons, and M. Schulz (2005), Relative contribution of electrons to the stormtime total ring current energy content, *Geophysical Research Letters*, *32*(3), L03,110, doi:10.1029/2004GL021672.

Liuzzo, L. R., A. J. Ridley, N. J. Perlongo, E. J. Mitchell, M. Conde, D. L. Hampton, W. A. Bristow, and M. J. Nicolls (2015), High-latitude ionospheric drivers and their effects on wind patterns in the thermosphere, *Journal of Geophysical Research: Space Physics*, *120*(1), 715–735, doi:10.1002/2014JA020553.

Love, J. J., and J. L. Gannon (2009), Revised <I>D_{st}</I> and the epicycles of magnetic disturbance: 19582007, *Annales Geophysicae*, *27*(8), 3101–3131, doi:10.5194/angeo-27-3101-2009.

Lu, G., M. E. Hagan, K. Häusler, E. Doornbos, S. Bruinsma, B. J. Anderson, and H. Korth (2014), Global ionospheric and thermospheric response to the 5 April 2010 geomagnetic storm: An integrated data-model investigation, *Journal of Geophysical Research: Space Physics*, *119*(12), 10,358–10,375, doi:10.1002/2014JA020555.

Lunt, N., L. Kersley, and G. J. Bailey (1999), The influence of the protonosphere on GPS observations: Model simulations, *Radio Science*, *34*(3), 725–732, doi:10.1029/1999RS900002.

Lyon, J., J. Fedder, and C. Mobarry (2004), The Lyon-Fedder-Mobarry (LFM) global MHD magnetospheric simulation code, *Journal of Atmospheric and Solar-Terrestrial Physics*, *66*, 1333–1350, doi:10.1016/j.jastp.2004.03.020.

Lyons, L. R., R. M. Thorne, and C. F. Kennel (1972), Pitch-angle diffusion of radiation belt electrons within the plasmasphere, *Journal of Geophysical Research*, *77*(19), 3455–3474, doi:10.1029/JA077i019p03455.

Mandea, M., and M. Purucker (2005), Observing, Modeling, and Interpreting Magnetic Fields of the Solid Earth, *Surveys in Geophysics*, *26*(4), 415–459, doi: 10.1007/s10712-005-3857-x.

Mandea, M., et al. (2000), International Geomagnetic Reference Fieldthe eighth generation, *Earth, Planets and Space*, *52*(12), 1119–1124, doi:10.1186/BF03352342.

Mannucci, A. J. (2005), Dayside global ionospheric response to the major interplanetary events of October 2930, 2003 Halloween Storms, *Geophysical Research Letters*, *32*(12), L12S02, doi:10.1029/2004GL021467.

Mannucci, A. J., B. D. Wilson, D. N. Yuan, C. H. Ho, U. J. Lindqwister, and T. F. Runge (1998), A global mapping technique for GPS-derived ionospheric total electron content measurements, *Radio Science*, *33*(3), 565–582, doi: 10.1029/97RS02707.

Marklund, G. T. (2009), Electric fields and plasma processes in the Auroral downward current region, below, within, and above the acceleration region, *Space Science Reviews*, *142*(1-4), 1–21, doi:10.1007/s11214-008-9373-9.

Mayr, H. G., I. Harris, and N. W. Spencer (1978), Some properties of upper atmosphere dynamics, *Reviews of Geophysics*, *16*(4), 539–565, doi: 10.1029/RG016i004p00539.

McComas, D. J., S. J. Bame, B. L. Barraclough, J. R. Donart, R. C. Elphic, J. T. Gosling, M. B. Moldwin, K. R. Moore, and M. F. Thomsen (1993), Magnetospheric plasma analyzer: Initial three-spacecraft observations from geosynchronous orbit, *Journal of Geophysical Research: Space Physics*, *98*(A8), 13,453–13,465, doi: 10.1029/93JA00726.

McComas, ., . Bame, . Barker, . Feldman, . Phillips, . Riley, and . Griffee (1998), Solar Wind Electron Proton Alpha Monitor (SWEPAM) for the Advanced Composition Explorer, *Space Science Reviews*, (1), 563–612, doi:10.1023/A:1005040232597.

McIlwain, C. (1986), A Kp dependent equatorial electric field model, *Advances in Space Research*, *6*(3), 187–197, doi:10.1016/0273-1177(86)90331-5.

Meier, M. M., and M. Hubiak (2010), Measurements of the radiation quality factor Q at aviation altitudes during solar minimum (20062008), *Advances in Space Research*, *45*(9), 1178–1181, doi:10.1016/j.asr.2009.08.008.

Mendillo, M. (2006), Storms in the ionosphere: Patterns and processes for total electron content, *Reviews of Geophysics*, *44*(4), RG4001, doi:10.1029/2005RG000193.

Mendillo, M., H. Rishbeth, R. Roble, and J. Wroten (2002), Modelling F2-layer seasonal trends and day-to-day variability driven by coupling with the lower atmosphere, *Journal of Atmospheric and Solar-Terrestrial Physics*, *64*(18), 1911–1931, doi:10.1016/S1364-6826(02)00193-1.

Mendillo, M., C.-L. Huang, X. Pi, H. Rishbeth, and R. Meier (2005), The global ionospheric asymmetry in total electron content, *Journal of Atmospheric and Solar-Terrestrial Physics*, *67*(15), 1377–1387, doi:10.1016/j.jastp.2005.06.021.

Meredith, N. P., A. D. Johnstone, S. Szita, R. B. Horne, and R. R. Anderson (1999), Pancake electron distributions in the outer radiation belts, *Journal of Geophysical Research: Space Physics*, *104*(A6), 12,431–12,444, doi:10.1029/1998JA900083.

Meredith, N. P., R. B. Horne, A. D. Johnstone, and R. R. Anderson (2000), The temporal evolution of electron distributions and associated wave activity following substorm injections in the inner magnetosphere, *Journal of Geophysical Research: Space Physics*, *105*(A6), 12,907–12,917, doi:10.1029/2000JA900010.

Meredith, N. P., R. B. Horne, R. M. Thorne, D. Summers, and R. R. Anderson (2004), Substorm dependence of plasmaspheric hiss, *Journal of Geophysical Research*, *109*(A6), A06,209, doi:10.1029/2004JA010387.

Merkin, V. G., and J. G. Lyon (2010), Effects of the low-latitude ionospheric boundary condition on the global magnetosphere, *Journal of Geophysical Research: Space Physics*, *115*(A10), n/a–n/a, doi:10.1029/2010JA015461.

Middleton, H. R., S. E. Pryse, A. G. Wood, and R. Balthazor (2008), The role of the tongue-of-ionization in the formation of the poleward wall of the main trough in the European post-midnight sector, *Journal of Geophysical Research: Space Physics*, *113*(A2), n/a–n/a, doi:10.1029/2007JA012631.

Mikkelsen, I. S., T. S. Jørgensen, M. C. Kelley, M. F. Larsen, E. Pereira, and J. Vickrey (1981), Neutral winds and electric fields in the dusk auroral oval 1. Measurements, *Journal of Geophysical Research*, *86*(A3), 1513, doi:10.1029/JA086iA03p01513.

Millward, G. H., H. Rishbeth, T. J. Fuller-Rowell, A. D. Aylward, S. Quegan, and R. J. Moffett (1996), Ionospheric F ₂ layer seasonal and semiannual variations, *Journal of Geophysical Research: Space Physics*, *101*(A3), 5149–5156, doi:10.1029/95JA03343.

Mitchell, E. J., P. T. Newell, J. W. Gjerloev, and K. Liou (2013), OVATION-SM: A model of auroral precipitation based on SuperMAG generalized auroral electrojet and substorm onset times, *Journal of Geophysical Research: Space Physics*, *118*(6), 3747–3759, doi:10.1002/jgra.50343.

Miyoshi, Y. S., V. K. Jordanova, A. Morioka, M. F. Thomsen, G. D. Reeves, D. S. Evans, and J. C. Green (2006), Observations and modeling of energetic electron dynamics during the October 2001 storm, *Journal of Geophysical Research*, *111*(A11), A11S02, doi:10.1029/2005JA011351.

Moen, J., and A. Brekke (1993), The solar flux influence on quiet time conductances in the auroral ionosphere, *Geophysical Research Letters*, *20*(10), 971–974, doi:10.1029/92GL02109.

Moldwin, M. B., L. Downward, H. K. Rassoul, R. Amin, and R. R. Anderson (2002), A new model of the location of the plasmapause: CRRES results, *Journal of Geophysical Research*, *107*(A11), 1339, doi:10.1029/2001JA009211.

Moussas, X., J. Polygiannakis, P. Preka-Papadema, and G. Exarhos (2005), Solar cycles: A tutorial, *Advances in Space Research*, *35*(5), 725–738, doi:10.1016/j.asr.2005.03.148.

Muella, M. T. A. H., E. R. de Paula, P. R. Fagundes, J. A. Bittencourt, and Y. Sahai (2010), Thermospheric Meridional Wind Control on Equatorial Scintillations and the Role of the Evening F-Region Height Rise, EB Drift Velocities and F2-Peak Density Gradients, *Surveys in Geophysics*, *31*(5), 509–530, doi:10.1007/s10712-010-9101-3.

Muldrew, D. B. (1965), F -layer ionization troughs deduced from Alouette data, *Journal of Geophysical Research*, *70*(11), 2635–2650, doi:10.1029/JZ070i011p02635.

Müller, S., H. Lühr, and S. Rentz (2009), Solar and magnetospheric forcing of the low latitude thermospheric mass density as observed by CHAMP, *Annales Geophysicae*, *27*(5), 2087–2099, doi:10.5194/angeo-27-2087-2009.

Müller-Wodarg, I., A. Aylward, and T. Fuller-Rowell (2001), Tidal oscillations in the thermosphere: a theoretical investigation of their sources, *Journal of Atmospheric and Solar-Terrestrial Physics*, *63*(9), 899–914, doi:10.1016/S1364-6826(00)00202-9.

Newell, P. T., and J. W. Gjerloev (2011), Evaluation of SuperMAG auroral electrojet indices as indicators of substorms and auroral power, *Journal of Geophysical Research*, *116*(A12), A12,211, doi:10.1029/2011JA016779.

Newell, P. T., T. Sotirelis, and S. Wing (2009), Diffuse, monoenergetic, and broadband aurora: The global precipitation budget, *Journal of Geophysical Research: Space Physics*, *114*(A9), n/a–n/a, doi:10.1029/2009JA014326.

Newell, P. T., A. R. Lee, K. Liou, S.-I. Ohtani, T. Sotirelis, and S. Wing (2010), Substorm cycle dependence of various types of aurora, *Journal of Geophysical Research*, *115*(A9), A09,226, doi:10.1029/2010JA015331.

Ni, B., R. M. Thorne, R. B. Horne, N. P. Meredith, Y. Y. Shprits, L. Chen, and W. Li (2011a), Resonant scattering of plasma sheet electrons leading to diffuse auroral precipitation: 1. Evaluation for electrostatic electron cyclotron harmonic waves, *Journal of Geophysical Research: Space Physics*, *116*(A4), n/a–n/a, doi:10.1029/2010JA016232.

Ni, B., R. M. Thorne, N. P. Meredith, R. B. Horne, and Y. Y. Shprits (2011b), Resonant scattering of plasma sheet electrons leading to diffuse auroral precipitation: 2. Evaluation for whistler mode chorus waves, *Journal of Geophysical Research: Space Physics*, *116*(A4), n/a–n/a, doi:10.1029/2010JA016233.

Ni, B., J. Liang, R. M. Thorne, V. Angelopoulos, R. B. Horne, M. Kubyshkina, E. Spanswick, E. F. Donovan, and D. Lummerzheim (2012), Efficient diffuse auroral electron scattering by electrostatic electron cyclotron harmonic waves in the outer magnetosphere: A detailed case study, *Journal of Geophysical Research: Space Physics*, *117*(A1), n/a–n/a, doi:10.1029/2011JA017095.

Nopper, R. W., and R. L. Carovillano (1978), Polar-equatorial coupling during magnetically active periods, *Geophysical Research Letters*, *5*(8), 699–702, doi:10.1029/GL005i008p00699.

Odom, C. D., et al. (1997), ARIA II neutral flywheel-driven field-aligned currents in the postmidnight sector of the auroral oval: A case study, *Journal of Geophysical Research*, *102*(A5), 9749, doi:10.1029/97JA00098.

Orlova, K., and Y. Shprits (2014), Model of lifetimes of the outer radiation belt electrons in a realistic magnetic field using realistic chorus wave parameters, *Journal of Geophysical Research: Space Physics*, *119*(2), 770–780, doi:10.1002/2013JA019596.

Orlova, K., Y. Shprits, and M. Spasojevic (2016), New global loss model of energetic and relativistic electrons based on Van Allen Probes measurements, *Journal of Geophysical Research: Space Physics*, *121*(2), 1308–1314, doi:10.1002/2015JA021878.

Papitashvili, V. O., and F. J. Rich (2002), High-latitude ionospheric convection models derived from Defense Meteorological Satellite Program ion drift observations and parameterized by the interplanetary magnetic field strength and direction, *Journal of Geophysical Research: Space Physics*, *107*(A8), SIA 17–1–SIA 17–13, doi:10.1029/2001JA000264.

Parker, E. (1958), Dynamics of the Interplanetary Gas and Magnetic Fields., *apj*, *128*, 664, doi:10.1086/146579.

Paxton, L. J., et al. (1999), <title>Global ultraviolet imager (GUVI): measuring composition and energy inputs for the NASA Thermosphere Ionosphere Mesosphere Energetics and Dynamics (TIMED) mission</title>, in *SPIE's International Symposium on Optical Science, Engineering, and Instrumentation*, edited by A. M. Larar, pp. 265–276, International Society for Optics and Photonics, doi:10.1117/12.366380.

Paxton, L. J., et al. (2004), <title>GUVI: a hyperspectral imager for geospace</title>, in *Fourth International Asia-Pacific Environmental Remote Sensing Symposium 2004: Remote Sensing of the Atmosphere, Ocean, Environment, and Space*, edited by C. A. Nardell, P. G. Lucey, J.-H. Yee, and J. B. Garvin, pp. 228–240, International Society for Optics and Photonics, doi:10.1117/12.579171.

Perlongo, N. J., and A. J. Ridley (2016), Universal time effect in the response of the thermosphere to electric field changes, *Journal of Geophysical Research: Space Physics*, *121*(4), 3681–3698, doi:10.1002/2015JA021636.

Peterson, W. K., E. N. Stavros, P. G. Richards, P. C. Chamberlin, T. N. Woods, S. M. Bailey, and S. C. Solomon (2009), Photoelectrons as a tool to evaluate spectral variations in solar EUV irradiance over solar cycle timescales, *Journal of Geophysical Research: Space Physics*, *114*(A10), n/a–n/a, doi:10.1029/2009JA014362.

Pettigrew, E. D., S. G. Shepherd, and J. M. Ruohoniemi (2010), Climatological patterns of high-latitude convection in the Northern and Southern hemispheres: Dipole tilt dependencies and interhemispheric comparisons, *Journal of Geophysical Research: Space Physics*, *115*(A7), n/a–n/a, doi:10.1029/2009JA014956.

Peymirat, C. (2002), Neutral wind influence on the electrodynamic coupling between the ionosphere and the magnetosphere, *Journal of Geophysical Research*, *107*(A1), 1006, doi:10.1029/2001JA900106.

Pi, X., A. J. Mannucci, U. J. Lindqwister, and C. M. Ho (1997), Monitoring of global ionospheric irregularities using the Worldwide GPS Network, *Geophysical Research Letters*, *24*(18), 2283–2286, doi:10.1029/97GL02273.

Powell, K. G., P. L. Roe, T. J. Linde, T. I. Gombosi, and D. L. De Zeeuw (1999), A Solution-Adaptive Upwind Scheme for Ideal Magnetohydrodynamics, *Journal of Computational Physics*, *154*(2), 284–309, doi:10.1006/jcph.1999.6299.

Prölss, G. (1987), Storm-induced changes in the thermospheric composition at middle latitudes, *Planetary and Space Science*, *35*(6), 807–811, doi:10.1016/0032-0633(87)90041-9.

Prölss, G. W. (1980), Magnetic storm associated perturbations of the upper atmosphere: Recent results obtained by satellite-borne gas analyzers, *Reviews of Geophysics*, *18*(1), 183, doi:10.1029/RG018i001p00183.

Pulkkinen, A., et al. (2017), Geomagnetically induced currents: Science, engineering and applications readiness, *Space Weather*, doi:10.1002/2016SW001501.

Qian, L., S. C. Solomon, and T. J. Kane (2009), Seasonal variation of thermospheric density and composition, *Journal of Geophysical Research: Space Physics*, *114*(A1), n/a–n/a, doi:10.1029/2008JA013643.

Qian, L., A. G. Burns, S. C. Solomon, and W. Wang (2013), Annual/semiannual variation of the ionosphere, *Geophysical Research Letters*, *40*(10), 1928–1933, doi:10.1002/grl.50448.

Qian, L., A. G. Burns, W. Wang, S. C. Solomon, and Y. Zhang (2016), Longitudinal variations of thermospheric composition at the solstices, *Journal of Geophysical Research: Space Physics*, *121*(7), 6818–6829, doi:10.1002/2016JA022898.

Rawer, K., D. Bilitza, and S. Ramakrishnan (1978), Goals and status of the International Reference Ionosphere, *Reviews of Geophysics*, *16*(2), 177, doi:10.1029/RG016i002p00177.

Rees, D., and T. J. Fuller-Rowell (1989), The Response of the Thermosphere and Ionosphere to Magnetospheric Forcing, *Philosophical Transactions of the Royal Society A: Mathematical, Physical and Engineering Sciences*, *328*(1598), 139–171, doi:10.1098/rsta.1989.0029.

Reigber, C., H. Lühr, and P. Schwintzer (2002), CHAMP mission status, *Advances in Space Research*, *30*(2), 129–134, doi:10.1016/S0273-1177(02)00276-4.

Rentz, S., and H. Lühr (2008), Climatology of the cusp-related thermospheric mass density anomaly, as derived from CHAMP observations, *Annales Geophysicae*, *26*(9), 2807–2823, doi:10.5194/angeo-26-2807-2008.

Rich, F. J., and M. Hairston (1994), Large-scale convection patterns observed by DMSP, *Journal of Geophysical Research*, *99*(A3), 3827, doi:10.1029/93JA03296.

Richards, P. G., J. A. Fennelly, and D. G. Torr (1994), EUVAC: A solar EUV Flux Model for aeronomic calculations, *Journal of Geophysical Research*, *99*(A5), 8981, doi:10.1029/94JA00518.

Richmond, A. (1992), Assimilative mapping of ionospheric electrodynamics, *Advances in Space Research*, *12*(6), 59–68, doi:10.1016/0273-1177(92)90040-5.

Richmond, A. D., and S. Matsushita (1975), Thermospheric response to a magnetic substorm, *Journal of Geophysical Research*, *80*(19), 2839–2850, doi:10.1029/JA080i019p02839.

Richmond, A. D., and J. P. Thayer (2000), Ionospheric electrodynamics: A tutorial, pp. 131–146, American Geophysical Union, doi:10.1029/GM118p0131.

Rideout, W., and A. Coster (2006), Automated GPS processing for global total electron content data, *GPS Solutions*, *10*(3), 219–228, doi:10.1007/s10291-006-0029-5.

Ridley, A., Y. Deng, and G. Tóth (2006), The global ionospherethermosphere model, *Journal of Atmospheric and Solar-Terrestrial Physics*, *68*(8), 839–864, doi:10.1016/j.jastp.2006.01.008.

Ridley, A. J., and M. W. Liemohn (2002), A model-derived storm time asymmetric ring current driven electric field description, *Journal of Geophysical Research: Space Physics*, *107*(A8), SMP 2–1–SMP 2–12, doi:10.1029/2001JA000051.

Ridley, A. J., G. Crowley, and C. Freitas (2000), An empirical model of the ionospheric electric potential, *Geophysical Research Letters*, *27*(22), 3675–3678, doi:10.1029/1999GL011161.

Ridley, A. J., T. I. Gombosi, and D. L. DeZeeuw (2004a), Ionospheric control of the magnetosphere: conductance, *Annales Geophysicae*, *22*(2), 567–584, doi:10.5194/angeo-22-567-2004.

Ridley, A. J., T. I. Gombosi, and D. L. DeZeeuw (2004b), Ionospheric control of the magnetosphere: conductance, *Annales Geophysicae*, *22*(2), 567–584, doi: 10.5194/angeo-22-567-2004.

Rishbeth, H. (1998), How the thermospheric circulation affects the ionospheric F2-layer, *Journal of Atmospheric and Solar-Terrestrial Physics*, *60*(14), 1385–1402, doi:10.1016/S1364-6826(98)00062-5.

Rishbeth, H. (2004), Questions of the equatorial F2-layer and thermosphere, *Journal of Atmospheric and Solar-Terrestrial Physics*, *66*(17), 1669–1674, doi: 10.1016/j.jastp.2004.07.008.

Rishbeth, H. (2006), F-region links with the lower atmosphere?, *Journal of Atmospheric and Solar-Terrestrial Physics*, *68*(3), 469–478, doi: 10.1016/j.jastp.2005.03.017.

Rishbeth, H., and M. Mendillo (2001), Patterns of F2-layer variability, *Journal of Atmospheric and Solar-Terrestrial Physics*, *63*(15), 1661–1680, doi:10.1016/S1364-6826(01)00036-0.

Rishbeth, H., and I. C. F. Müller-Wodarg (1999), Vertical circulation and thermospheric composition: a modelling study, *Annales Geophysicae*, *17*(6), 794–805, doi:10.1007/s00585-999-0794-x.

Rishbeth, H., T. Fuller-Rowell, and D. Rees (1987), Diffusive equilibrium and vertical motion in the thermosphere during a severe magnetic storm : A computational study, *Planetary and Space Science*, *35*(9), 1157–1165, doi:10.1016/0032-0633(87)90022-5.

Rishbeth, ., . Ganguly, and . Walker (1978), Field-aligned and field-perpendicular velocities in the ionospheric F2-layer, *Journal of Atmospheric and Terrestrial Physics*, *40*, 767–784.

Ritter, P., H. Lühr, and E. Doornbos (2010), Substorm-related thermospheric density and wind disturbances derived from CHAMP observations, *Annales Geophysicae*, *28*(6), 1207–1220, doi:10.5194/angeo-28-1207-2010.

Robinson, R. M., R. R. Vondrak, K. Miller, T. Dabbs, and D. Hardy (1987), On calculating ionospheric conductances from the flux and energy of precipitating electrons, *Journal of Geophysical Research*, *92*(A3), 2565, doi:10.1029/JA092iA03p02565.

Roble, R. G., and E. C. Ridley (1987), An auroral model for the NCAR thermospheric general circulation model (TIGCM), *Annales Geophysicae*.

Roble, R. G., and E. C. Ridley (1994), A thermosphere-ionosphere-mesosphere-electrodynamics general circulation model (time-GCM): Equinox solar cycle minimum simulations (30-500 km), *Geophysical Research Letters*, *21*(6), 417–420, doi: 10.1029/93GL03391.

Roble, R. G., R. E. Dickinson, and E. C. Ridley (1982), Global circulation and temperature structure of thermosphere with high-latitude plasma convection, *Journal of Geophysical Research*, *87*(A3), 1599, doi:10.1029/JA087iA03p01599.

Roble, R. G., E. C. Ridley, and R. E. Dickinson (1987), On the global mean structure of the thermosphere, *Journal of Geophysical Research*, *92*(A8), 8745, doi:10.1029/JA092iA08p08745.

Roble, R. G., E. C. Ridley, A. D. Richmond, and R. E. Dickinson (1988), A coupled thermosphere/ionosphere general circulation model, *Geophysical Research Letters*, *15*(12), 1325–1328, doi:10.1029/GL015i012p01325.

Roeder, J. L., and H. C. Koons (1989), A survey of electron cyclotron waves in the magnetosphere and the diffuse auroral electron precipitation, *Journal of Geophysical Research*, *94*(A3), 2529, doi:10.1029/JA094iA03p02529.

Russell, C. T., and R. L. McPherron (1973), Semiannual variation of geomagnetic activity, *Journal of Geophysical Research*, *78*(1), 92–108, doi:10.1029/JA078i001p00092.

Sabine, E. (1856), On the periodical laws discoverable in the mean effects of the larger geomagnetic disturbanc, *Philos. Trans. R. Soc. London*, *146*(357).

Sato, T., and G. F. Rourke (1964), F -region enhancements in the Antarctic, *Journal of Geophysical Research*, *69*(21), 4591–4607, doi:10.1029/JZ069i021p04591.

Scherliess, L., D. C. Thompson, and R. W. Schunk (2008), Longitudinal variability of low-latitude total electron content: Tidal influences, *Journal of Geophysical Research: Space Physics*, *113*(A1), n/a–n/a, doi:10.1029/2007JA012480.

Schield, M. A., J. W. Freeman, and A. J. Dessler (1969), A source for field-aligned currents at auroral latitudes, *Journal of Geophysical Research*, *74*(1), 247–256, doi:10.1029/JA074i001p00247.

Schulz, M. (1974), Particle lifetimes in strong diffusion, *Astrophysics and Space Science*, *31*(1), 37–42, doi:10.1007/BF00642599.

Schumaker, T. L., M. S. Gussenhoven, D. A. Hardy, and R. L. Carovillano (1989), The relationship between diffuse auroral and plasma sheet electron distributions near local midnight, *Journal of Geophysical Research: Space Physics*, *94*(A8), 10,061–10,078, doi:10.1029/JA094iA08p10061.

Schunk, R., L. Scherliess, J. J. Sojka, D. C. Thompson, and L. Zhu (2005), Ionospheric Weather Forecasting on the Horizon, *Space Weather*, *3*(8), n/a–n/a, doi:10.1029/2004SW000138.

Schunk, ., and . Nagy (2004), Ionospheres, *Ionospheres*.

Sckopke, N. (1966), A general relation between the energy of trapped particles and the disturbance field near the Earth, *Journal of Geophysical Research*, *71*(13), 3125–3130, doi:10.1029/JZ071i013p03125.

Shepherd, S. G. (2014), Altitude-adjusted corrected geomagnetic coordinates: Definition and functional approximations, *Journal of Geophysical Research: Space Physics*, *119*(9), 7501–7521, doi:10.1002/2014JA020264.

Shim, J. S., et al. (2012), CEDAR Electrodynamics Thermosphere Ionosphere (ETI) Challenge for systematic assessment of ionosphere/thermosphere models: Electron density, neutral density, NmF2, and hmF2 using space based observations, *Space Weather*, *10*(10), n/a–n/a, doi:10.1029/2012SW000851.

Shprits, Y. Y., S. R. Elkington, N. P. Meredith, and D. A. Subbotin (2008a), Review of modeling of losses and sources of relativistic electrons in the outer radiation belt I: Radial transport, *Journal of Atmospheric and Solar-Terrestrial Physics*, *70*(14), 1679–1693, doi:10.1016/j.jastp.2008.06.008.

Shprits, Y. Y., D. A. Subbotin, N. P. Meredith, and S. R. Elkington (2008b), Review of modeling of losses and sources of relativistic electrons in the outer radiation belt II: Local acceleration and loss, *Journal of Atmospheric and Solar-Terrestrial Physics*, *70*(14), 1694–1713, doi:10.1016/j.jastp.2008.06.014.

Singh, A. K., R. Rawat, and B. M. Pathan (2013), On the UT and seasonal variations of the standard and SuperMAG auroral electrojet indices, *Journal of Geophysical Research: Space Physics*, *118*(8), 5059–5067, doi:10.1002/jgra.50488.

Smith, ., . L'Heureux, . Ness, . Acuña, . Burlaga, and . Scheifele (1998), The ACE Magnetic Fields Experiment, *Space Science Reviews*, (1), 613–632, doi:10.1023/A:1005092216668.

Sojka, J., and R. Schunk (1997), Simulations of high latitude ionospheric climatology, *Journal of Atmospheric and Solar-Terrestrial Physics*, *59*(2), 207–229, doi:10.1016/S1364-6826(96)00037-5.

Sojka, J. J., M. David, R. W. Schunk, and R. A. Heelis (2012), A modeling study of the longitudinal dependence of storm time midlatitude dayside total electron content enhancements, *Journal of Geophysical Research: Space Physics*, *117*(A2), n/a–n/a, doi:10.1029/2011JA017000.

Spiro, R. W., R. A. Heelis, and W. B. Hanson (1978), Ion convection and the formation of the mid-latitude F region ionization trough, *Journal of Geophysical Research*, *83*(A9), 4255, doi:10.1029/JA083iA09p04255.

Stern, D. P. (1975), The motion of a proton in the equatorial magnetosphere, *Journal of Geophysical Research*, *80*(4), 595–599, doi:10.1029/JA080i004p00595.

Strickland, D. J., R. R. Meier, R. L. Walterscheid, J. D. Craven, A. B. Christensen, L. J. Paxton, D. Morrison, and G. Crowley (2004), Quiet-time seasonal behavior of the thermosphere seen in the far ultraviolet dayglow, *Journal of Geophysical Research*, *109*(A1), A01,302, doi:10.1029/2003JA010220.

Strickland, D. J., et al. (2007), Constraining and validating the Oct/Nov 2003 X-class EUV flare enhancements with observations of FUV dayglow and E -region electron densities, *Journal of Geophysical Research: Space Physics*, *112*(A6), n/a–n/a, doi:10.1029/2006JA012074.

Sugiura, M., T. Kamei, A. Berthelier, and M. Menvielle (1991), Equatorial Dst Index: 1957-1986.

Sutton, E. K. (2009), Normalized Force Coefficients for Satellites with Elongated Shapes, *Journal of Spacecraft and Rockets*, *46*(1), 112–116, doi:10.2514/1.40940.

Sutton, E. K., R. S. Nerem, and J. M. Forbes (2007), Density and Winds in the Thermosphere Deduced from Accelerometer Data, *Journal of Spacecraft and Rockets*, *44*(6), 1210–1219, doi:10.2514/1.28641.

Testud, J., P. Amayenc, and M. Blanc (1975), Middle and low latitude effects of auroral disturbances from incoherent-scatter, *Journal of Atmospheric and Terrestrial Physics*, *37*(6-7), 989–1009, doi:10.1016/0021-9169(75)90011-2.

Thayer, J. P. (1998), Height-resolved Joule heating rates in the high-latitude E region and the influence of neutral winds, *Journal of Geophysical Research*, *103*(A1), 471, doi:10.1029/97JA02536.

Thayer, J. P., G. Crowley, R. J. Niciejewski, T. L. Killeen, J. Buchau, and B. W. Reinisch (1995), Ground-based observations of ion/neutral coupling at Thule and Qânâq, Greenland, *Journal of Geophysical Research*, *100*(A7), 12,189, doi:10.1029/95JA00131.

Themens, D. R., P. T. Jayachandran, M. J. Nicolls, and J. W. MacDougall (2014), A top to bottom evaluation of IRI 2007 within the polar cap, *Journal of Geophysical Research: Space Physics*, *119*(8), 6689–6703, doi:10.1002/2014JA020052.

Thomas, E. G., J. B. H. Baker, J. M. Ruohoniemi, L. B. N. Clausen, A. J. Coster, J. C. Foster, and P. J. Erickson (2013), Direct observations of the role of convection electric field in the formation of a polar tongue of ionization from storm enhanced density, *Journal of Geophysical Research: Space Physics*, *118*(3), 1180–1189, doi:10.1002/jgra.50116.

Thomas, E. G., J. B. H. Baker, J. M. Ruohoniemi, A. J. Coster, and S.-R. Zhang (2016), The geomagnetic storm time response of GPS total electron content in the North American sector, *Journal of Geophysical Research: Space Physics*, *121*(2), 1744–1759, doi:10.1002/2015JA022182.

Thorne, R. M., B. Ni, X. Tao, R. B. Horne, and N. P. Meredith (2010), Scattering by chorus waves as the dominant cause of diffuse auroral precipitation., *Nature*, *467*(7318), 943–6, doi:10.1038/nature09467.

Toffoletto, F., S. Sazykin, R. Spiro, and R. Wolf (2003a), Inner magnetospheric modeling with the Rice Convection Model, *ssr*, *107*, 175–196, doi:10.1023/A:1025532008047.

Toffoletto, F., S. Sazykin, R. Spiro, and R. Wolf (2003b), Inner magnetospheric modeling with the Rice Convection Model, *Space Science Reviews*, *107*(1/2), 175–196, doi:10.1023/A:1025532008047.

Tóth, G., et al. (2005), Space Weather Modeling Framework: A new tool for the space science community, *Journal of Geophysical Research*, *110*(A12), A12,226, doi:10.1029/2005JA011126.

Tóth, G., et al. (2012), Adaptive numerical algorithms in space weather modeling, *Journal of Computational Physics*, *231*(3), 870–903, doi:10.1016/j.jcp.2011.02.006.

Tsurutani, B. (2004), Global dayside ionospheric uplift and enhancement associated with interplanetary electric fields, *Journal of Geophysical Research*, *109*(A8), A08,302, doi:10.1029/2003JA010342.

Tsurutani, B. T., O. P. Verkhoglyadova, A. J. Mannucci, G. S. Lakhina, G. Li, and G. P. Zank (2009), A brief review of solar flare effects on the ionosphere, *Radio Science*, *44*(1), n/a–n/a, doi:10.1029/2008RS004029.

Tsyganenko, N. A., H. J. Singer, and J. C. Kasper (2003), Storm-time distortion of the inner magnetosphere: How severe can it get?, *Journal of Geophysical Research: Space Physics*, *108*(A5), doi:10.1029/2002JA009808.

Vasyliunas, V. M. (1970), Mathematical Models of Magnetospheric Convection and its Coupling to the Ionosphere, pp. 60–71, Springer Netherlands, doi:10.1007/978-94-010-3284-1_6.

Vasylinas, V. M. (2005), Meaning of ionospheric Joule heating, *Journal of Geophysical Research*, *110*(A2), A02,301, doi:10.1029/2004JA010615.

Vasylinas, V. M. (2012), The physical basis of ionospheric electrodynamics, *Annales Geophysicae*, *30*(2), 357–369, doi:10.5194/angeo-30-357-2012.

Vladimer, J. A., P. Jastrzebski, M. C. Lee, P. H. Doherty, D. T. Decker, and D. N. Anderson (1999), Longitude structure of ionospheric total electron content at low latitudes measured by the TOPEX/Poseidon satellite, *Radio Science*, *34*(5), 1239–1260, doi:10.1029/1999RS900060.

Volland, H. (1973), A semiempirical model of large-scale magnetospheric electric fields, *Journal of Geophysical Research*, *78*(1), 171–180, doi:10.1029/JA078i001p00171.

Volland, H. (1995), *Handbook of atmospheric electrodynamics*, CRC Press.

Wang, C., G. Hajj, X. Pi, I. G. Rosen, and B. Wilson (2004), Development of the Global Assimilative Ionospheric Model, *Radio Science*, *39*(1), n/a–n/a, doi: 10.1029/2002RS002854.

Wang, H., A. J. Ridley, and J. Zhu (2015), Theoretical study of zonal differences of electron density at midlatitudes with GITM simulation, *Journal of Geophysical Research: Space Physics*, *120*(4), 2951–2966, doi:10.1002/2014JA020790.

Wang, W., T. Killeen, A. Burns, and R. Roble (1999), A high-resolution, three-dimensional, time dependent, nested grid model of the coupled thermosphereionosphere, *Journal of Atmospheric and Solar-Terrestrial Physics*, *61*(5), 385–397, doi: 10.1016/S1364-6826(98)00079-0.

Wang, W., J. Lei, A. G. Burns, M. Wiltberger, A. D. Richmond, S. C. Solomon, T. L. Killeen, E. R. Talaat, and D. N. Anderson (2008), Ionospheric electric field variations during a geomagnetic storm simulated by a coupled magnetosphere ionosphere thermosphere (CMIT) model, *Geophysical Research Letters*, *35*(18), L18,105, doi: 10.1029/2008GL035155.

Webb, D. F., N. U. Crooker, S. P. Plunkett, and O. C. St. Cyr (2001), The Solar Sources of Geoeffective Structures, pp. 123–141, American Geophysical Union, doi: 10.1029/GM125p0123.

Weimer, D. R. (1996), A flexible, IMF dependent model of high-latitude electric potentials having Space Weather applications, *Geophysical Research Letters*, *23*(18), 2549–2552, doi:10.1029/96GL02255.

Weimer, D. R. (2001), An improved model of ionospheric electric potentials including substorm perturbations and application to the Geospace Environment Modeling November 24, 1996, event, *Journal of Geophysical Research: Space Physics*, *106*(A1), 407–416, doi:10.1029/2000JA000604.

Weimer, D. R. (2005), Improved ionospheric electrodynamic models and application to calculating Joule heating rates, *Journal of Geophysical Research*, *110*(A5), A05,306, doi:10.1029/2004JA010884.

Weimer, D. R., C. K. Goertz, D. A. Gurnett, N. C. Maynard, and J. L. Burch (1985), Auroral zone electric fields from DE 1 and 2 at magnetic conjunctions, *J. Geophys. Res*, *90*(A8), 7479, doi:10.1029/JA090iA08p07479.

Weimer, D. R., D. A. Gurnett, C. K. Goertz, J. D. Menietti, J. L. Burch, and M. Sugiura (1987), The current-voltage relationship in auroral current sheets, *Journal of Geophysical Research: Space Physics*, *92*(A1), 187–194, doi:10.1029/JA092iA01p00187.

Welling, D. T., and S. G. Zaharia (2012), Ionospheric outflow and cross polar cap potential: What is the role of magnetospheric inflation?, *Geophysical Research Letters*, *39*(23), n/a–n/a, doi:10.1029/2012GL054228.

Welling, D. T., V. K. Jordanova, A. Glocer, G. Toth, M. W. Liemohn, and D. R. Weimer (2015a), The two-way relationship between ionospheric outflow and the ring current, *Journal of Geophysical Research: Space Physics*, *120*(6), 4338–4353, doi: 10.1002/2015JA021231.

Welling, D. T., et al. (2015b), The Earth: Plasma Sources, Losses, and Transport Processes, *Space Science Reviews*, *192*(1-4), 145–208, doi:10.1007/s11214-015-0187-2.

Wiltberger, M., W. Wang, A. Burns, S. Solomon, J. Lyon, and C. Goodrich (2004), Initial results from the coupled magnetosphere ionosphere thermosphere model: magnetospheric and ionospheric responses, *Journal of Atmospheric and Solar-Terrestrial Physics*, *66*(15), 1411–1423, doi:10.1016/j.jastp.2004.03.026.

Winglee, R. M., D. Chua, M. Brittnacher, G. K. Parks, and G. Lu (2002), Global impact of ionospheric outflows on the dynamics of the magnetosphere and cross-polar cap potential, *Journal of Geophysical Research*, *107*(A9), 1237, doi:10.1029/2001JA000214.

Wintoft, P. (2011), The variability of solar EUV: A multiscale comparison between sunspot number, 10.7cm flux, LASP MgII index, and SOHO/SEM EUV flux, *Journal of Atmospheric and Solar-Terrestrial Physics*, *73*(13), 1708–1714, doi: 10.1016/j.jastp.2011.03.009.

Wolf, R., R. Spiro, G.-H. Voigt, P. Reiff, C.-K. Chen, and M. Harel (1982), Computer simulation of inner magnetospheric dynamics for the magnetic storm of July 29, 1977, *jgr*, *87*, 5949–5962, doi:10.1029/JA087iA08p05949.

Wolf, R. A. (1970), Effects of ionospheric conductivity on convective flow of plasma in the magnetosphere, *Journal of Geophysical Research*, *75*(25), 4677–4698, doi: 10.1029/JA075i025p04677.

Wright, J. W. (1963), The F -region seasonal anomaly, *Journal of Geophysical Research*, *68*(14), 4379–4381, doi:10.1029/JZ068i014p04379.

Yang, N., et al. (2016), Statistical analysis of the mid-latitude trough position during different categories of magnetic storms and different storm intensities, *Earth, Planets and Space*, *68*(1), 171, doi:10.1186/s40623-016-0554-6.

Yizengaw, E., M. Moldwin, D. Galvan, B. Iijima, A. Komjathy, and A. Mannucci (2008), Global plasmaspheric TEC and its relative contribution to GPS TEC, *Journal of Atmospheric and Solar-Terrestrial Physics*, *70*(11), 1541–1548, doi: 10.1016/j.jastp.2008.04.022.

Young, D. T., H. Balsiger, and J. Geiss (1982), Correlations of magnetospheric ion composition with geomagnetic and solar activity, *Journal of Geophysical Research*, *87*(A11), 9077, doi:10.1029/JA087iA11p09077.

Yu, Y., and A. J. Ridley (2013), Exploring the influence of ionospheric O ⁺ outflow on magnetospheric dynamics: The effect of outflow intensity, *Journal of Geophysical Research: Space Physics*, *118*(9), 5522–5531, doi: 10.1002/jgra.50528.

Yu, Y., V. K. Jordanova, A. J. Ridley, J. M. Albert, R. B. Horne, and C. A. Jeffery (2016), A new ionospheric electron precipitation module coupled with RAM-SCB within the geospace general circulation model, *Journal of Geophysical Research: Space Physics*, *121*(9), 8554–8575, doi:10.1002/2016JA022585.

Zaharia, S., V. Jordanova, M. Thomsen, and G. Reeves (2008), Self-consistent geomagnetic storm simulation: The role of the induced electric fields, *Journal of Atmospheric and Solar-Terrestrial Physics*, *70*(2), 511–518, doi:10.1016/j.jastp.2007.08.067.

Zaharia, S., V. K. Jordanova, D. Welling, and G. Tóth (2010), Self-consistent inner magnetosphere simulation driven by a global MHD model, *Journal of Geophysical Research: Space Physics*, *115*(A12), n/a–n/a, doi:10.1029/2010JA015915.

Zeng, W., and J. L. Horwitz (2008), Storm enhanced densities (SED) as possible sources for Cleft Ion Fountain dayside ionospheric outflows, *Geophysical Research Letters*, *35*(4), L04,103, doi:10.1029/2007GL032511.

Zhang, J., et al. (2007), Solar and interplanetary sources of major geomagnetic storms (Dst 100 nT) during 1996-2005, *Journal of Geophysical Research: Space Physics*, *112*(A10), n/a–n/a, doi:10.1029/2007JA012321.

Zhang, S.-R., J. C. Foster, J. M. Holt, P. J. Erickson, and A. J. Coster (2012), Magnetic declination and zonal wind effects on longitudinal differences of ionospheric electron density at midlatitudes, *Journal of Geophysical Research: Space Physics*, *117*(A8), n/a–n/a, doi:10.1029/2012JA017954.

Zhang, X. X., C. Wang, T. Chen, Y. L. Wang, A. Tan, T. S. Wu, G. A. Germany, and W. Wang (2005), Global patterns of Joule heating in the high-latitude ionosphere, *Journal of Geophysical Research*, *110*(A12), A12,208, doi:10.1029/2005JA011222.

Zhao, B., et al. (2013), East-west differences in F -region electron density at midlatitude: Evidence from the Far East region, *Journal of Geophysical Research: Space Physics*, *118*(1), 542–553, doi:10.1029/2012JA018235.

Zheng, Y., P. C. Brandt, A. T. Y. Lui, and M.-C. Fok (2008), On ionospheric trough conductance and subauroral polarization streams: Simulation results, *Journal of Geophysical Research*, *113*(A4), A04,209, doi:10.1029/2007JA012532.

Zhou, Y., S. Ma, H. Lühr, C. Xiong, and C. Reigber (2009), An empirical relation to correct storm-time thermospheric mass density modeled by NRLMSISE-00 with CHAMP satellite air drag data, *Advances in Space Research*, *43*(5), 819–828, doi: 10.1016/j.asr.2008.06.016.

Zhu, J., and A. J. Ridley (2014), The effect of background conditions on the ionospheric response to solar flares, *Journal of Geophysical Research: Space Physics*, *119*(6), 5060–5075, doi:10.1002/2014JA019887.

Zhu, J., A. J. Ridley, and Y. Deng (2016), Simulating electron and ion temperature in a global ionosphere thermosphere model: Validation and modeling an idealized substorm, *Journal of Atmospheric and Solar-Terrestrial Physics*, *138-139*, 243–260, doi:10.1016/j.jastp.2016.01.005.

Zou, S., M. B. Moldwin, M. J. Nicolls, A. J. Ridley, A. J. Coster, E. Yizengaw, L. R. Lyons, and E. F. Donovan (2013), Electrodynamics of the high-latitude trough: Its relationship with convection flows and field-aligned currents, *Journal of Geophysical Research: Space Physics*, *118*(5), 2565–2572, doi:10.1002/jgra.50120.

Zou, S., M. B. Moldwin, A. J. Ridley, M. J. Nicolls, A. J. Coster, E. G. Thomas, and J. M. Ruohoniemi (2014), On the generation/decay of the storm-enhanced density plumes: Role of the convection flow and field-aligned ion flow, *Journal of Geophysical Research: Space Physics*, *119*(10), 8543–8559, doi:10.1002/2014JA020408.